THE STUDY OF TAYLOR-COUETTE FLOWS WITH SUPERIMPOSED ISOTHERMAL AND HEATED AXIAL FLOWS AT HIGH TAYLOR NUMBERS

Thesis by

Angela Chao-Hsuan Shih

In Partial Fulfillment of the Requirements

for the Degree of

Doctor of Philosophy

California Institute of Technology

Pasadena, California

1994

(Submitted March 17, 1994)

Acknowledgements

I would like thank my advisor, Professor Melany Hunt. She has guided me through this research with the greatest patience. In the past four years, we have been through some of the most important events in our lives: Professor Hunt giving birth to Claire, and my wedding. She encourages me when I am discouraged, and helps me when problems are encountered. I also want to thank Professor Allan Acosta for initializing this project, and for his valuable advice. I am also grateful to Professors E. John List, Edward Zukoski, and Rolf Sabersky for taking their valuable time to review my thesis and be a part of my examining committee. I also would like to thank Dr. S. Gopalakrishnan and Mr. Carl Reimers of the pump division in BW/IP International, who made this research possible.

I also would like to acknowledge my friends: I-Ming Chen, Sue Beatty, Shu-San Hsiau, Rajash Kedia, Venkatta Natarajan, Nick Glumac, Peter Pich, and Wen-Jean Hseuh for their help and support. I would like to thank Brian Rague for his help in electronic instruments. My thanks to Marty Gould, Mike Gerfen and George Yamamoto, who helped me design and build the experiment. Special thanks to Cecilia Lin who aided me in preparing some of the figures.

I would especially like to thank my parents. They taught me almost everything I know. Without them, I would not be the person I am today. I would like to thank Fuji,

who is a source of fun and joy when I am depressed. My deepest thanks go to my husband, Frank Wei. We were finally married in June, 1993. He is always behind me one hundred percent. He laughs with me and always provides a shoulder for me to cry on during sad moments.

My deepest regret is that my grandfather passed away in December, 1993, four months before I obtain my Ph.D. degree. I wish that he could have been here to share my joy.

Abstract

This experimental study investigates the effect of an isothermal or heated superimposed axial flow on a Taylor-Couette flow in an open, vertical annulus with the inner cylinder rotating. The tangential component of the velocity is measured using a hot-wire anemometer, and the velocity power spectra are calculated. The flows studied are for Taylor numbers ranging from 1.2×10^7 to 2.4×10^7, and the axial Reynolds number from 0 to 2500. At a low axial Reynolds number, the power spectrum of the velocity measurements shows a single dominant frequency. The frequency is indicative of the uniformly-spaced vortices passing through the anemometer, and roughly corresponds with the axial velocity divided by the vortex spacing. As the rotational speed is increased at a fixed axial flow rate, the dominant frequency decreases, indicating a change in the size of the vortices. As the axial Reynolds number is increased at a fixed rotational speed, the power spectra first indicate a decrease in the dominant frequency, and then a subsequent increase in the other frequencies. For very large axial flow rates, the power spectra indicate a broad distribution in frequencies.

The experiment also include the measurements of the transient and the local fluid temperatures, and the corresponding temperature spectra are calculated. Heating of the axial flow also changes the characteristic of the velocity spectra, where peaks at higher

frequencies emerge in the spectra. In heated flows, the peaks of the greatest spectral strength in the velocity and temperature spectra are different, possibly indicating that the largest temperature and velocity fluctuations occur in different directions. The average temperature measurements indicate that as the axial flow rate is increased, the mean temperature distribution curves shift upward. The temperature ratio, $(T_{max} - T_{min})/(T_{in} - T_{out})$, also increases with an increasing in the axial Reynolds numbers.

Table of Contents

List of Figures

List of Tables

Nomenclature

b gap width of the annulus

h annulus height

g gravitational constant

Gr_a Grashof number based on ΔT_a, $b^3 g\beta\Delta T_a/\nu^2$

Gr_h Grashof number based on ΔT_a, $h^3 g\beta\Delta T_a/\nu^2$

Gr_r Grashof number based on ΔT_r, $b^3 g\beta\Delta T_r/\nu^2$

l distance measured from the bottom of the annulus

Re_a axial Reynolds number, $2bw/\nu$

R rotational Reynolds number, $r_i\omega b/\nu = (Ta\ R_i/b)^{1/2}$

R_c critical rotational Reynolds number, $r_i\omega_c b/\nu$

R_i radius of inner cylinder

R_m mean radius, $(R_i + R_o)/2$

R_o radius of outer cylinder

r radial position, measured from the centerline of the inner cylinder

r' non-dimensional radius, $(r-R_i)/b$

T temperature

Ta Taylor number, $\omega^2 r_i b^3/\nu^2$

Ta_c critical Taylor number

U_i peripheral velocity of the inner cylinder

u tangential velocity

v radial velocity

w axial velocity

β coefficient of thermal expansion

δ_θ displacement thickness

ΔT_a temperature difference between the inlet and ambient

ΔT_r temperature difference across the annular gap

η radius ratio, R_i/R_o

λ wavelength

ν kinematic viscosity

ω rotational speed

Chapter 1

Introduction

1.1 Motivation

Flow in annulus formed by two concentric cylinders that rotate with respect to each other has been the focus of many analytical and experimental studies (Kataoka, 1985; DiPrima and Swinney, 1981). The nature of the flow is dependent on the geometry of the annulus (aspect ratio, h/b; radii ratio, $\eta \equiv R_i/R_o$), the end condition of the annulus (enclosed-end or throughflow), the axial flow velocity and the rotational speed. There are also many studies that analyze the effect of temperature on Taylor-Couette flow. This configuration occurs in various turbomachines in which a coolant is injected axially into the annulus to lubricate the shaft and to reduce the temperature of the rotating shaft. One example is the primary recirculating pump in the nuclear power plant. A simple layout of the pump is shown in Figure 1.1.

The pump is operated in an environment where the temperature exceeds 250 °C. Cold water at 60 °C is injected from the top of the shaft into the annular space between the rotating shaft and shaft cover. As hot water of 280 °C, driven by impeller motion, is pushed up the annulus from the bottom, a thermal mixing region between the cold and

the hot water is created. It is within this thermal mixing region that axial and circumferential cracks have been observed both on the shaft and shaft housing, also shown in Figure 1.1. In a study done by Gopalakrishnan et al. of the pump division for BW/IP International, Inc., it is determined that the cracks are mostly caused by large thermal fluctuations at frequencies below 25 Hz. In a series of papers by Kato et al. (1992, 1993), Watanabe et al. (1993), Narabayashi et al. (1993) and Shiina et al. (1993), the temperature fluctuation mechanisms and heat transfer characteristics of the recirculating pump were studied both analytically and experimentally. In their studies, a mock-up pump structure with similar dimensions as the full size pump was first constructed. It consisted of a pump cover, shaft, journal, hydrostatic bearing, mechanical shaft seal housing and a recirculating impeller. Hot water at 278 °C was maintained at 7 MPa by a nitrogen pressurizer and was supplied to the test section by an external pump. Cold water was introduced near the top of the shaft and flows downward through the clearance between the pump cover and shaft. Sixty thermocouples of 0.5 mm diameter are attached to the surface of the shaft and the shaft cover by silver brazing to measure the temperature fluctuations. The results of the mock- up test show that the mean axial temperature distribution curve shifts upward with increase of the rotating speed (Taylor number) and with decrease of the axial flow rate. The studies also suggested that the magnitude of the temperature fluctuations increases as the axial flow rate of the cold water injectant increases. They concluded that the large magnitude of the temperature fluctuation is the main cause of the cracks. The flow disturbance due to the effects of the axial flow and the rotating shaft near the lower end of the annulus gap was believed

to be the major cause of the temperature fluctuations. To solve the problem of large temperature fluctuations, a new device called the seal purge heater which heats the axial flow before being injected into the annulus was proposed. The performance of the seal purge heater was tested in a mock-up test, and was shown that it does reduce the magnitude of temperature fluctuations. A flow visualization study was also performed for flow near the heater area, and no vortices were observed. Nevertheless, to understand the fundamental driving factor in large temperature fluctuations and to further predict the steady and fluctuating shaft temperatures in such a configuration, the focus of the present work is to examine Taylor-Couette flows with a superimposed isothermal and heated-axial flows to determine the flow characteristics and the mixing of the axial coolant for a range of operating conditions.

1.2 Taylor-Couette Flow

The basic flow in a cylindrical annulus with the inner cylinder rotating and outer one at rest is known as the Couette flow. The Couette flow is stable when the rotational speed is low, and the velocity distribution is given by the following function:

$$v = w = 0 \quad \text{and} \quad u = Ar + \frac{B}{r} \tag{1.1}$$

$$\text{where} \quad A = -\frac{R_i^2}{R_o^2 - R_i^2}\,\omega \quad \text{and} \quad B = -\frac{R_i^2 R_o^2}{R_o^2 - R_i^2}\,\omega$$

In 1923, Taylor calculated the critical rotational speed at which the basic Couette flow becomes unstable resulting in a steady secondary motion in the form of cellular toroidal vortices (Taylor vortices). A non-dimensional parameter, the Taylor number, arises from

the problem when determining the critical rotational speed. The Taylor number, defined as $\omega^2 R_i b^3/\nu^2$, is an important parameter in terms of characterizing and predicting the behavior of the flow. The square root of the Taylor number, known as the modified Reynolds number R_m, is also often used. For an infinitely long annulus in which the gap spacing b is much smaller than the mean radius ($b << R_m$) and with the outer cylinder at rest, the critical Taylor number is approximately 1708 (Kataoka, 1985). The existence of the Taylor vortices have been confirmed by many visualization studies (Coles, 1965; Burkhalter and Koschmieder, 1973; Koschmieder, 1979).

As shown by Taylor, the rotational speeds of the cylinders are critical in influencing the flow in a concentric annulus. In 1965, in an apparatus with $\eta = 0.874$ ($\eta = R_i/R_o$) and $l/b = 27.9$, Coles investigated the effect of the rotational speeds of the inner and outer cylinder on Taylor-Couette flow. By increasing the rotational speed to approximately 20% greater than the critical value, a pattern of travelling waves that are periodic in the azimuthal direction is observed to appear on the vortices. He found that by varying the rotational speed of the inner cylinder slowly, there can be as many as 26 different states observed for a fixed rotational speed. In addition, while the rotational Reynolds number, $R = \omega R_i b/\nu$, is increased from 114 to 1348, the state of the flow is taken from 28 cells in the annulus column and 0 azimuthal wave to 18 cells and 3 waves. In this speed range, more than 70 transitions occur from one state to the other. Thus, Coles showed that the number of toroidal vortices and the number of travelling waves are not unique, but depend on the rotational speed of the inner cylinder and the initial conditions of the flow. However, regardless of the state of the flow, he discovered that

the angular speed of the azimuthal waves is always at 0.34 times the rotational speed of the inner cylinder.

It becomes difficult to distinguish different dynamical regimes in Taylor-Couette flow as rotational speed increases by only examining the time records of flow photograph or the velocity traces. In some cases, the spectral analysis of the velocity time series data can be helpful to identify the transitions from one flow regime to the other. Transitions that visualization results cannot identify can be detected by changes in the power spectra, such as the broadening of a spectral peak or the appearance of a new frequency. Therefore, many researchers examine the power spectra of velocities to study the different modes in Taylor-Couette flow.

As the rotational speed is increased from near criticality to near two orders of magnitude higher, Taylor-Couette flow undergoes several transitions before it finally becomes turbulent. To study the transition to turbulence, Fenstermacher, Swinney and Gollub (1979) used the technique of laser-Doppler velocimetry and examined the power spectra of the radial component of the velocity The experiment was performed using an enclosed cylindrical annulus with $l/b = 20$ and $\eta = 0.877$ with water at different temperatures as the working fluid. At just above the transition point from Couette flow at $R/R_c = 1.2$, similar to Coles' finding, Fenstermacher et al. observed that the flow is wavy vortex flow and the corresponding velocity power spectra contain a single frequency reflecting the azimuthal wave passing through the measurement point. Becayse only one frequency is observed in the power spectrum, this flow regime is often called the singly periodic or the singly wavy vortex mode. As the rotational speed is further increased, at

$R/R_c = 5.6$, the power spectra show a single dominant frequency and its harmonics. At $R/R_c = 10.06$, a second fundamental frequency is observed at a lower frequency and two orders of magnitudes less than the original one. At this point, the corresponding visualization results indicate that the vortices are still present, and there is an increase of the small scale structure in the flow. The first chaotic element in the flow is identified at $R/R_c \approx 12$ when a broad weak component is observed in the power spectra. And at $R/R_c = 21.9 \pm 0.2$, the power spectra do not show any sharp peaks although the broad weak component persists, which indicates that the azimuthal waves on the vortices have disappeared. This is confirmed by the visualization results. Moreover, measurements of the time-average of the velocity field reveals that even at $R/R_c = 43.9$, some form of the vortex structure still remains.

Gorman and Swinney (1982) were interested in studying the characteristics of flows just before the onset of weak turbulence in a Taylor Couette system. Within the range of flows that they studied, Gorman and Swinney discovered that in addition to the frequency reflecting the travelling azimuthal waves, there is a second fundamental frequency with a smaller magnitude present in the radial velocity spectrum using flow-visualization and spectral techniques. This second frequency corresponds to the frequency of modulation of the azimuthal waves. As a result, this flow regime just before the onset of turbulence is termed Modulated Wavy Vortex Flow regime (MWVF). As many as 12 distinct wave patterns were discovered by Gorman and Swinney in MWVF, and they are characterized by two integers m and k where m is the number of azimuthal waves and k is related to the modulation phase angle. When $k = 0$, all the azimuthal waves are

flattened rather than S-shaped, and when k = 1, successive waves are flattened in sequence.

Brandstater et al. (1983) tried to gain a better understanding of the dynamics of the Taylor-Couette system using time-delaying reconstruction techniques. In the process, they discovered that there is a low-dimensional strange attractor within the Taylor-Couette system. Later, the dimension of the attractors are calculated using experimental data (Brandstater and Swinney, 1987). In the experiment, the radial component of the velocity was determined using laser-Doppler velocimetry. Consequently, phase portrait, power spectra and circle maps are obtained from the velocity data to calculate the dimension of the attractor (Brandstater et al., 1983; Brandstater and Swinney, 1987). Brandstater and Swinney showed that the dimension of the attractor in the Taylor-Couette flow is 2.0 for modulated wave flow, and when $R/R_c > 11.7 \pm 0.2$, the dimension becomes a non-integer greater than 2, marking the onset of chaos. At $R/R_c = 12$ ($Ta/Ta_c = 144$), the dimension of the strange attractor is calculated to be 2.4. Moreover, when the rotational Reynolds number is increased beyond the onset of chaos ($R/R_c > 11.7$), the dimensions also increase. For $R/R_c = 20$, the dimension was calculated to be greater than 4.

The flows of interest in the present work are for rotational speeds significantly larger than the critical speed, approximately 10^4 Ta_c ($R/R_c \approx 100$). In an enclosed annulus, flows with Taylor numbers of this magnitude are referred to as turbulent Taylor vortex flows (Koschmieder, 1979; Barcilon et al., 1979; DiPrima and Swinney, 1981). For Taylor numbers greater than 400 Ta_c ($R > 20\ R_c$), the toroidal vortices are apparent, but the azimuthal waves on the vortices have disappeared. Burkhalter and Koschmieder

(1973) were interested in how changes in the annulus end conditions influenced the wavelength of the vortices at moderate and large Taylor numbers. Two vertical annuli with $\eta = 0.727$ and 0.505 and three different working fluids were used in the experiment, and a cathetometer was used to measure the size or height of the Taylor vortices. Burkhalter and Koschmieder tested the effects of three different end conditions: a non-rotating solid end boundary, rotating solid end boundary, and a free surface at the top end with either a rotating or non-rotating bottom end boundary. They observed that the size of the end cells does change. The change is independent of the sizes of the rest of the Taylor vortices in the fluid column, and is caused by the boundary conditions near the ends of the annulus. When the ends of the annulus are solid rotating boundaries, the size of the end cell increases with Taylor number when the flow is singly periodic. For non-rotating solid end conditions, the end cell size is independent of the Taylor number for Ta/Ta_c ranging from 1 to 80. Similarly, for the case of the top end being a free surface and the bottom end non-rotating, the size of the end cell remains unchanged as Taylor number is increased. In addition, Burkhalter and Koschmieder observed that at large Taylor numbers, for $Ta/Ta_c > 4695$, the number of vortices in the annulus decreases as Taylor number increases. This phenomenon is observed up to $Ta/Ta_c = 1.1 \times 10^4$. In a long annulus ($l/b \approx 125$) with stationary end conditions, Koschmieder (1979) also measured the wavelength of the toroidal vortices using visualization techniques by seeding aluminum powder in water. For $Ta > 100\ Ta_c$ ($R > R_c$), Koschmieder discovered that the wavelengths of the vortices have a clear-cut dependence on initial conditions. Moreover,

in both of the narrow and wide gap cases, for η = 0.896 and 0.727, the wavelengths are independent of the Taylor number.

Because of their interest in the flow characteristics of high-Taylor-number Couette flows, Barcilon et al. (1979) studied the vortex structures with Ta/Ta_c ranging from 10^3 to 10^5. Using an enclosed annulus with η = 0.908 and l/b = 65, Barcilon et al. observed azimuthal waves at the Taylor cell boundary at Ta/Ta_c = 1.24 until Ta/Ta_c = 445. A 'herring-bone'-like pattern was also observed as white streaks near the outer walls from the visualization results. Barcilon et al. suggested that the streaks are the Görtler vortices resulting from the centrifugal instability, and they are on a much smaller scale than the Taylor vortices. Furthermore, when the Taylor number is increased from 400 Ta_c to 8 x 10^4 Ta_c, the form of Taylor vortices are still visible. This demonstrates that even at high Taylor number, the Taylor-Couette flow nevertheless maintains a form of structure to some degree.

The studies by Smith and Townsend (1982) and Townsend (1984) examined flows for even higher Taylor numbers, between 10^4 and 10^6 times the critical value. In their experiments, a small axial flow, less than 0.5% of the rotating speed of the inner cylinder, was superimposed on the Taylor motion to convect the vortices past the fixed sensors. Their results suggested that for Taylor numbers less than 3 x 10^5 Ta_c, the flow remains axisymmetric. The flow consists of a system of toroidal vortices encircling the cylinder, and they are superimposed on a background of irregular noise. For $Ta/Ta_c > 5 \times 10^5$, the toroidal eddies become irregular and cannot be clearly distinguished.

1.3 Taylor-Couette Flow With An Isothermal Axial Flow

The system of Taylor Couette flow with an axial flow is found in many industrial problems of cooling rotating machinery and in applications in rotary chemical reactors and mixers. In additional to the Taylor number, the axial Reynolds number, defined as $Re_a = 2bw/\nu$, also helps characterize the flow. To investigate the effect of axial flows, Kaye and Elgar (1958) measured all three components of velocity using hot-wire anemometry in combination with visualization results. They identified that there are four flow modes over a range of Taylor and axial Reynolds numbers for adiabatic and diabatic flow conditions in the annulus. These modes are laminar flow, turbulent flow, laminar flow plus vortices, and turbulent flow plus vortices. Similar lines of demarcation for the four modes were also identified by Astill (1964) through quantitative measurements at different axial positions along the annulus. Using air as the working fluid and by injecting smoke into the annulus gap, Astill observed how the flow changes from one mode to the other for $Re_a < 600$. However, for $Re_a > 600$, it was impossible to observe the onset of turbulence through smoke injection. Consequently, hot-wire anemometer measurements were used. Astill found that the Taylor vortices originate near the inner wall. In addition, the distance from the entrance to the point where vortices originate increases with increasing axial Reynolds number, and decreases with increasing Taylor number. For a flow with a developing tangential boundary layer, the critical Taylor number Ta^* is based on displacement thickness, δ_θ^*, and the transition from Couette flow to vortex flow occurs when:

$$Ta^* \equiv \frac{\omega R_i \delta_\theta^*}{\nu}\left(\frac{\delta_\theta^*}{R_i}\right)^{1/2} > 24 \qquad (1.2)$$

The stability characteristics of flow between concentric rotating cylinders with an axial flow have been studied by several investigators. Chandrasekhar (1960, 1962), using a perturbation method to predict the onset of instability in a narrow gap, found a relationship between the critical Taylor number and the axial Reynolds number as:

$$Ta_c(Re_a) = Ta_c(Re_a = 0) + 26.5\ Re_a^2, \qquad \text{as } Re_a \rightarrow 0 \tag{1.3}$$

Snyder (1962) also investigated the effect of axial flow on the critical Taylor number. In a vertical annulus with $\eta = 0.95$ and $l/b = 285$ with water as the working fluid, Snyder showed that for $Re_a \leq 2$, the experimental results for the onset of the Taylor instability were in good agreement with the relationship found by Chandrasekhar. His results were within 5% with calculations by Chandrasekhar for Re_a between 5 and 40. However, for $Re_a > 40$, the discrepancy increases to 15%. DiPrima (1960) and Krueger and DiPrima (1964) also solved the eigenvalue problem using Galerkin method, and they found that the critical Taylor number increases as axial Reynolds number increases. However, Krueger and DiPrima discovered that their calculation produced results indicating a smaller critical Taylor number than those predicted by Chandrasekhar.

The onset of Taylor instability is observed by Astill (1964) in his visualization study as the 'first discernible ripple' in the velocity trace. It was also an indicator of flow transition from laminar to the laminar-plus-vortices mode. For axial Reynolds numbers ranging from 86 to 2000, Gravas and Martin (1978) measured the velocity using hot-wire anemometer in axial and tangential flows in annuli of radius of ratios 0.9, 0.81 and 0.576. They discovered that the instability first occurs close to the inner rotating cylinder, irrespective of the annulus radius ratio, the azimuthal orientation and the axial Reynolds

numbers. It then spreads outward radially as the Taylor number increases. Their results also indicate an increase in the critical Taylor number with increasing axial Reynolds number. For $Re_a = 2000$, the critical Taylor number is approximately $Ta_c \approx 10^5$, almost two orders of magnitude larger than without axial flow. For values of Re_a greater than 2000, a reduced dependence of the critical Taylor number on the axial flow is indicated. Sorour and Coney (1979a) also studied experimentally the effect of axial flow on the critical Taylor number for two annulus gap widths. They showed that for low axial flows, the Taylor instability first occurs in the center of the gap. At higher axial flow rates, the instability was first noticed near the inner, rotating cylinder.

Simmers and Coney (1979, 1980) studied the effects of a superimposed axial flow on the velocity distribution in a Taylor-Couette system. Using hot-wire anemometry, velocity profiles are measured in a vertical annulus with $\eta = 0.8$ and 0.955 for $Re_a = 400$ and 1200. They discovered that for adiabatic flow, the axial velocity profile is parabolic for Couette flow; however, after the onset of Taylor vortex flow, the axial profile becomes increasingly flattened as Re_a^2 increases. The tangential velocity profile in Couette flow is a straight line. As Ta is increased to beyond criticality, the tangential profile is characterized by a central region with a small velocity gradient bounded by regions of large gradient near the annulus walls.

When the axial flow is small, the Taylor vortices maintain their structures and drift with the axial flow. However, when the axial flow is slightly larger, the laminar Taylor vortices are observed to be tilted at an angle. This flow regime is called the spiral flow (Kataoka, 1981). Sorour and Coney (1979b) studied the evolution of high-Taylor-number

spiral flows with increasing Taylor numbers at a constant axial Reynolds number. In a vertical annulus with $\eta = 0.8$, the velocity power spectra were taken at two radial positions in the gap, at $r' = 0.3$ and 0.9, and in two directions, parallel and perpendicular to the axial flow. In an example with $Re_a = 100$, they showed that near the onset of instability, a single predominant frequency is first noted in the power spectrum near the inner rotating cylinder, indicating that the vortices originate near the inner cylinder. For a given axial Reynolds number in the range of $40 \leq Re_a \leq 400$ and for $2.5 \leq Ta/Ta_c \leq 7.7$, the spectra show multifrequency characteristics, indicating that the wavy mode exists for this range of Taylor number. When the Taylor number is increased to the range of $31 \leq Ta/Ta_c \leq 770$, the spectra show that the waviness has disappeared. Instead, only a single predominant frequency exists in the velocity spectra. The wavelengths and drift velocity of the vortices are also measured by Sorour and Coney. They showed that for Ta/Ta_c ranging from 50 to 770, both the drift velocity and the wavelengths of the Taylor cells increase as the Taylor number increases. In addition, they are the largest near the midgap of the annulus and the smallest near the outer cylinder.

Wan and Coney (1980, 1982abc) also studied the characteristics of spiral vortex flow in a series of papers. Calculating the velocity spectra for $Re_a = 500$, 1500, and 2500 for both narrow gap ($\eta = 0.955$) and wide gap ($\eta = 0.8$) cases, they showed in their 1980 paper that as the Taylor number increases, the initial spiral vortex flow breaks down into quasiperiodic mode, where azimuthal waves are observed on the vortex boundaries, and then to chaotic mode, where no significant peaks are observed in the velocity spectrum. However, at Taylor numbers of 10^6 and above, a re-emergence of order, the re-

establishment of turbulent vortex flow is observed for both the narrow and wide gap cases. In their subsequent paper (1982a), they performed a visualization study using oil. Wan and Coney confirmed their previous results of how the spiral vortex flow transitions to other flow modes. In another study (1982b), the velocity is measured in the Taylor-Couette system with axial flow and the corresponding power spectra and auto correlation are calculated. They presented the x-probe signal and the auto- and cross-correlogram for Ta = 1.0 x 10^4 to 1.22 x 10^7, η = 0.8 and Re_a = 500. They observed that when the flow is in the spiral vortex mode at Re_a = 500, the flow characteristics remain unchanged in both the axial and tangential direction with increasing Taylor numbers. In the turbulent vortex regime, at Ta = 1.22 x 10^7, the flow is more periodic in the axial direction than in the tangential direction. In a separate paper, Wan and Coney (1982c) also measured the radial velocity component. They calculated the power spectra and the auto-correlations and plotted the probability histogram to compute skewness and kurtosis. The velocity measurements were taken at r' = 0.25 and 0.75, for Re_a = 500 and Ta ranging from 1.05 x 10^4 to 1.25 x 10^7. Wan and Coney observed that axial flow reduces the radial velocity fluctuations and is stabilizing to the flow. In addition, when the flow is in the turbulent vortex mode, the vortices have the greatest intensity near the outer wall of the annular gap, whereas the spiral vortex instability is first observed near the inner wall.

1.4 Diabatic Taylor-Couette Flows

The inclusion of a temperature gradient may affect rotating flows in a vertical annulus in three different ways: through the density dependence of the centrifugal force, by

introducing natural convection, and by varying the fluid viscosity. Most of the previous non-isothermal studies have examined flows in an enclosed annulus with a temperature difference between the inner and outer cylinders. The experimental studies by Snyder and Karlsson (1965) and by Sorour and Coney (1979c) investigated the effect of the radial temperature gradient on the onset of the Taylor instability. The Snyder and Karlsson experiments demonstrated that if the temperature difference between the cylinders was small, the critical Taylor numbers are larger than for an isothermal flow, and the flow consists of toroidal vortices. However, if the temperature differences are more than a few degrees, the critical Taylor number decreases, and the flow is in the form of spiral cells. These results are independent of the direction of the temperature gradient. Moreover, the spiral cells arising from the thermal gradient are not the same as the spiral cells formed when an axial flow is imposed. In the latter case, the two cells which make up a wavelength of the disturbance are of equal widths while in the previous case, the cells are of unequal widths as described by Taylor (1923). The study by Sorour and Coney shows that the radial temperature gradient always decreases the critical Taylor number, and that the flow is always in the form of axisymmetric Taylor vortices for all conditions in which a radial temperature gradient exists.

The linear stability analyses by Ali and Weidman (1990) and Chen and Kuo (1990) indicate that the stability of the flows depends on the Taylor number, the Grashof number $Gr_r = b^3 g\beta\Delta T_r/\nu^2$ (ΔT_r is the temperature difference between the two cylinder), and the fluid Prandtl number. Ali and Weidman concluded that increasing Prandtl numbers decrease the stability of the Taylor-Couette system. The work by Chen and Kuo

confirms that by including both the dependence of the gravitational and centrifugal potentials on the density variation, the stability analysis qualitatively agrees with the experimental results of Snyder and Karlsson and less favorably of Sorour and Coney.

Interested in the nature of flow in the mixed convection region, Ball and Farouk (1989) and Ball et al. (1989) performed a flow visualization study, using smoke injected into the enclosed vertical annulus formed by concentric cylinders with $\eta = 0.438$ and stationary ends, to determine the effects of buoyancy on the development and structure of Taylor vortices. The inner rotating cylinder is heated with the outer cylinder kept isothermal creating a radial temperature gradient. They found that the qualitative behavior of the mixed convection flows is dependent upon the value of σ, defined as Gr_r/R^2. Ball et al. further suggested that the nature of the flows is determined completely by σ in the range of R and Gr_r studied; that is, the same flow behavior is observed regardless whether the experiment was performed with Gr_r held constant relative to increasing R or with R held constant with increasing Gr_r. In the case with a rotating inner cylinder, with $\sigma = 0.04$, evenly spaced pairs of counter-rotating cells are evident in the flow. The rotation of the vortex is considered positive when the flow next to the heated inner cylinder is in the upward direction. When σ is increased to 0.1, the size of the positive vortex has increased, and the ratio of the positive cell size to the negative one is measured to be 1.6. As σ is increased to values above 0.15, a transition to a helical waveform is observed. When $\sigma = 0.18$, the spiral cell is a single helical vortex with a pitch angle of approximately 20 degrees, and it turns with an angular velocity of approximately 0.04 times the rotational speed of the inner cylinder. At $\sigma = 0.3$, the flow returns to an

axisymmetric state that consists of pairs of counter-rotating cells with the size ratio between the positive and negative cells to be 3.3. The spiral form of flow is observed to be a transitory form for $0.15 < \sigma < 0.3$. As σ is increased to be above 0.3, the cellular structure in the flow is replaced by the formation of one large toroidal cell similar to those formed in natural convection flow.

The non-isothermal studies by Snyder (1965) and Sorour and Coney (1979c) also include experiments with a superimposed axial flow. The experiments by Snyder show that for $Re_a > 20$, the critical Taylor number with a radial temperature gradient are unchanged from the critical Taylor numbers in isothermal flow. The study by Sorour and Coney show similar results for their measurements in a narrow annulus (η=0.955). However, their wide-gap experiments ($\eta = 0.8$) show that the critical Taylor numbers are larger for a downward flow in an annulus with a temperature gradient than in an isothermal annulus or in a non-isothermal annulus with an upward flow. In addition, for the narrow gap case, a spiral cell in downward diabatic flow is more compressed at the same axial Reynolds number than in upward diabatic flow, and the wavenumbers in upward diabatic flow and adiabatic flow are similar. Increasing the axial Reynolds number compresses the spiral cells more for all flow conditions. For the wide gap case, the compression of the spiral cells increases with increase of temperature difference for downward axial flow, but the cells are less affected by temperature difference for upward axial flow. Increasing the axial Reynolds number also compresses the spiral cells for all thermal conditions for the narrow gap case, and the wave numbers all approach a common value when $Re_a \geq 350$. For the wide gap case, increasing the axial Reynolds

number allows the spiral cells to grow for the downward diabatic case, and the effect is just the opposite for both the adiabatic and diabatic upward cases. For $Re_a \geq 350$, the wave numbers for all flow conditions reach a constant.

1.5 Current Study

The current experiment simulates the flow configuration of the pump described in section 1.1. While it is impossible to duplicate the actual configuration, a model is established in terms of matching the relevant dimensionless parameters when the pump is operating under normal conditions. A list of these parameters is provided in Table 1.1. As shown in the table, in the attempt to match the non-dimensional parameters, air is used instead of water because it is less viscous and requires less power to rotate at the desired rotational speed. Hot air is injected axially from the bottom up the annulus instead of cold air being injected from the top since it is easier to heat air than to cool it for a large temperature difference. However, this should not affect the results since the direction of the density gradient is similar to that of the pump. The maximum temperature of air is limited by the softening temperature of the lucite outer cylinder. Note that comparable values are achieved for the Taylor number and the axial Reynolds number, but the Grashof number based on annulus height and vertical temperature difference is several orders of magnitude less in the current experiment. However, it will be determined later in the study whether this Grashof number is important or a different definition is more desirable.

The present study examines the effects of an isothermal or heated axial flow on Taylor vortices at large rotational speeds, from Ta = 1.1 x 10^7 to 2.4 x 10^7, and for axial Reynolds numbers between 0 and 2500. In this range of Taylor number, the flow is in the turbulent vortex mode. The results of the isothermal study are used as a basis for comparison with the diabatic study. The tangential velocity component is measured using a single wire probe at various axial and radial positions. A x-wire probe is also used to measure the tangential and axial velocity profiles. Thermocouples along the inner and outer cylindrical walls are used to measure the axial and radial temperature distribution in diabatic conditions. Transient temperature measurements are taken at similar location as the tangential velocity measurement using a very fine thermocouples. The corresponding velocity and temperature power spectra are then calculated using the fluctuating measurements.

Unlike previous studies, measurements are taken systematically as the axial flow rate is varied for a fixed rotational speed, and then as the rotational speed is increased at a fixed axial flow rate. Moreover, the impact of a superimposed isothermal or heated axial flow on the flow field of Taylor-Couette flow with the flow in the turbulent vortex mode has not been previously addressed.

Chapter 2

Experimental Apparatus and Procedures

2.1 Facility

The experimental setup consists of three main subsystems: the blower assembly, the test section, and the data acquisition system. A schematic of the setup is shown in Figure 2.1, and each subsystem will be described in detail below.

As shown in Figure 2.2, the blower assembly consists of a dc blower, a variac, a transformer, and a heater/air duct. The blower is connected to the inlet of the heater/air duct, and the outlet of the duct is connected to insulated aluminum ducts leading to the two sideports of the test section. Heated air then enters the test section through the two side ports.

The test section, as shown in Figure 2.3, is comprised of the two concentric vertical cylinders, the motor, the slip ring assembly, and the associated instrumentation and support structures. The inner rotating cylinder is made from a 20.96 cm O.D. aluminum tubing. The inner cylinder is machined with an uncertainty less than 0.005 cm. Also, insulation material is placed inside the aluminum tube to prevent heat losses. The flow exiting the annulus is guided out to the environment by an exit flange mounted at

the top of the rotating cylinder. The inner rotating cylinder is mounted to a hollow shaft supported by two pillow block bearings at both ends, and the shaft is then connected to the motor through a flexible coupling. The pillow block bearings are mounted on the supporting structure. The support structure is a hollow cylinder of aluminum with wall thickness of 1.27 cm, height of 43.18 cm, and radius of 17.15 cm. The bases of the cylinder are made of aluminum plates 2.54 cm thick. The pillow block bearings are then mounted on the base plates of the support structure. The shaft is driven by a Sabina 220 volt, 2 hp d.c. motor with a maximum rotation rate of 1750 RPM. A "MF" type adjustable speed drive manufactured by Sabina Electric & Engineering is used to vary the rate of rotation. To eliminate vibrations, both the support structure and the motor are mounted on a vertical steel plate anchored on the reeomfprced cpmcrete nio;domg structure. This setup virtually eliminates any problems associated with mis-alignment or transmission of vibration to the inner cylinder. To measure the rotational speed, an optical encoder is mounted on the end of the shaft at the bottom of the motor.

To minimize heat loss to the environment, the outer stationary cylinder is made with two concentric Plexiglass tubes of O.D.'s 24.13 cm and 27.94 cm separated by a 1.59 cm air gap. The outer stationary cylinder, together with the inner rotating cylinder, comprise the vertical annulus which is 50.80 cm high with gap width of 1.27 cm. This corresponds to an aspect ratio, h/b, of 40, and a gap/radius ratio, b/r_m of 0.125. Six 0.635 cm diameter holes at different axial locations, 10.16 cm, 17.78 cm, 25.4 cm, 40.64 cm, 48.26 cm and 50.80 cm from the bottom of the annulus are drilled on the outer cylinder to provide access for velocity and temperature measuring instruments. To allow cross

correlation measurements, four other holes are drilled in the circumferential directions. The locations for the holes are at 25.4 cm and 40.64 cm from the bottom of the annulus, and 1.5 cm and 25.4 cm away in the azimuthal direction from the previous holes. Figure 2.4 shows the locations of these holes. These holes are plugged when not in use. Moreover, to make temperature measurements along the inner and outer annulus walls, thermocouples are mounted on both the inner and the outer cylinders.

Both the temperature and velocity outputs are obtained through the data acquisition system. The data acquisition system consists of a personal computer installed with an analog/digital input/output board and its accessories. The board can then be connected to other I/O boards and expansion boards according to different measurement needs.

2.2 Velocity Measurement

2.2.1 Instrumentation

In the experiment, all the velocity measurements are done using a hot-wire anemometer system manufactured by Dantec Electronic, Inc. The complete system consists of the 56B12 half size main frame, the 56C01 CTA (Constant Temperature Anemometer), the 56C17 CTA Bridge, the probe holder, and the hot-wire probe. The half size main frame provides power supply for the hot-wire anemometer and allows 7 one-inch plug-in modules of CTA/Bridge combination. The CTA and bridge are part of a complete circuit of a flow anemometer. The resistance of the bridge is adjustable, providing control over the overheat ratio of the probe.

Two types of probes are used to measure velocity. The 55P11 miniature wire probe with a single sensor is used to measure the velocity trace, and the averaged tangential and axial velocity profiles are measured using the 55P62 miniature x-wire probe with dual sensors. Both probes have straight prongs, and the sensor planes of both probes are perpendicular to the probe axis. The cylindrical sensors on both probes use platinum-plated tungsten wires with diameter of 5 μm and length of 1.25 mm. The maximum operating ambient temperature for wire sensors is 150°C. The velocity limits for these probes are 0.2 m/s and 500 m/s in air with the maximum frequency response obtainable at 400kHz. The probes are connected to a probe support by means of a plug- and socket arrangement. The prongs embedded in a ceramic tube extend approximately 2 mm beyond the rear end of the ceramic tube, and this extension serve as plug pins through which the electrical connection to the probe support is made. The probe support is then inserted into a stainless-steel mounting tube.

To hold the hot-wire anemometer probes firmly in position during velocity measurements, a probe stand with holders is manufactured, as shown in Figure 2.5. The probe stand is equipped with two probe mounts so that it can hold two probes at the same time for simultaneous measurements. One of the probe mounts has a traverse which can slide the probe in and out radially. A micrometer is installed on the traverse to determine the exact radial position of the probe.

2.2.2 Calibration

The hot-wire anemometer provides outputs in terms of voltage. In order to convert the voltage into velocity, the anemometer must be calibrated. It is calibrated using the blower/heater assembly described in Figure 2.2. Each probe is calibrated in isothermal or heated air flows. For the single-sensor probes, the calibration procedures are as follows. With the blower set at a given flow rate and at a set overheat ratio, the sensor is placed in the air stream such that the wire is perpendicular to the direction of the flow. An inclined manometer measures the dynamic pressure of the flow, which can be converted to the actual speed of the air flow, v_a, and a voltmeter connected to the output of the anemometer reads the corresponding voltage, V. This procedure is performed for six to seven axial velocities. Since $v_a^{1/2}$ varies linearly with V^2, a least square fit of the data points will provide the calibration constants m and c. The measured voltage can then be converted into velocities using the following equation:

$$v_a = (m\ V^2 + c)^2 \tag{2.1}$$

The x-wire probe is calibrated a little differently. To calibrate the x-wire probe, the probe is placed such that both sensor wires are at 45° angles from the horizontal plane, and the plane of the sensors is parallel to the direction of the mean flow. Since the major contribution to the voltage of the anemometer output comes from only the velocity component perpendicular to the sensor wire, the relationships between the velocity calculated from the pressure drop and voltage are as follows:

$$v_{1a}\cos\theta = (m_1\ V_1^2 + c_1)^2$$

$$v_{2a}\sin\theta = (m_2\ V_2^2 + c_2)^2 \tag{2.2}$$

The m's and c's are the calibration constants. The subscripts 1 and 2 denote the contribution from each wire, and θ is the inclination angle that sensor 1 makes with the horizontal plane. In the current experiment, two components of velocity are measured using the x-wire probe, the tangential and the axial components. When v_{1a} and v_{2a} are converted from the voltage outputs V_1 and V_2, the tangential and axial velocity components are calculated using the following equations:

$$u = v_{1a} \cos\theta + v_{2a} \sin\theta$$

$$w = -v_{1a} \sin\theta + v_{2a} \cos\theta \qquad (2.3)$$

The single-wire probes are also calibrated in a heated jet. Following similar calibration procedures, a different set of calibration constants is obtained for heated flows.

2.2.3 Measurement Procedures

Velocity traces of the tangential component in both isothermal and diabatic flows are taken at 25.4 cm (l/b = 20) and at 48.76 cm (l/b = 37) from the bottom of the annulus using a single-wire probe. The hot-wire sensor is oriented in the direction such that the wire is parallel to the shaft axis. Each velocity trace contains 4096 points and is taken at a sampling rate of 500 Hz. The frequency information is extracted from the velocity traces using the power spectrum analysis. The calculations for velocity spectra analysis is shown in Appendix A. Velocity traces were also measured at other gap locations near the mid-height, at r' = 0.1 and 0.9 and the power spectra were calculated.

Velocity cross-correlations are performed on results taken using two single-wire probes mounted at different axial or circumferential positions. The outputs from the two

probes are taken simultaneously, and then the two sets of outputs are cross-correlated. To determine the wavelengths of the Taylor vortices, the two probes are placed at different axial locations: at l/b = 20 and 26, at l/b = 20 and 32, and at l/b = 32 and 36. To investigate in the existence of azimuthal waves, the two probes are placed at different circumferential positions at 2.54 cm apart and 26.67 cm apart near the mid-height.

The tangential velocity profiles are obtained at various axial positions and at different rotational speeds (at l/b=8, 20, 32) using the x-wire sensor. To obtain the average velocity at a set radial position, the hot-wire probe is traversed across the gap with the exact radial position determined by the micrometer mounted on the traverse, and at each measurement point, 3000 data points are taken at a sampling rate of 300 Hz.

2.2.4 Error Analysis

Errors are present in the results arising from uncertainty occurred during measurements and uncertainty in the calibration constants. During calibration procedure, the dynamic pressure is registered as a difference in height measured by the inclined manometer. The actual air velocity is then calculated from the dynamic pressure, and the results are correlated with the voltage to obtain the calibration constants (Sec. 2.2.2). All the calculations of the uncertainties are shown in Appendix B.

The uncertainty of the manometer is 0.127 cm. For the average of velocities used during calibration, this corresponds to a relative uncertainty of 2.5%. The uncertainty of the voltage measurement is 0.001 volts, which is negligible. Thus, the velocity calculated using the dynamic pressure has a relative uncertainty of 1.25%. The calibration results

of a particular probe are used to calculate the uncertainties of the calibration constants m and c. The relative uncertainties for m and c are calculated to be 2.7% and 5.6% respectively, and this results in a relative uncertainty of 12% for velocity measured using the hot-wire probe with the upper bound of the uncertainty to be 17%. (See Appendix B.)

Velocity conversion error also occurs when the axial flow is heated. Although new conversion constants, m and c, are recalculated using hot air in calibration, the absolute magnitude of the velocity can still be affected when there is a temperature difference between the air used in calibration and during experiment. To see if this error will change the characteristics of the velocity spectra, a measured voltage trace in the experiment is converted to velocities using two different sets of calibration constants, the isothermal and the heated ones. It is discovered that only the magnitude of the strengths are affected in the two power spectra. The frequencies of the peaks and the relative strengths between the peaks are the same between the spectra.

Since the wire of the probe is always oriented perpendicular to the tangential direction, when the magnitude of the axial flow becomes large, the direction of the main flow is no longer perpendicular to the wire. The conversion constants are calculated when the mean flow is perpendicular to the sensor wire. As a result, errors occur during the conversion process. The effect of increasing axial flow to the hot-wire probe is to offset the voltage output by a certain amount. When a measured voltage output is shifted up by 0.1 volts, this does not change the waveform of the converted velocities. Similar to the case when different calibration constants are used, only the spectral density is affected, but the rest of the velocity spectra remain unchanged.

When the velocity spectra are obtained in heated flows, the velocity spectra will become noisier. During measurements, the small thermocouple is placed ahead and slightly behind the hot-wire anemometer probe. This may create some disturbances to the flow when the velocity is measured. Whenever an intrusive method is used in measurements, the disturbance to the flow is unavoidable. However, in the current experiment, the disturbances are on a much smaller scale and the magnitude of fluctuation that it causes is not large enough to change the overall structure of the flow. In addition, the operating principle of CTA is based on the temperature difference between the sensor wire and the environment. The hot-wire sensor is not able to distinguish the difference between temperature and velocity fluctuations. As a result, temperature fluctuation of the environment may be registered as a velocity fluctuation in the output. The velocity spectra in heated flows will reflect this effect. Nevertheless, the magnitude of the temperature fluctuation during a measurement will not exceed 5 or 6 degrees such that the temperature effect should not be large enough to influence the overall characteristic of the velocity spectra.

2.3 Temperature Measurement

2.3.1 Instrumentation

To make temperature measurements, thermocouples are mounted on both the inner and the outer cylinders. Thirty-seven E-type thermocouples with bead diameter of 0.0762 cm are mounted in different axial and angular locations on the inner cylinder. Their locations are shown in Figure 2.6. The thermocouples are installed by drilling through the

aluminum tube, placing a small plastic sleeve into the cylinder wall and epoxying the thermocouples into the sleeve. The thermocouple beads are flush with the cylinder surface. The plastic sleeve reduces the conductive heat transfer from the cylinder wall to the thermocouple beads and, thus, allows for more representative measurement of the fluid temperature. Through similar means, ten thermocouples are mounted on the outer cylinder, and their locations are shown in Figure 2.7. These thermocouples on the inner and outer cylinders are used to measure the average temperature profiles within the annulus. To measure local transient temperatures within the flow, extra holes are drilled on the outer cylinder to allow access for some very fine thermocouples (0.001 cm wire diameter). The estimated frequency response of these fine thermocouples is 90 Hz to 180 Hz for velocities ranging from 1 m/s to 20 m/s. For transient temperature measurements, the fine-gauge thermocouple is placed close to the hot-wire probe at a similar location.

The thermocouple wires from the inner rotating cylinder are connected to the stationary data acquisition system through the use of a 60-channel slip ring assembly. The thermocouple wires are connected to the lead wires from the slip ring assembly through log terminals mounted on a platform at the top of the inner cylinder. The lead wires are then fed through the center of the hollow shaft and exit at the bottom of the shaft to the slip ring assembly mounted above the motor. Copper wires are welded to the slip ring output to connect to the data acquisition system.

2.3.2 Measurement Procedures

The thermocouple leads are connected to the Metrobyte Exp-20 board. The room temperature, which is used as a reference temperature for the thermocouples, is obtained using the cold junction compensator (CJC) built in the board. The gain on the board is set at 100 for E-type thermocouples. The voltage outputs of the thermocouple obtained from the data acquisition system are linearized by software. After cold-junction compensation, the outputs are then translated into units of temperature.

The transient temperature is measured at the same axial positions as the velocity, at l/b = 20 and 32, using the fine thermocouples. The thermocouples are placed 2.54 cm away circumferentially from the hot-wire probe. To reduce the interference the thermocouple would have on velocity measurements, they are not at the same gap location as the hot-wire probes but are placed slightly behind. The temperature traces consist of 4096 points sampled at 400 Hz, which is used to calculate the temperature power spectra.

2.3.3 Error Analysis

The accuracy for the E-type Thermocouples is ± 1°C. However, there are other problems encountered during measurement that result in higher uncertainties for the thermocouples. For average temperature measurements, there is the problem of temperature drift with the cold junction compensator built in the data acquisition board. The reference temperature given by the cold junction compensator tends to increase as the compensator becomes heated with prolong use. Also, the thermocouples that are placed closer to the CJC on the data acquisition board tend to have a higher temperature reading than those that are

placed further from the CJC. Moreover, while the inner cylinder is rotating, the noise level of each channel of the slip ring assembly is different; thus, its contribution to noise in temperature measurement for each thermocouple is different. In an attempt to reduce the uncertainty, in addition to the CJC, a hand-held thermometer is also used to provide the reference temperature. Before each experiment, using corrected room temperature as the reference, the room air temperature is measured by all the thermocouples mounted on the cylinders with the inner cylinder rotating. To estimate the errors caused by the slip-ring assembly, all the results are first averaged. Then, the result of each thermocouple is compared with the average value to obtain the difference between them. The temperature difference is used later to correct the temperature measured in the experiment.

For the small thermocouple used in transient temperature measurements, a different problem is encountered. Since the thermocouple is very fine, it is very sensitive to any small disturbances of its surroundings. As a result, the temperature spectra obtained are very noisy. If the thermocouple's response frequency is at the lowest limit calculated at 90 Hz, then only the features in the temperature spectra below 45 Hz should be considered valid according to the sampling theorem, which suggests that the sampling rate should be at least twice the highest frequency present in the measured signal.

2.4 Slip Ring Assembly

The slip ring assembly is an electromechanical unit that provides a method of transmitting electrical signals from a source on a rotating surface to a stationary data acquisition system. The self-contained 60-channel slip ring assembly, manufactured by Fabricast,

Inc., has rigid tube housing, which eliminates bearing alignment problems, and exposed stator terminals. Each ring on the slip ring assembly has two silver graphite brushes, and the rings are made of coin silver capable of carrying a current up to 5 amps. The noise of the slip ring assembly is 10 milliohms maximum.

2.5 Blower/Heater Assembly

The dc blower, manufactured by Dynamic Air Engineering, Inc., is capable of delivering 200 CFM at 0.7 inch of water. Power to the blower is provided by an ac/dc transformer, which converts the line ac voltage to dc voltage at the blower's power supply. The output of the blower is controlled by a variac, which takes an input of 120 volt and has an output voltages ranging from 0 to 120 volt with maximum current rated at 5 Amperes. The axial velocity in the gap is measured by using the hot-wire anemometer with the variac output at different settings such that a relationship between the flow rate of the blower and the variac output is obtained.

The axial Reynolds numbers are based on the axial velocity in the gap and gap width. The axial velocity in the gap is measured using the hot-wire anemometer. At low axial flow rates, since the axial velocity is near or below 0.2 m/s, which is the lower limit of the anemometer probe, the uncertainty of the axial Reynolds number is great. However, at higher axial velocities, the uncertainty of the axial Reynolds number is about 20%, as calculated in section 2.2.4.

The heater consists of the electric coil lining around the air duct. Temperature of heated air is controlled through another variac, which has a maximum voltage output of

120 volts and current output of 15 Amperes. A voltmeter/ammeter combination is connected to the line of power input to ensure that the current input does not exceed the limit of the variac.

2.6 Optical Encoder

An optical encoder manufactured by Dynapar Corp. is mounted on the end of the shaft to measure the rotational speed of the shaft (inner cylinder). The encoder produces 1000 pulses with an index per revolution. The output of the encoder is sampled using the data acquisition at the maximum sampling rate of 100 Khz, then the rotational speed of the shaft is calculated knowing the number of pulses present in the finite length of time.

2.7 Data Acquisition

Data from the experiment is acquired using a personal computer and an I/O board with accessories. The computer, manufactured by Zenith Data Systems, operates at a clock speed of 16 Mhz. Manufactured by MetraByte Corp., model Das-20, the analog and digital I/O board plugs directly into an expansion slot within the computer. The connections to the Das-20 are made through a 50 pin connector that extends out of the rear of the computer.

The Das-20 uses an A/D converter which has an 8.5 microsecond conversion rate and it has a sample and hold time of 800 nanosecond. As a result, the board is capable of a 100 Khz sampling rate in the direct memory access data transfer mode. The D/A converters on the board have 12-bit (one part in 4096) resolution and have switch

selectable output ranges. Currently, the Das-20 is operated in 16 channel single ended input modes with the output ranges controlled by software.

The STA-20 screw terminal board is used to bring all connections of the Das-20 board out to screw terminals for convenience of use. Exp-20 multiplexer board is used to expand the input capabilities of the Das-20 board. Each Exp-20 includes 16 differential inputs that can be multiplexed into a single Das-20 input channel, thus increasing the capacity of a single Das-20 to 256 channels. The Exp-20 is equipped with an on-board amplifier, which provides switch selectable gains, and a temperature sensor allowing the monitoring of the cold-junction temperature. Therefore, temperature data are acquired primarily through the Exp-20 boards. In addition, the Exp-20 board has a built-in 60 hz low pass filter, which allows for some form of noise control.

The SSH-4 simultaneous sample and hold board allows analog input data to be acquired from 2, 3 or 4 inputs with less than 40 nanoseconds of channel to channel sample time uncertainty. When using the x-wire probe in velocity measurements, it is necessary to use the SSH-4 to obtain simultaneous outputs from each of the wires of the probe.

2.8 Startup Procedures

For isothermal experiments, the rotation of the inner cylinder is first started when there is no axial flow, and it is increased slowly until the desired rotational speed is reached. The rotational speed of the inner cylinder is measured by the optical encoder. Then, velocity measurements are taken as the axial flow is increased. At each setting of axial

flow, several trial measurements are taken to make sure that the flow has reached a steady state before the actual measurement is taken. After a set of measurements is completed for different axial flows with Re_a ranging from 0 to 2500, the rotational speed is increased to a different value before another set of measurements is taken for the same range of axial Reynolds number.

For diabatic experiments, heated air is first injected into the annulus when there is no rotation. Once the air in the test section has reached the desired temperature, the blower is turned off. The rotation of the inner cylinder is then turned on, and both velocity and temperature measurements are taken at this point when the axial Reynolds number is zero. Measurements are taken for increasing axial Reynolds numbers. However, to make sure that the system has reached a steady state, for each axial flow rate, at least half an hour or more is allowed before measurements are taken. Using the thermocouples mounted on the inner and the outer cylinders, the average temperatures of the system at different axial and circumferential locations are taken every five minutes to make sure that system has equilibrated. Actual measurements are taken only when the temperature drift of the system is less than 0.5 degree for a half-hour period.

Chapter 3

Isothermal Experimental Results

3.1 General Velocity Profiles

Smith and Townsend (1982) plotted the distributions of the angular-momentum ratios, ur/U_iR_i, over the range of Taylor numbers that they studied. Part of their results is shown in Figure 3.1. Even though the range of Taylor numbers in the current experiment is not the same as in Smith and Townsend's study, Figure 3.1 also shows the angular-momentum ratios plotted for different Taylor numbers as a function of radial position at the mid-height of the annulus (l/b=20) for the current experiment. For r' between 0.1 and 0.9, the momentum ratios increase slightly as rotational speed increases although the values of the ratios stay close to 0.45 at all speeds. Large angular-momentum gradients are observed near the walls, with the thickness of the gradients no more than one-tenth of the gap width.

Tangential velocity profiles with and without axial flow at $Ta = 1.5 \times 10^7$ have been plotted at different axial locations (at l/b = 8, 20 and 32) to see if the flow near mid-height of the annulus (l/b=20) is fully developed. The velocity is measured by using both the single-wire and the x-wire probes, and the measurements made by both probes show

similar results. At $Re_a = 0$, Figure 3.2a shows that the velocity profiles at different axial locations are similar. At $Re_a = 10$, similar profiles are still observed as shown in Figure 3.2b. However, at the higher axial Reynolds number, at $Re_a = 1000$, Figure 3.2c shows that the profile at l/b = 8 is different from the others for l/b = 20 and 32. The flat portion of the tangential velocity profile is observed to be at a much lower value than those measured at l/b = 20 and 32, due to lack of diffusion of the tangential momentum. Simmers and Coney (1979) observed that at 0.56 m from the entrance corresponding to l/b = 20 using their dimensions, the results for $Re_a^2/Ta = 0.703$ and 0.253 are very similar to those obtained under fully developed conditions. They also indicate that in the Taylor vortex regime, the development length decreases as Re_a^2/Ta increases. In the current experiment, the maximum Re_a^2/Ta ratio is 0.52, with $Re_a = 2500$ and $Ta = 1.2 \times 10^7$. Based on their results and current measurements, within the range of parameters studied in the current experiment, the flows are considered fully developed.

3.2 Effect of An Isothermal Axial Flow

The focus of this chapter is on the effect of an isothermal axial flow on Taylor-Couette flows for large Taylor numbers. The results shown here are taken at 25.4 cm from the bottom of the annulus (l/b=20) and at the mid-gap location. The flows studied are for Taylor numbers ranging from 1.2×10^7 to 2.1×10^7, and for axial Reynolds numbers ranging from 0 to 2500. As examples, the power spectra of the tangential velocity component, plotted in semi-log scale, for $Ta = 1.42 \times 10^7$ and various axial Reynolds numbers are shown as follows.

Figure 3.3a shows the velocity power spectrum for Ta = 1.42 x 10^7, and $Re_a = 0$. The spectrum shows a significant peak near 1 Hz, and other peaks of smaller magnitude which constitutes a broadband background continuum. Plotted in semi-log scale, the average power density of the broadband continuum decays linearly for nearly an order of a magnitude between the frequencies of 0 to 40 Hz, and for frequencies higher than 40 Hz, the magnitude has stayed fairly constant. The values of the power density of the broadband range in between 10^{-3} and 10^{-4} m^2/sec^2.

Since measurements are made at a fixed location, the spectrum in Figure 3.3a reflects that the Taylor vortices without axial flow are fairly stationary, and the fluctuations are mostly slow-varying and not periodic. This is confirmed by the autocorrelogram shown in Figure 3.3b. In the power spectrum, the large peak at 1 Hz may be the result of two possible effects: azimuthal waves of low wave numbers near the cell boundaries, or oscillation of the vortices within the annulus gap. The visualization results by Barcilon et al. (1979) show that for $Ta/Ta_c = 300$, there are azimuthal waves of low wave numbers at the flow boundary. For $Ta/Ta_c = 750$, the waves are less apparent, and for $Ta/Ta_c = 915$, the waves are hard to distinguish. In general, Barcilon et al. reported that for $Ta/Ta_c > 445$, the waviness of cell boundaries is replaced by oscillation of the vortex centers. Koschmieder (1979) also observed the disappearance of the azimuthal waves and the establishment of axisymmetric turbulent vortex flow at $Ta = 700Ta_c$. Fenstermacher, Swinney and Gollub (1979) showed that at $Re_a/Re_{ac} \approx 21.9$, corresponding to $Ta/Ta_c \approx 480$, the power spectrum of the radial velocity component shows no sharp peaks although a broad base component has appeared. Together with the

visualization results, Fenstermacher, Swinney and Gollub concluded that the disappearance of the sharp peak in the velocity spectrum corresponds to the disappearance of the azimuthal waves. The current measurements are taken in the range of Taylor numbers corresponding to Ta/Ta_c = 7000 to 12300, which is beyond the critical transition point of disappearing azimuthal waves observed by Barcilon et al., Koschmieder, and Fenstermacher, Swinney and Gollub. Therefore, the more likely explanation of the low frequency peak in the spectrum is that the vortices drift within the gap possibly due to the open ends of the annulus. Spectra for other Taylor numbers (not shown) indicate similar characteristics.

One concern regarding the broadband noise is determining what is causing it. There are several possible explanations regarding the broadband background in the velocity spectrum. The broadband component either reflects the fluctuating nature of the flow, or it is due to the electronic noise of the instrumentation. It is also possible that it is inherent within the process of calculating the power spectrum where leakage and aliasing errors are expected. To understand the nature of the broadband noise, the velocity power spectra are calculated when the anemometer is held in still air, and also for a smaller Taylor number, at $Ta = 5 \times 10^6$. The spectra are shown in Figures 3.4a and 3.4b. The velocity spectrum of still air reflects the magnitude of electronic noise from the instruments. It is shown that the background noise is in the order of 10^{-10} m^2/s^2, while the magnitude of the maximum peak is at 10^{-7} m^2/sec^2, which is still several orders of magnitudes less than 10^{-4} m^2/sec^2. For $Ta = 5 \times 10^6$, the velocity spectrum indicates a broadband spectrum with linear decaying between 0 and 50 Hz. The average magnitude

of the broadband continuum for frequencies larger than 50 Hz is 10^{-5} m^2/sec^2, an order of magnitude less than 10^{-4} m^2/sec^2. These indicate that the broadband component shown in the velocity spectrum in Figure 3.3a does reflect the fluid fluctuation rather than instrumental noise. Moreover, Brandstater and Swinney (1987) suggest that the broadband noise in power spectra can be caused by two different processes, stochastic or deterministic. The decay of spectral power differs for these two processes at large frequencies. Based on the papers by Sigeti and Horsthemke (1987) and Greenside et al. (1982), Brandstater and Swinney concluded that a stochastic differential equation model follows a power-law decay while a deterministic model shows exponential decay. The spectral decay shown in Figure 3.3a reflects an exponential decay as indicated by the linear behavior on the semilog plot. This suggests that the broadband noise in the data set arise from a deterministic process.

Imposing even a slight axial flow, the power spectrum of the flow changes. Figure 3.5a shows the velocity spectrum for $Re_a = 10$, and at the same Taylor number as above. The spectrum indicates the emergence of a sharp component frequency near 6 Hz and its corresponding harmonics over a background of broadband noise. The magnitude of the broadband noise has been suppressed relative to the sharp peak. The corresponding velocity trace, shown in Figure 3.5b, shows small scale fluctuations embedded in a slow-varying periodic motion of larger magnitudes. The velocity trace is similar to the traces of turbulent vortex flows as shown by Kaye and Elgar (1958), Smith and Townsend (1982) and Wan and Coney (1982). The autocorrelation result, shown in Figure 3.5c, indicates that the flow is becoming more periodic.

Figure 3.6a and 3.6b are the velocity spectrum and autocorrelogram for $Re_a = 70$. Figure 3.6a indicates a similar spectrum as in Figure 3.5a; however, the sharp dominant peak and its harmonics have become even more apparent with suppressed broadband noises. The strength of the sharp dominant peak and the periodicity of the autocorrelogram reflect a strongly periodic motion in the flow. At this point, the flow is still axisymmetric. The toroidal vortices of uniform sizes and shapes drift with the mean axial flow past the fixed sensor and cause the periodic motion reflected in the velocity spectrum and autocorrelogram. As Re_a is increased to $Re_a = 160$, the characteristics of the velocity spectrum changes again, as shown in Figure 3.7a. Instead of showing a single sharp peak and its harmonics, the linewidth of the peaks has broadened and several peaks at other fundamental frequencies have emerged in the lower frequency range. The broad peak near 11 Hz consists of the harmonics of the peaks near 5 Hz, 5.8 Hz and 7 Hz. The large peak near 2.5 Hz is the corresponding subharmonic. The disappearance of the single sharp spectral peak and its harmonics indicates the diminishing strengths of the turbulent vortices; however, this does not imply the disappearance of the vortices, as the autocorrelogram shows in Figure 3.7b. Even though the spectrum does not display a single dominant peak, the autocorrelogram still indicates some form of periodicity in the flow. Due to the disturbance of the axial velocity to the flow field, the sizes and shapes of the counter-rotating turbulent vortices may become less uniform. As a result, as the vortices of different sizes and shapes pass a single measurement point, the resulting velocity trace will not be as periodic as in the case with

low axial flow. Also similar to Figure 3.3a, the spectral power of the broadband noise decays for an order of magnitude for frequencies ranging from 0 to 50 Hz.

For Re_a = 220, as shown in Figure 3.8a, a single sharp peak reemerges at 6.5 Hz, and a broad peak near 1 Hz is also observed. The spectral density of the broadband noise shows a linear decay of one order of magnitude for frequencies between 0 to 40 Hz. For frequencies greater than 40 Hz, the spectral density of the broadband noise is relatively constant. The corresponding autocorrelogram in Figure 3.8b shows that the flow actually becomes more periodic than when Re_a is 160. If the single sharp peak is still indicative of the vortex passage frequency, assuming the sizes of the vortices did not vary from those when Re_a = 70, then the sharp peak should be near 20 Hz rather than at 6.5 Hz. Two explanations to the discrepancies are offered here. First, at this higher axial flow rate, the sizes of the vortices have actually grown. Or second, this sharp peak is no longer indicative of the vortex passage frequency; instead, it represents a periodic disturbance of other forms, such as the reappearance of azimuthal waves. Since there are no relevant visualization results available, it is difficult to determine what is happening in the flow.

At Re_a = 330, Figure 3.9a shows a spectrum with a dominant frequency near 6.2 Hz, and a second fundamental frequency near 14.5 Hz. Even with the presence of a sharp peak in the spectrum, the corresponding autocorrelogram, shown in Figure 3.9b, does not reflect the same waveform as in Figure 3.5b. Shown in Figures 3.10 and 3.11, corresponding to Re_a = 500 and 670, as the axial velocity is further increased, the dominant peak near 6 Hz has gradually broadened. Linear decaying of the broadband

noise near 0 to 50 Hz is also observed in both spectra. At Re_a = 980, as shown in Figure 3.12a, the single peak has become almost indistinguishable from the broadband noise, and the corresponding autocorrelogram does not reflect any form of periodicity as shown in Figure 3.12b; and for Re_a > 1300, the flow has become turbulent such that the spectrum contains no significant peaks as shown in Figure 3.13.

Gollub and Benson (1980), in their Rayleigh-Bénard experiment, described the route to chaos as the Rayleigh number increases in terms of the power spectra obtained in the experiment. The power spectra, from order to chaos, changes from (1) spectrum with a single sharp peak with its harmonics to (2) spectrum with two frequency peaks, (3) spectrum with peaks that are linear combinations of the two major frequencies, (4) back to spectrum with a single peak on a background of broadband noise, and then to a (5) spectrum with no sharp peaks. Gollub and Benson mentioned that in (4), even though the spectrum exhibits the feature of a periodic flow with a single sharp peak, the flow is in fact aperiodic. Bergé, Pomeau and Vidal (1986) have also described the existence of "windows of periodicity" in the route from order to chaos. Therefore, the single peak observed in spectra with Re_a ranging from 220 to 670 may be the result of interaction of several non-linear disturbances in the flow such that they become phase-locked. Currently, an increase of the axial flow from Re_a = 10 to 1300 and greater has produced power spectra similar to those observed by Benson and Gollub. This indicates that the mechanism involved in bringing turbulent vortex flow to turbulence when the axial Reynolds number is increased may be similar to the effect of Rayleigh number on the Rayleigh-Bénard cells.

The power spectra shown above are non-unique. A similar trend is observed, but the exact velocity power spectra cannot be reproduced from day to day. Coles (1965) has shown that the state of the flow field is not uniquely determined by the Taylor number. Koschmeider (1979) also shows that depending upon how the experiment is started, suddenly or gradually, the final state of the flow field is different. The current experiment starts suddenly with a high rotation speed, and then measurements are made as the axial Reynolds number is increased slowly from 0 to 2500. The experiment does not always start from the same rotational speeds. As a result of different initial conditions, the frequencies of the sharp peaks in the velocity spectra are not necessarily of the same value for the same Taylor number and axial Reynolds number. In addition, the strength of the peak with the maximum spectral density also differs.

The total power, sum of the spectral density at all frequencies, can be viewed as the total energy of the system. Thus, the ratio of spectral density at each frequency to the total power reflects the relative amount of energy that the fluctuations at different frequencies contribute to the system. A plot of the accumulative energy contribution as a function of frequency for different Re_a is shown in Figure 3.14. When Re_a is 70, the curve is not smooth; instead, several distinct steps are observed. The frequency where the step is present corresponds to a sharp peak in the power spectrum. This indicates that at $Re_a = 70$, the energy of the system is not distributed evenly to all frequencies. Rather, a large percentage of the energy is associated with several frequencies only. As Re_a increases, the curves becomes smoother, reflecting that the system's energy becomes more evenly distributed to all frequencies. Moreover, with increasing axial Reynolds number,

the energy distribution curves become more tilted to the right reflecting that more energy is distributed towards higher frequencies and the flow is becoming more turbulent. Nevertheless, for all the cases studied, frequencies of 75 Hz or less contribute to 70% of the total energy. Only 10% of the total energy is contributed by frequencies between 150 Hz and 250 Hz. This shows that most of the fluid motion fluctuates in frequencies below 75 Hz.

3.3 Effect of Rotational Speeds

Two effects of varying the Taylor numbers are observed from the velocity power spectra. First, as the rotational speed is increased (increasing Ta), the location of the sharp frequency component shifts to higher values. This effect is most apparent for the low axial flow rates. Figure 3.15 contains the velocity spectra at a constant axial flow rate for different Taylor numbers, at $Re_a = 10$. The figure, plotted in linear scale, shows that the single dominant peak and its harmonics shift to higher values as Ta increases. Smith and Townsend (1982) indicated that when the vortices are made to drift past a stationary measurement point by imposing a small axial flow (with magnitude less than 1% of the circumferential flow), the anemometer output will oscillate with a passage frequency equal to axial velocity divided by the wavelength of the vortex spacing. In the current experiment, the axial velocities at $Re_a = 10$ and 70 are less than 0.5% of the circumferential velocity. Therefore, based on findings of Smith and Townsend (1982), the dominant frequency should be indicative of the size of the vortices--the higher the dominant frequency, the smaller the vortices. To verify this hypothesis, cross correlation

measurements are taken at different axial locations and at various rotational speed to determine the wavelengths of the vortices. The anemometer probes are placed at three different sets of axial locations, with the probes 7.62 cm and 15.24 cm apart. From the cross correlation results, the delay time, δt, between the signals of the two probes is obtained. The period T_λ is the time it takes for a single vortex to pass one fixed anemometer positions, and is obtained from results of the cross correlation and power spectra. From previous works (Burkhalter and Koschmieder, 1973; Koschmieder, 1979), the wavelengths of the vortices are assumed to be close to 2b. Since d > 2b, there can be more than one vortex between the probes at any given time. The wavelengths can then be calculated using the following equation, where n is a positive integer indicating possible number of vortices between the probes:

$$\frac{d}{(n \pm \delta t/T_\lambda)} = \lambda \qquad (1)$$

Once λ is calculated, the corresponding drift velocity of the vortices, v_λ, which is different from the axial velocity, can then be calculated by dividing the wavelength, λ, by the period, T. From previous studies, it is anticipated that the drift velocity will be close to the average axial velocity. When comparing v_λ with the axial velocity measured, if v_λ deviates from the measured average axial velocity by more than 25%, then the corresponding wavelengths are deleted from the data set. Figure 3.16 reflects the result of this calculation. Figure 3.16 shows the plot of wavelength, normalized by the gap width, at various Taylor numbers. The top value on the error bar is the maximum wavelength possible, and the middle and the bottom values represents the average and the minimum respectively. The results indicate that as the axial convective speed of the

vortices remain relatively constant with increasing Taylor numbers, the wavelengths of the vortices decrease as the Taylor numbers increase. This finding contradicts the findings of Koschmieder (1979), who indicates that the wavelength of the vortices is independent of the Taylor numbers. However, Koschmieder's experiment has an enclosed annulus, and the current experiment is the throughflow case. Burkhalter and Koschmieder (1973) have observed that for different end conditions for the enclosed case, the sizes of the end cell differ as Taylor number is varied, and the sizes of the vortices in the annulus are restricted by the end conditions. Since the current experiment has open ends, the sizes of the vortices are not restricted by end conditions so the sizes of the vortices may vary as the Taylor number is varied.

The other effect of varying Taylor number is as the Taylor number increases, the magnitude of the spectral density of the broadband noise appears suppressed relative to the spectral magnitude of the sharp peaks. For $Re_a = 0$ and $Ta = 2.06 \times 10^7$, as shown in Figure 3.17a, compared with Figure 3.3a, the velocity spectra are basically similar, but the magnitude of the broadband noise for the higher Taylor number case is suppressed compared with the case for $Ta = 1.42 \times 10^7$. Similar effect can be observed for other axial Reynolds numbers, as shown in Figure 3.17b, 3.17c and 3.17d, for $Re_a = 10$, 220, and 670, and $Ta = 2.06 \times 10^7$.

3.4 Results Across the Gap

Measurements were also made across the fluid gap to help visualize the flow distribution within the gap for $Ta = 1.6 \times 10^7$ and various axial Reynolds numbers. In

the following, Figure *a's, *b's and *c's show the velocity spectra measured 0.127 cm from the inner annulus wall, midgap, and 0.127 cm from outer annulus wall respectively (r' = 0.1, 0.5, 0.9). Figure 3.18a, 3.18b and 3.18c show the velocity spectra at $Re_a = 0$. Figure 3.18a and 3.18c are similar, both showing a sharp dominant peak at a frequency near 1.5 Hz, and two smaller peaks with broad linewidth near the 10 Hz range. The sharp peak at low frequency indicates the oscillation of the Taylor vortices within the gap. The smaller peaks near 10 Hz possibly reflect the existence of the Görtler vortices, which are of smaller sizes than the Taylor vortices. The Görtler vortices have been observed by Barcilon et al. (1979) as a 'herring-bone'-like pattern visible at the walls. Velocity traces are shown in Figure 3.18d and 3.18e. Both figures indicate periodic motions near the boundaries of the annulus, which verify the spectra results. However, even though the velocity traces have the same periodicity, they exhibit different waveforms, which is also shown by Smith and Townsend (1982). This implies that the flows near the annulus boundaries fluctuate at the same frequency, but they show different flow patterns. In contrast with spectra near the walls, Figure 3.18b shows a spectrum that has no significant sharp peaks, although a small peak at the same frequency as observed in the spectra near the walls is present. The flow in midgap apparently is less influenced by the fluid motion that results in a strong periodicity near the walls.

With low imposed axial flow, for $Re_a = 10$, the velocity spectra near the walls and in midgap all exhibit the same characteristics as shown in Figure 3.19a, 3.19b and 3.19c. All show a single sharp peak near 10 Hz and its harmonics, indicating that the flow is periodic. The fact that similar velocity spectra are obtained across the gap indicates that

under this flow condition, the vortices occupy the whole gap space. This finding is supported by the results obtained from Sorour and Coney (1979) and Simmers and Coney (1980). The spectra for flow near the walls show that the relative magnitude of the broadband noise to the sharp dominant peak is smaller compared with the case for flow near the midgap, indicating that the movement of the vortices are more discernable near the boundaries. At this stage, the vortices move as solid bodies, dragging the surrounding fluid with them as they move up the annulus. Similar velocity spectra are also observed for $Re_a = 70$.

For $Re_a = 160$, as shown in Figure 3.20a, 3.20b and 3.20c, the single dominant frequency and its harmonics are still visible in the spectra. However, the spectrum near the inner wall shows that the linewidth of the dominant frequency at 7 Hz has broadened, and there is a second frequency near 5 Hz that is also part of the broad peak. The spectrum at midgap shows a much weaker dominant peak relative to the broadband noise; the second frequency at 5 Hz is not as apparent as in the case near the inner wall. Near the outer wall, the sharp peaks are replaced by peaks with broader linewidths and the frequency of the greatest spectral strength has shifted to near 5 Hz instead of 7 Hz. If the dominant peak is indicative of the vortex passage frequency, then this reflects possibly that the shapes of the vortices are not toroidal. Rather, they may have obtained the shapes shown in Figure 3.21.

Figures 3.22a, 3.22b and 3.22c are the velocity spectra for $Re_a = 220$. At this higher axial Reynolds number, for flow near the walls, the velocity spectra still indicate a single dominant frequency and its harmonics, but the linewidths of the peaks have broadened,

and broadband noise is more apparent in the spectra. However, for flow near midgap, the velocity spectrum reflects only a broadband noise without any significant sharp peak. The characteristic of linear decaying of the broadband boise is more apparent for spectra near the walls than for the spectrum at midgap. At Re_a = 330, similar spectra as in Figures 3.22abc are observed.

For Re_a = 500, Figures 3.23a and 3.23c show that single dominant frequency can no longer be identified from the power spectra. The spectra exhibit the characteristic of broadband noise for flow near the walls. At this point, the velocity power spectra do not provide any hint of existence of any flow structure. Figure 3.23b shows a single peak slightly above the broadband noise for flow in the midgap. As described previously, the flow is non-periodic despite the existence of a peak in the velocity spectrum. For Re_a = 670, the power spectra exhibit similar characteristics as in Figures 3.23a through 3.23c. Figure 3.24a, 3.24b and 3.24c show similar velocity spectra for Re_a = 980. The spectra all indicate a sharp peak slightly above the broadband noise, similar to Figure 3.23c. As described previously, at this axial Reynolds number, the sharp peak in the velocity spectrum does not reflect that the flow is periodic. In fact, the flow may be aperiodic, and the sharp peak may be the result of phase-locking of non-linear disturbances. At Re_a = 1300, similar spectra are observed across the gap as shown in Figures 3.24a through 3.24c. When Re_a is increased to 1600, the spectrum near the inner wall reflects several sharp peaks can still be identified in the spectrum with the broadband background shown in Figure 3.25a. The spectrum of a single peak with broadband noise is observed for flow in midgap, but the spectrum near the outer wall indicate lack of any sharp peaks as shown

in figures 3.25b and 3.25c. When Re_a is greater than 2000, the spectra across the gap all show the broadband spectra similar to those shown in Figures 3.25c.

In general, the axial flow has impact on the whole flow across the gap for r'= 0.1 to 0.9. At low axial Reynolds numbers, Re_a = 10 and 70, the effect of the axial flow is felt equally across the gap when the uniform-sized turbulent vortices fill the whole gap space. However, when Re_a = 160, the dominant fluctuating frequencies near the walls and near the center of the gap are different. Since the axial velocity varies radially and is maximum near the midgap and decreasing sharply to zero near the walls, the impact of the mean axial flow should be the most apparent in the midgap while the flows near the walls experience the effect of a sharp velocity gradient. As the vortices are destroyed by increasing axial flows when Re_a is 220 and greater, the velocity spectra near the walls begin to exhibit different characteristics as flow near the center of the gap, indicating the effects of the axial velocity gradient near the walls. When Re_a is above 1300, the spectra at different gap positions become similar again, all showing the characteristics of turbulent flow, indicating that at large axial flow rates, the flow is turbulent throughout the gap space.

3.5 Effect of Exit Condition

Flow characteristics near the top of the annulus, at l/b=3, are also of interest since this is where the mixing problem is observed in the prototype. Velocity power spectra and autocorrelograms presented here are for Ta=1.45 x 10^7, almost at the same Taylor number as the results presented in previous sections. This will serve as a basis for comparison

that at the same axial Reynolds number and Taylor number, how different are the flows near the mid-height of the annulus and near the top at the mixing region.

Obviously, flows near the top of the annulus are influenced by the exit condition, as demonstrated by the velocity spectrum and autocorrelogram for $Re_a = 0$ shown in Figure 3.26a and 3.26b. The velocity spectrum shows a sharp peak near 20 Hz and broader peaks near 10 Hz and 30 Hz whereas the spectrum near the mid-height shows a sharp peak near 1 Hz. The corresponding autocorrelogram indicates a curious waveform that is a combination of waveforms at several frequencies. Even when there is no axial flow present, the motion of the vortices near the annulus exit is definitely more violent and fluctuates at a much higher frequency.

At $Re_a = 70$, when the flow near the midgap is strongly periodic, it is not the case for flow near the exit. The velocity spectrum and corresponding autocorrelogram shown in Figures 3.27a and 3.27b indicate that no form of periodicity can be deduced from them. The spectrum shows only broadband noise that decays linearly for frequencies between 0 and 50 Hz. Any form of structural integrity that exists in the mid-height of the annulus is destroyed here.

When Re_a is 160, the velocity spectrum indicates a sharp peak near 5 Hz and a second peak near 25 Hz, but the corresponding autocorrelogram does not reflect any form of periodicity in the flow as shown in Figures 3.28a and 3.28b. Similar kind of spectra and autocorrelograms that do not show any periodic nature are observed for higher axial Reynolds numbers. However, it is interesting to show that at the highest axial Reynolds number investigated, at $Re_a = 2500$, in addition to the broadband background, a sharp

peak is observed near 3 Hz in the velocity spectrum shown in Figure 3.29a. The corresponding autocorrelogram in Figure 3.29b also indicates a somewhat periodic waveform. This is in complete contrast to the velocity spectrum for flow near mid-height where no sharp peaks are observed and the flow is assumed to be fully turbulent. It is possible that near the exit of the flow, air of the surrounding is entrained into the annulus such that a slow vortex-like circulating motion is created, and this is reflected in the velocity spectrum and autocorrelogram.

3.6 Summary and Discussion

To further understand the effects of axial flow and Taylor number, and how these effects differ in different gap locations, the results of the power spectra are summarized in the following figures. Figure 3.30a shows how the frequency with the greatest power density in each spectrum varies with the axial Reynolds numbers and with Taylor numbers. At $Re_a = 0$, the frequencies of the maximum peak are approximately equal to 1 Hz for different Taylor numbers. As Re_a is increased to 10, the frequencies corresponding to the maximum peak range from 6 to 11 Hz, with the largest frequency corresponding to the largest Taylor number. At this axial Reynolds number, the velocity spectra for different Taylor numbers all indicate that the flow is periodic. At $Re_a = 70$, the frequency values decrease again. In this case, the frequency values for the higher Taylor numbers ($Ta > 1.42 \times 10^7$) have fallen below the values for the lower Taylor numbers. However, as Re_a is further increased to 160, the trend of larger frequency corresponding to larger Ta has reappeared. For the range of Re_a between 220 and 670,

two general trends are discovered. First, the frequency values increase as Taylor numbers increase; second, the frequency values slowly decrease as the axial Reynolds numbers increase. As Re_a is increased to 980, the frequency values start to rise for $Ta \leq 1.42 \times 10^7$, showing a knee at $Re_a = 670$. For $Ta > 1.42 \times 10^7$, the frequency values still decrease as Re_a is increased. As the axial Reynolds number is increased further, the frequency values for the higher Taylor numbers also increase for subsequent axial Reynolds numbers. The location of the "bend" corresponds to the axial Reynolds number where a lack of sharp spectral peaks is observed in the velocity power spectra. As shown in Figure 3.30a, the "bend" occurs at higher axial Reynolds numbers for the cases of higher Taylor numbers indicating the delay in the onset of turbulence at higher rotational speeds. In addition, once the regime of strong turbulent flow has been reached, there is greater uncertainty in identifying a single sharp frequency component.

Results with data taken at a later date show similar trends in Figure 3.30b. The stratification of frequency values at different Taylor numbers and the occurrence and delaying effects of the "bend" are apparent. However, the exact frequency values at the same Taylor and axial Reynolds numbers are not repeatable. Partly, this is due to the uncertainty in the axial velocity, but this also indicates that the results are highly dependent on the initial condition and history of the flow as explained previously.

The effects of axial Reynolds numbers and Taylor numbers on the strength of the maximum peak of the velocity spectrum are summarized in Figure 3.31. Figure 3.31 indicates that maximum strength of the dominant peak is largest at the lower axial Reynolds numbers. The spectra at the lower axial Reynolds numbers indicate a single

dominant frequency and its harmonics, reflecting a strong periodic signal caused by the movements of the vortices. The strength of the peaks decreases as axial Reynolds number increases. However, at Re_a = 670, the strength of the peak rises slightly again. As the level of turbulence increases at Re_a = 980 and beyond, spectral strengths of the dominant frequency decrease and become fairly constant for Re_a>1300 for all Taylor numbers.

To study how the effect of axial flow differs across the gap, Figure 3.32 shows the plot of value of the frequency with the maximum magnitude in the velocity spectrum vs. the axial Reynolds number for the flow near the walls and in the midgap. At low Re_a, the values of the frequency with the greatest magnitude are the same across the gap. However, at Re_a = 160, the values begin to differ. The value near the outer cylinder drops first, and at Re_a = 220, the frequency value near the inner cylinder also begins to drop. After this point, the frequency values for the inner and outer walls increase as Re_a increase, while those for the midgap case decreases. This indicates that the flow near the boundaries fluctuates at nearly the same frequency while the rate of fluctuation is different near the midgap. When Re_a = 980, the velocity spectra show only broadband noise and the frequency of the maximum spectral strengths are the same across the gap, indicating that the flow fluctuates at the same rate across gap.

Figure 3.33 shows a plot of maximum spectral strength vs. axial Reynolds numbers and gap location. The figure indicates that the velocity spectra show the maximum strength for the velocity spectra with a single sharp peak at low Re_a. At low axial Reynolds number, the vortices are blown past the measurement point. As each vortex is blown past the anemometer, it registers as a period of sinusoidal wave on the

velocity trace. As this fluctuation is very periodic, the periodicity is reflected in the strength of the power spectrum. The spectral strengths are the greatest near the walls, indicating that as the vortices move as solid bodies, at the boundaries of the flow the velocity fluctuation is more discernable. The spectral strength then decreases for Re_a = 160 to 670. As there is no longer a strong periodic motion in the system, the energy of the system is no longer concentrated on a few frequencies, but becomes more evenly distributed. Before the onset of turbulence, the spectral strength increases slightly, and it reaches a minimum at the high axial Reynolds numbers, where the flow has reached full scale turbulence.

To understand the effect of exit conditions for flow field near the top, plots similar to Figures 3.30ab and 3.31 that show the effects of axial Reynolds number and Taylor number on the frequency of the greatest spectral strength and the magnitude of the greatest spectral strength are presented here. In contrast to Figures 3.30ab and 3.31, no general trends are observed in Figures 3.34 and 3.35. Figure 3.34 shows that in contrast to Figure 3.310, no 'bend' is observed. Moreover, for $Re_a < 980$, while the frequencies with the greatest spectral density for velocity spectra at mid-height of annulus are limited to 10 Hz and below, near the top, the frequencies vary from a minimum of 0.1 Hz to above 30 Hz. Figure 3.35 indicates that the greatest spectral strength is observed when there is no axial flow, and the magnitude of it is not greatly influenced by Taylor number or axial Reynolds number.

Chapter 4

Diabatic Experimental Results

4.1 Effect of Heated Axial Flows

4.1.1 Near Mid-height of the Annulus

The velocity spectra are taken for Ta = 1.48 x 10^7 at different axial Reynolds numbers and Grashof numbers. The Grashof number is defined as $b^3 g\beta\Delta T_a/\nu^2$, where ΔT_a is the temperature difference between the axial flow at inlet and the ambient temperature. The Taylor number and axial Reynolds number used here are defined using the value of kinematic viscosity measured in room temperature. This makes it easier to compare the diabatic results to the isothermal ones. However, the impact of viscosity variation due to temperature change will be addressed later in the chapter.

For low degree of heating, the fluid is heated to only about 10 degrees above room temperature, corresponding to Gr_a approximately equal to 2600. Figure 4.1a through 4.1d show the corresponding velocity spectra for Re_a = 0, 10, 670, and 1300. Figure 4.1a is the velocity spectrum when there is no axial flow present. The spectrum still indicates a peak below 1 Hz, similar to Figure 3.3a. However, Figure 4.1a does not reflect the characteristic of the linear decay as shown in Figure 3.3, and the magnitude of the

broadband noise is stronger. Figure 4.1b, at Re_a = 10, the single peak near 4 Hz and its harmonic are observed in the spectrum, similar to Figure 3.4a, but the strengths of the sharp peaks are not as strong as in the isothermal case. At the same time, the peak at a frequency less than 1 Hz has nearly the same strength as the dominant peak and small peaks at high frequencies are also observed. The fact that the location of the dominant frequency has shifted to a lower value may indicate that the sizes of the vortices have increased. As mentioned previously, the Taylor number used here is based on kinematic viscosity defined at room temperature. For air, a 10-degree change in the temperature corresponds to approximately 1 x 10^{-6} m^2/s change in the kinematic viscosity, which represents about a ten-percent decrease for the Taylor number, and a five-percent decrease for the axial Reynolds number. Thus, increasing the temperature of the system in an effect results in a decrease of the Taylor and axial Reynolds numbers for the system, even if the rotational speed and the axial velocity have stayed the same. The velocity spectrum at Re_a = 670, shown in Figure 4.1c, also reflects a sharp peak at a lower frequency near 3 Hz. In Figure 4.1d, at Re_a = 1300, many peaks of similar strengths are observed at frequencies between 0 to 20 Hz. The linearwidths of the peaks are so wide such that it becomes difficult to identify each peak separately from the broadband background.

If the axial flow is heated to a higher temperature, approximately 20 degrees above room temperature, corresponding to Gr_a = 4800, the broadband background is the predominant characteristic of the velocity spectra shown in Figure 4.2a through 4.2d. In Figure 4.2a at Re_a = 0, three broad peaks near 1 Hz, 5 Hz and 8 Hz are observed. The peaks have large linewidths such that they make up a continuous broadband continuum

that decays linearly between the frequencies of 0 and 10 Hz. For Re_a = 10, a sharp peak near 2 Hz and a broad peak near 7 Hz are observed as shown in Figure 4.2b. The broad peak is made of peaks ranging from 4 to 7 Hz that are of similar strengths. Similarly, a sharp peak near 3 Hz and a broad peak near 7 Hz are observed for spectrum at Re_a = 670, similar to Figure 3.11. As Re_a is increased to 1300, only the broadband continuum is observed. When Gr_a is finally increased to 6700, when the axial flow is heated to 30 degrees above ambient temperature, then the velocity spectra all exhibit the characteristic of the broadband continuum. At this level of heating, the temperature difference across the gap is approximately 5 degrees. The flow characteristic is not only influenced by the existance of the Taylor cells, it is also affected by the Bénard cells present in both axial and the radial directions due to the axial and radial temperature gradients. As a result, the characteristics of the fluid motion are complex, and are reflected in the velocity spectra as broadband spectra.

The energy distribution curves similar to Figure 3.14 are plotted for different Grashof numbers and axial Reynolds numbers as shown in Figure 4.3. To show how heated axial flow has affected the energy distribution of the system, Figure 4.3 shows the energy distribution curves for different axial Reynolds number at Gr_a = 0 and 6700. The influence of increasing axial Reynolds numbers on the energy distribution curves is greater for isothermal axial flows than for heated ones. When the axial flow is heated, the energy curves all shift to the right and the slopes of the curves are not as steep as those for isothermal axial flows. For diabatic flow conditions, between 0 to 40 Hz, the contribution to total energy is 30%, and it decreases to 20%, 15 %, 15%, 10% and 10%

for frequency ranges of 40 Hz to 80 Hz, 80 Hz to 120 Hz, 120 Hz to 160 Hz, 160 Hz to 200 Hz, and 200 Hz to 250 Hz respectively. As described previously, for isothermal axial flows, 70% of the total energy of the system is concentrated for frequencies ranging from 0 to 75 Hz, while 50% of it is for frequencies between 0 to 40 Hz. In the case of heated axial flows, 70% of the total energy is contained in the frequency range from 0 to 120 Hz, though it is more evenly distributed.

Figures 4.4a, 4.4b and 4.4c show the effect of axial Reynolds number on the energy distribution curve at fixed Grashof numbers. Figure 4.4a, for Gr_a = 2600, the shapes of the curves for different axial Reynolds numbers are very similar. However, the energy curves shift a little to the left as the axial Reynolds numbers increases, reflecting that more of the system's total energy is distributed at lower frequencies. One possible explanation for this phenomenon is that at this Grashof number, the effect of the axial flow is stronger than buoyancy for higher axial Reynolds numbers. Since the axial flow affects the flow mostly in frequencies ranging from 0 to 70 Hz, this shifts the energy curves to the left. Similar characteristics are observed for Gr_a = 4800 as shown in Figure 4.4b. At Gr_a = 6700, Figure 4.4c indicates that increasing the axial Reynolds number has little effect on either the shape or the location of the energy distribution curves. At this Grashof number, the effect of buoyancy determines the flow characteristics rather than that of increasing axial Reynolds number; thus, no changes are observed for the energy curves.

In general, as the temperature of the axial flow increases, the flow becomes more turbulent. This is reflected both in the velocity power spectra and the energy curves. If

the velocity spectra originally contain sharp peaks, then the sharp peaks gradually broaden or disappear and more small peaks at higher frequencies are observed as the Grashof number is increased. The cumulative energy curves also reflect that the energy of the system is distributed more to higher frequencies in heated flows than in isothermal ones.

4.1.2 Near the Mixing Region

Near the top of the annulus, at l/b = 37, for isothermal axial flows, no trend is discovered from the velocity spectra when the axial Reynolds number is increased. The effect of the heated axial flow is felt differently closer to the top of the annulus than the mid-height. Because of the way the Grashof number is defined, it fails to take into consideration that the average fluid temperatures are different at different axial positions within the annulus. In fact, both the average fluid temperature and the temperature difference across the gap are less for flow at l/b = 37 than at l/b = 20. These effects are shown in the following velocity power spectra.

At Gr_a = 2600, velocity spectra corresponding to Re_a = 0, 10, 670, 1300 and 2000 are shown in Figures 4.5a through 4.5e. When there is no axial flow, Figure 4.5a shows that in addition to the peak near 1 Hz, 3 broad peaks near 3.7 Hz, 8.3 Hz and 12 Hz are also observed. Figure 4.5a is actually similar to Figure 4.1b, which is the spectrum near mid-height with Re_a = 0. This reflects that the Taylor vortices near the top drift slowly upward even when there is no axial flow present. At Re_a = 10, a sharp peak near 2 Hz is observed, and two smaller peaks near 4 Hz and 12 Hz are also present, as shown in Figure 4.5b. When Re_a is increased to 670, Figure 4.5c shows that many peaks of similar

strength emerge between the frequencies of 0 and 15 Hz, and it is difficult to distinguish them from the broadband background. Both Figures 4.5d and 4.5e, at Re_a = 1300 and 2000, exhibit only broadband characteristics. One major difference between these spectra and the spectra near the mid-height is that the characteristic of linear decay of the broadband noise are apparent here, similar to the spectra for isothermal flows in Figures 3.26a, 3.27a, 3.28a and 3.29a. This is not observed for the spectra near the mid-height. In addition, a low frequency peak near 1 to 2 Hz is always in the spectra even when the axial Reynolds number is at 2000.

When Gr_a is increased to 6700, at Re_a = 0, a sharp peak near 14 Hz is observed in the velocity spectrum shown in Figure 4.6a. This sharp peak is the part of a very broad peak centered near 10 Hz and has a linewidth of 20 Hz. When the axial Reynolds number is increased to 10, Figure 4.6b shows that the sharp peak has disappeared and only the broadband continuum remains. Figure 4.6c shows that at Re_a = 670, sharp peaks of decreasing spectral strengths between 0 to 30 Hz are apparent in the power spectrum. When Re_a is further increased to 1300, the velocity spectrum consists of two broad peaks near 2 Hz and 10 Hz as shown in Figure 4.6d.

The corresponding energy distribution curves for Gr_a = 6700 are shown in Figure 4.7. No significant trend is discovered when the axial Reynolds number is increased, but they exhibit a different form than those observed near the mid-height of the annulus. The curves are not as flat as those in Figure 4.5. More of the total energy of the system is distributed to lower frequencies near the upper region of the annulus than near the mid-height. At l/b = 37, half of the system's total energy is concentrated in frequencies below

20 Hz, and 70% of the total energy is distributed to frequencies between 0 to 45 Hz. This indicates that motions near the upper annulus has a slower fluctuating rate than motions near the mid-height.

4.2 Effect of Rotational Speed In Heated Flows

To demonstrate how the rotational speed affects the flow characteristics when the axial flow is heated, Figure 4.8a through 4.8d are the velocity spectra taken in mid-height (l/b = 20) for Gr_a = 3600, Re_a = 10, and various Taylor numbers ranging from 1.2 x 10^7 to 2.4 x 10^7. As shown in the figures, all of the spectra show similar characteristics where a dominant sharp peak can be distinguished from the background noise. The harmonics of the dominant peaks and peaks at other frequencies are apparent, and the characteristic of linear decay of the broadband background is reflected in all the spectra. The dominant sharp peak is observed to shift a little to the right as the rotational speed increases as shown in Figure 4.9. This phenomenon is not observed when the rotational speed is increased at higher Grashof numbers, neither is it observed in the spectra with higher axial flow rates. Moreover, the velocity spectra taken near the upper annulus are also unaffected by the increase of the rotational speed.

4.3 Temperature Measurements

4.3.1 Temperature Distribution and Spectral Analysis

In the experiment, at the measurement locations at l/b = 20 and 37, less than one degree of temperature difference is observed circumferentially. At Gr_a = 6700, the axial

temperature distributions at different axial Reynolds numbers are shown in Figure 4.10. The temperature distribution curves shift upward as the axial Reynolds number is increased. This result is similar to the findings of the Japanese researchers (Kato et al., 1992 and 1993; Watanabe et al., 1993; Narabayashi et al., 1993; Shiina et al., 1993) since the axial injectant in their studies are colder than the temperature of the surrounding instead of hotter. No change in the axial temperature distributions is observed with increasing rotation speed. For Gr_a = 6700, the temperature difference across the gap is about 5 °C near the mid-height of the annulus, and it decreases to about 3 °C near the upper annulus region.

At Gr_a = 2600 and Ta = 1.48 x 10^7, the temperature spectra at both l/b = 20 and 37 for the axial Reynolds numbers studied all show broadband characteristics only. This is expected since at this low degree of heating, the magnitude of the temperature fluctuation is not large enough such that it is still within the uncertainty of the thermocouples. At Gr_a = 4800, the temperature spectra at l/b = 20 for axial Reynolds numbers of 0, 10, 670, 1300 and 2000 are shown in Figures 4.11a through 4.11e. For Re_a = 0, a sharp peak is observed in the spectrum at 1 Hz. As the axial Reynolds number is increased, the sharp peak persists in the power spectra, but it is shifting to the right as shown in Figures 4.11b through 4.11d. This indicates that as the axial Reynolds number is increased, fluctuations at higher rates become more dominant. When Re_a is increased to 2000, the spectrum in Figure 4.11e shows broadband continuum with a sharp peak at 0.1 Hz. The corresponding temperature for l/b = 37 are shown in Figures 4.12a through 4.12e. At Re_a = 0, no sharp peaks are observed in these spectra and they appeared to be

very noisy. A possible explanation for the lack of sharp peaks in the spectra is that at this point, the level of heating may not be enough for large temperature fluctuations.

When Gr_a is 6700, a strong peak near 9 Hz and its harmonic are observed in the spectrum for $Re_a = 0$ shown in Figure 4.13a. If Taylor vortices still exist under these flow conditions, because of the temperature gradient across the gap, the vortex boundary near the inner wall will have a higher temperature than near the outer wall. As each vortex in the vortex-pair rotates in opposite directions, this may create alternating cold and hot boundaries within the vortex-pair. As the hot/cold vortex-pair are convected upward by the buoyancy force, this causes a periodic temperature fluctuation when temperature is measured at a fixed position, and this is reflected in the temperature spectrum as a strong peak. When Re_a is increased to 10, a broad peak near 4.5 Hz is observed in the spectrum as reflected in Figure 4.13b. The shift of the peak to the left possibly indicates growth of the wavelengths of the vortices. As Re_a is further increased to 670, Figure 4.13c indicates that several sharp peaks are observed in the spectrum. The spectrum reflects only broadband noise when Re_a is increased to 1300, although a linear decaying of the spectral density is observed between 0 to 30 Hz shown in Figure 4.13d.

The corresponding temperature spectra at $l/b = 37$ exhibit different characteristics as those in mid-height as shown in Figure 4.14a through 4.14e. At $Re_a = 0$, instead of a sharp peak and its harmonic, several peaks of broad linewidths centered near 1 Hz, 10 Hz, 20 Hz and 25 Hz are observed. Figure 4.14b also exhibits similar characteristic as Figure 4.14a when Re_a is increased to 10. When Re_a is increased to 670, the peaks have broadened such that they become part of the broadband background as shown in Figure

4.14c. A similar spectrum is observed in Figure 4.14d. It is noted that for Figures 4.14a through 4.14d, the peaks at frequencies between 0 and 10 Hz have spectral strengths almost one order of magnitude greater than for those at other frequencies, reflecting that the temperature fluctuations of greater magnitudes fluctuate at a rate less than 10 Hz. This possibly implies that temperature fluctuations near the mixing region are due to cold air penetration, and this effect is at low frequencies.

4.3.2 Comparisons Between the Velocity and Temperature Results

At first, the characteristics of temperature fluctuation are expected to be very similar to the velocity variations in the flow when they are measured at the same location. Thus, the velocity and temperature spectra should be very similar. However, as reflected in the spectra, they are actually very different in some cases. In the cases where sharp peaks can be identified from the spectra, the frequencies of the peaks are different for velocity and temperature spectra as shown in Table 4.1.

Table 4.1 indicates the frequencies with the maximum spectral strength in both the temperature and velocity spectra at both measurement locations, at l/b = 20 and 37. When there are several peaks with similar spectral strengths, all of them are listed in the table. If the spectra is noisy such that no sharp peaks with the greatest spectral strength can be identified, then it is indicated as N/A in the table. As the table shows, near the mid-height of the annulus, at low axial flow rates, even though the frequencies with the maximum strengths are not the same for temperature and velocity spectra, they are still quite close. But for the cases of higher axial Reynolds numbers, and for measurements

taken at upper annulus, the frequencies are quite different. One possible explanation is that unlike the hot-wire anemometer, the thermocouple is not direction sensitive. The hot-wire probe is always placed such that it is most sensitive to disturbances in the tangential direction, although the hot-wire output is affected by fluctuations in other directions. It is possible that at higher axial flow rates, the temperature fluctuation with the greatest strength is in a direction other than the tangential direction. The peak with the greatest strength in the velocity spectrum reflects the fluctuation in the tangential direction while the one in the temperature spectrum represents fluctuation in another direction.

4.4 Summary and Discussion of the Diabatic Results

The summary graphs similar to Figures 3.30a and 3.31 which plot the frequency with the greatest strength and the greatest spectral density as a function of axial Reynolds number and Taylor number are not plotted here. There are two explanations for not plotting them. In diabatic flows, both the temperature and velocity power spectra are often very noisy, consisting of several peaks of similar spectral density. It then becomes difficult to identify the frequency of the single peak with a greatest power density. This is reflected in Table 4.1. Also, as described in Section 2.2.4, the spectral density of the power spectrum is influenced by the difference between the temperatures of the mean flow in calibration and in the experiment. As a result, the spectral densities are not compared. Moreover, the kinematic viscosity of air increases 1×10^{-6} m^2/s for every 10-degrees increase above room temperature. This results in a decrease of ten-percent and five-percent for the Taylor and axial Reynolds number. Thus, even at the same rotational

speed and the same axial flow rate, the corresponding Taylor number and axial Reynolds number are different for different Grashof numbers, making it difficult to determine the actual effects of the Taylor and the axial Reynolds numbers. Instead of showing summaries of the frequencies and the spectral strengths, two non-dimensional temperature ratios are defined and they are plotted as a function of the axial flow rate and the rotational speed.

The temperature ratio, $(T_{max} - T_{min})/(T_{avg} - T_{amb})$, serves as a measure in determining the magnitude of the largest temperature fluctuation relative to the heating level of the fluid at the measurement location. T_{max} and T_{min} are the maximum and miminum temperatures observed in the temperature trace, and T_{avg} and T_{amb} denote the average fluid temperature at the measurement position and the ambient temperature respectively. As described previously, at the same Grashof number, the average fluid temperature near the upper annulus is lower than the temperature in the mid-height. This definition of temperature ratio takes this into consideration. A second temperature ratio, defined as $(T_{max} - T_{min})/(T_{in} - T_{out})$, is a measure of the magnitude of the temperature fluctuation relative to the overall heating level of the system, where T_{in} and T_{out} are the inlet and outlet temperatures respectively.

Figures 4.15a and 4.15b show how the percentage of temperature fluctuation varies as the axial Reynolds number vary for different temperature ratio definitions at Gr_a = 6700. Figure 4.15a is for temperature ratio definition of $(T_{max} - T_{min})/(T_{avg} - T_{amb})$, and at l/b = 20 and 37. In both cases, the temperature fluctuation percentage decreases as the axial Reynolds number increases, and a sharper decrease is shown for l/b = 37. However,

the values of the fluctuation percentage are consistently larger for l/b = 37 than l/b = 20. With a different temperature ratio definition, $(T_{max} - T_{min})/(T_{in} - T_{out})$, the trend reverses, as shown in Figure 4.15b. For both l/b = 20 and l/b = 37, the fluctuation percentage increases as the axial Reynolds number increases. This reflects that, depending upon how the temperature ratio is defined, different trends are observed in terms of how the axial Reynolds number affects the magnitude of temperature fluctuation. Figure 4.16a through 4.16d show the effect of the Taylor number on temperature fluctuation at l/b = 20 and 37. For either temperature ratio definition, no trend is observed as the Taylor number is increased.

Chapter 5

Concluding Remarks

There have been many previous studies on Taylor-Couette flows, for both adiabatic and diabatic flow conditions. A large number of the studies were devoted to the study of the stability of Taylor-Couette system with or without axial flow, such as works by Chandrasekhar (1960, 1962), DiPrima (1960), Krueger and DiPrima (1964), Gravas and Martin (1978), and Chen and Kuo (1990). Other researchers studied and identified the various modes and transitional regions within the Taylor-Couette flow, examples include the works of Kaye and Elgar (1958), Astill (1964), Gorman and Swinney (1982), Fenstermacher and Swinney (1979), the series of papers by Wan and Coney (1980, 1982abc) and Simmers and Coney (1979,1980). Most of these works are for flows in an enclosed annulus, and are for Taylor-Couette flows in the laminar-plus-vortices regime.

The current research examines flows in the turbulent vortex regime in an open annulus. Several other researchers, such as Koschmieder (1979), Smith and Townsend (1982) and Townsend (1984), also studied the flow characteristics of turbulent Taylor vortex flow. However, unlike the current work, these studies are for adiabatic flow condition and did not include the effect of a superimposed axial flow. The current work

studies the characteristics of turbulent vortex flow with increasing axial Reynolds number and increasing Taylor number using spectral analysis. It discusses the effect of heated axial flows at different temperatures on the turbulent vortex flow. In addition to the study of the velocity field under diabatic condition, this work also examines the characteristics of the temperature profiles within the annulus. Morever, the current experiment models the flow condition in an annulus gap between a primary loop recirculating (PLR) pump shaft and the casing cover where large temperature fluctuations are observed. Thus, the characteristics of thermal mixing near the exit of the annulus is also studied in the current work.

This experiment ingestigates the effect of isothermal and heated axial flow on flow in a vertical annulus with a rotating inner cylinder for large Taylor numbers ranging from 1.2×10^7 to 2.4×10^7. In this range of Taylor numbers, the flow is in the turbulent vortex regime. The velocity measurements are taken using the hot-wire anemometer and the flow is fully developed. In the isothermal case, when there is no or low axial flow present, the flow is axisymmetric. At low axial Reynolds number of 10 and 70, the power spectrum of the tangential velocity component reflects a single dominant peak and its harmonics, indicating the flow is periodic. In addition, the dominant frequency in the velocity spectrum increases as rotational speed increases. For the same rotational speed, increasing the axial flow rates increase the turbulence level in the flow. When Re_a is greater than 980, the velocity power spectra exhibit no significant peaks as the flow becomes fully turbulent. Basically, the flow exhibits similar characteristics across the

annulus gap. However, the fluctuating frequency near the walls may be different than in midgap, and the spectral intensity is stronger near the walls.

For the diabatic flow condition, the current experiment models the thermal mixing problem observed in the annulus gap formed by the PLR pump shaft and shaft housing. As described previously, in terms of the two non-dimensional numbers, the Taylor number and the axial Reynolds number, the experiment matches the actual problem fairly well. However, the Grashof number based on annulus height that can be achieved in the current experiment is several orders of magnitude less than in the pump, though the Grashof number based on the gap width is only slightly less. Further comparison of the current experimental results with the test results of the actual pump will determine how the current study can help resolve the thermal fatigue problem in the pump.

Kato et al. (1993) have shown the mean temperature distribution curves shift upward with an increase of the rotational speed and decrease in the cold seal purge flow rate (axial flow rate). In the current experiment, a similar effect is observed that when the axial flow rate is increased, the mean temperature distribution curves shift downward with the decrease of the hot axial flow rate as shown in Figure 4.10. However, a change of the rotational speed does not affect the temperature distribution curves. The current experiment studies the effect of a much narrower range of rotational speed (1100 to 1500 RPM) than in the study by Kato et al. (280 to 1395 RPM), and this difference in rotational speeds is not enough to shift the temperature distribution curves. Kato et al.'s paper also reports that the magnitude of temperature fluctuation (T_{max} - T_{min}) increases as the seal purge flow rate increases. Since the temperature difference between the inlet

and outlet of the annulus is a constant in the pump for different seal purge flow rates, Kato's result implies that the temperature ratio, $(T_{max} - T_{min})/(T_{in} - T_{out})$, increases as the seal purge flow rate increases. This is similar to the result of the current experiment where the same temperature is observed to increase as the axial flow rate is increased, as shown in Figure 4.15b.

Kato et al. (1993), Watanabe et al. (1993) and Shiina et al. (1993) all performed a fast Fourier transform (FFT) analysis of the temperature data. The FFT analysis did not give meaningful frequency spectra. But, in a visualization done by Narabayashi (1993), a wavy boundary between the cold purge water and the hot water was observed, and it was rotating at almost half the speed of the rotating shaft. In Gopalakrishnan's crack propagation study (1992), it is determined that the cracks are mostly caused by fluctuations under 25 Hz. In the current experiment, there are sharp peaks observed in some of the velocity and temperature spectra in heated flows, and most of the dominant peaks are below 25 Hz. For spectra at l/b= 37, near the mixing region, the sharp peaks observed in the temperature spectra are at lower frequencies between 0 to 10 Hz. Nevertheless, at l/b = 37 for $Gr_a = 6700$, a broad peak centered near 10 Hz, half the speed of the inner cylinder, is present in both the temperature and velocity spectra as shown in Figures 4.6a through 4.6d and 4.14e through 4.14e. This seems to confirm Narabayashi's finding.

Several other factors that are not studied in the current experiment may also influence the magnitude of the thermal fluctuations. There are spiral grooves on the pump shaft that may influence the flow characteristic, and the discharge flow rate from

a hydraulic bearing near the exit of the annulus may worsen the temperature fluctuations, as shown by Kato at al. The current experiment cannot model the effect of varying kinematic viscosity along the axial direction because the experiment cannot duplicate the kind of temperature difference between the inlet and the outlet. Moreover, an increase of the air temperature results in increase of kinematic viscosity whereas the opposite effect is observed for viscosity of water. The motion of the impeller, which is not modelled in the experiment, may also be an important factor in causing temperature fluctuations. Nevertheless, under the scope of the current study, the experiment has demonstrated successfully the effects of axial flow and rotational speed on temperature fluctuations. Dr. Gopalakrishnan of BW/IP International and the Japanese researchers have proposed a new device called the seal purge heater, which heats the seal purge flow before it is injected into the annulus, to solve the thermal fluctuation problem. They claimed that the mock up test results indicate that the heater does reduce the magnitude of the temperature fluctuations. Future work should focus on determining the effect of other factors not investigated in the current experiment, on temperature fluctuations, and on studying the effectiveness of the seal purge heater in eliminating the thermal fatigue problem.

Bibliography

Ali, M. and Weidman, P.D., 1990, "On the Stability of Circular Couette Flow with Radial Heating," *J. Fluid Mech.,* Vol. 220, pp. 53-84.

Astill, K.N., 1964, "Studies of the Developing Flow Between Concentric Cylinders with the Inner Cylinder Rotating," *J. Heat Transfer,* Vol. 86, pp. 97-105.

Ball, K.S. and Farouk, B., 1989, "A Flow Visualization Study of the Effects of Buoyancy on Taylor Vortices," *Phys. Fluids A*, Vol. 1, No. 9, pp. 1502-1507.

Ball, K.S., Farouk, B. and Dixit, V.C., 1989, "An Experimental Study of Heat Transfer in a Vertical Annulus with a Rotating Inner Cylinder," *Int. J. Heat Mass Transfer*, Vol. 32, No. 8, pp. 1517-1527.

Barcilon, A., Brindley, J., Lessen, M., and Mobbs, F.R., 1979, "Marginal Instability in Taylor-Couette Flows at a Very High Taylor Number," *J. Fluid Mech.*, Vol. 94, pp. 453-463.

Bergé, P., Pomeau, Y., and Vidal, C., 1986, *Order within Chaos*, John Wiley & Sons, New York.

Brandstater, A. and Swinney, H.L., 1987, "Strange Attractors in Weakly Turbulent Couette-Taylor Flow," *Phys. Review A*, Vol. 35, No. 5, pp. 2207-2220.

Brandstater, A., Swift, J., Swinney, H.L., Wolf, A., Farmer, J.D., Jen, E., and Crutchfield, P.J., 1983, "Low-Dimensional Chaos in a Hydrodynamic System," *Physical Review Letters*, Vol. 51, No. 16, pp. 1442-1445.

Burkhalter, J.E. and Koschmieder, E.L., 1973, "Steady Supercritical Taylor Vortex Flow," *J. Fluid Mech.*, Vol. 58, Part 3, pp. 547-560.

Chandrasekhar, S., 1960, "The Hydrodynamic Stability of Viscid Flow Between Coaxial Cylinders," *Proc. Nat. Acad. Sci.*, Vol. 46, pp. 141-143.

Chandrasekhar, S., 1962, "The Stability of Spiral Flow Between Rotating Cylinders," *Proc. R. Soc. Lond.*, Vol. A265, pp. 189-197.

Chen, J. and Kuo, J., 1990, "The Linear Stability of Steady Circular Couette Flow with a Small Radial Temperature Gradient," *Phys. Fluids A*, Vol. 2, pp. 1585-1591.

Coles, D., 1965, "Transition in Circular Couette Flow," *J. Fluid Mech.*, Vol. 21, pp. 385-425.

DiPrima, R.C., 1960, "The Stability of a Viscous Fluid Between Rotating Cylinders with an Axial Flow," *J. Fluid Mech.*, pp. 621-631.

DiPrima, R.C. and Swinney, H.L., 1981, "Instabilities and Transition in Flow Between Concentric Rotating Cylinders," *Hydrodynamic Instabilities and the Transition to Turbulence* (eds. Swinney and Gollub), Springer, Berlin, pp. 139-180.

Fenstermacher, P.R., Swinney, H.L. and Gollub, J.P., 1979, "Dynamical Instabilities and the Transition to Chaotic Taylor Vortex Flow," *J. Fluid Mech.*, Vol. 94, Part 1, pp. 103-128.

Gollub, J.P. and Benson, S.V., 1980, "Many Routes to Turbulent Convection," *J. Fluid Mech.*, Vol. 100, Part 3, pp. 449-470.

Gopalakrishnan, S., Vaghasia, G.K., and Reimers, C.R., 1992, "Crack Propagation in Main Coolant Pumps," *Internal Report of the Pump Division of BW/IP International, Inc.*

Gorman, M. and Swinney, H.L., 1982, "Spatial and Temporal Characteristics of Modulated Waves in the Circular Couette System," *J. Fluid Mech.*, Vol. 117, pp. 123-142.

Gravas, N. and Martin, B.W., 1978, "Instability of Viscous Axial Flow in Annuli Having a Rotating Inner Cylinder," *J. Fluid Mech.*, Vol. 86, pp. 385-394.

Greenside, H.S., Ahlers, G., Hohenberg, P.C. and Walden, R.W., 1982, "A Simple Stochastic Model for the Onset of Turbulence in Rayleigh-Bénard Convection," *Physica*, Vol. 5D, pp. 322-334.

Kataoka, K., 1985, "Taylor Vortices and Instabilities in Circular Couette Flows," *Encyclopedia of Fluid Mechanics,* Vol. 1, (ed. Cheremisinoff, N.P.), Gulf Publishing Company, Houston, pp. 237-274.

Kato, H., Kanno, H., Hosokawa, M., Watanabe, A., Shitara, C., Ashizawa, K., Miyano, H., Narabayashi, T., Iikura, T., Hayashi, M., Endoh, A., and Takehara, H., 1992, "The Development of Advanced Nuclear Primary Loop Recirculating Pump (PLR Pump) for BWR Plant Considering Thermal Fatigue Problem," *Essay Collection of Japan Owners Group of Nuclear Reactor Power Station.*

Kato, H., Kanno, H., Hosokawa, M., Watanabe, A., Shitara, C., Ashizawa, K., Miyano, H., Narabayashi, T., Iikura, T., Hayashi, M., Endoh, A., and Takehara, H., 1992, "The Development of Advanced Nuclear Primary Loop Recirculating Pump (PLR Pump) for BWR Plant Considering Thermal Fatigue Problem," *Proc. of the ASME Winter Annual Meeting*, pp. 157-162.

Kato, H., Kanno, H., Hosokawa, M., Watanabe, A., Shitara, C., Ashizawa, K., Miyano, H., Narabayashi, T., Iikura, T., Hayashi, M., Endoh, A., and Takehara, H., 1993, "Experimental Studies of Temperature Fluctuation Phenomena for Nuclear Reactor Primary Loop Recirculation Pump (PLR Pump)," *Proc. of the ICOPE.*

Kaye, J. and Elgar, E.C., 1958, "Modes of Adiabatic and Diabatic Fluid Flow in an Annulus with an Inner Rotating Cylinder," *Trans. A.S.M.E.*, Vol. 80, pp. 753-765.

Koschmieder, E.L., 1979, "Turbulent Taylor Vortex Flow," *J. Fluid Mech.*, Vol. 93, pp. 515-527.

Krueger, E.R. and DiPrima, R.C., 1964, "The Stability of a Viscous Fluid between Rotating Cylinders with an Axial Flow," *J. Fluid Mech.*, Vol. 9, pp. 528-538.

Narabayashi, T., Miyano, H., Komita, H., Iikura, T., Shiina, K., Kato, H., Watanabe, A., and Takahashi, Y., 1993, "Study on Temperature Fluctuation Mechanisms in an Annulus Gap between PLR Pump Shaft and Casing Cover," *Proc. of the Second ICONE.*

Shiina, K., Nakamura, S., Mizushina, Y., Yanagida, T., Endo, A., Takehara, H., Narabayashi, T., Kato, H., and Watanabe, A., 1993, "Heat Transfer Characteristics of Fluid Flow in an Annulus with an Inner Rotating Cylinder Having a Labyrinth Structure," *Proc. of the 3rd World Conference on Experimental Heat Transfer and Thermodynamics.*

Sigeti, D. and Horsthemke, W., 1987, "High-Frequency Power Spectra for Systems Subject to Noise," *Phys. Review A.*, Vol. 35, No. 5, pp. 2276-2282.

Simmers, D.A. and Coney, J.E.R., 1979, "The Experimental Determination of Velocity Distribution in Annular Flow," *Int. J. Heat & Fluid Flow*, Vol. 1, No. 4, pp. 177-184.

Simmers, D.A. and Coney, J.E.R., 1980, "Velocity Distributions in Taylor Vortex Flow with Imposed laminar Axial Flow and Isothermal Surface Heat Transfer," *Int. J. Heat & Fluid Flow*, Vol. 2, No. 2, pp. 85-91.

Smith, G.P. and Townsend, A.A., 1982, "Turbulent Couette Flow Between Concentric Cylinders at Large Taylor Numbers," *J. Fluid Mech.*, Vol. 123, pp. 187-217.

Snyder, H.A., 1962, "Experiments on the Stability of Spiral Flow at Low Axial Reynolds Numbers," *Proc. Roy. Soc. Lond*, Vol. A265, pp. 198-214.

Snyder, H.A., 1965, "Experiments on the Stability of Two Types of Spiral Flow," *Annals of Physics*, Vol. 31, pp. 292-313.

Snyder, H.A. and Karlsson, S.K.F., 1965, "Experiments on the Stability of Couette Motion with a Radial Thermal Gradient," *Physics Fluids*, Vol. 7, pp. 1696-1706.

Sorour, M.M. and Coney, J.E.R., 1979a, "An Experimental Investigation of the Stability of Spiral Vortex Flow," *J. Mech. Engng. Sci.*, Vol. 21, No. 6, pp. 397-402.

Sorour, M.M. and Coney, J.E.R., 1979b, "The Characteristics of Spiral Vortex Flow at High Taylor Numbers," *J. Mech. Engng. Sci.*, Vol. 21, No. 2, pp. 65-71.

Sorour, M.M. and Coney, J.E.R., 1979c, "The Effect of Temperature Gradient on the Stability of Flow between Vertical, Concentric, Rotating Cylinders," *Int. Mech. Engr. Sci.*, Vol. 21, No. 6, pp. 403-409.

Taylor, G.I., 1923, "Stability of a Viscous Liquid Contained Between Two Rotating Cylinders," *Phils. Trans. R. Soc. London, A*, Vol. 223, pp. 298-343.

Taylor, J., 1982, *An Introduction To Error Analysis: The Study of Uncertainties in Physical Measurements*, University Science Books, Mill Valley, pp. 153-172.

Townsend, A.A., 1984, "Axisymmetric Couette Flow at Large Taylor Numbers," *J. Fluid Mech.*, Vol. 144, pp. 329-362.

Wan, C.C. and Coney, J.E.R., 1980, "Transition Modes in Adiabatic Spiral Vortex Flow in Narrow and Wide Annular Gaps," *Int. J. Heat & Fluid Flow*, Vol. 2, No. 3, pp. 131-138.

Wan, C.C. and Coney, J.E.R., 1982a, "An Investigation of Adiabatic Spiral Vortex Flow in Wide Annular Gaps by Visualisation and Digital Analysis," *Int. J. Heat & Fluid Flow*, Vol. 3, No. 1, pp. 39-44.

Wan, C.C. and Coney, J.E.R., 1982b, "An Investigation of Adiabatic Spiral Vortex Flow by Means of Cross-Wire Probes," *Int. J. Heat & Fluid Flow*, Vol. 3, No. 3, pp.125-133.

Wan, C.C. and Coney, J.E.R., 1982c, "Radial Variation of Adiabatic and Diabatic Spiral Vortex Flow in a Wide Annular Gap," *Int. J. Heat & Fluid Flow*, Vol. 3, No. 2, pp. 101-109.

Watanabe, A., Takahashi, Y., Igi, T., Miyano, H., Narabayashi, T., Iikura, T., Sagawa, W., Hayashi, M., Endoh, A., Kato, H., Kanno, H., and Hosokawa, M., 1993, "The Study of Thermal Fatigue Problem on Reactor Recirculation Pump on BWR Plant," *Proc. of the ICOPE.*

Appendix A

Spectral Analysis

In the current experiment, a continuous function, f(t), is sampled at equal intervals to produce values F(0)...F(N-1), a data set consisting of N points. The waveform of its discrete Fourier transform function, H(k), is computed using the Fast Fourier Transform (FFT):

$$H(k) = \sum_{j=0}^{N-1} F(j) e^{(\frac{2\pi jki}{N})} \tag{A.1}$$

The power spectrum estimation used is an estimator called the periodogram, defined at N/2 + 1 frequencies as:

$$\begin{aligned} P(0) &= \frac{1}{N^2} |H(0)|^2 \\ P(k) &= \frac{1}{N^2} [\, |H(k)|^2 + |H(N-k)|^2] \quad k = 1,2,...(N/2-1) \\ P(N/2) &= \frac{1}{N^2} |H(N/2)|^2 \end{aligned} \tag{A.2}$$

where P(k) is the spectral estimate at a discrete frequency. The equation is normalized such that the sum of the N/2 + 1 values of P is equal to the mean squared amplitude of the function F(k).

In general, the spectral power in one "bin" k may contain leakage from frequency components that are actually several bins away. Windows are often used in spectral analysis to reduce the undesirable effects related to spectral leakage. Since the function is sampled for a finite length of time, discontinuities occur at the endpoints of the waveform. Windows are weighting functions applied to the raw data to reduce leakage. The window currently used in calculating the power spectra is the Hamming window, which is defined as:

$$w_j = 0.56 - 0.46 \cos(\frac{2\pi j}{N}) \qquad \text{(A.3)}$$

Appendix B

Error Analysis

As shown in Section 2.2.2, during calibration, the velocity is calculated from dynamic pressure measured in terms of inches of water, Δh, by the inclined manometer. The velocity, v_a, is calculated as:

$$v_a = \sqrt{\frac{2\rho_H g \Delta h}{\rho_a}} \tag{B.1}$$

where ρ_H and ρ_a are the densities of water and air respectively. The uncertainty in manometer measurement is .00127 cm, corresponding to a relative uncertainty of 2.5%. Thus, the relative uncertainty of v_a due to the relative uncertainty of the manometer is then calculated as follows:

$$\frac{\partial v_a}{v_a} = \frac{\delta(\sqrt{\Delta h})}{\sqrt{\Delta h}} = \frac{1}{2}\frac{\partial(\Delta h)}{\Delta h} \tag{B.2}$$

Thus, the relative uncertainty for the calculated velocity, v_a, is 1.25%.

Now, since the velocity measured is converted from voltage outputs, the uncertainty of the measured velocity is dependent on the uncertainties of the calibration

constants, m and c. The uncertainties of the calibration constants are calculated using the following relations (Taylor, 1982):

$$\sigma_c^2 = \frac{\sigma_y^2 \sum x_i^2}{\Delta} \quad , \quad \sigma_m^2 = \frac{N\sigma_y^2}{\Delta} \tag{B.3}$$

with σ_y and Δ defined as:

$$\sigma_y^2 = \frac{1}{N-2}\sum_{i=1}^{N}(y_i - c - mx_i)^2 \tag{B.4}$$

$$\Delta = N(\sum x_i^2) - (\sum x_i)^2$$

In the equations, N represents the number of points used for regression, and x and y correspond to square of the voltage and the square root of v_a. σ_y is the estimated uncertainty of $v_a^{1/2}$ assuming that the measurement of each v_a is normally distributed about its calculated value from the voltage outputs. Using the calibration results of one probe as example, the relative uncertainties of the calibration constants are 2.7% and 5.6% respectively. Once these uncertainties are found, then the relative uncertainty of the calculated velocity is calculated as:

$$\frac{\partial v}{v} = \frac{\delta(mV^2+c)^2}{(mV^2+c)^2} = 2\frac{\partial(mV^2+c)}{mV^2+c} \tag{B.5}$$

But the relative uncertainty of $(mV^2 + c)$ is defined as:

$$\frac{\partial(mV^2+c)}{mV^2+c} = \sqrt{\left(\frac{\partial m}{m}\right)^2 + \left(2\frac{\partial V}{V}\right)^2 + \left(\frac{\partial c}{c}\right)^2} \tag{B.6}$$

With the uncertainty of voltage negligible, combining equations (B.5) and (B.6), then the relative uncertainty of the calculated velocity is:

$$\frac{\partial v}{v} = 2\sqrt{\left(\frac{\partial m}{m}\right)^2 + \left(\frac{\partial c}{c}\right)^2} \tag{B.7}$$

And the upper bound of the relative uncertainty is:

$$\left(\frac{\partial v}{v}\right)_{upper} = 2\left(\frac{\partial m}{m} + \frac{\partial c}{c}\right) \tag{B.8}$$

The relative uncertainty and the upper bound of the uncertainty are calculated to be 12% and 16.6% respectively.

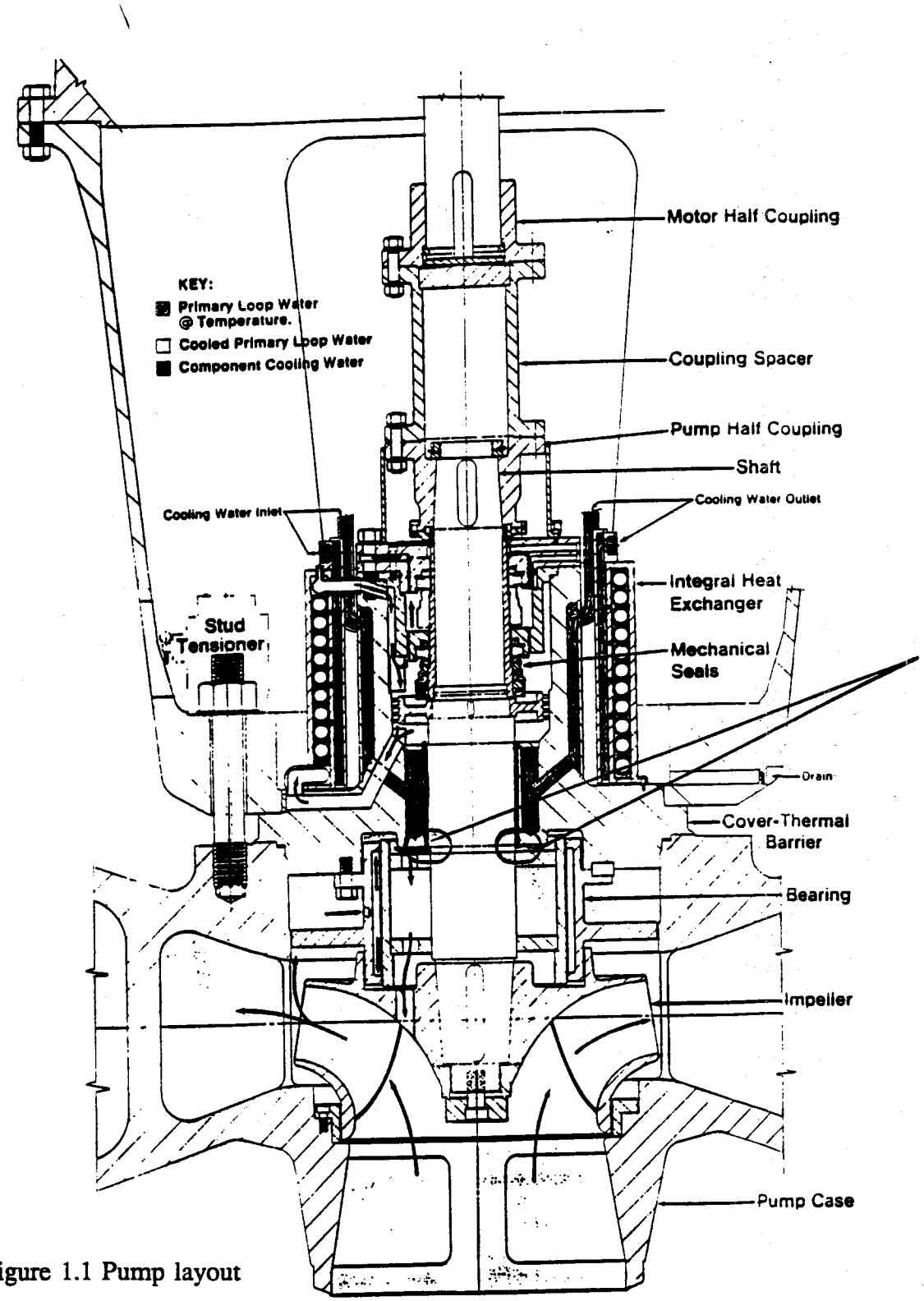

Figure 1.1 Pump layout

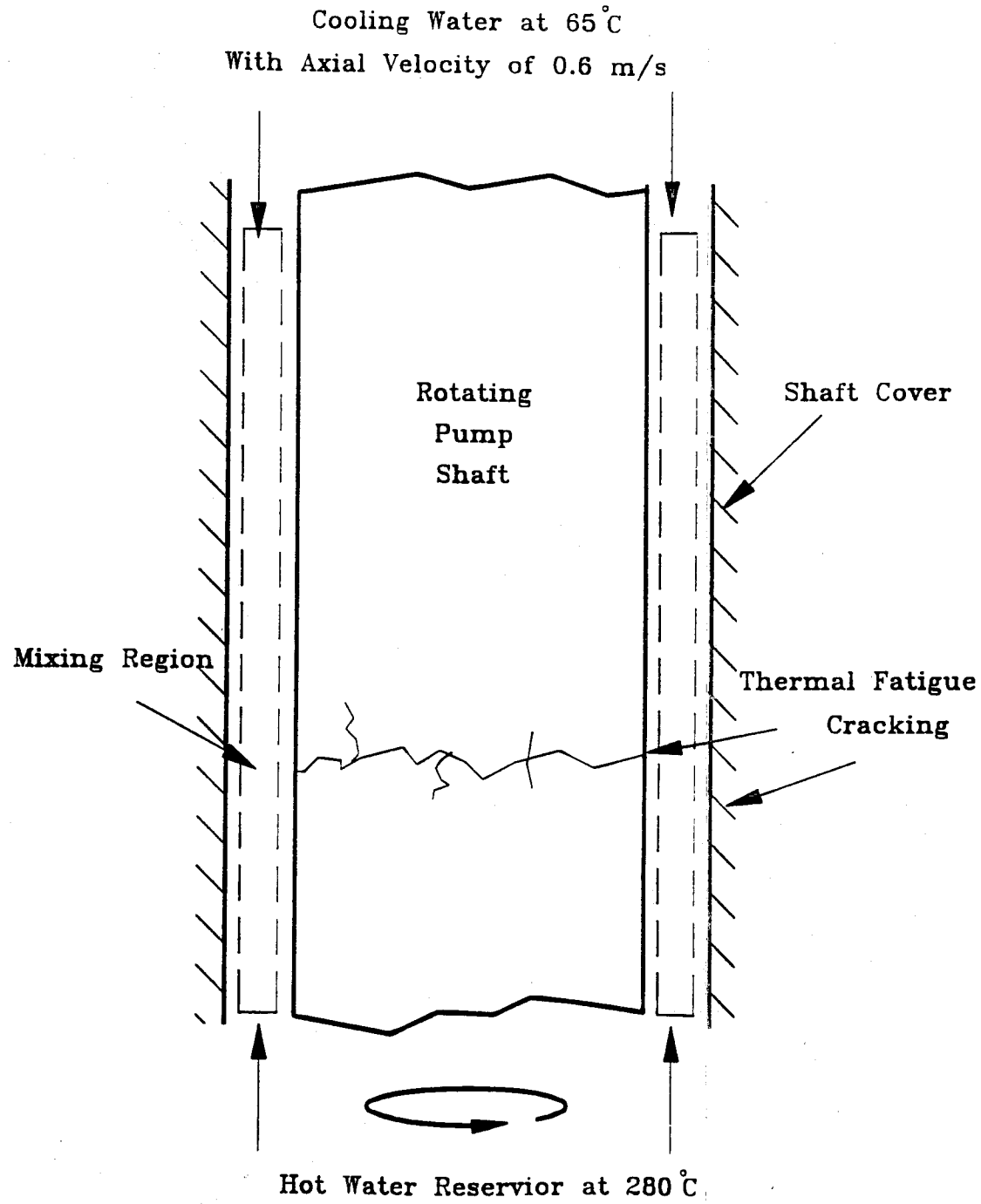

	Prototype	Experiment
Physical Parameters:		
Fluid	Water	Air
Height, h (m)	0.228	0.61
Inner radius, R_i (m)	0.1	0.10
Gap width, b (m)	6.4×10^{-4}	0.0127
Rotational Speed (RPM)	1500	1500
Working fluid temperature (°K)	550	293
Injectant fluid temperature (°K)	340	323
Mean temperature (°K)	445	308
Tangential velocity, U_i (m/s)	16	16
Axial velocity, w (m/s)	0.6	1.5
Nondimensional Parameters:		
Taylor number, $Ta = \omega^2 b^3 R_i/\nu^2$	2.1×10^7	2.1×10^7
Axial Reynolds number, $Re_a = 2bw/\nu$	1.8×10^3	2.5×10^3
Grashof number, $Gr_h = \Delta T_a \beta h^3/\nu^2$	4.6×10^{11}	7.4×10^8
Modified Grashof number, $Gr_a = Gr_h(b^3/h^3)$	7.8×10^3	6.7×10^3
Gap spacing to inner radius, b/R_i	6.4×10^{-4}	0.12
Height to gap spacing, h/b	390	48
Prandtl number, Pr	1.0	0.7

Table 1.1: Comparison of the prototypical and experimental parameters.

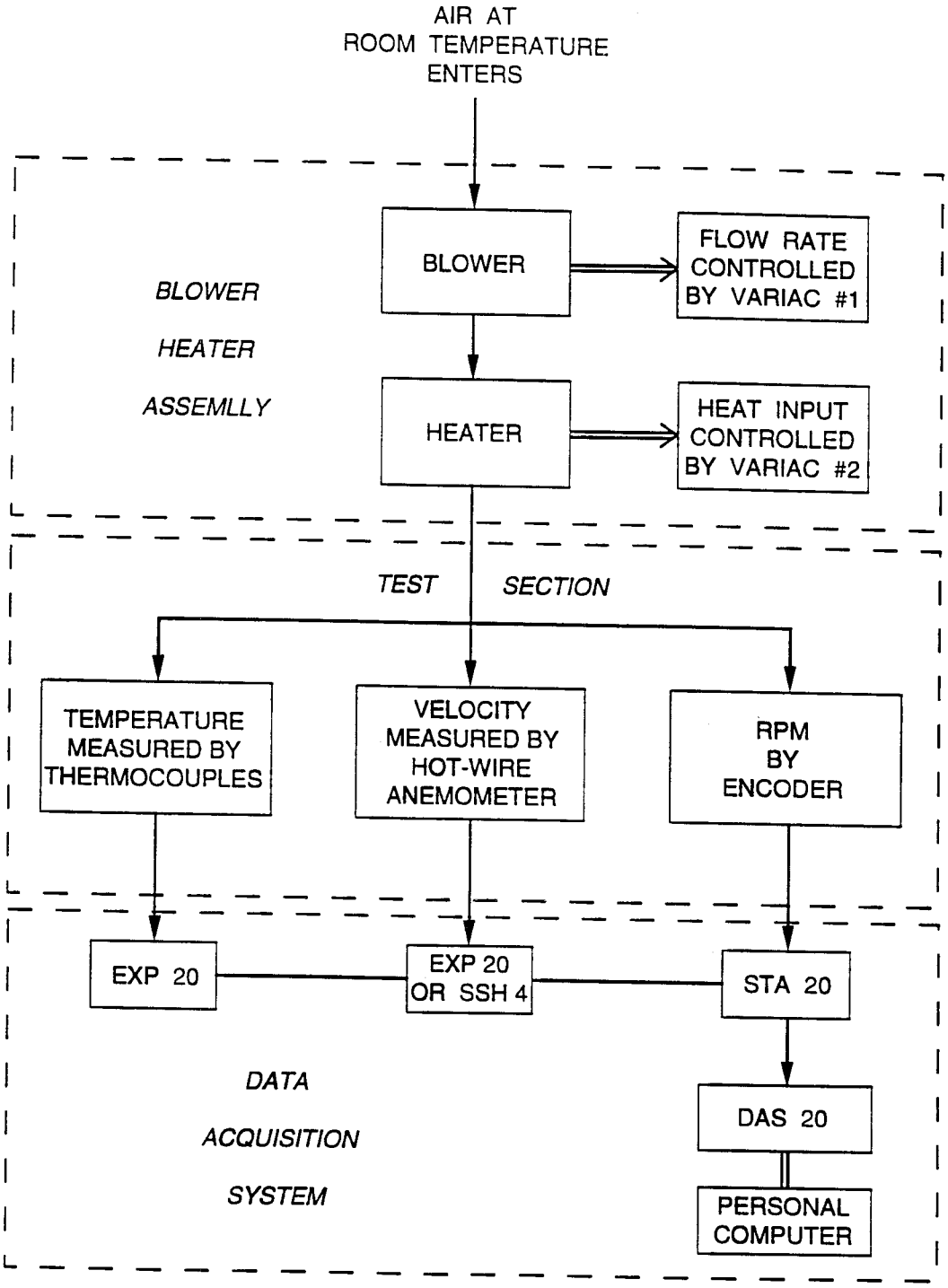

Figure 2.1 Schematic of experimental setup

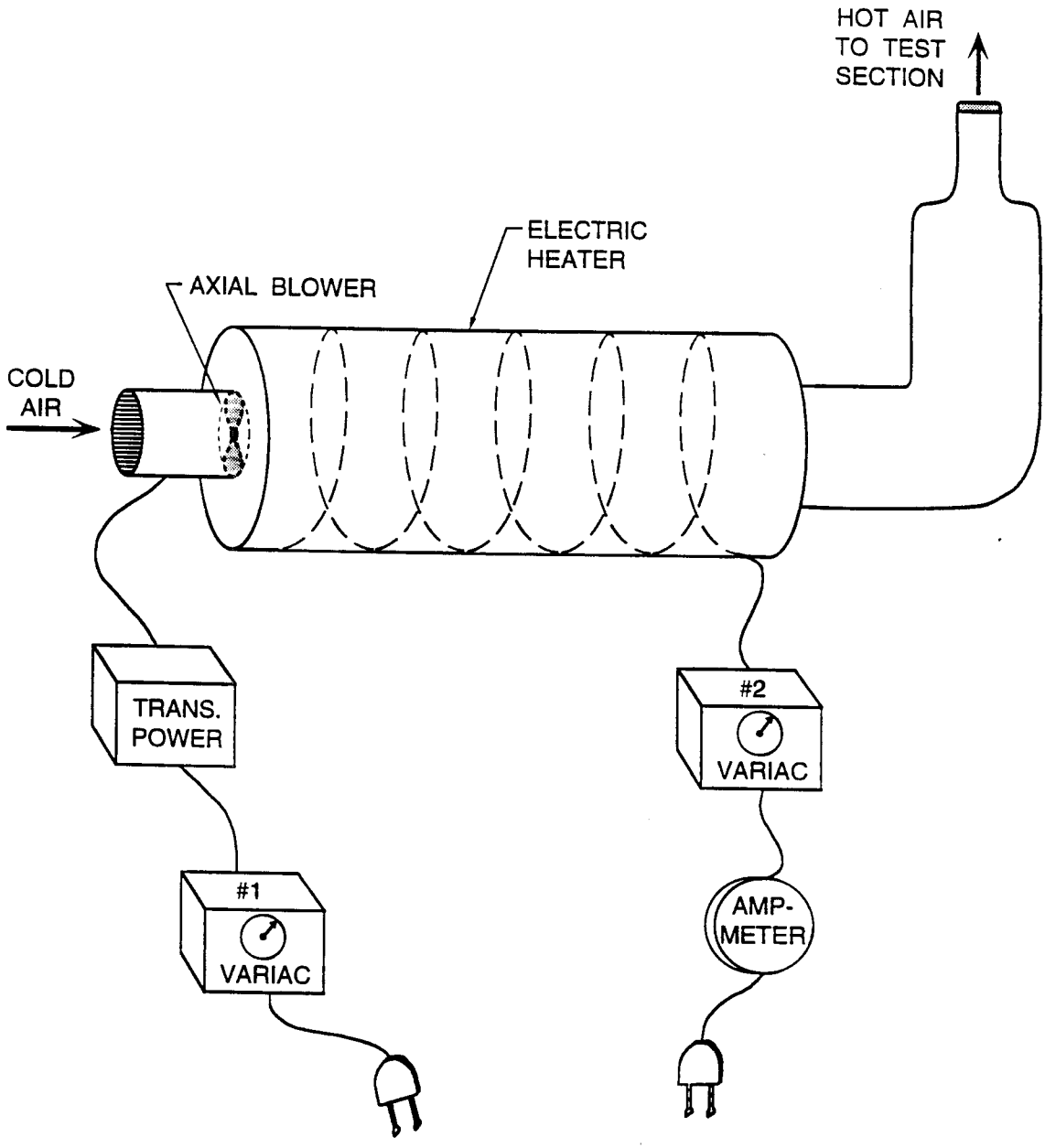

Figure 2.2 Blower/heater assembly

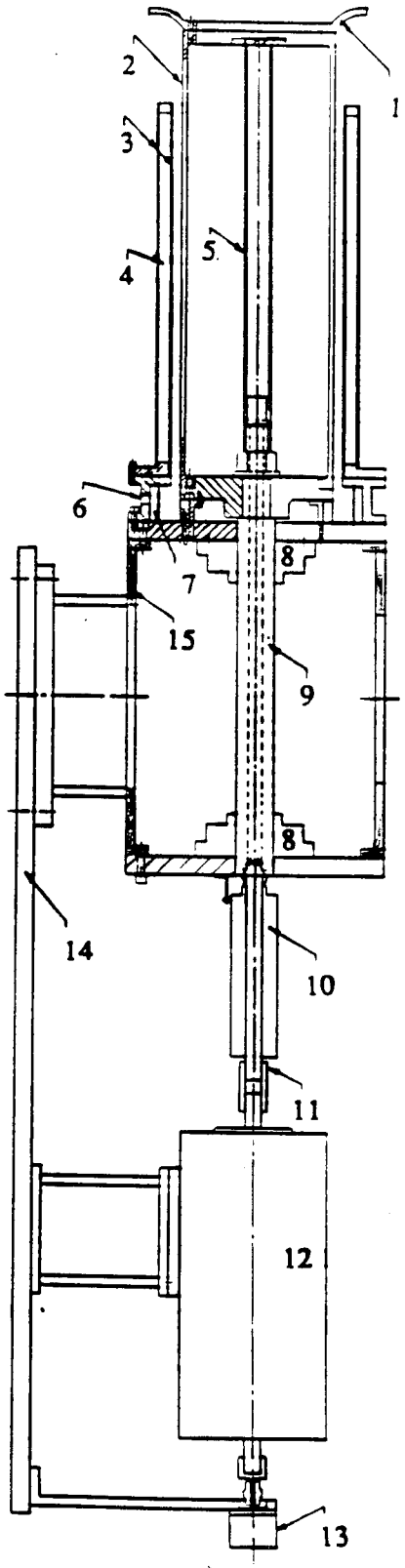

1. EXIT FLANGE
2. INNER ROTATING CYLINDER
3. STATIONARY PLEXIGLASS CYLINDER
4. AIR GAP
5. THERMOCOUPLE SUPPORT
6. INJECTION PORT
7. FLOW BAFFLE
8. BEARINGS
9. SHAFT
10. SLIP RING ASSEMBLY
11. SHAFT COUPLING
12. MOTOR
13. ENCODER
14. MOUNTING PLATE
15. SUPPORT STRUCTURE

Scale: 1/10

Figure 2.3 Test section

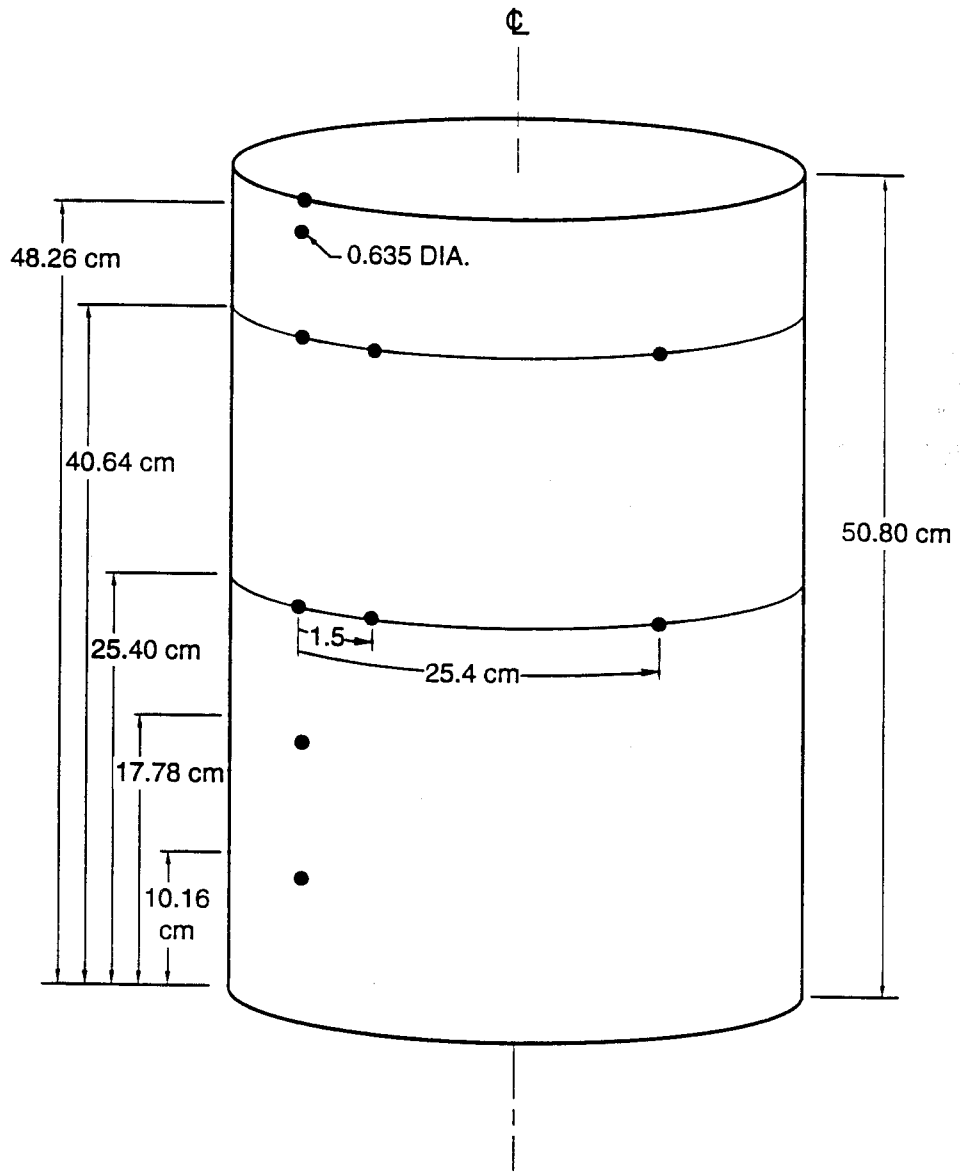

Figure 2.4 Locations of holes for access of hot-wire anemometer

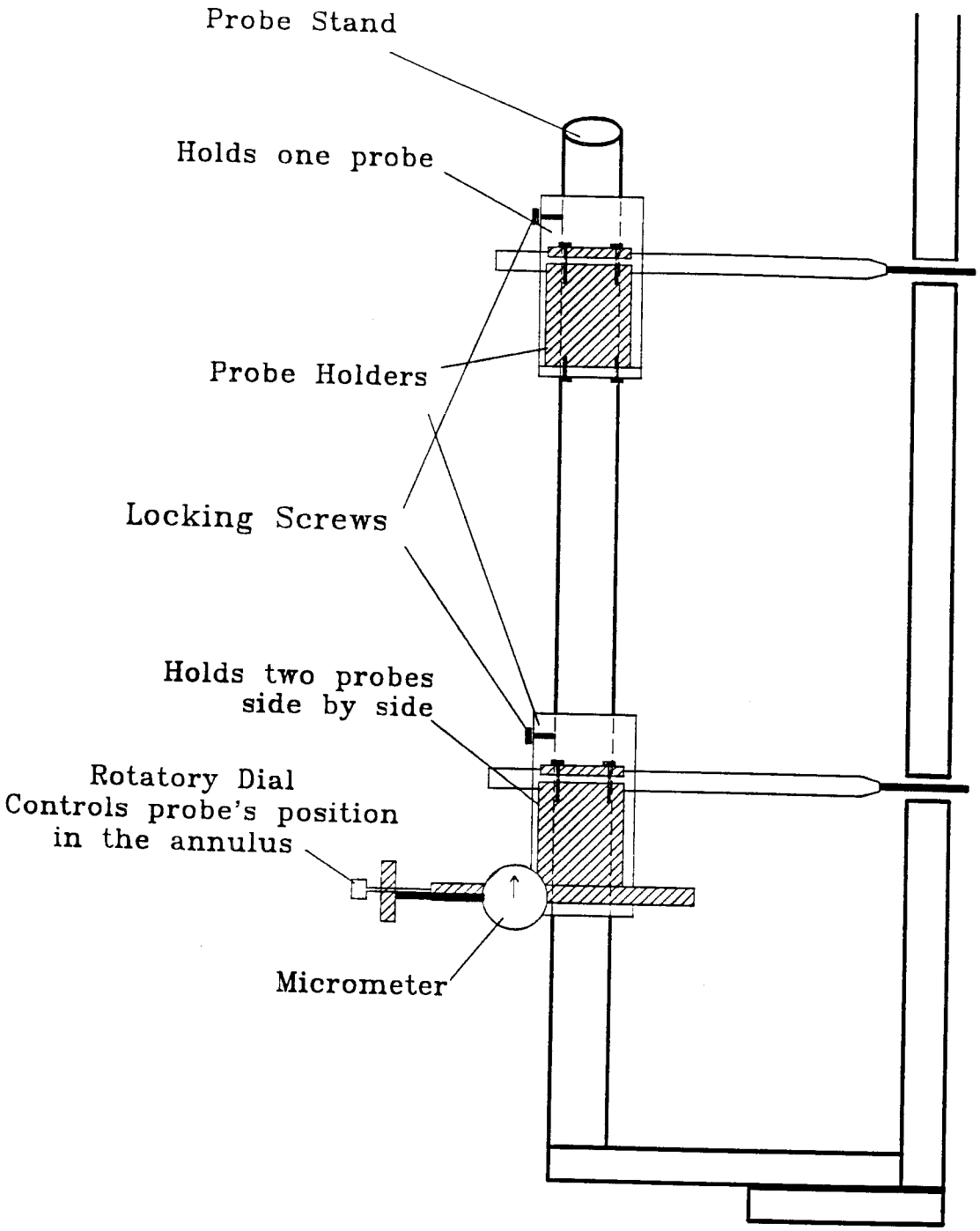

Figure 2.5 Probe stand and holders

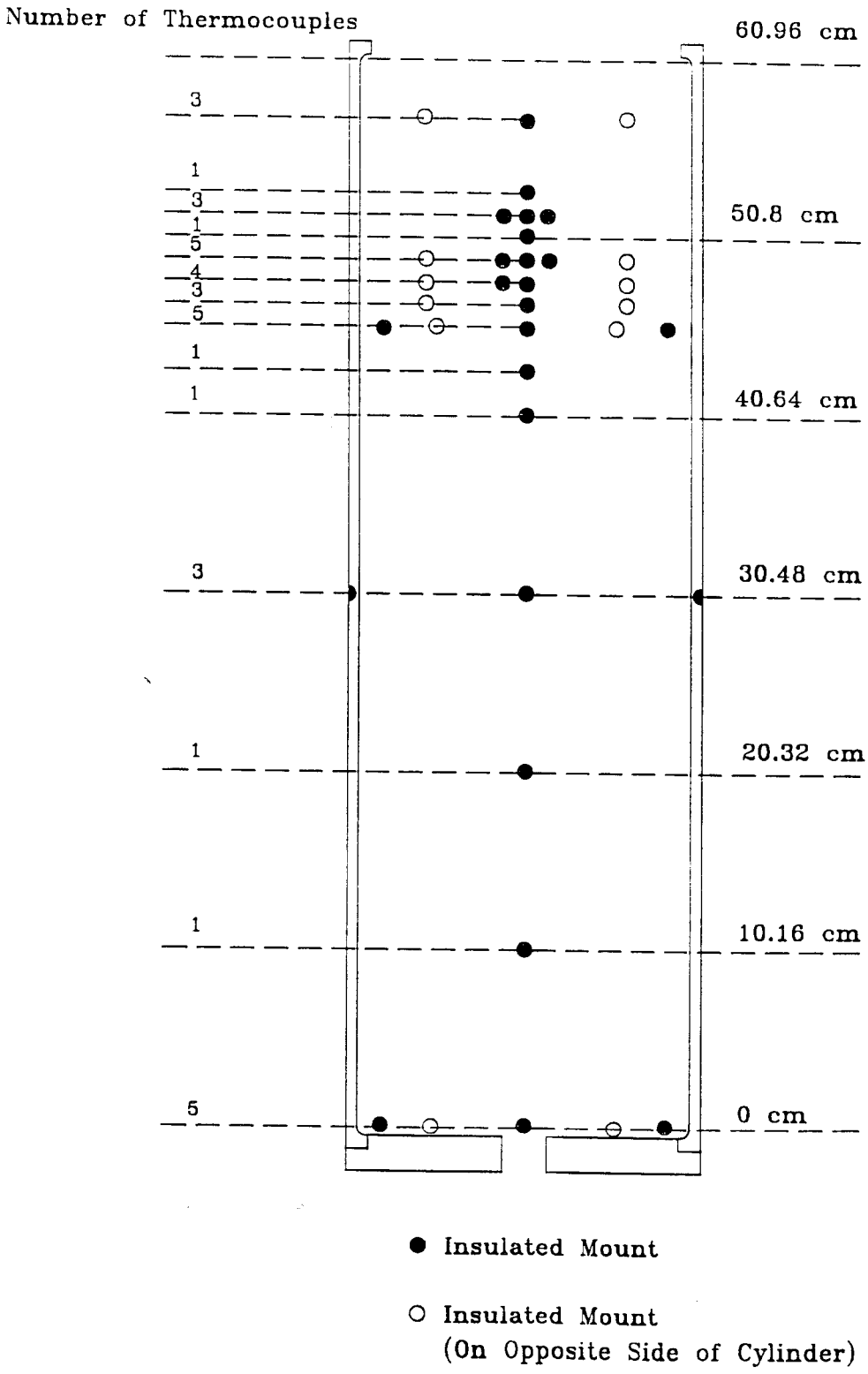

Figure 2.6 Thermocouple layout on the inner cylinder

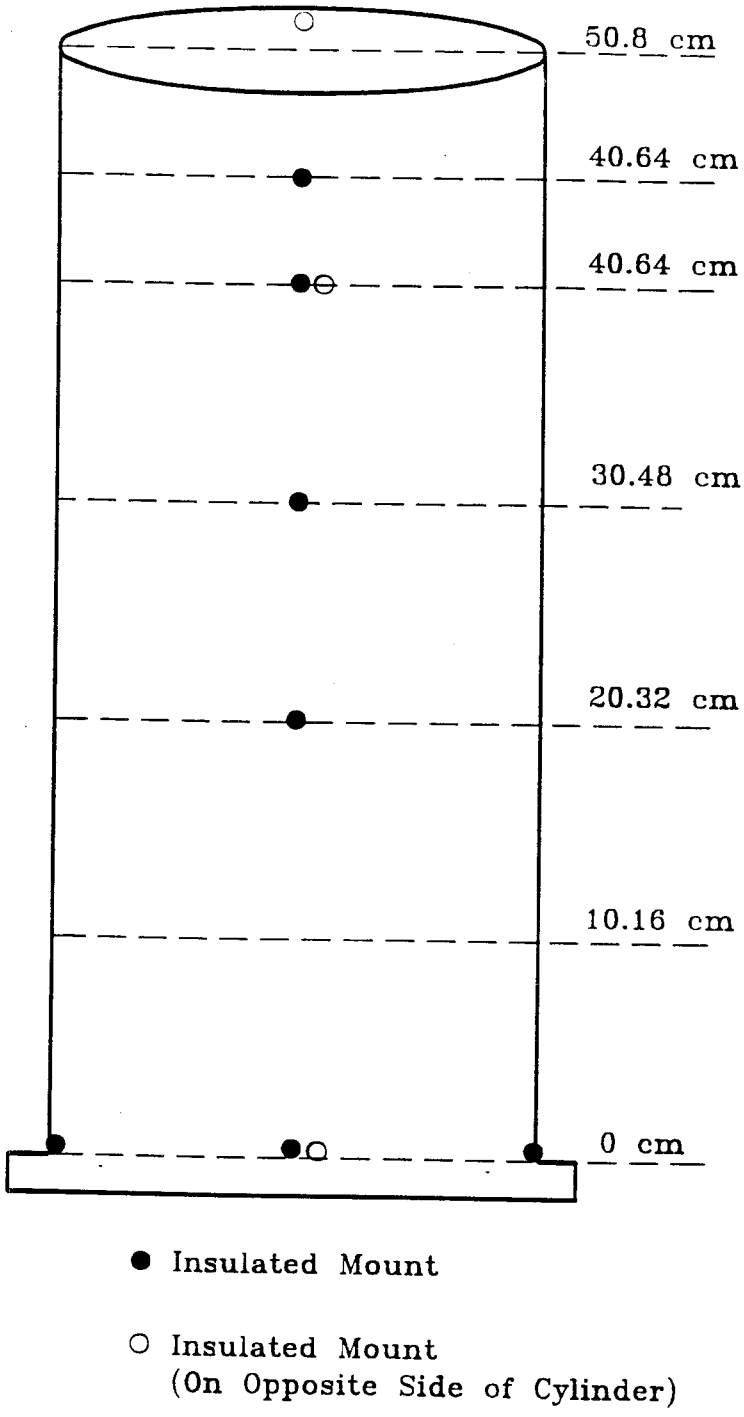

Figure 2.7 Thermocouple layout on the outer cylinder

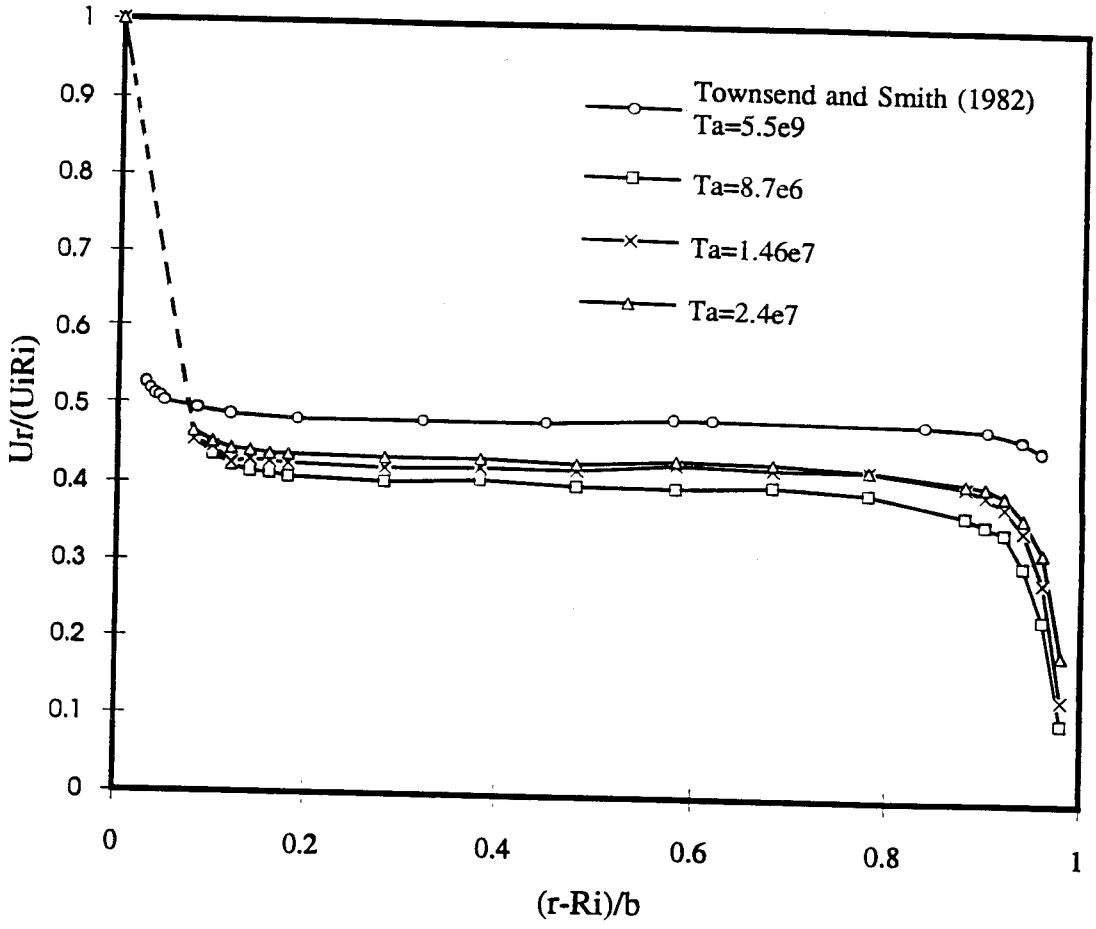

Figure 3.1 Radial Distribution of the angular momentum ratio, ur/U_iR_i, for different Taylor numbers

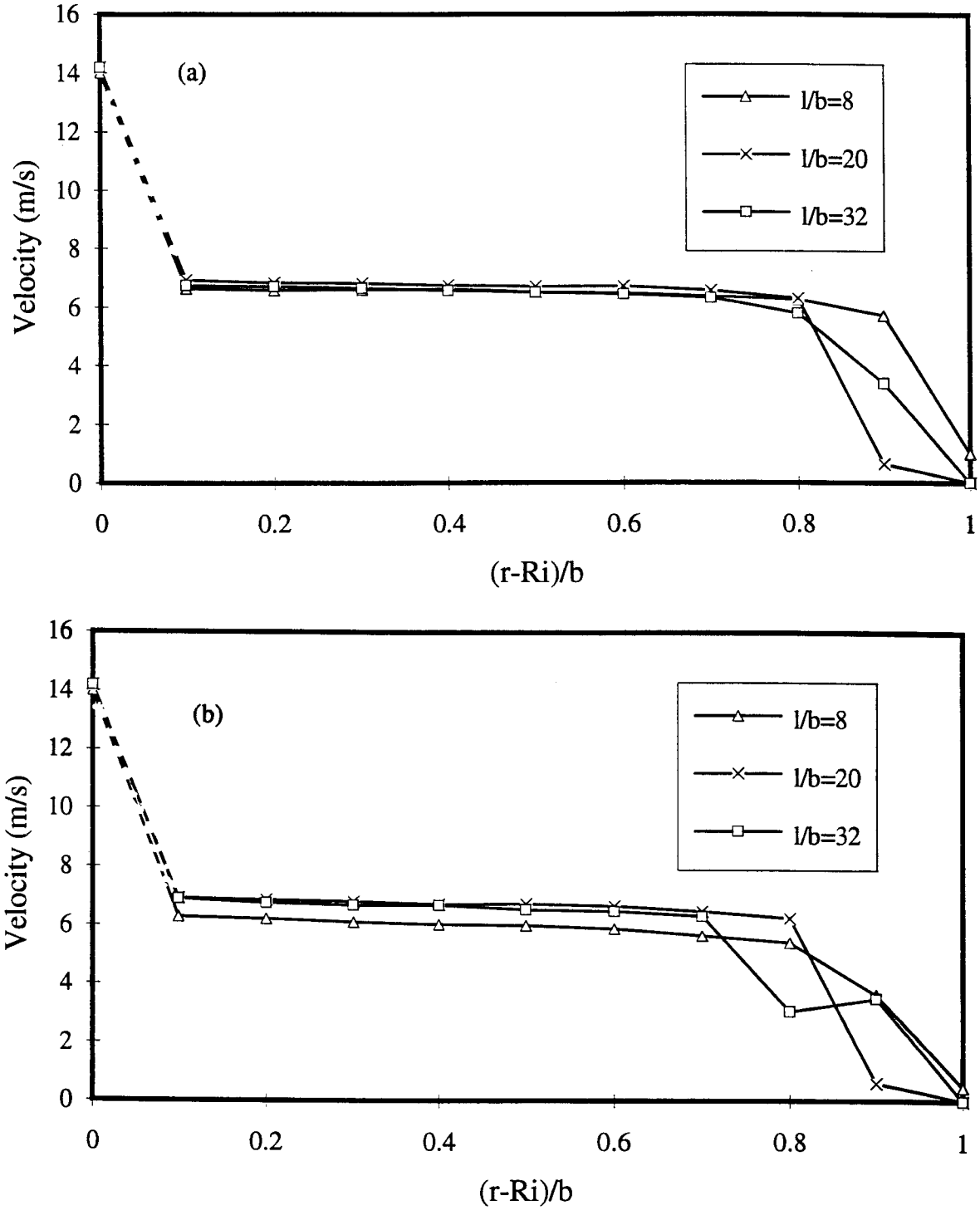

Figure 3.2 Tangential velocity profiles with Ta = 1.5 x 10^7 for different axial Reynolds numbers: (a) Re_a = 0, (b) Re_a = 10, and (c) Re_a = 1000.

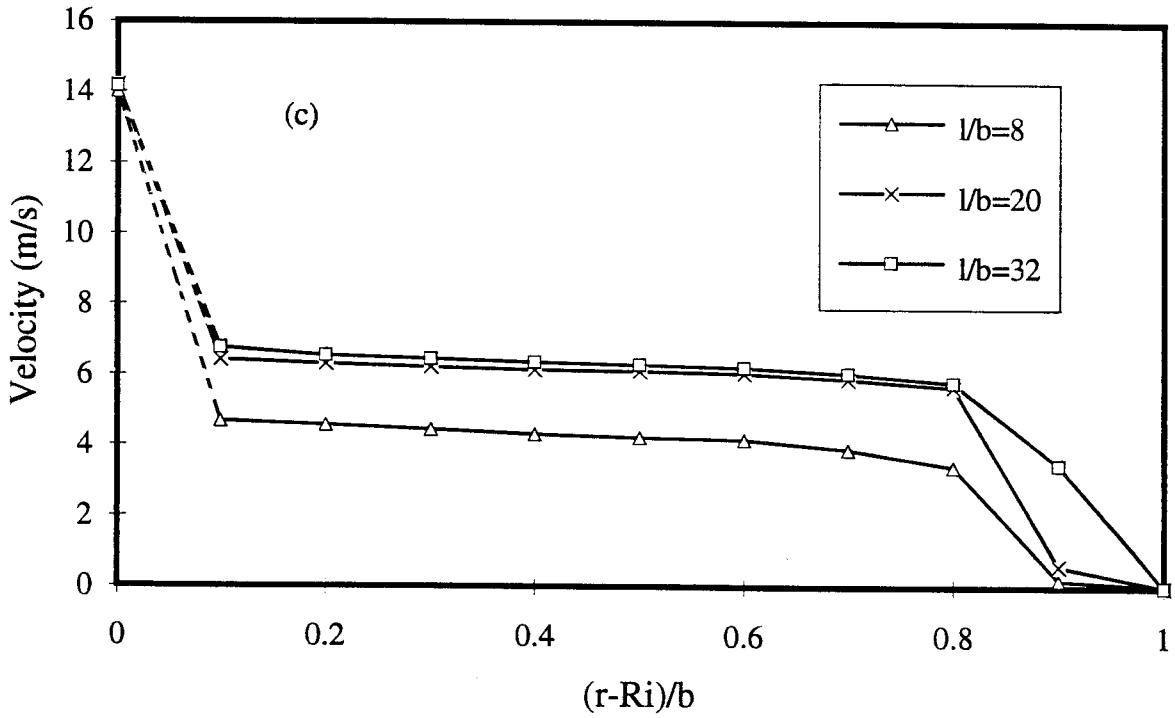
(c)
l/b=8
l/b=20
l/b=32
Velocity (m/s)
(r-Ri)/b
0
2
4
6
8
10
12
14
16
0
0.2
0.4
0.6
0.8
1

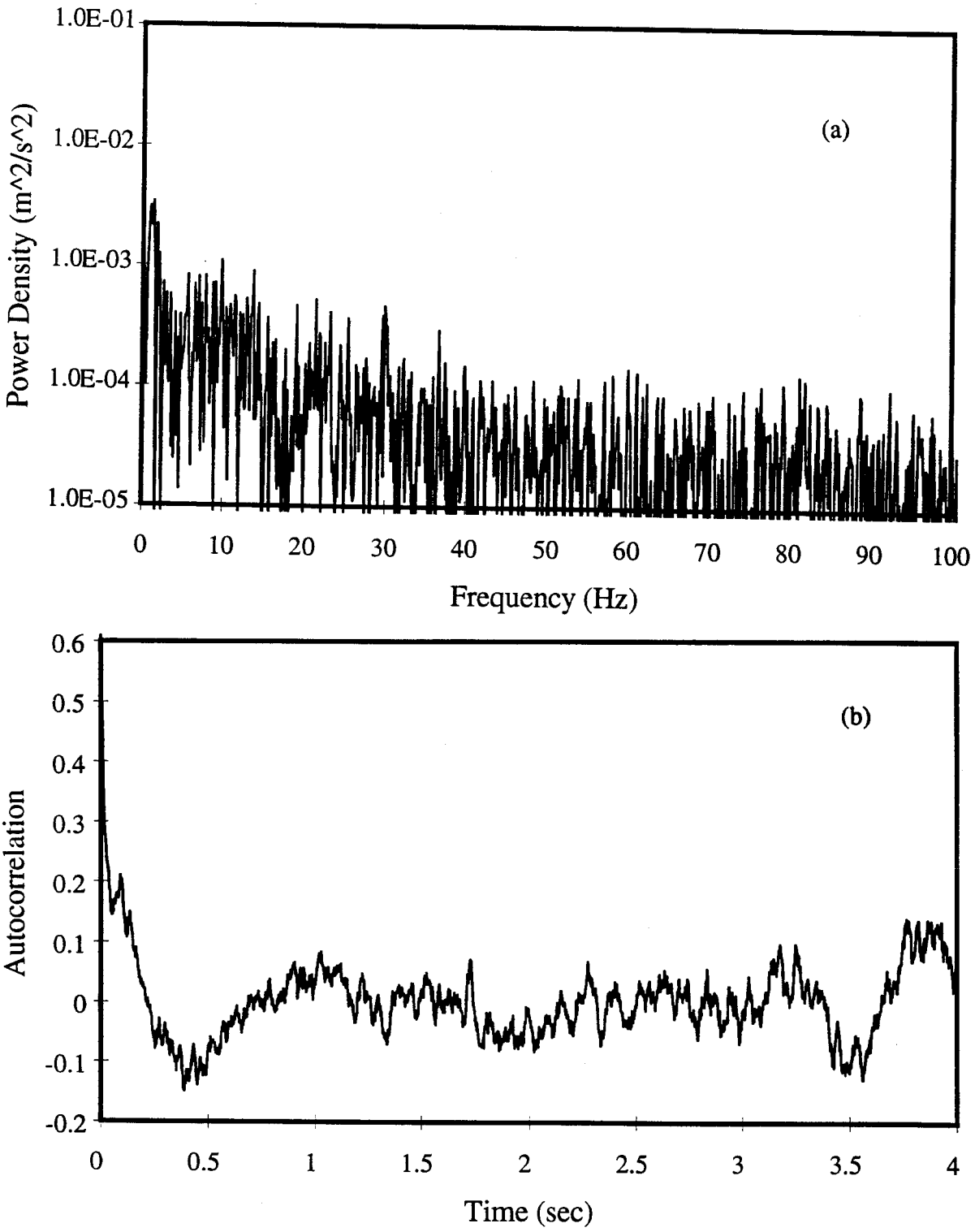

Figure 3.3 Power spectrum and autocorrelogram of the tangential velocity component with Ta = 1.42 x 10^7 and Re_a = 0, at l/b = 20: (a) power spectrum (b) autocorrelogram.

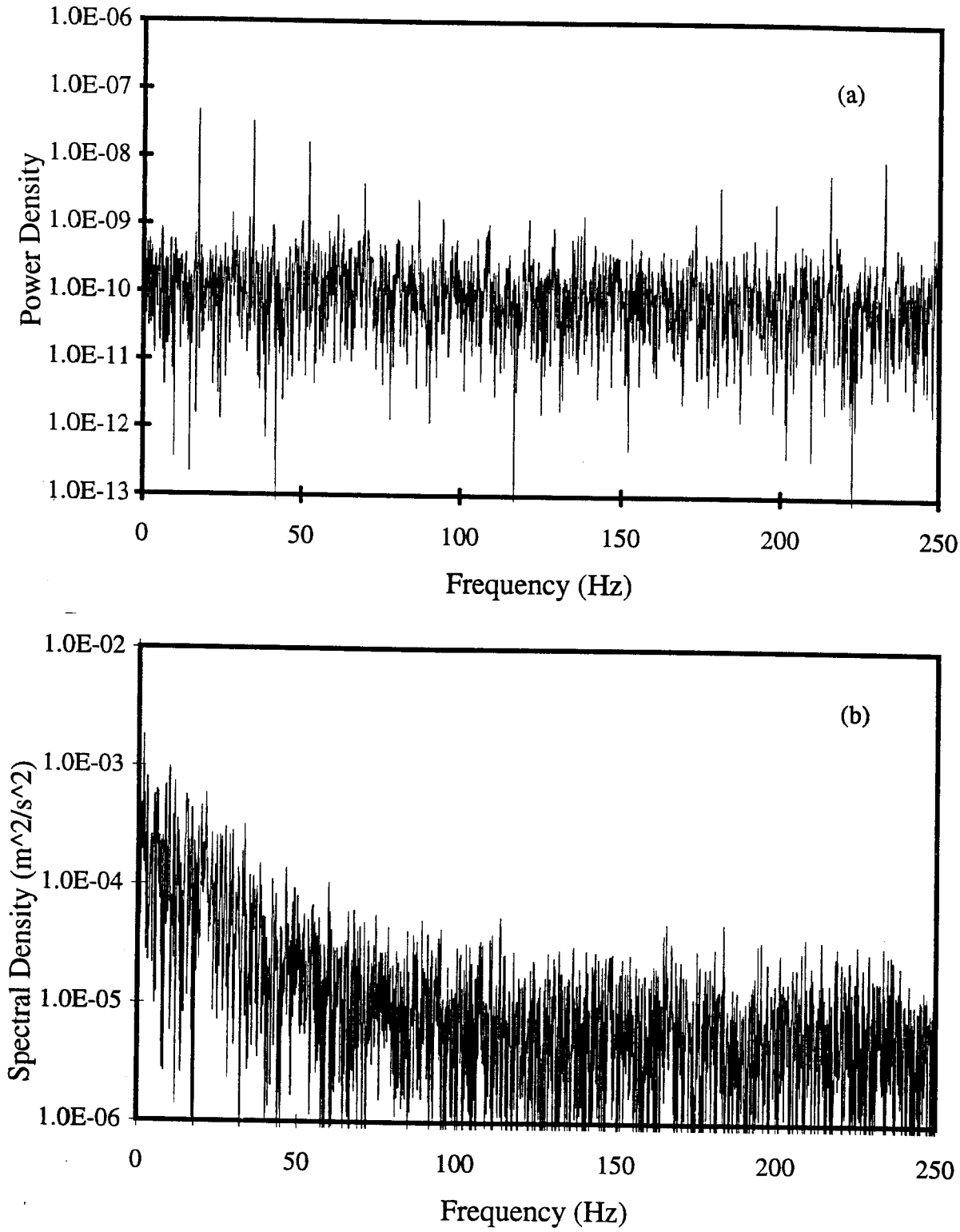

Figure 3.4 Noise study: (a) velocity spectrum in still air (b) power spectrum of the tangential velocity component at Ta = 5 x 10^6, Re_a = 0.

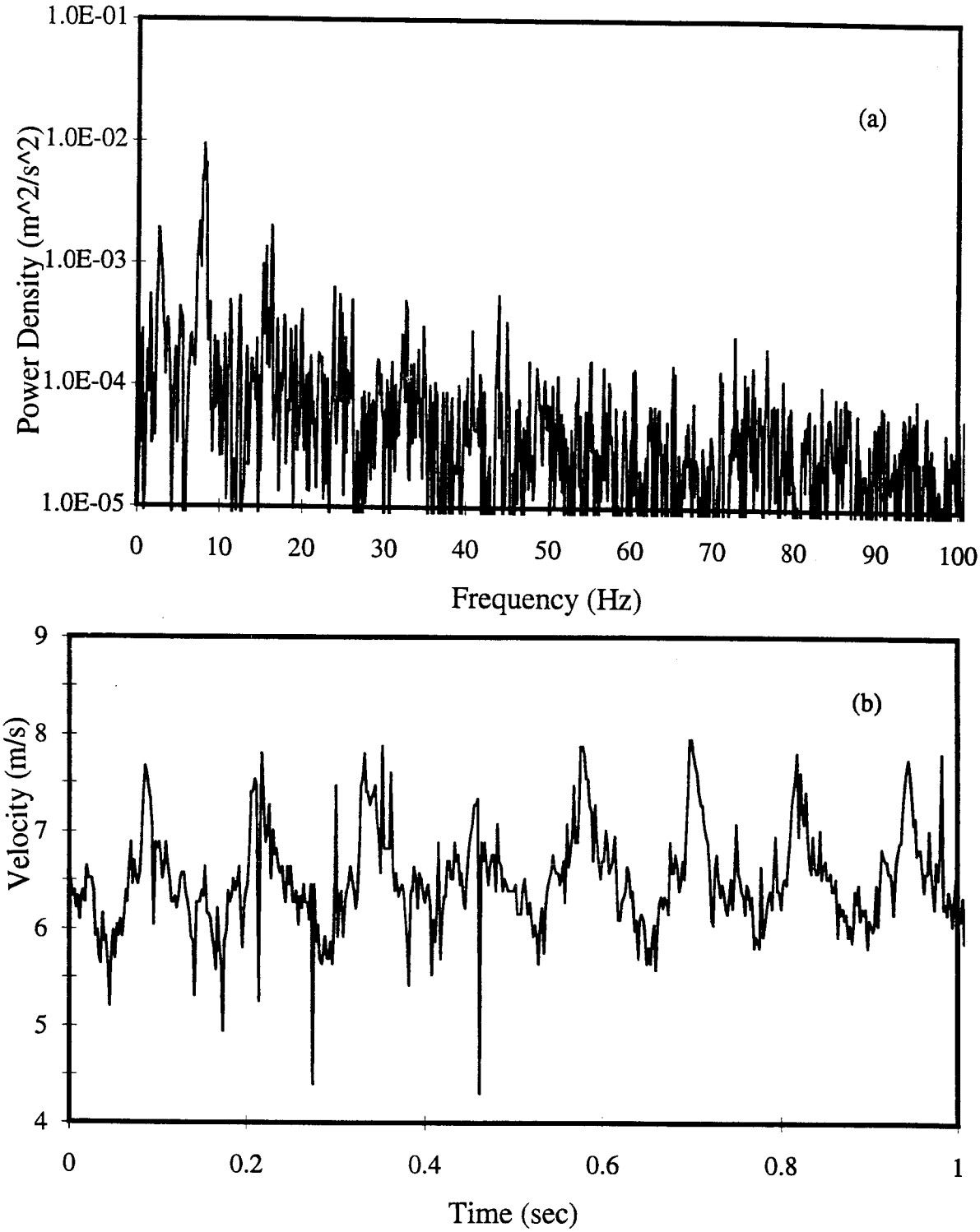

Figure 3.5 Power spectrum, velocity trace and autocorrelogram of the tangential velocity component with Ta = 1.42 x 10^7 and Re_a = 10, at l/b = 20: (a) power spectrum (b) velocity trace (c) autocorrelogram.

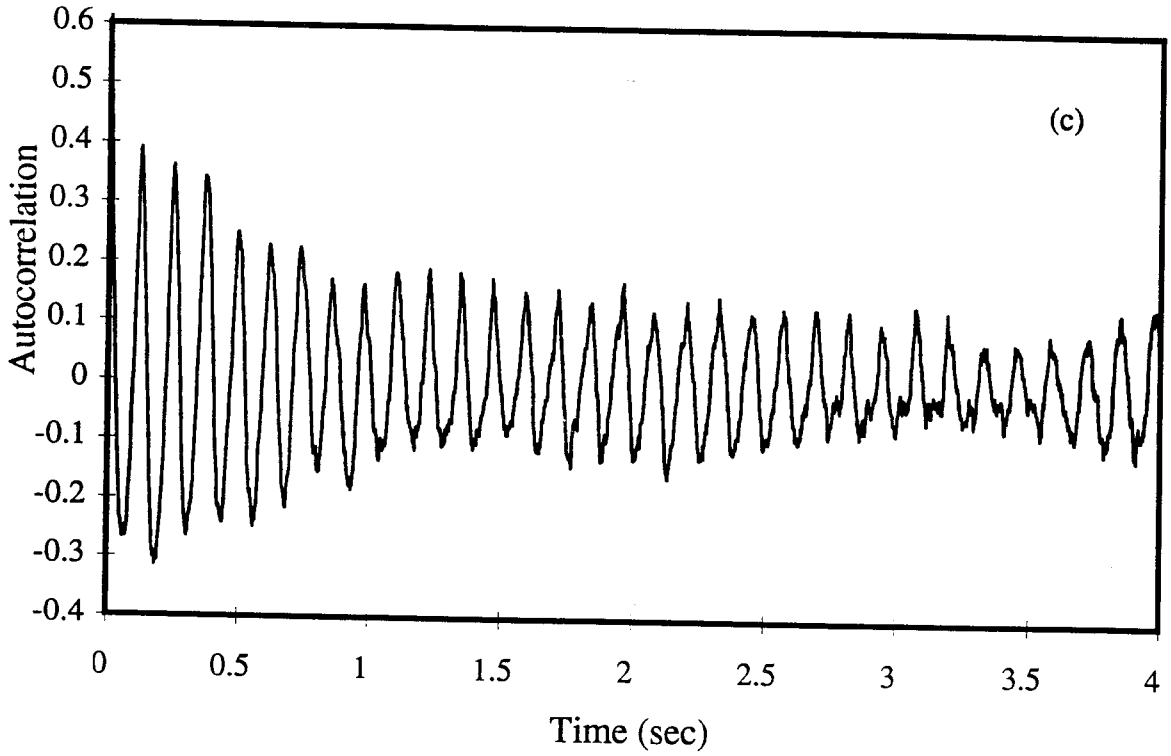
0.6
0.5
0.4
0.3
0.2
0.1
0
-0.1
-0.2
-0.3
-0.4
Autocorrelation
(c)
0
0.5
1
1.5
2
2.5
3
3.5
4
Time (sec)

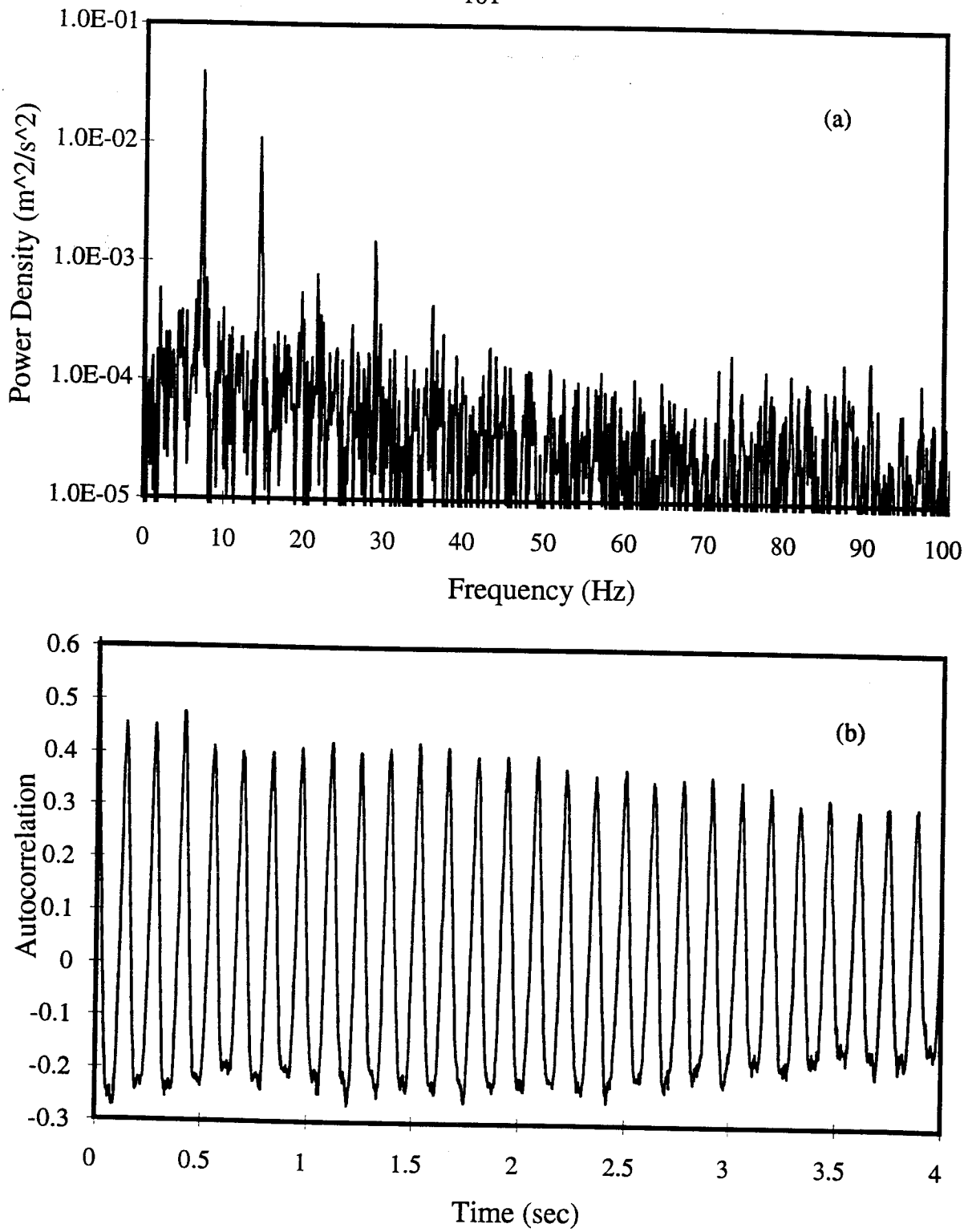

Figure 3.6 Power spectrum and autocorrelogram of the tangential velocity component with Ta = 1.42 x 10^7 and Re_a = 70, at l/b = 20: (a) power spectrum (b) autocorrelogram.

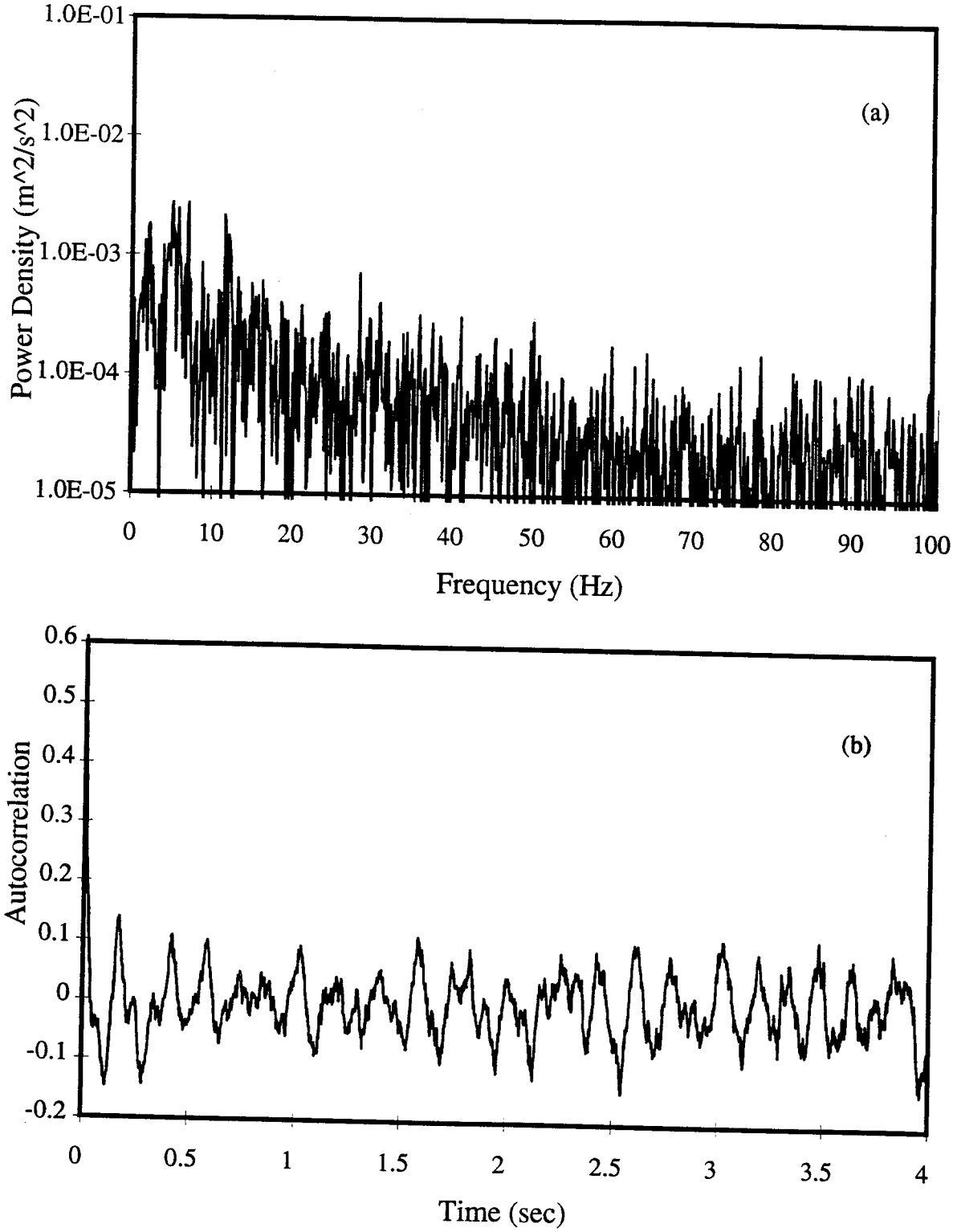

Figure 3.7 Power spectrum and autocorrelogram of the tangential velocity component with Ta = 1.42 x 10^7 and Re_a = 160, at l/b = 20: (a) power spectrum (b) autocorrelogram.

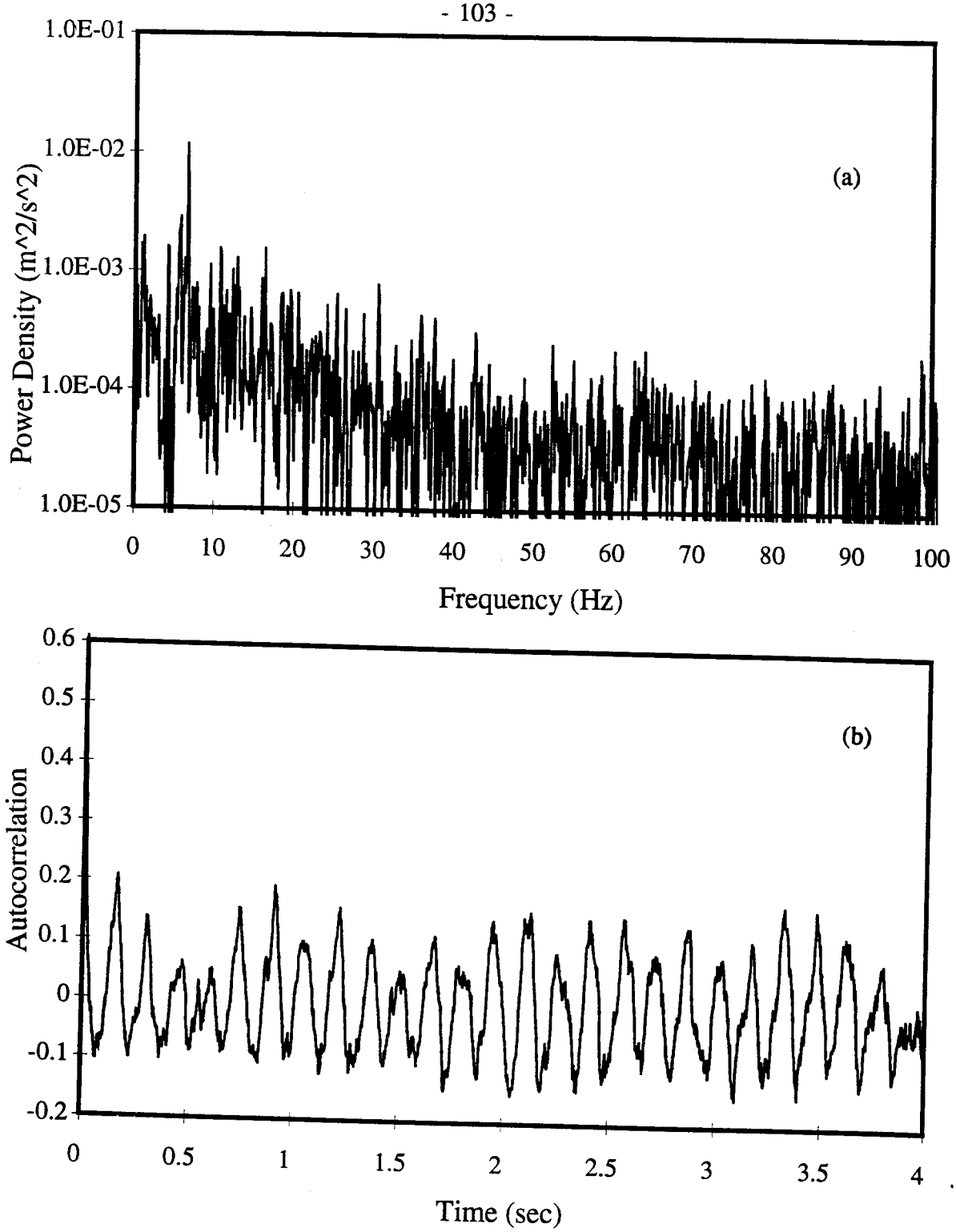

Figure 3.8 Power spectrum and autocorrelogram of the tangential velocity component with Ta = 1.42 x 10^7 and Re_a = 220, at l/b = 20: (a) power spectrum (b) autocorrelogram.

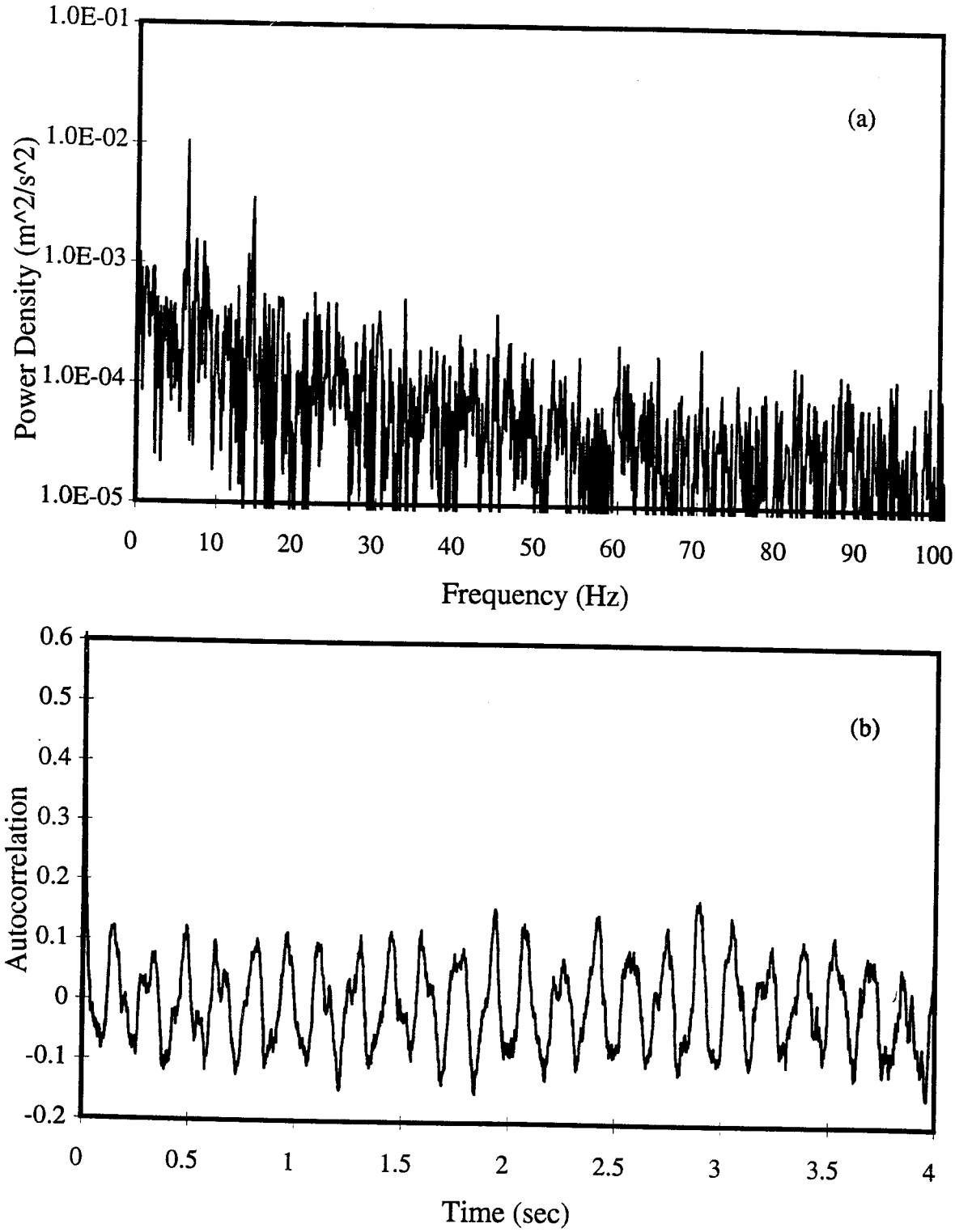

Figure 3.9 Power spectrum and autocorrelogram of the tangential velocity component with Ta = 1.42 x 10^7 and Re_a = 330, at l/b = 20: (a) power spectrum (b) autocorrelogram.

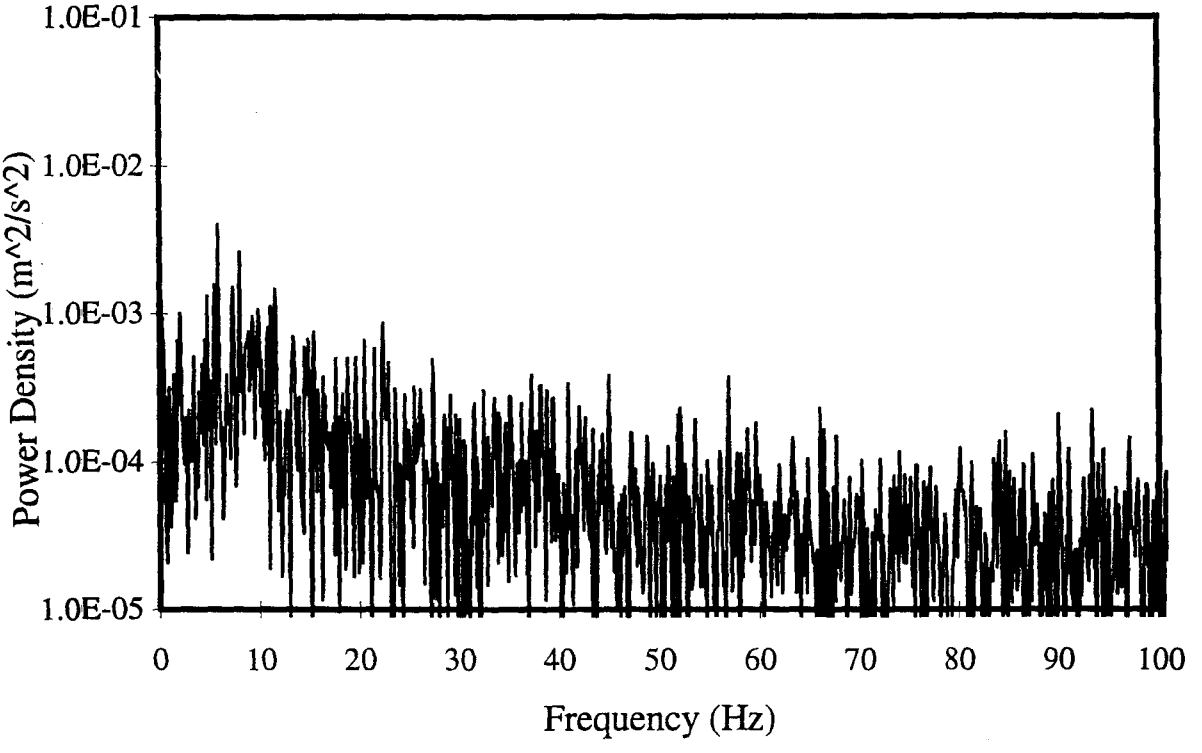

Figure 3.10 Power spectrum of the tangential velocity component with Ta = 1.42×10^7 and Re_a = 500, at l/b = 20.

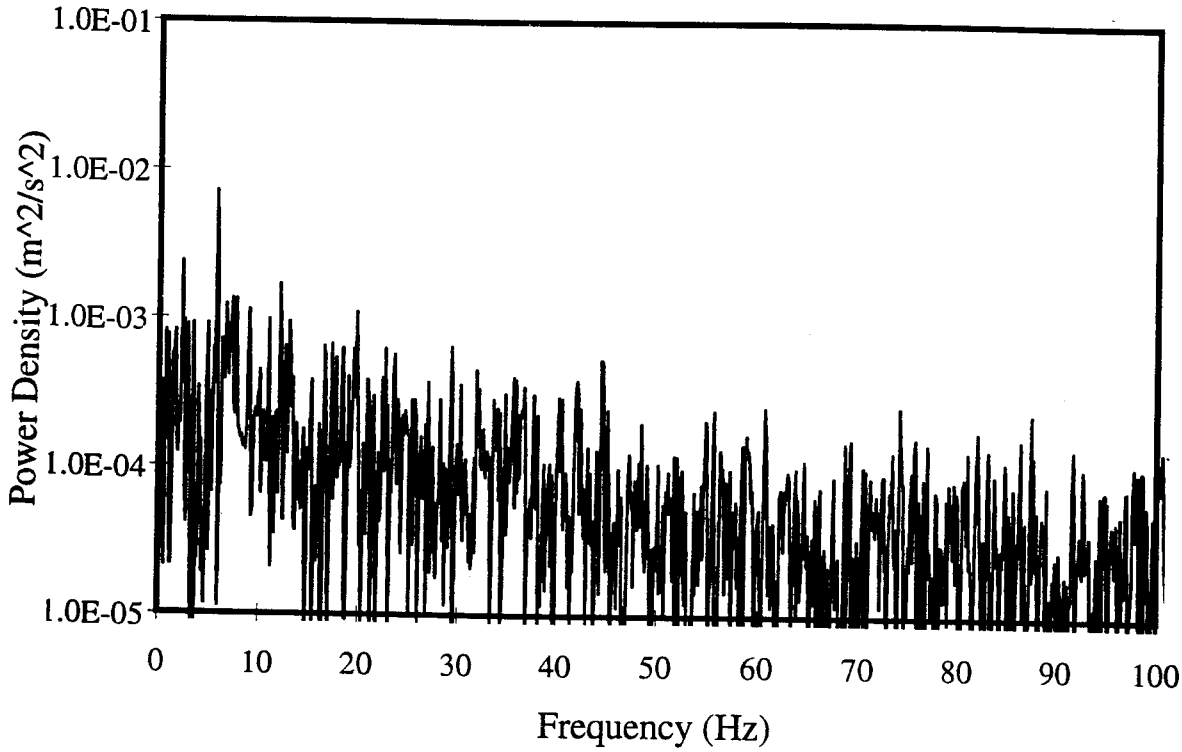

Figure 3.11 Power spectrum of the tangential velocity component with Ta = 1.42 x 10^7 and Re_a = 670, at l/b = 20.

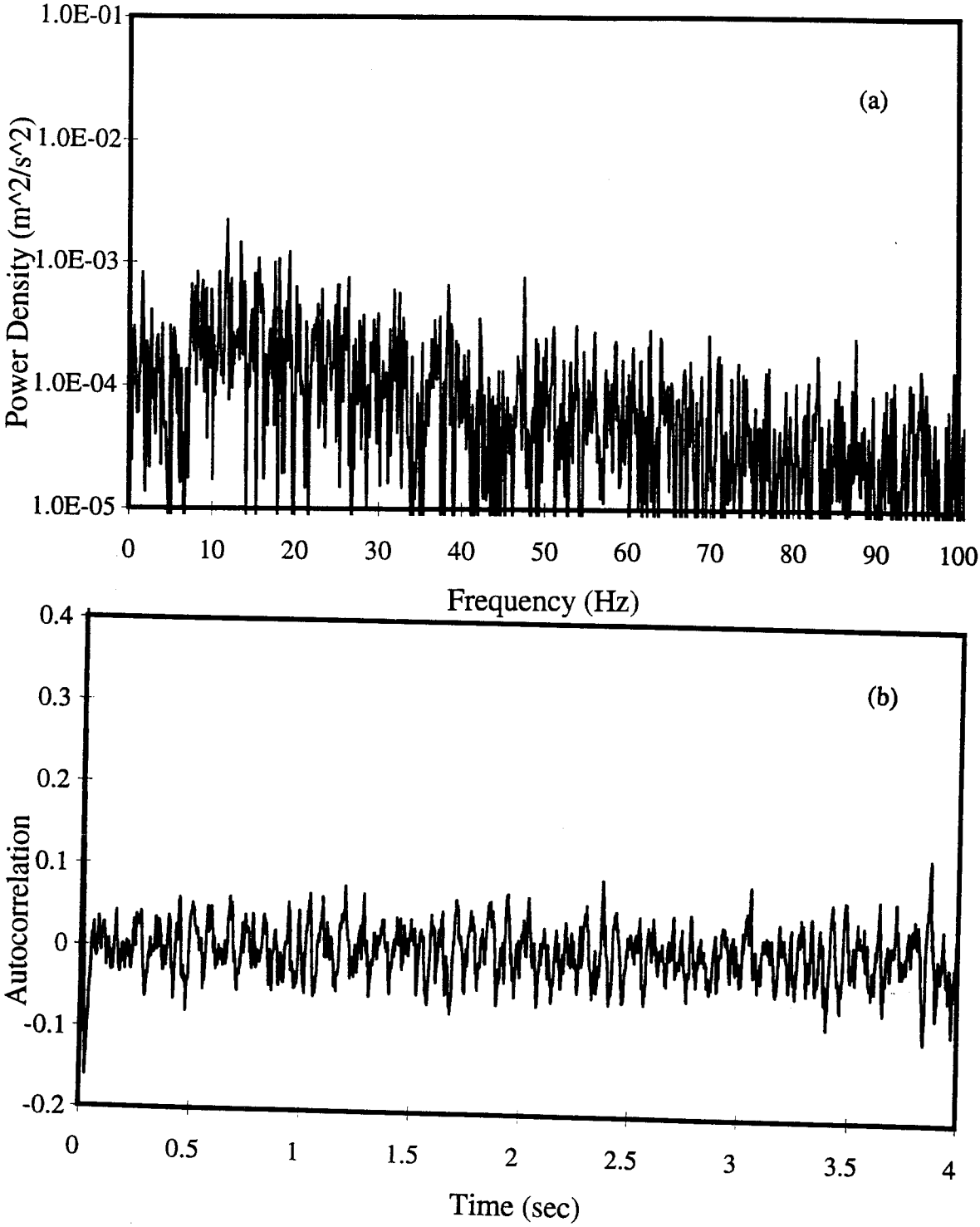

Figure 3.12 Power spectrum and autocorrelogram of the tangential velocity component with Ta = 1.42 x 10^7 and Re_a = 980, at l/b = 20 (a) velocity spectrum (b) autocorrelogram.

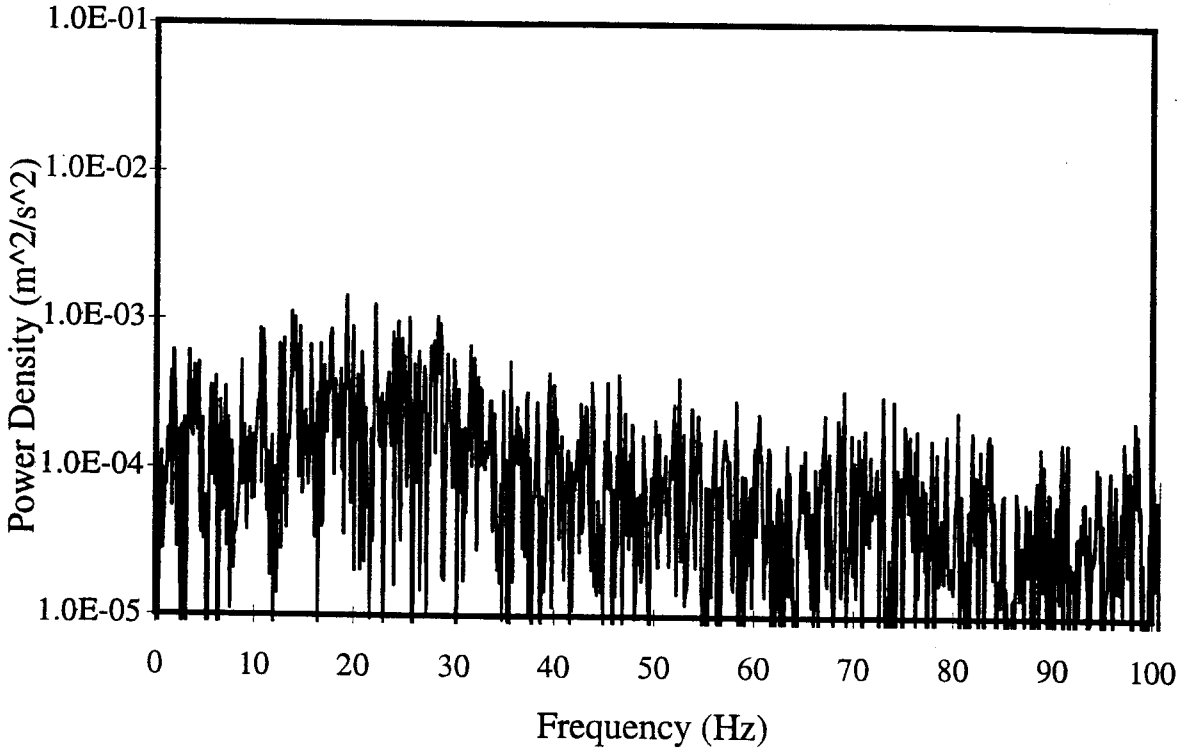

Figure 3.13 Power spectrum of the tangential velocity component with Ta = 1.42×10^7 and Re_a = 1300, at l/b = 20.

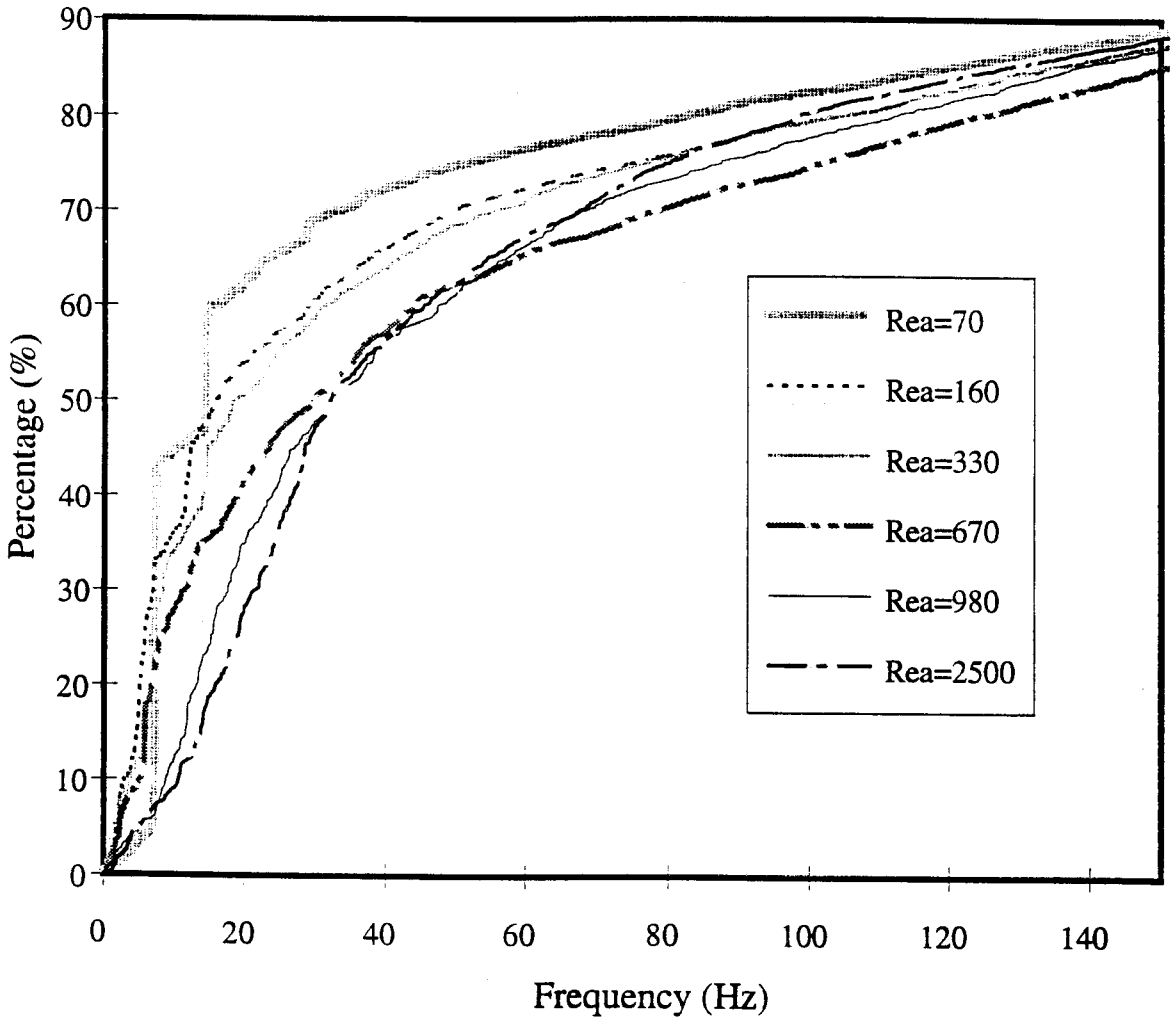

Figure 3.14 Percentage of the accumulative energy contribution as a function of frequency for different axial Reynolds numbers.

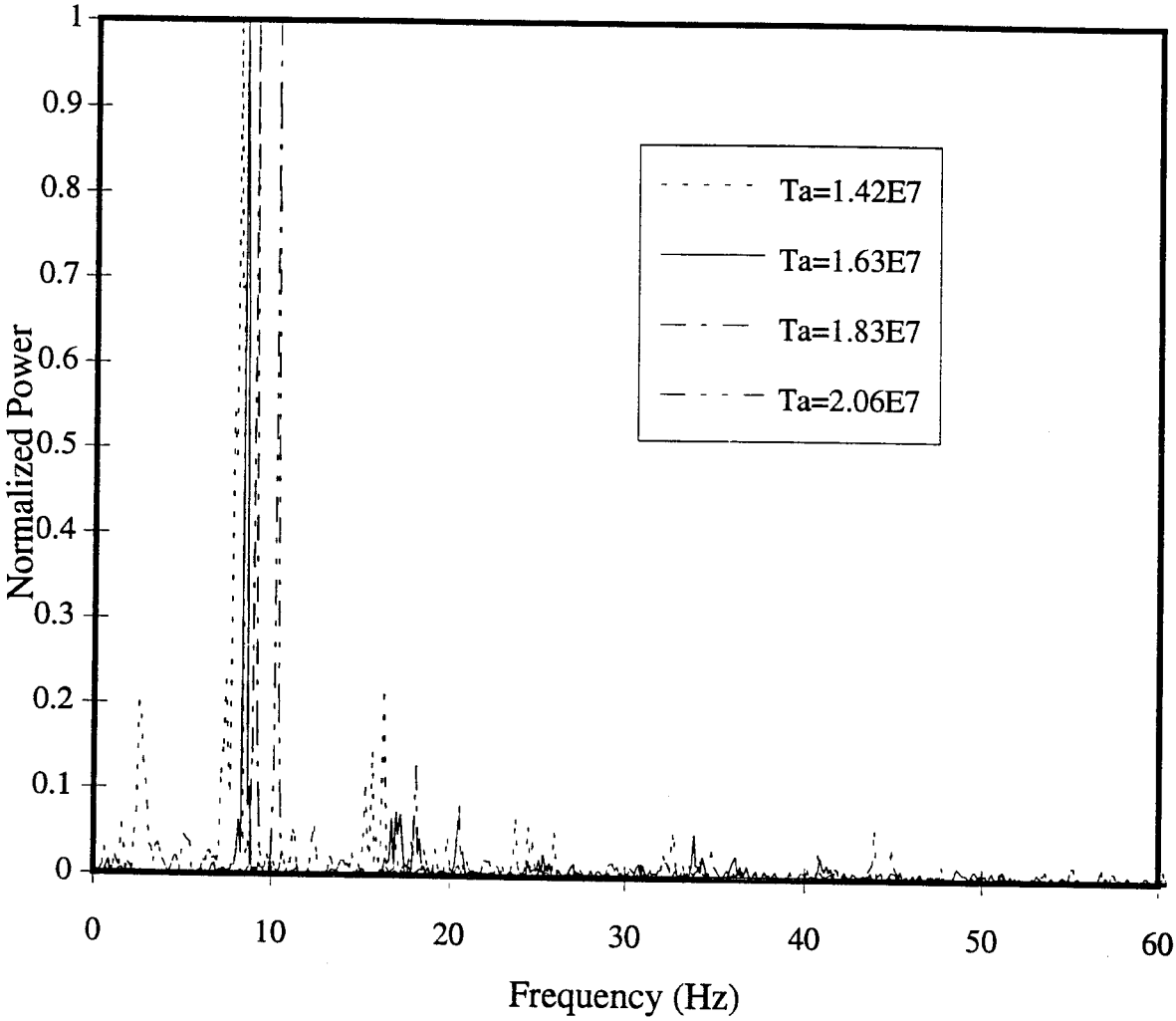

Figure 3.15 Power spectra of the tangential velocity component for Re_a = 10, but at different rotational speeds. From left to right, the dominant peaks are located at 8.06 Hz, 8.42 Hz, 9.02 Hz, and 10.25 Hz, corresponding to Ta = 1.42×10^7, 1.63×10^7, 1.83×10^7 and 2.06×10^7 respectively. Power density is normalized.

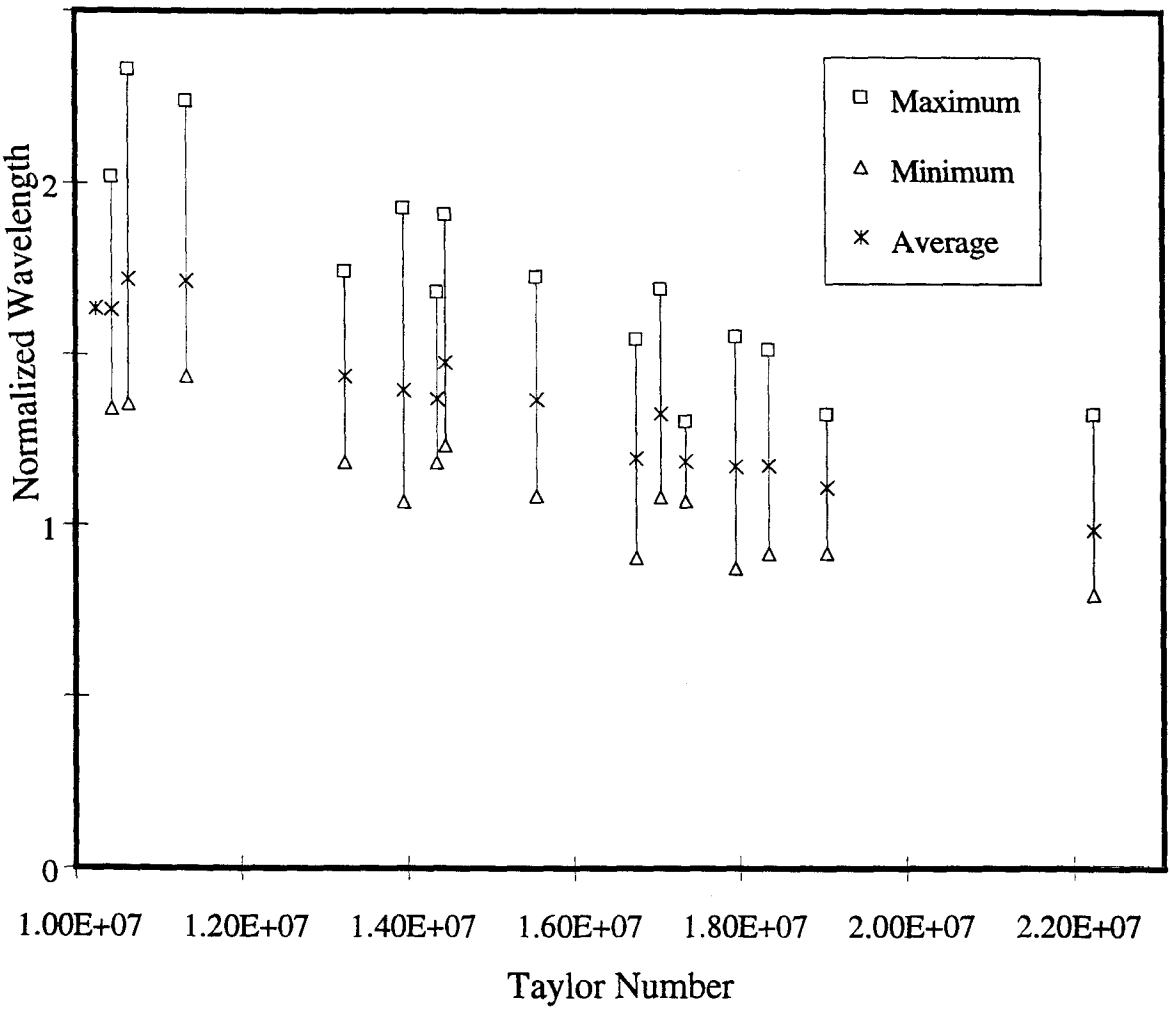

Figure 3.16 Wavelengths of the Taylor vortices vs. Taylor number. The wavelength is normalized by the gap width.

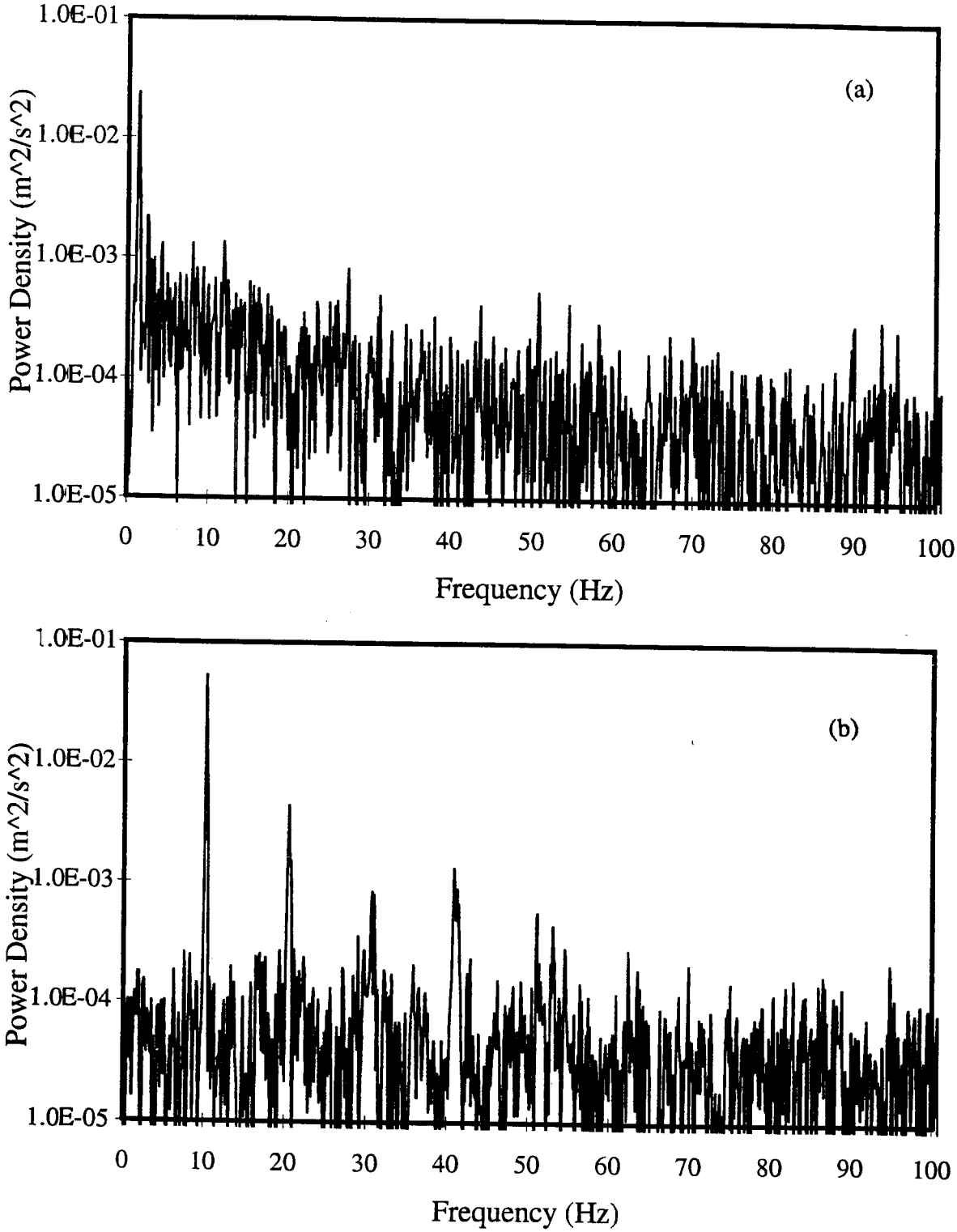

Figure 3.17 Power spectra of the tangential velocity component with Ta = 2.06 x 10^7 at l/b = 20 for various axial Reynolds numbers: (a) Re_a = 0 (b) Re_a = 10 (c) Re_a = 220 (d) Re_a = 670.

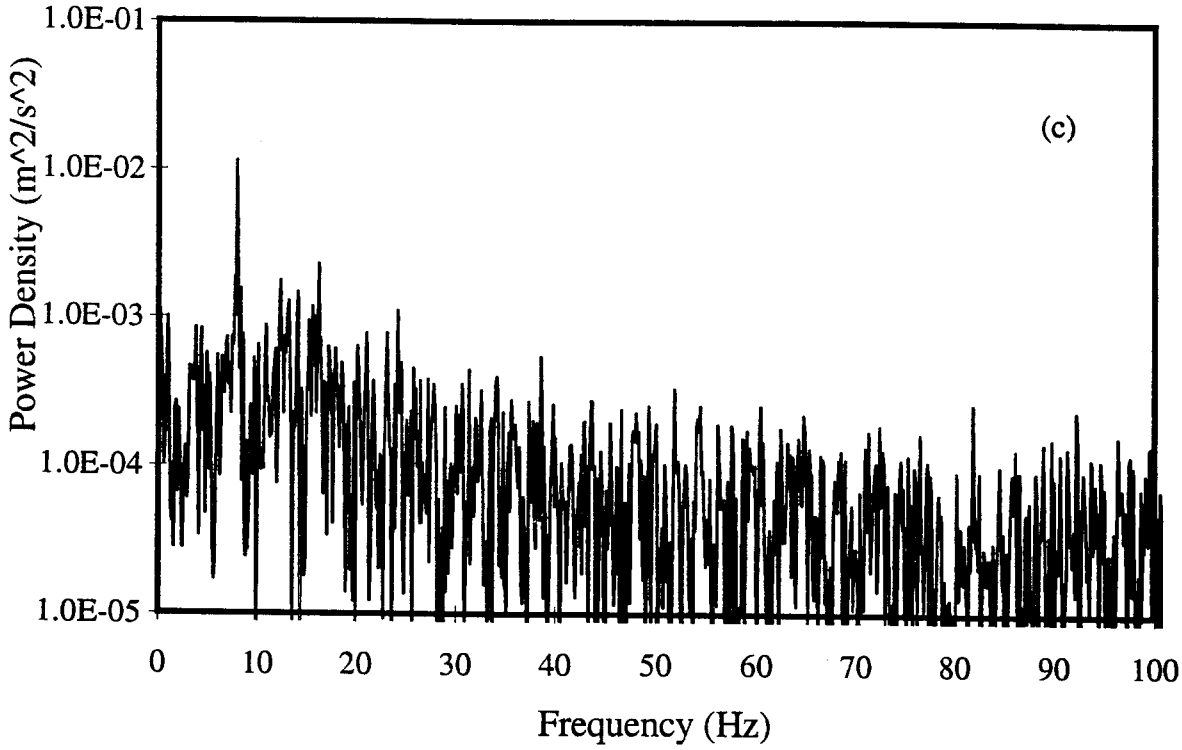
1.0E-01
1.0E-02
1.0E-03
1.0E-04
1.0E-05
Power Density (m^2/s^2)
(c)
0
10
20
30
40
50
60
70
80
90
100
Frequency (Hz)

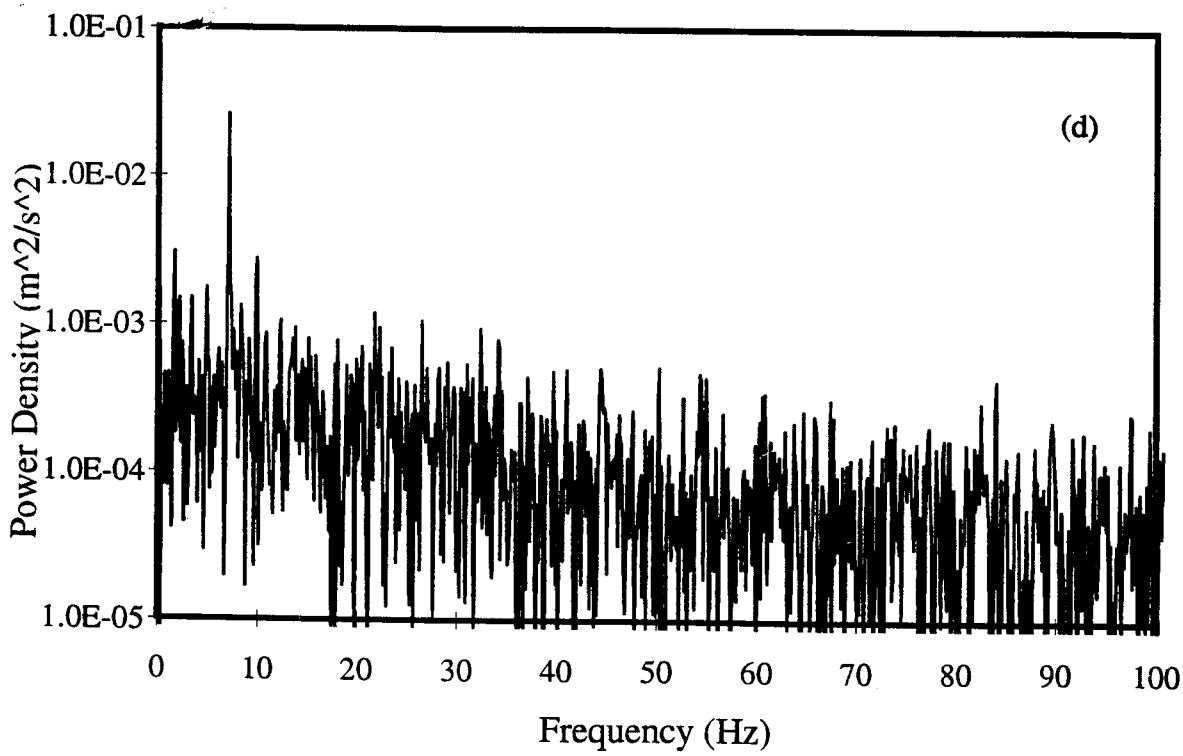
1.0E-01
1.0E-02
1.0E-03
1.0E-04
1.0E-05
Power Density (m^2/s^2)
(d)
0
10
20
30
40
50
60
70
80
90
100
Frequency (Hz)

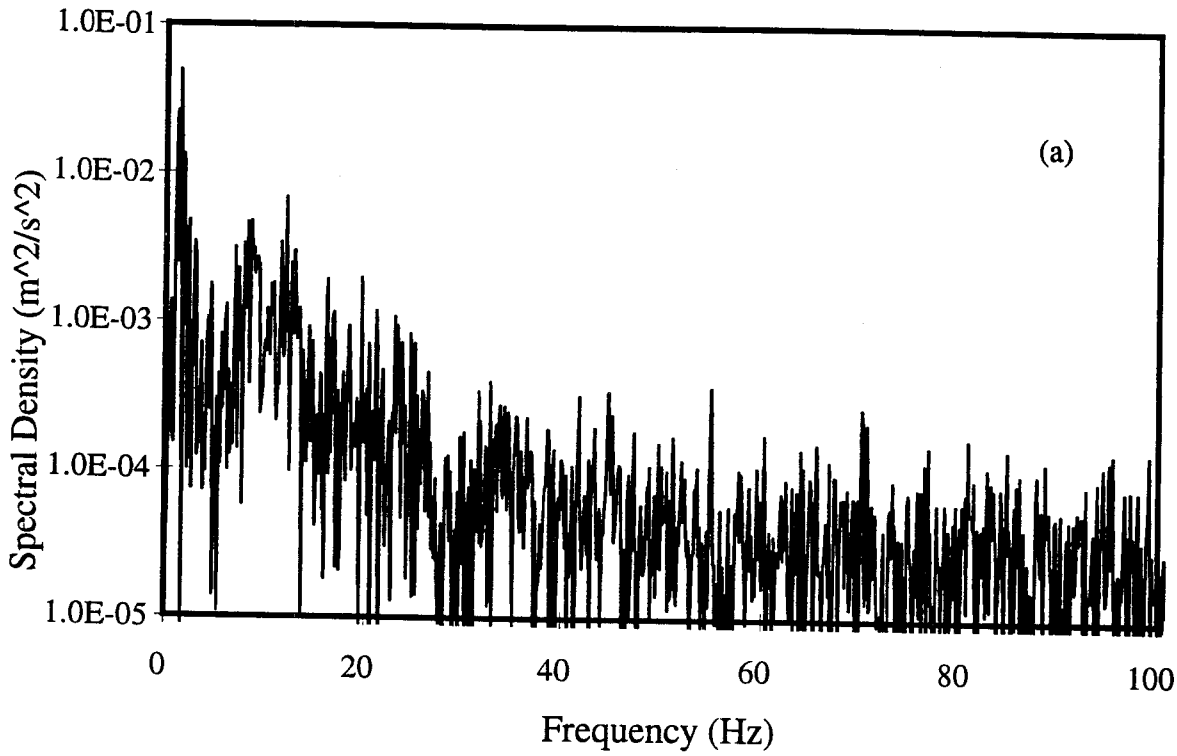

Figure 3.18 Power spectra of the tangential velocity component and velocity traces with Ta = 1.6 x 10^7 and Re_a = 0, at l/b = 20 and at different gap locations: (a) velocity spectrum at r' = 0.1 (b) velocity spectrum at r' = 0.5 (c) velocity spectrum at r' = 0.9 (d) velocity trace at r' = 0.1 (e) velocity trace at r' = 0.9.

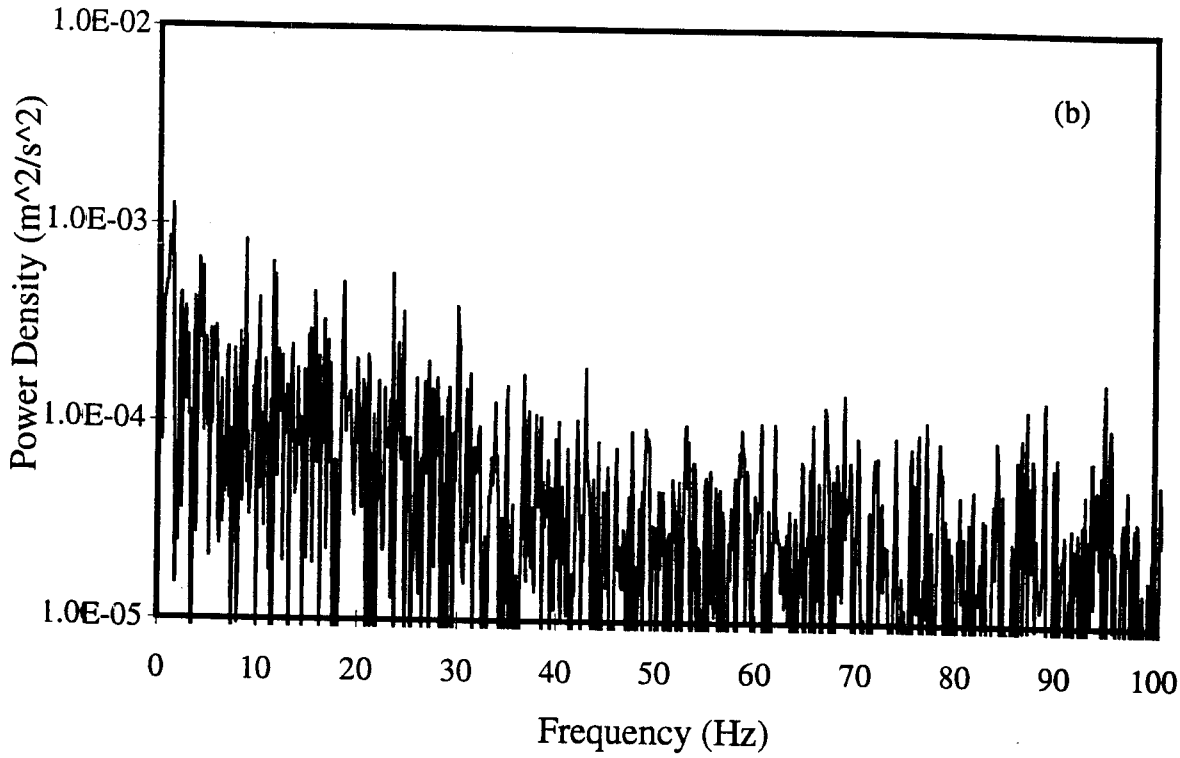
1.0E-02
1.0E-03
1.0E-04
1.0E-05
Power Density (m^2/s^2)
(b)
0
10
20
30
40
50
60
70
80
90
100
Frequency (Hz)

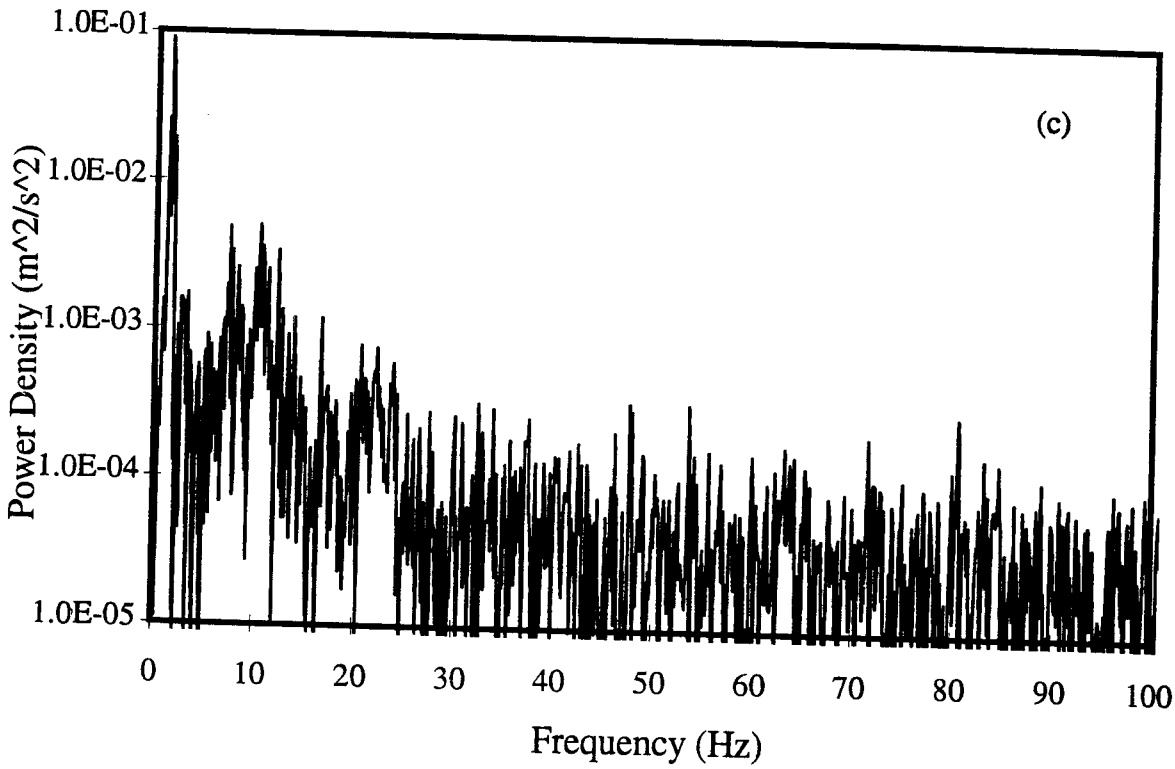
1.0E-01
1.0E-02
1.0E-03
1.0E-04
1.0E-05
Power Density (m^2/s^2)
(c)
0
10
20
30
40
50
60
70
80
90
100
Frequency (Hz)

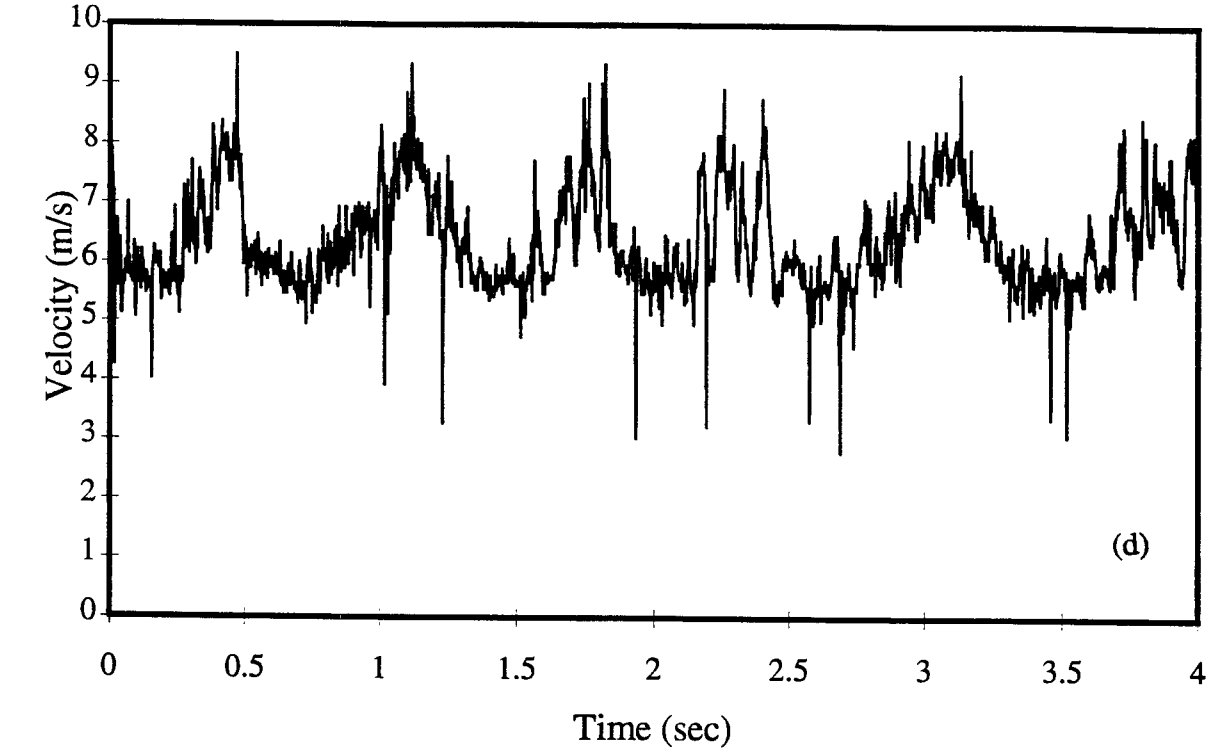
Velocity (m/s)
10
9
8
7
6
5
4
3
2
1
0
0
0.5
1
1.5
2
2.5
3
3.5
4
Time (sec)
(d)

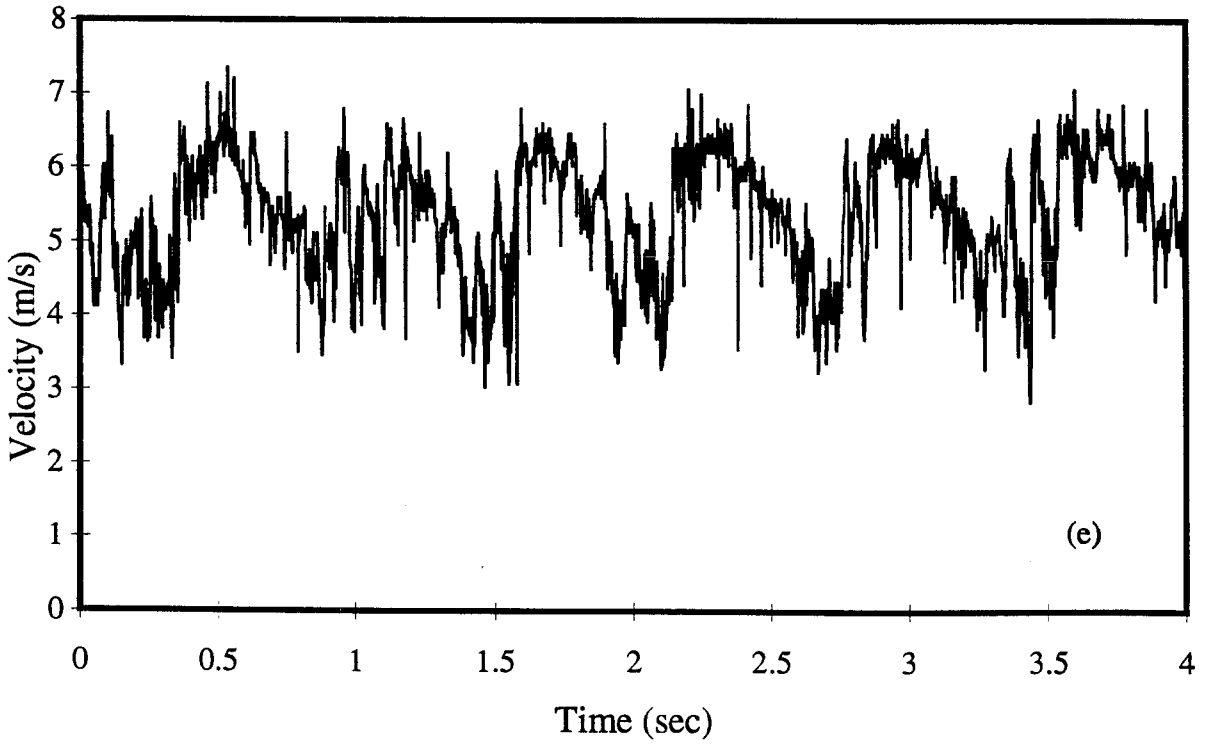
Velocity (m/s)
8
7
6
5
4
3
2
1
0
0
0.5
1
1.5
2
2.5
3
3.5
4
Time (sec)
(e)

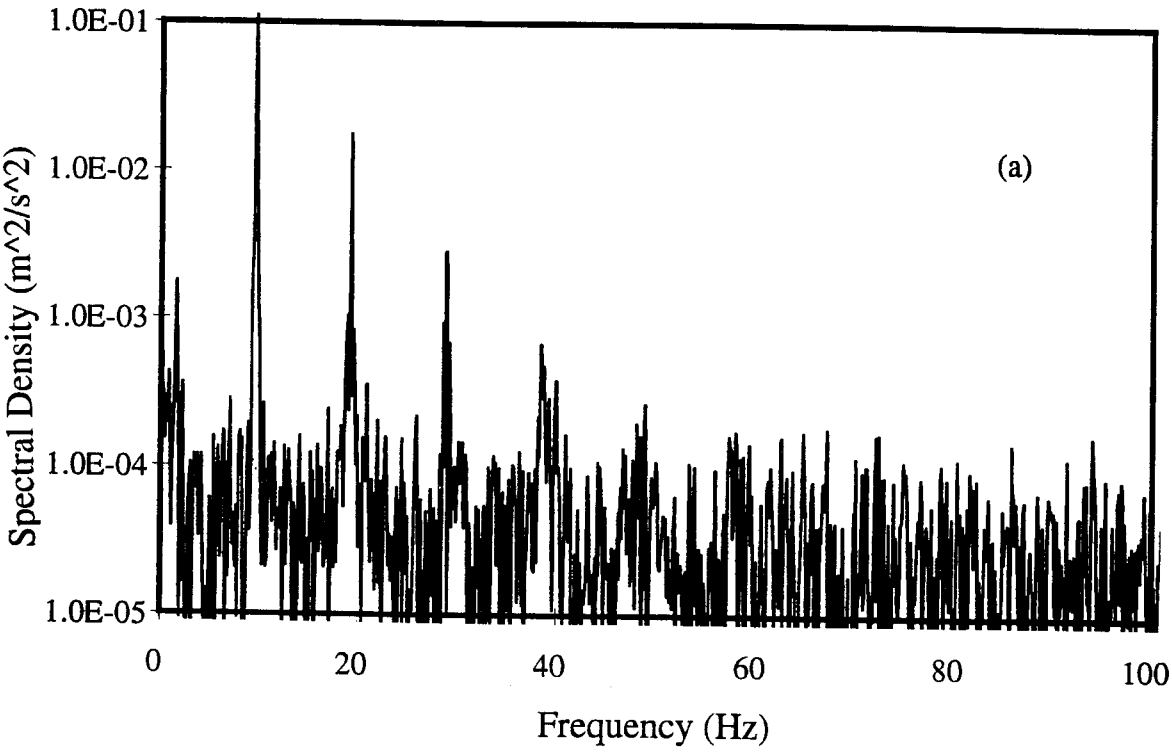

Figure 3.19 Power spectra of the tangential velocity component with Ta = 1.6 x 10^7 and Re_a = 10, at l/b = 20 and at different gap locations: (a) r' = 0.1 (b) r' = 0.5 (c) r' = 0.9.

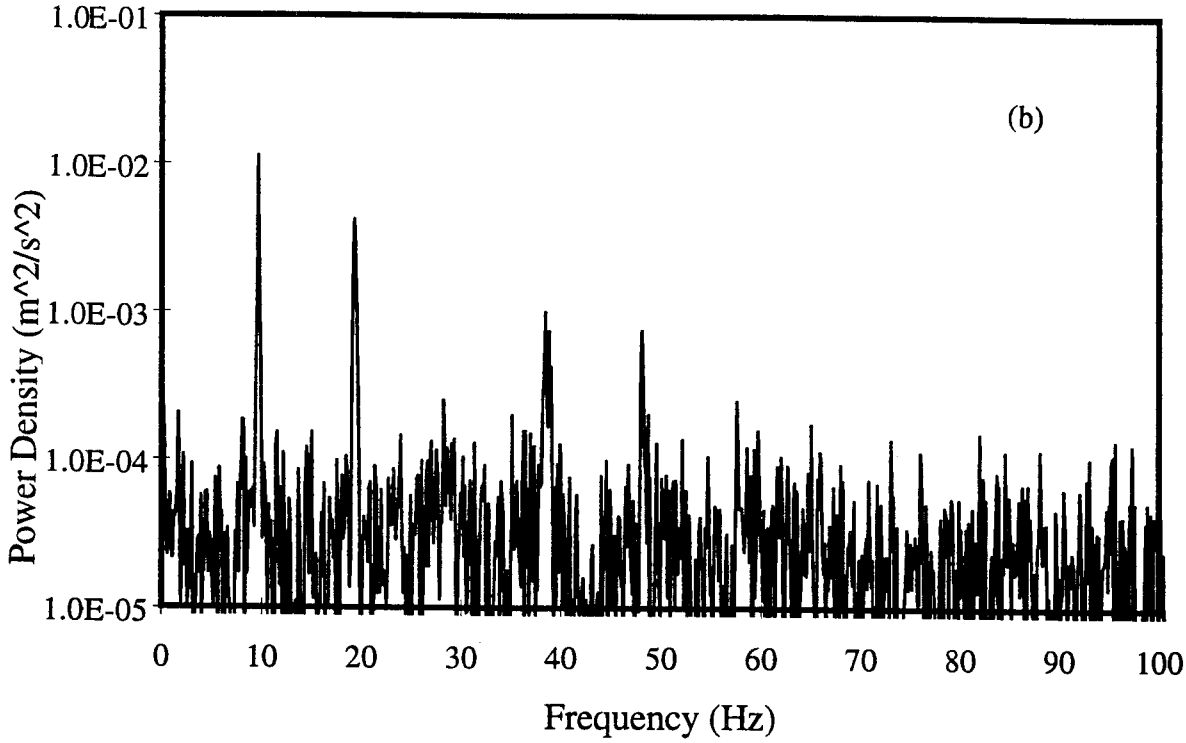
1.0E-01
1.0E-02
1.0E-03
1.0E-04
1.0E-05
Power Density (m^2/s^2)
(b)
0
10
20
30
40
50
60
70
80
90
100
Frequency (Hz)

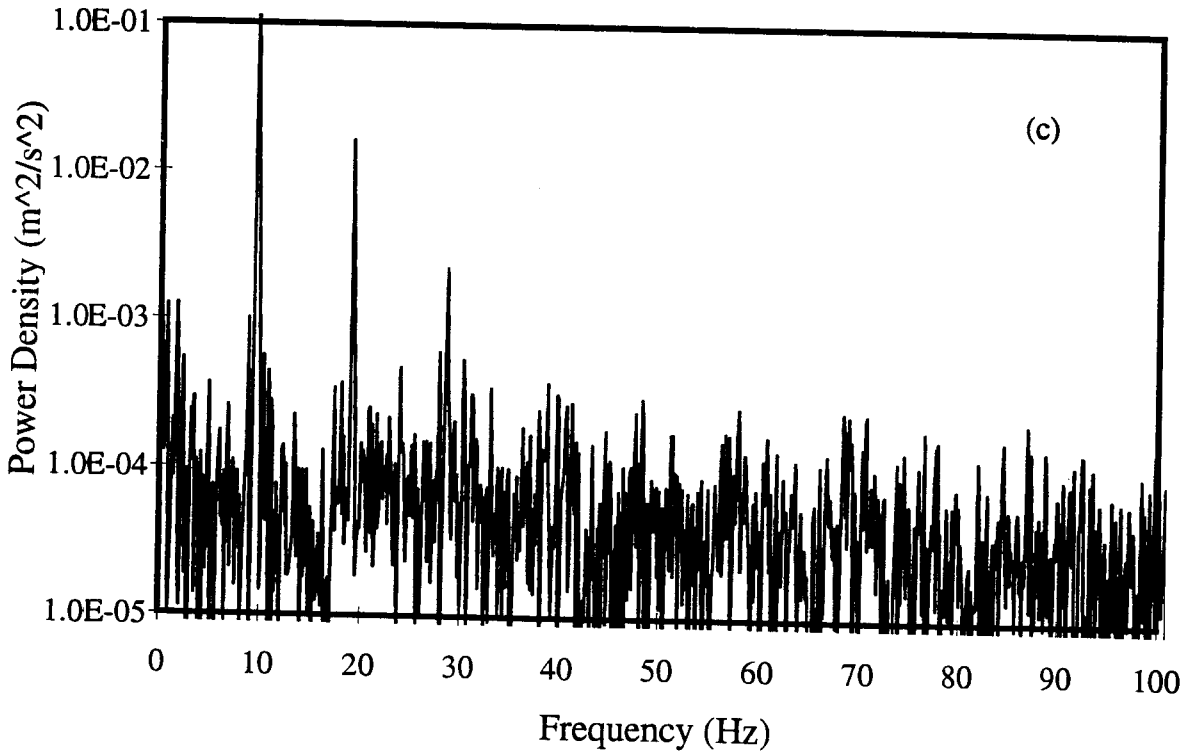
1.0E-01
1.0E-02
1.0E-03
1.0E-04
1.0E-05
Power Density (m^2/s^2)
(c)
0
10
20
30
40
50
60
70
80
90
100
Frequency (Hz)

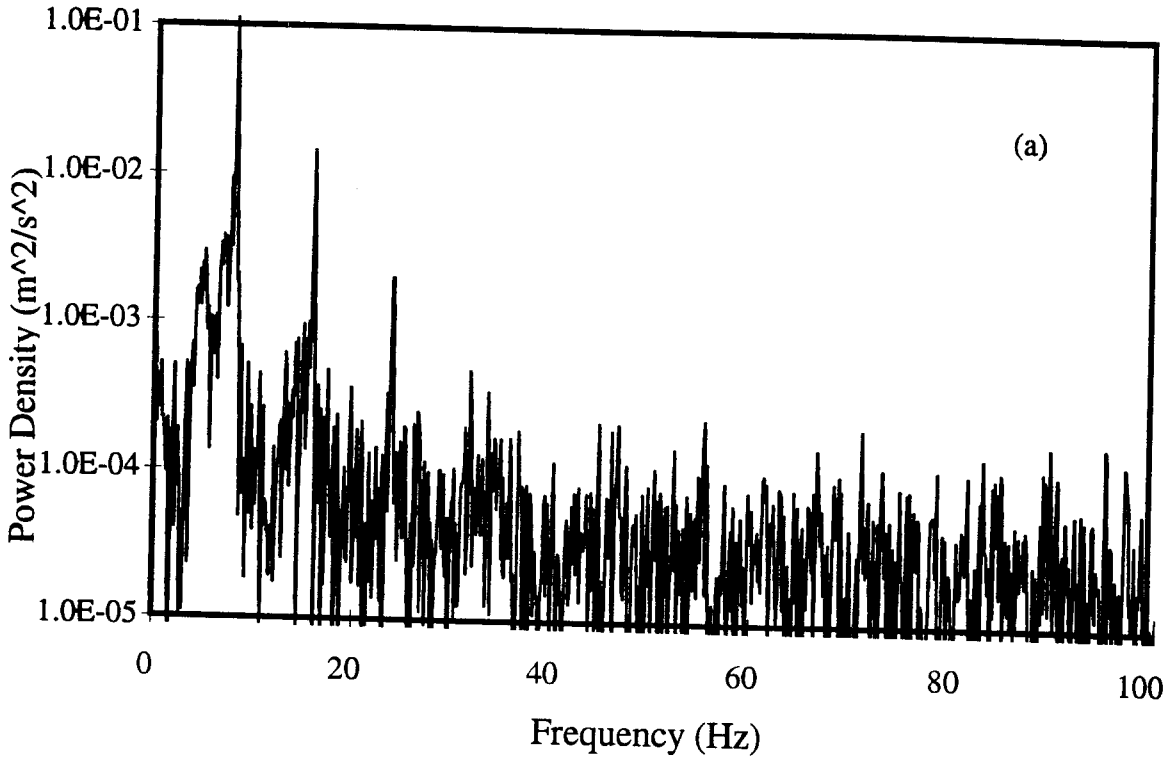

Figure 3.20 Power spectra of the tangential velocity component with Ta = 1.6 x 10^7 and Re_a = 160, at l/b = 20 and at different gap locations: (a) r' = 0.1 (b) r' = 0.5 (c) r' = 0.9.

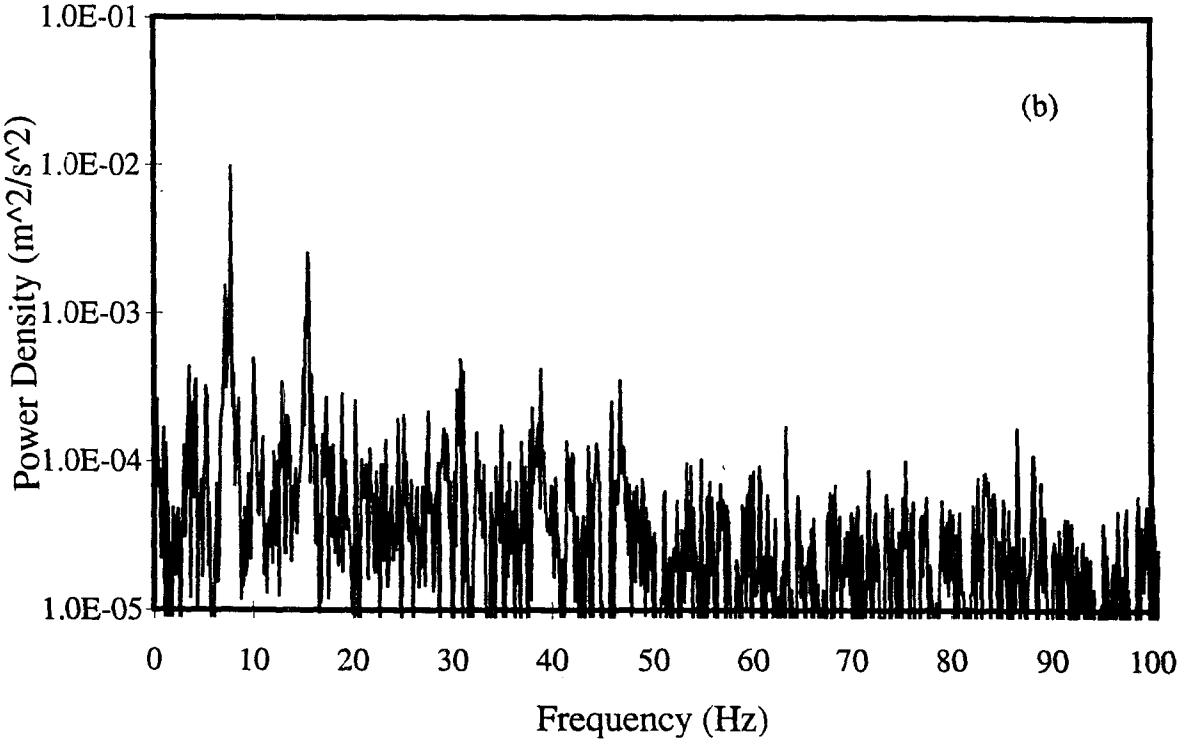
1.0E-01
1.0E-02
1.0E-03
1.0E-04
1.0E-05
Power Density (m^2/s^2)
(b)
0
10
20
30
40
50
60
70
80
90
100
Frequency (Hz)

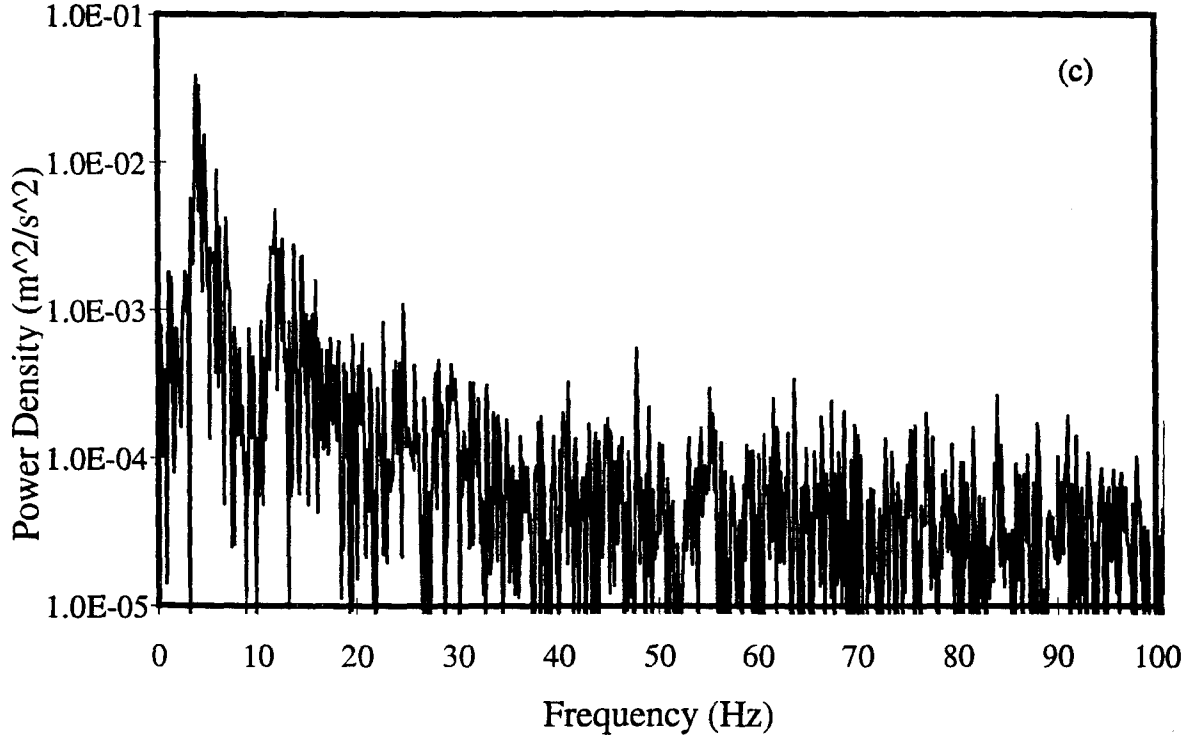
1.0E-01
1.0E-02
1.0E-03
1.0E-04
1.0E-05
Power Density (m^2/s^2)
(c)
0
10
20
30
40
50
60
70
80
90
100
Frequency (Hz)

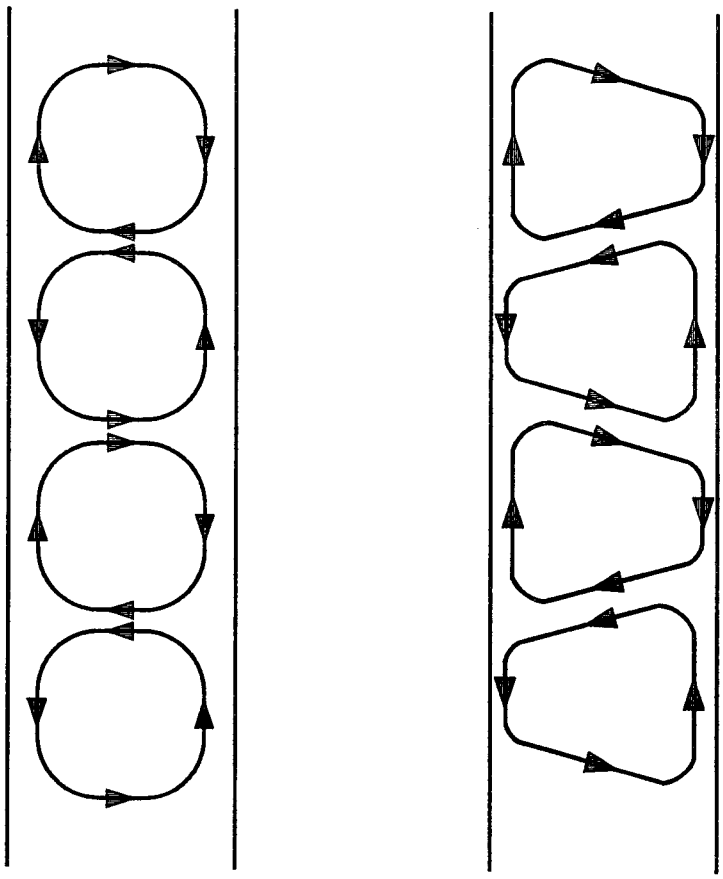

Toroidal Vortices

Vortices influenced by axial flow

Figure 3.21 Possible shapes of the Taylor vortices at $Re_a = 0$ and $Re_a = 160$.

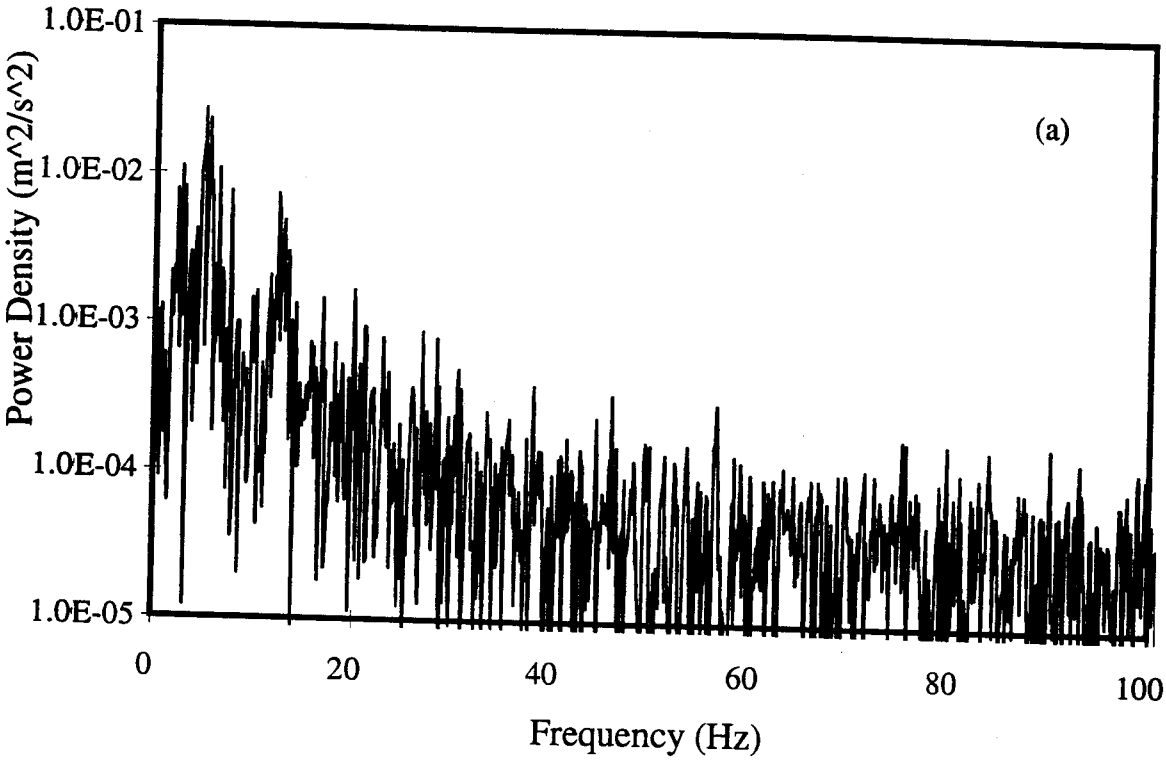

Figure 3.22 Power spectra of the tangential velocity component with Ta = 1.6 x 10^7 and Re_a = 220, at l/b = 20 and at different gap locations: (a) r' = 0.1 (b) r' = 0.5 (c) r' = 0.9.

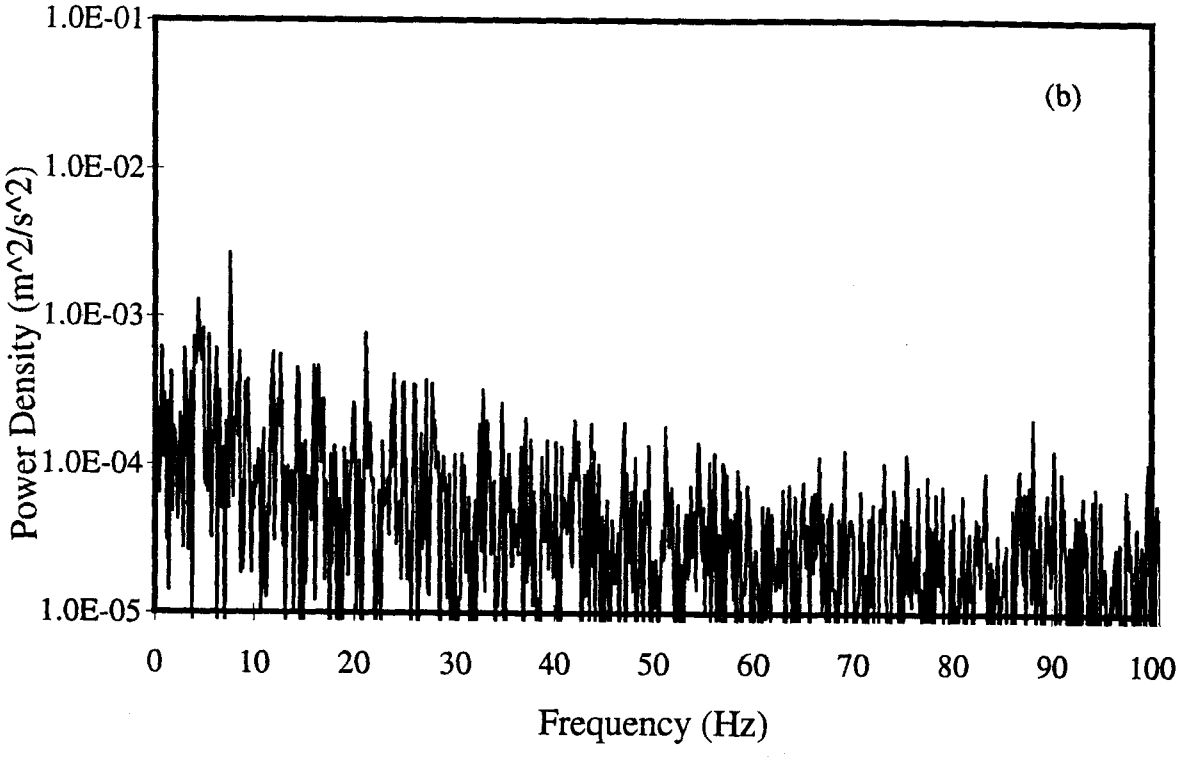
1.0E-01
1.0E-02
1.0E-03
1.0E-04
1.0E-05
Power Density (m^2/s^2)
(b)
0
10
20
30
40
50
60
70
80
90
100
Frequency (Hz)

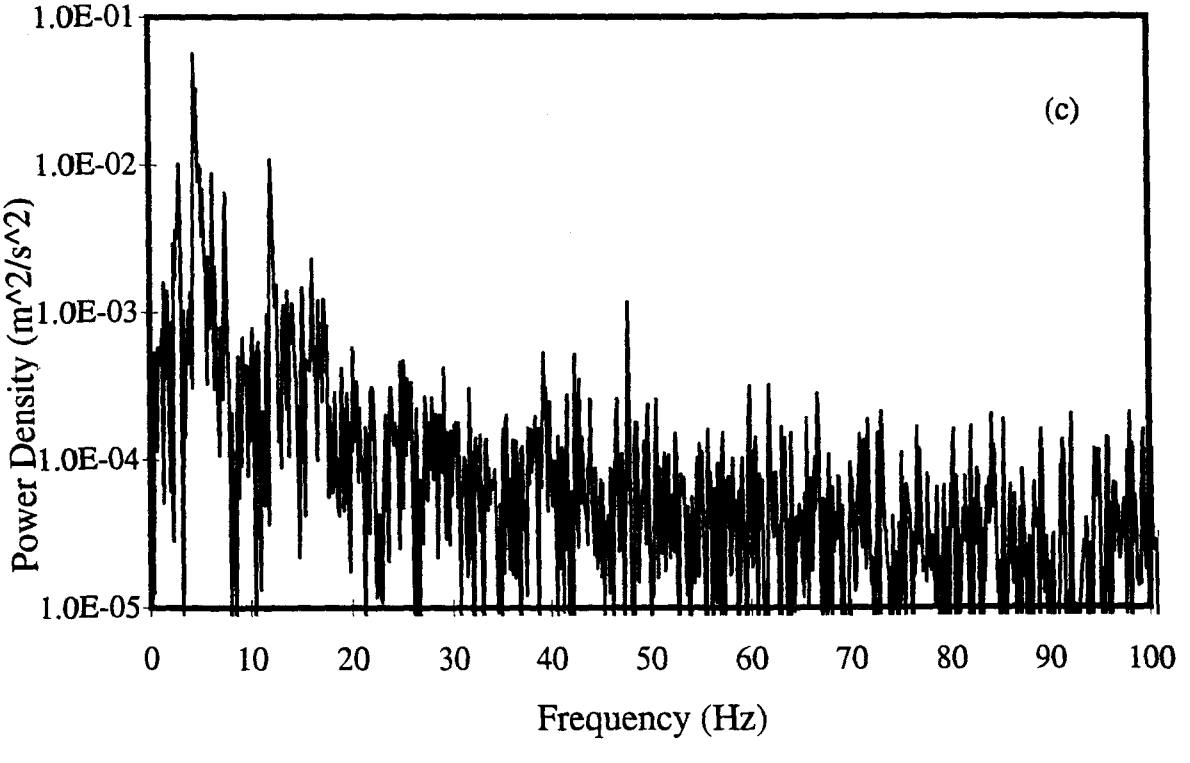
1.0E-01
1.0E-02
1.0E-03
1.0E-04
1.0E-05
Power Density (m^2/s^2)
(c)
0
10
20
30
40
50
60
70
80
90
100
Frequency (Hz)

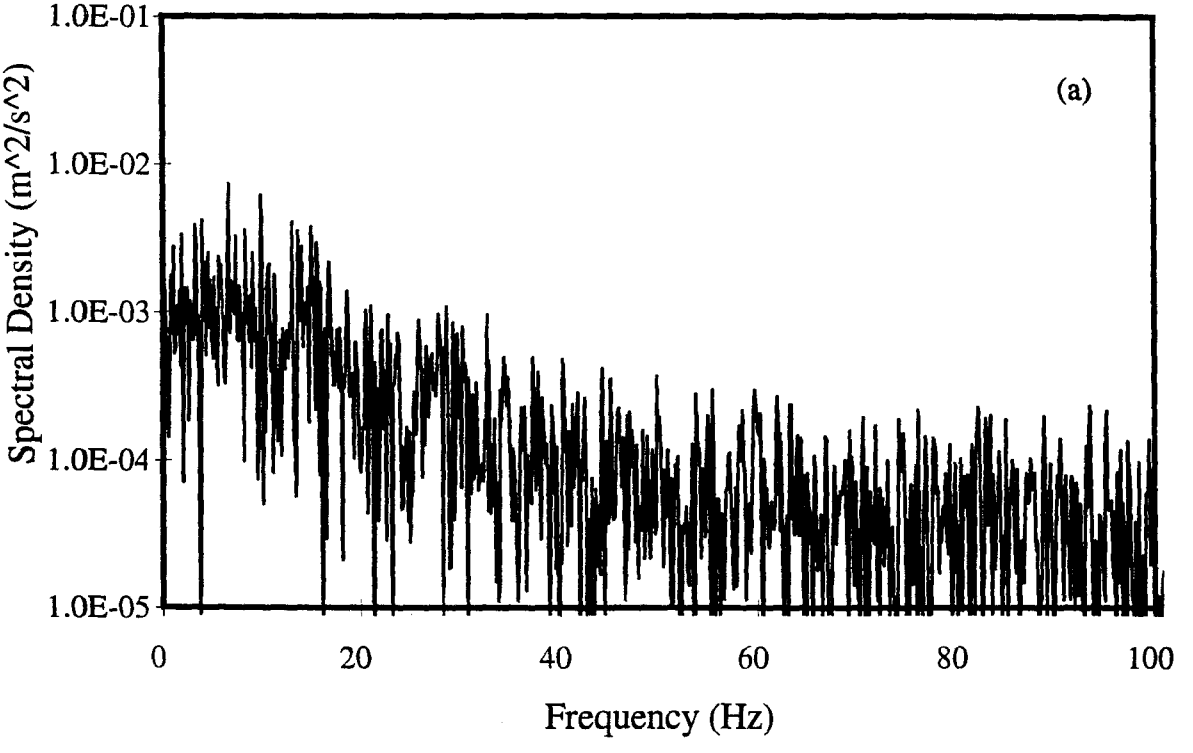

Figure 3.23 Power spectra of the tangential velocity component with Ta = 1.6 x 10^7 and Re_a = 500, at l/b = 20 and at different gap locations: (a) r' = 0.1 (b) r' = 0.5 (c) r' = 0.9.

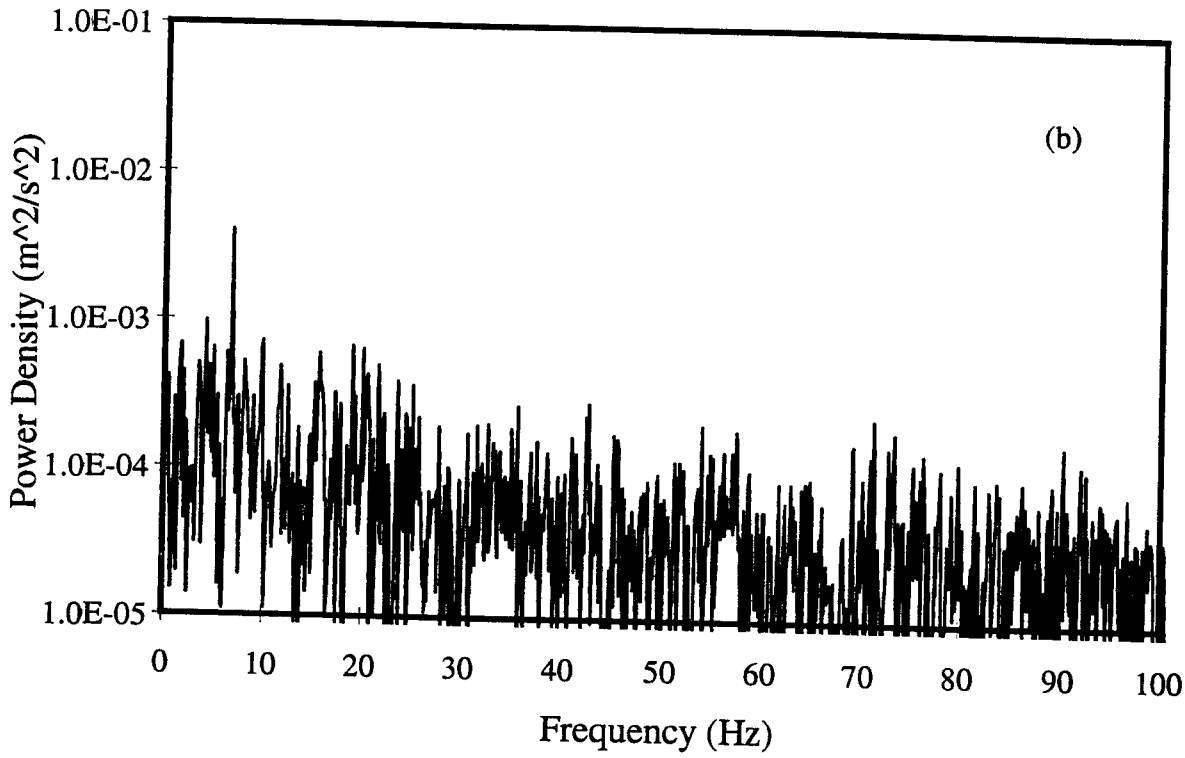
1.0E-01
1.0E-02
1.0E-03
1.0E-04
1.0E-05
Power Density (m^2/s^2)
(b)
0
10
20
30
40
50
60
70
80
90
100
Frequency (Hz)

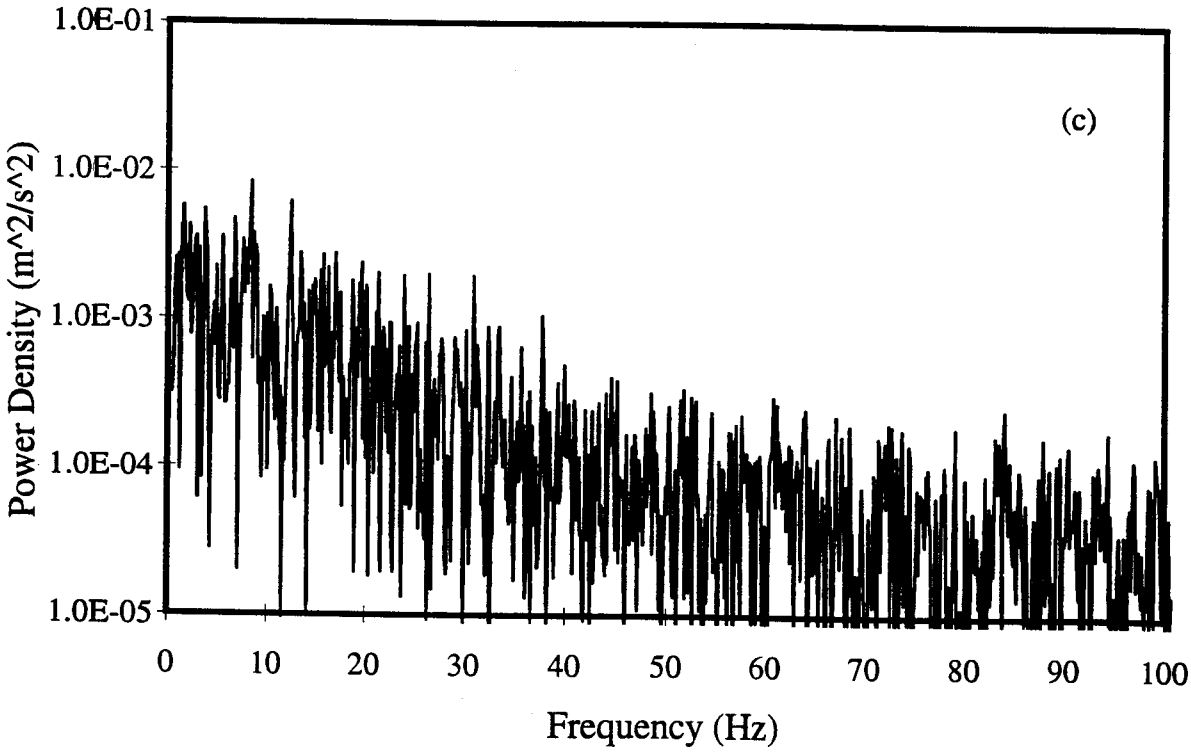
1.0E-01
1.0E-02
1.0E-03
1.0E-04
1.0E-05
Power Density (m^2/s^2)
(c)
0
10
20
30
40
50
60
70
80
90
100
Frequency (Hz)

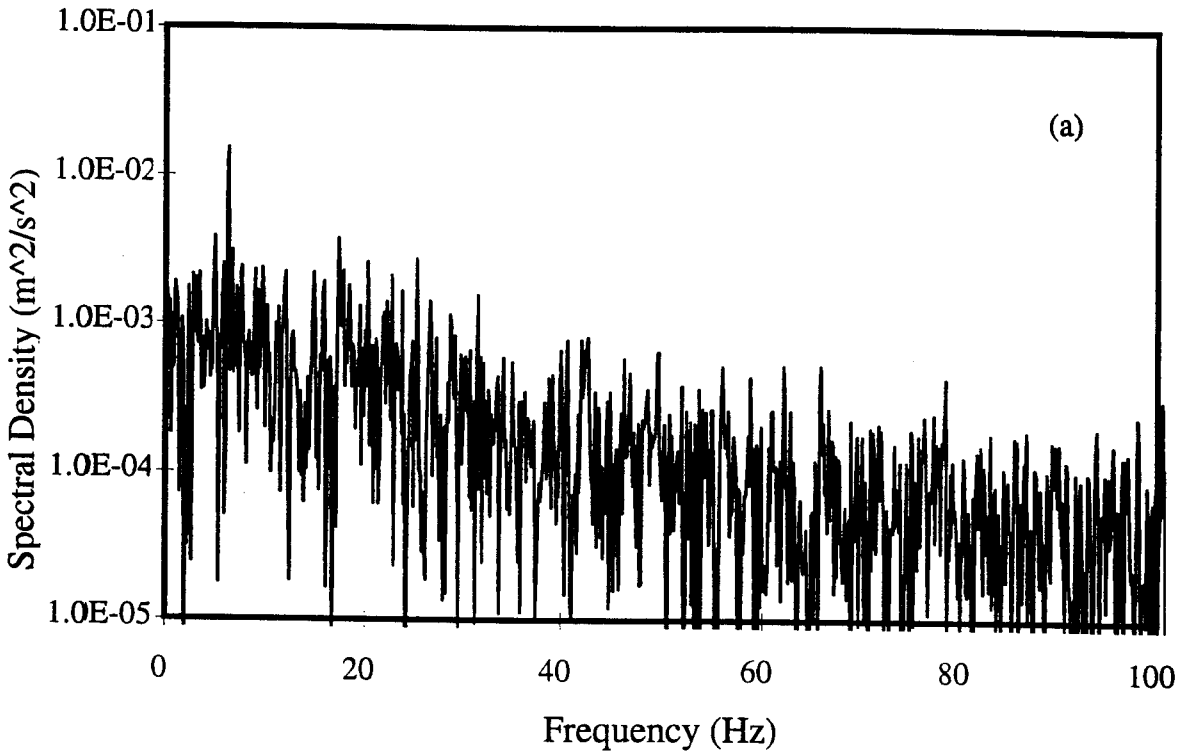

Figure 3.24 Power spectra of the tangential velocity component with Ta = 1.6 x 10^7 and Re_a = 980, at l/b = 20 and at different gap locations: (a) r' = 0.1 (b) r' = 0.5 (c) r' = 0.9.

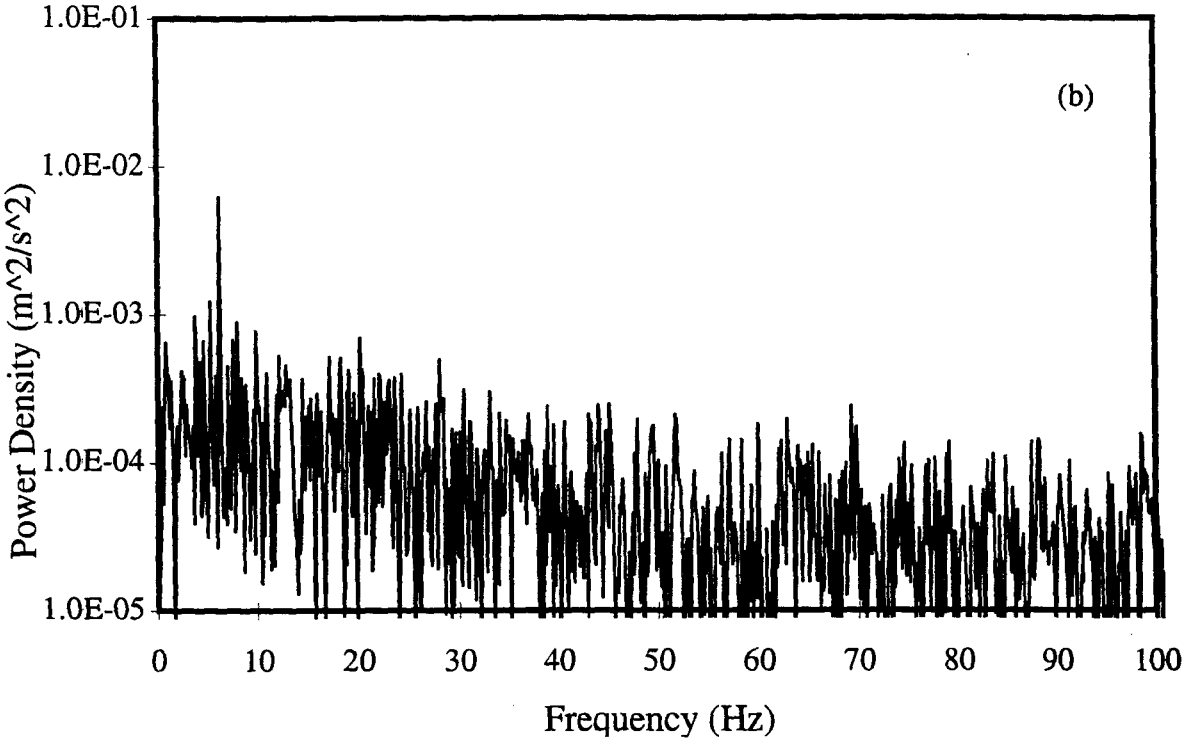
(b)
1.0E-01
1.0E-02
1.0E-03
1.0E-04
1.0E-05
Power Density (m^2/s^2)
0
10
20
30
40
50
60
70
80
90
100
Frequency (Hz)

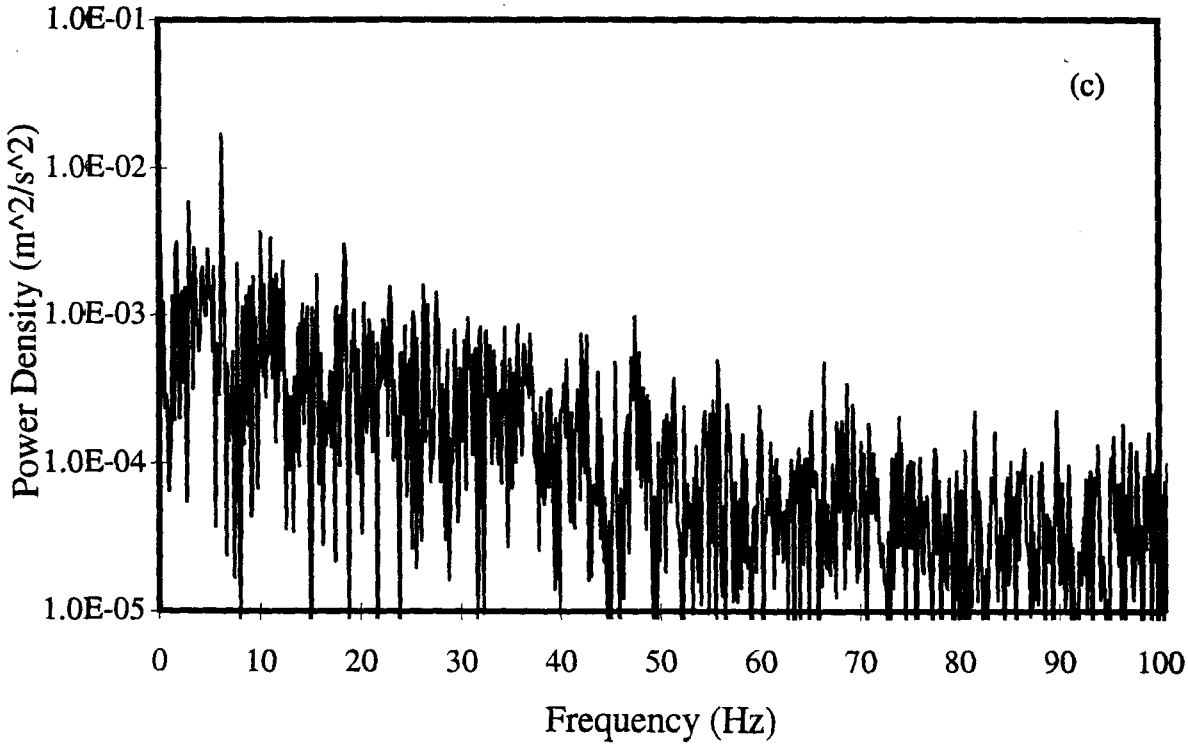
(c)
1.0E-01
1.0E-02
1.0E-03
1.0E-04
1.0E-05
Power Density (m^2/s^2)
0
10
20
30
40
50
60
70
80
90
100
Frequency (Hz)

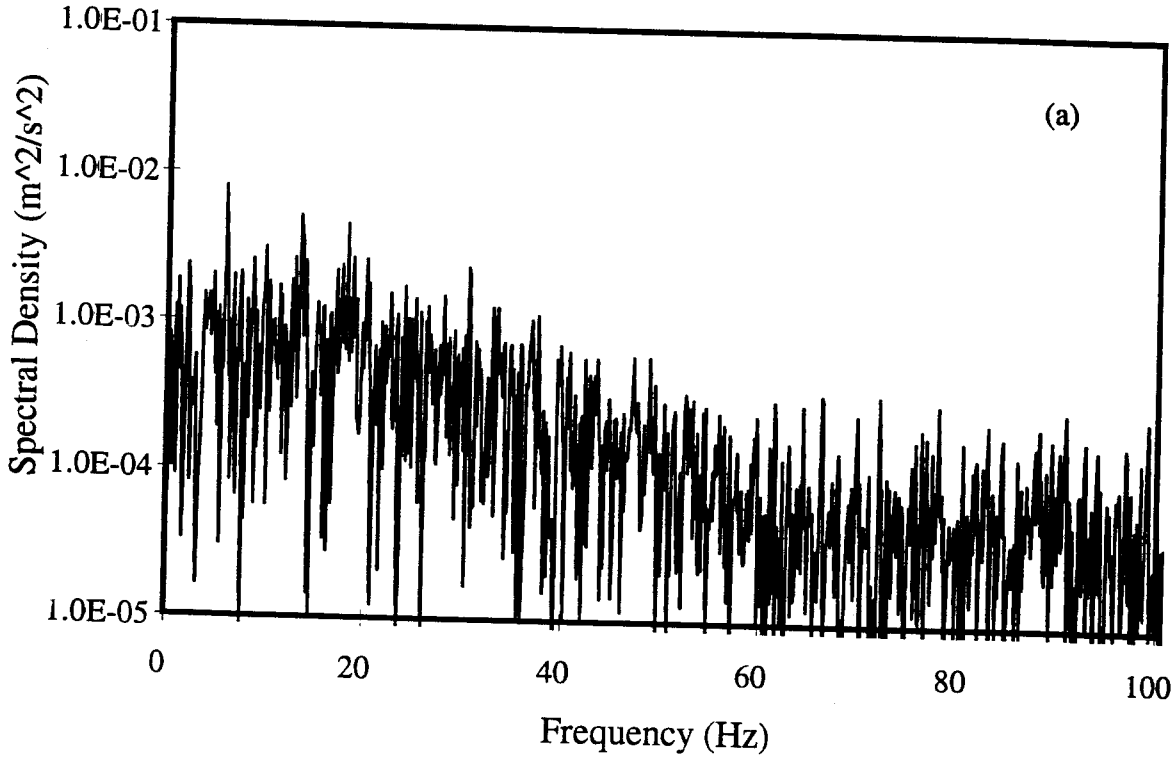

Figure 3.25 Power spectra of the tangential velocity component with Ta = 1.6 x 10^7 and Re_a = 1300, at l/b = 20 and at different gap locations: (a) r' = 0.1 (b) r' = 0.5 (c) r' = 0.9.

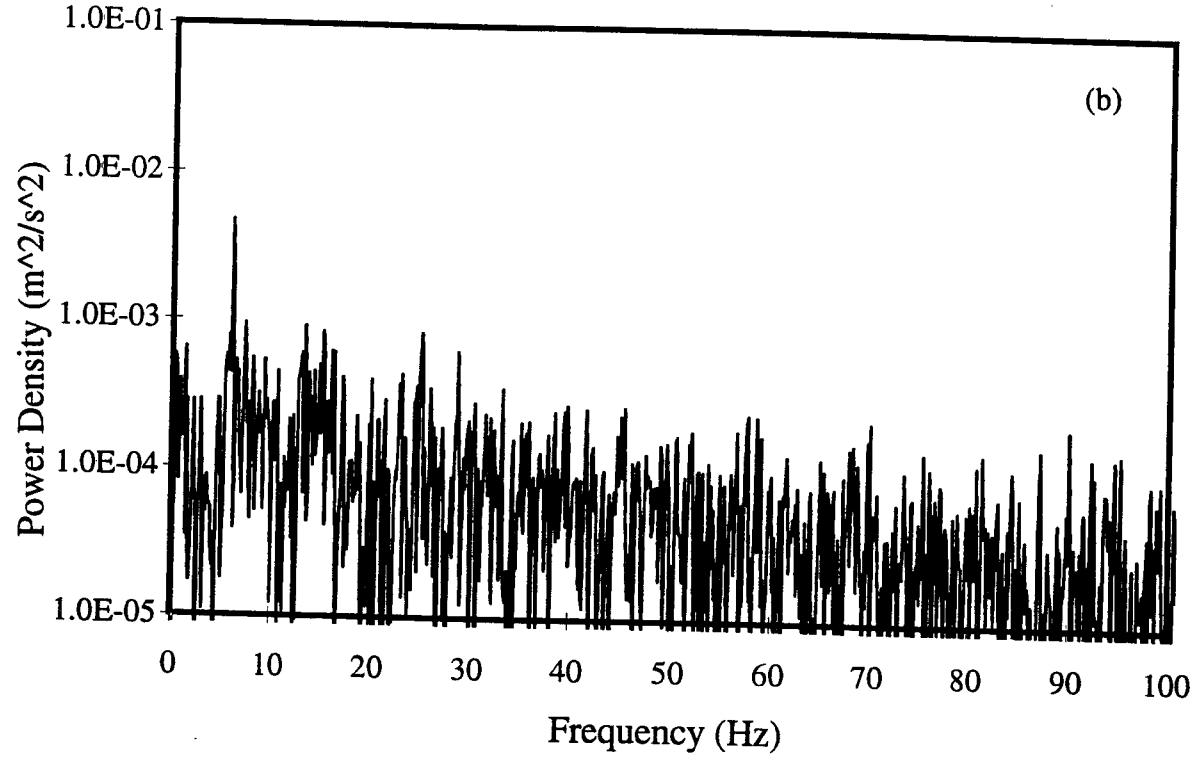
1.0E-01
1.0E-02
1.0E-03
1.0E-04
1.0E-05
Power Density (m^2/s^2)
(b)
0
10
20
30
40
50
60
70
80
90
100
Frequency (Hz)

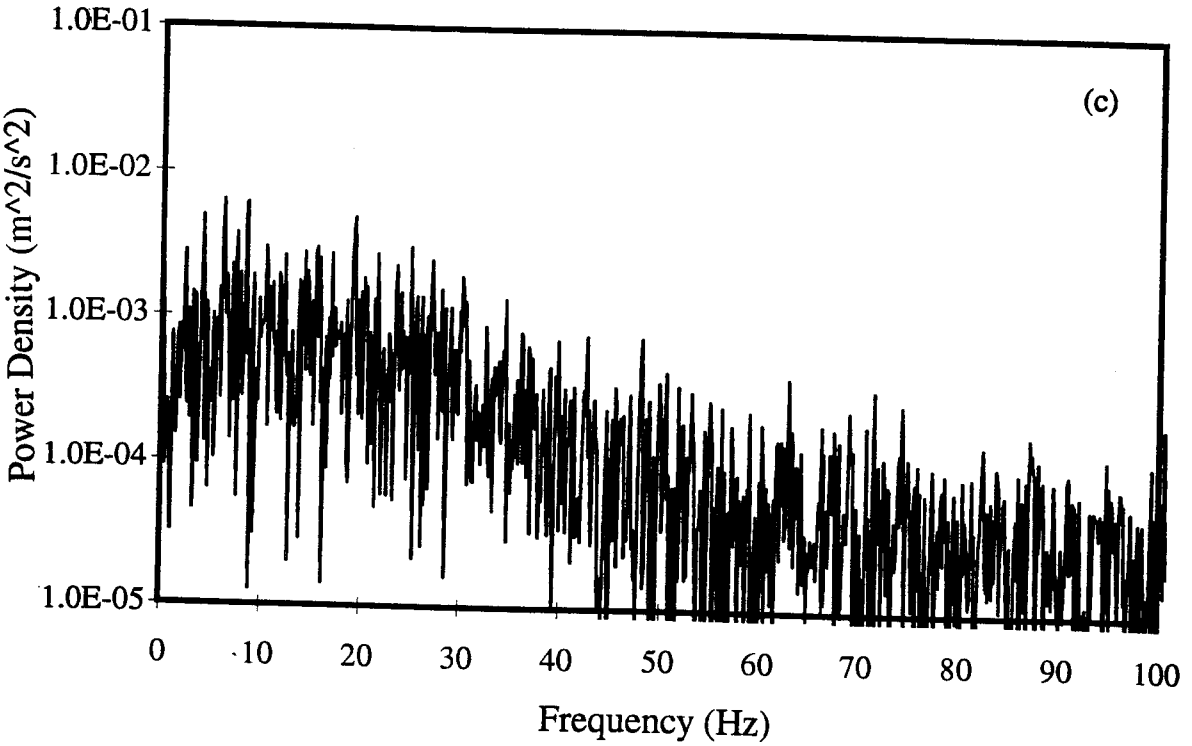
1.0E-01
1.0E-02
1.0E-03
1.0E-04
1.0E-05
Power Density (m^2/s^2)
(c)
0
10
20
30
40
50
60
70
80
90
100
Frequency (Hz)

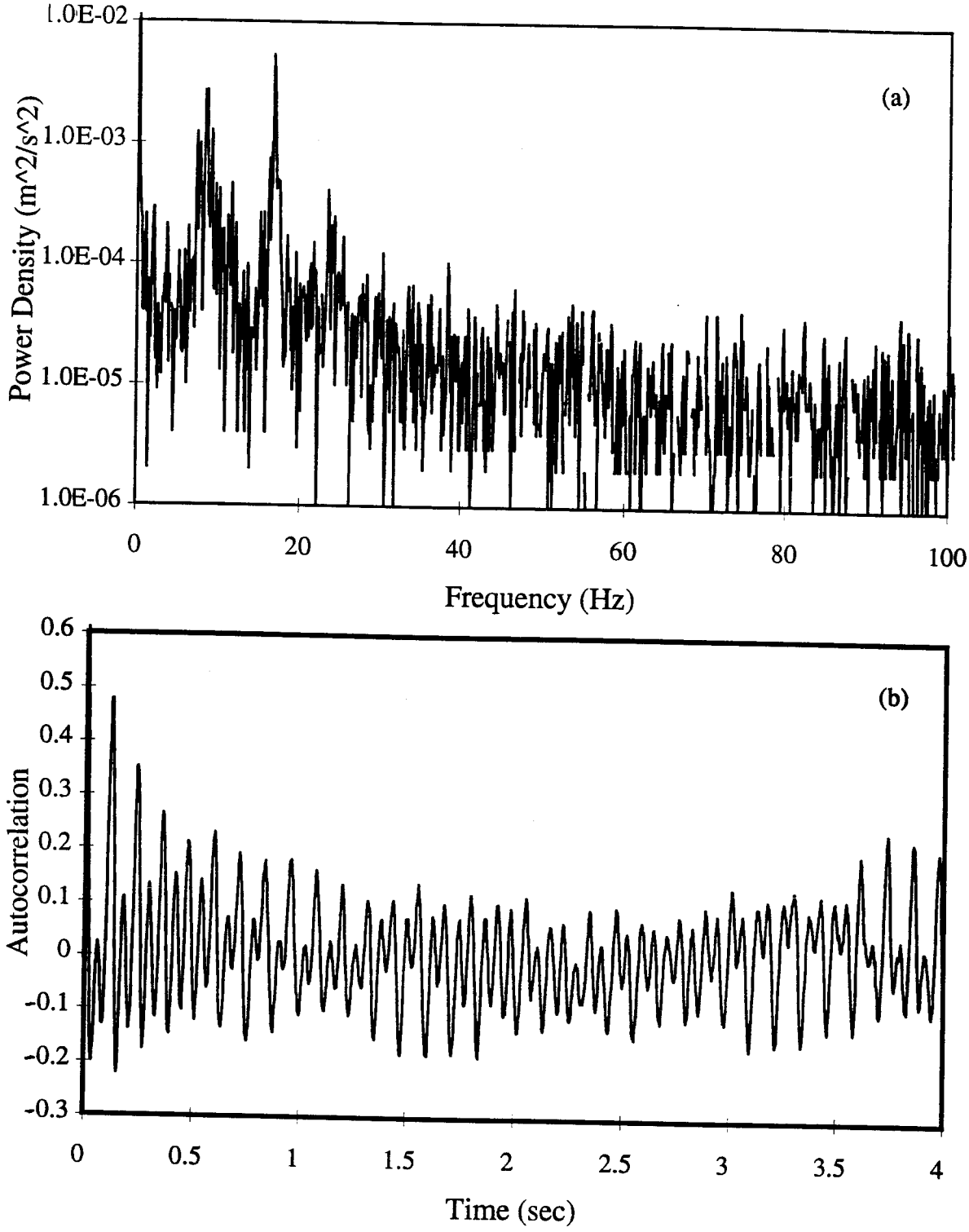

Figure 3.26 Power spectrum and autocorrelogram of the tangential velocity component with Ta = 1.45 x 10^7 and Re_a = 0, at l/b = 37: (a) power spectrum (b) autocorrelogram.

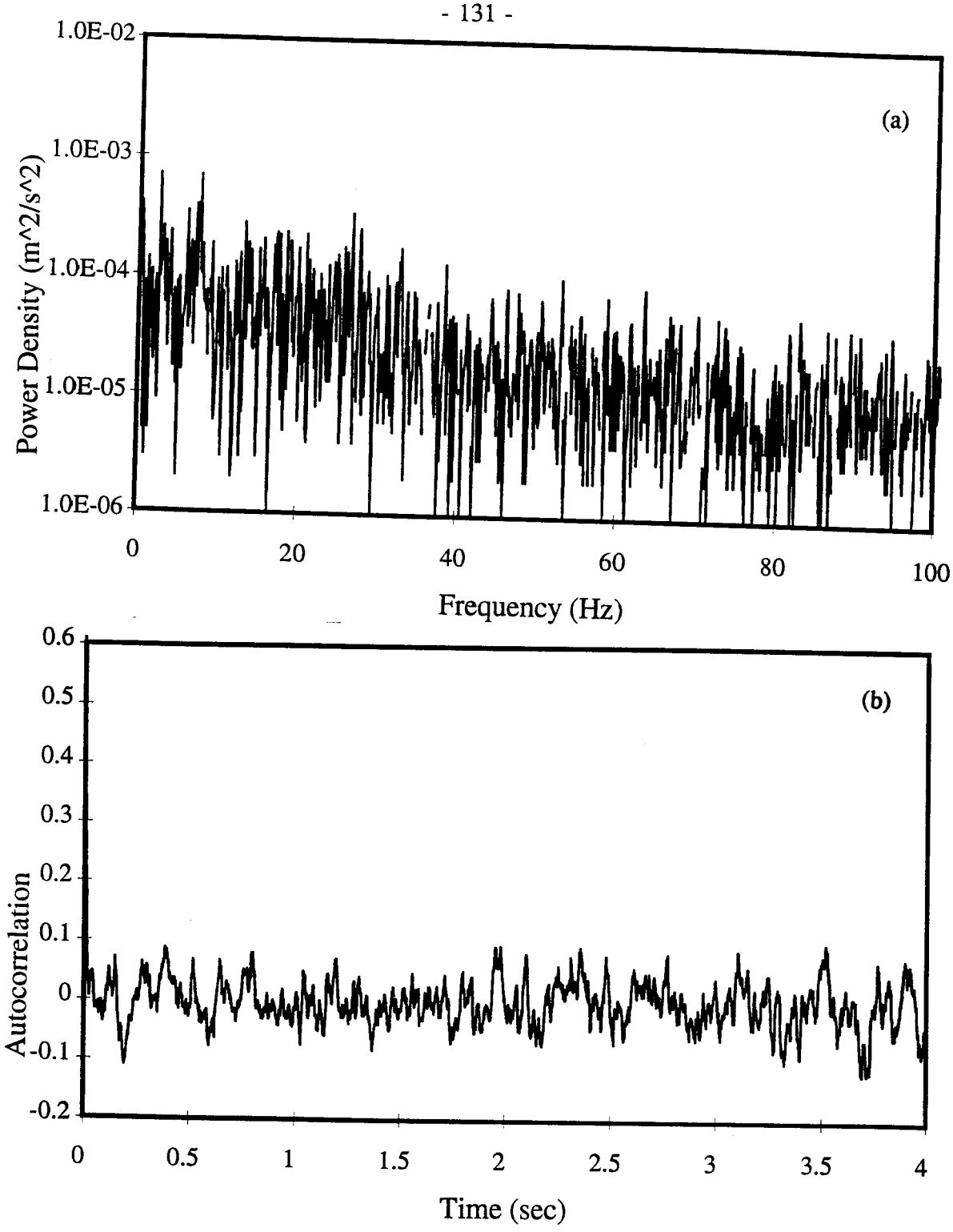

Figure 3.27 Power spectrum and autocorrelogram of the tangential velocity component with Ta = 1.45 x 10^7 and Re_a = 70, at l/b = 37: (a) power spectrum (b) autocorrelogram.

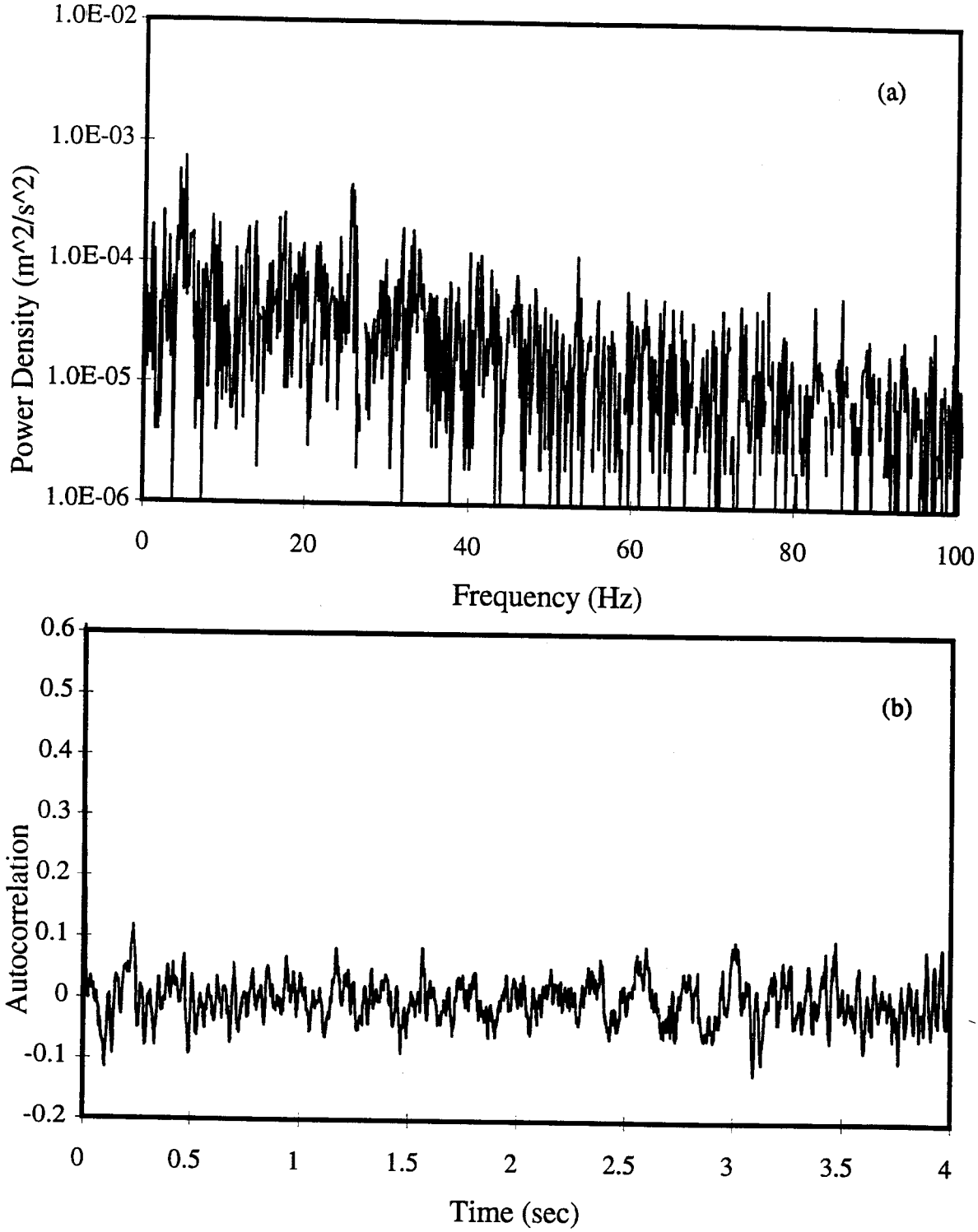

Figure 3.28 Power spectrum and autocorrelogram of the tangential velocity component with Ta = 1.45 x 10^7 and Re_a = 160, at l/b = 37: (a) power spectrum (b) autocorrelogram.

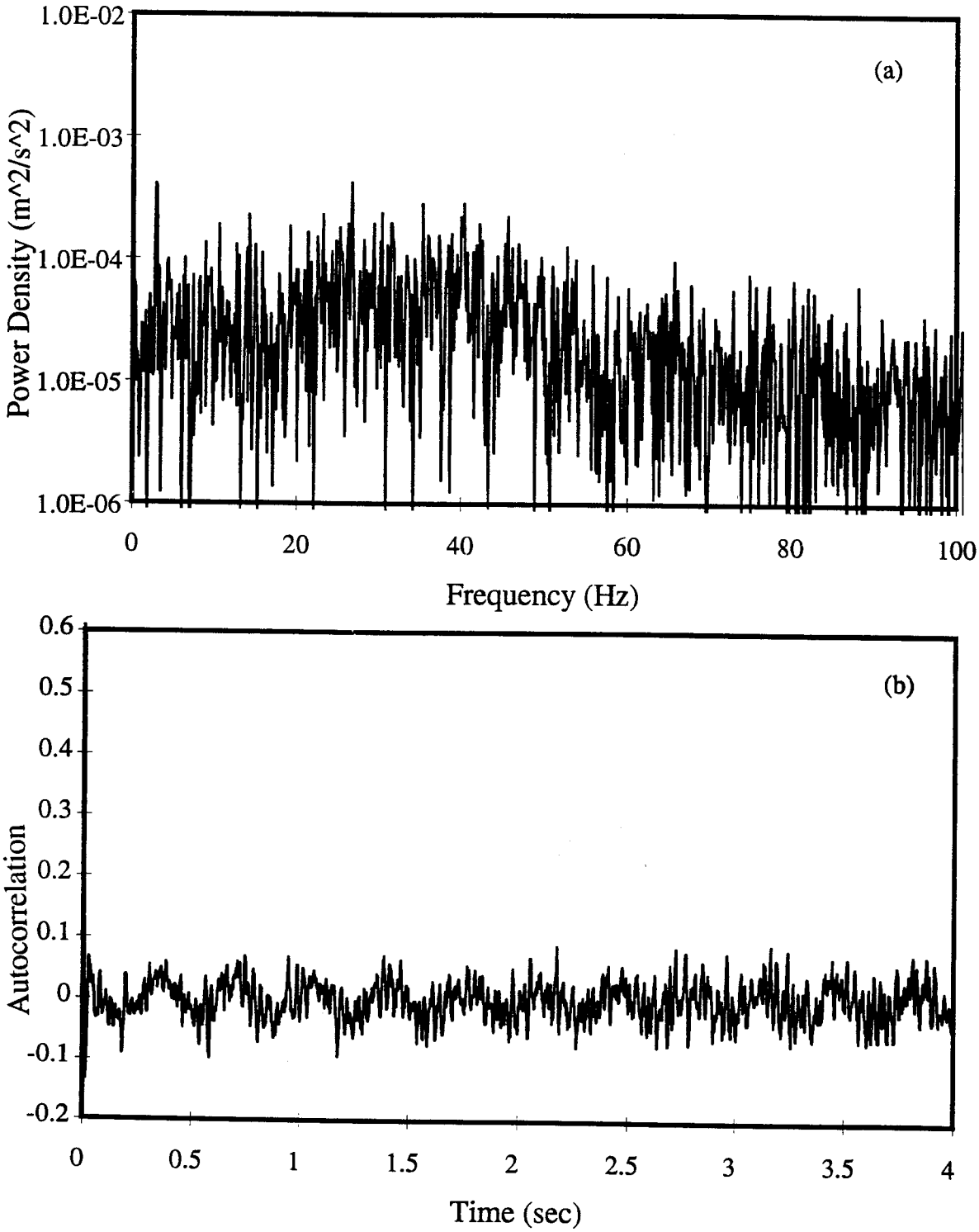

Figure 3.29 Power spectrum and autocorrelogram of the tangential velocity component with Ta = 1.45 x 10^7 and Re_a = 2500, at l/b = 37: (a) power spectrum (b) autocorrelogram.

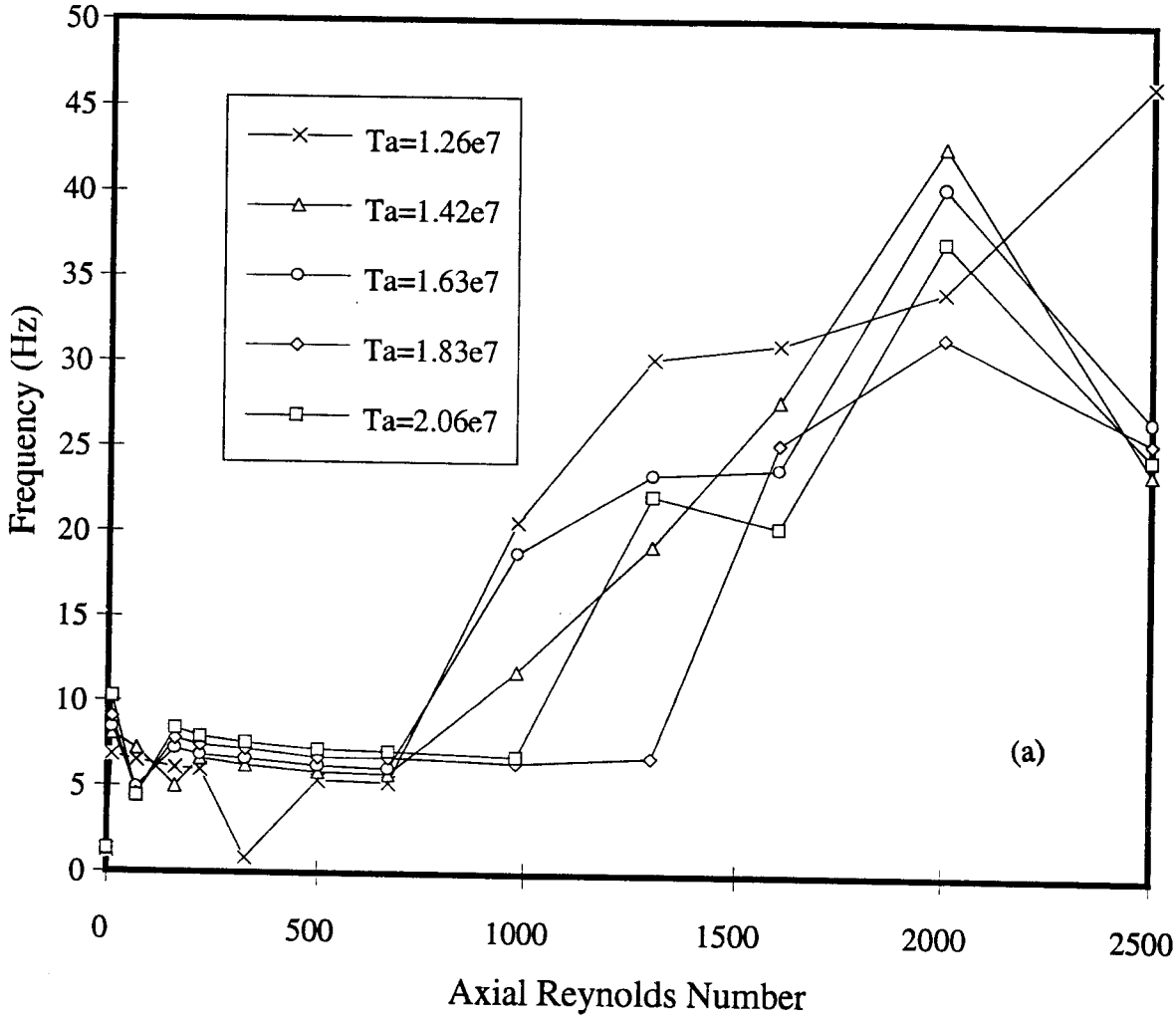

Figure 3.30 Frequency with the greatest power vs. axial Reynolds number at l/b = 20 for different ranges of Taylor numbers: (a) Ta = 1.26 x 10^7 to 2.06 x 10^7 (b) Ta = 1.12 x 10^7 to 2.1 x 10^7.

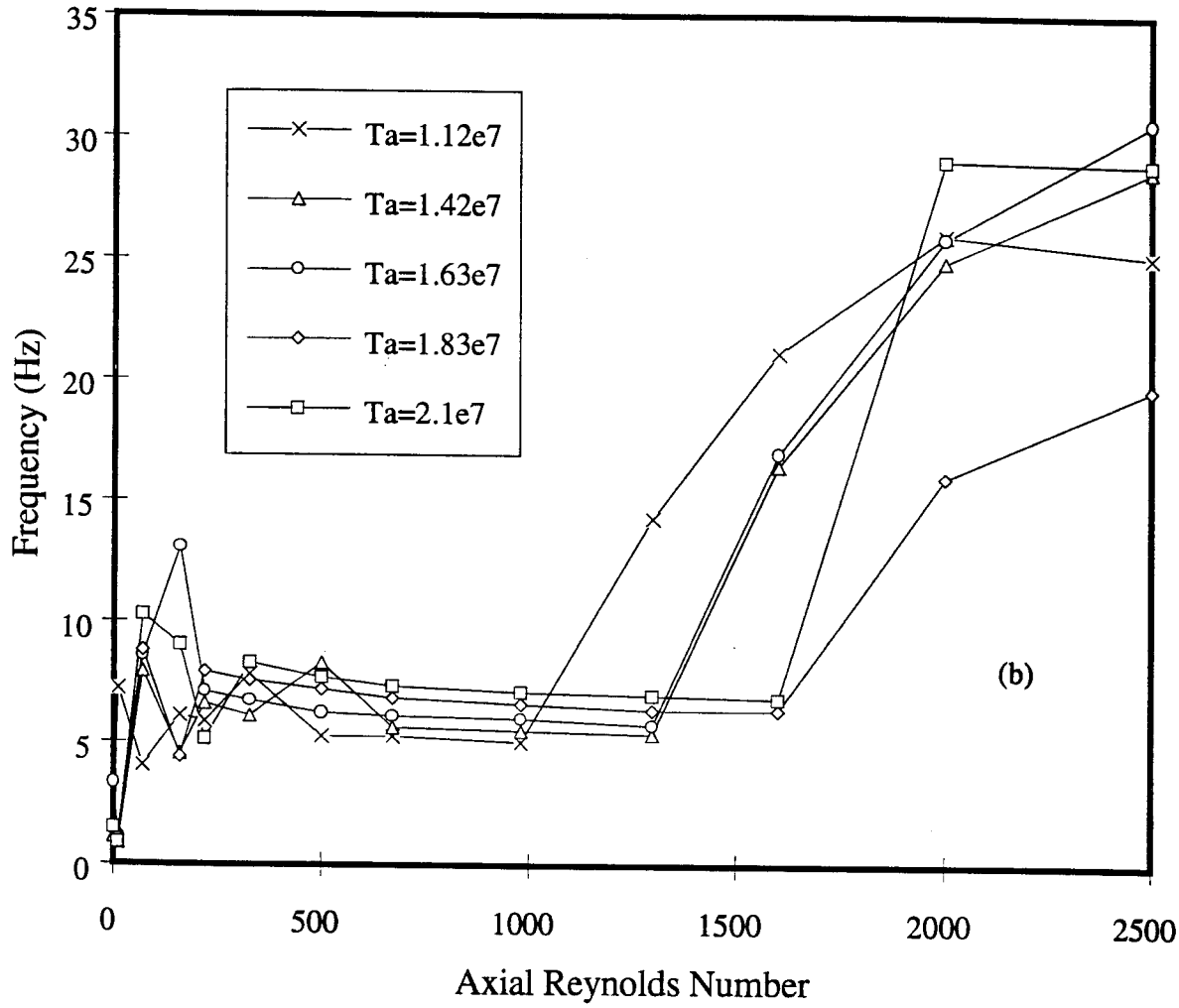
Ta=1.12e7
Ta=1.42e7
Ta=1.63e7
Ta=1.83e7
Ta=2.1e7
(b)
Frequency (Hz)
Axial Reynolds Number
0
5
10
15
20
25
30
35
0
500
1000
1500
2000
2500

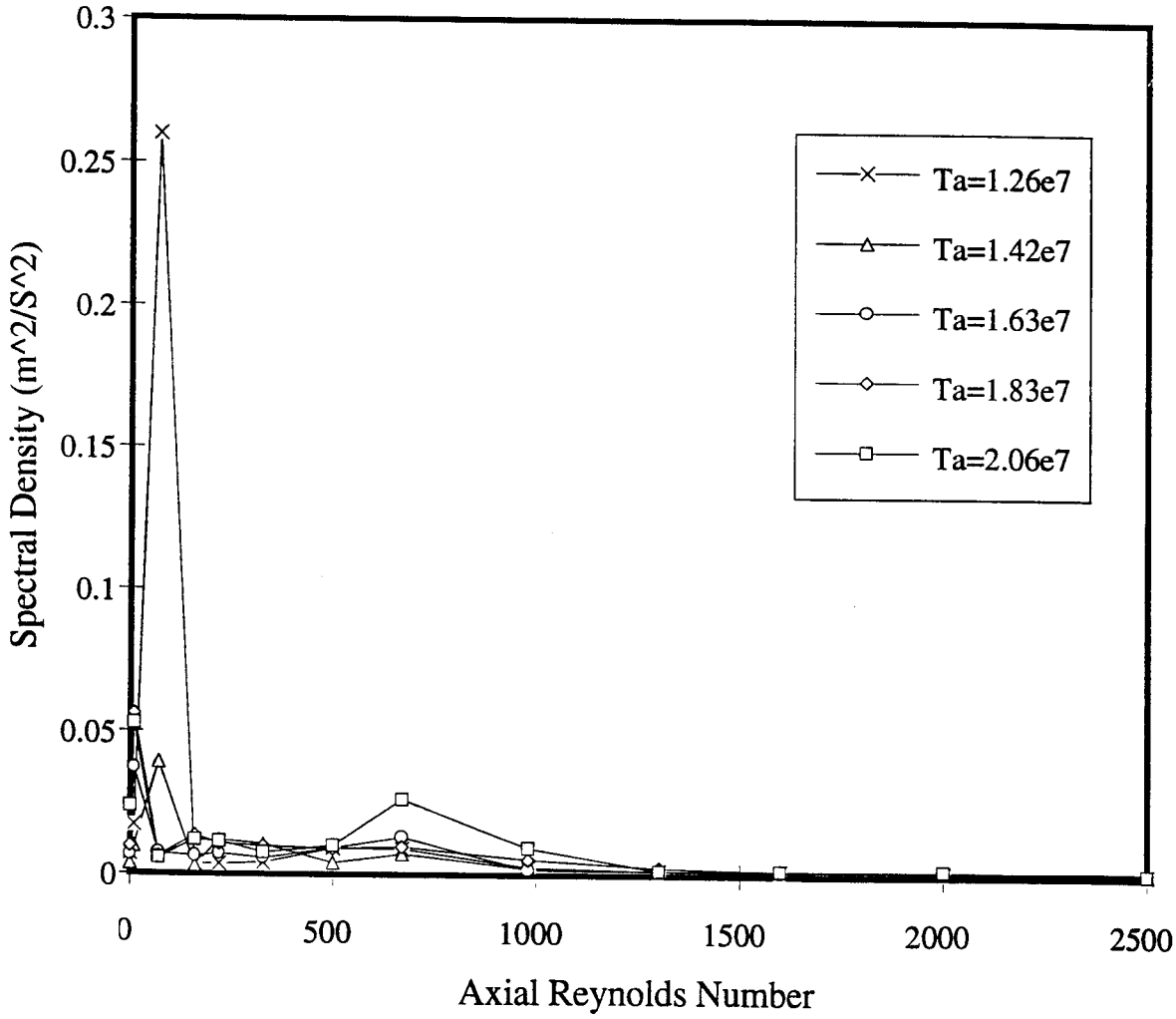

Figure 3.31 Strength of the maximum peak of the velocity spectrum vs. axial Reynolds number at l/b = 20 for different Taylor numbers ranging from Ta = 1.26 x 10^7 to 2.06 x 10^7.

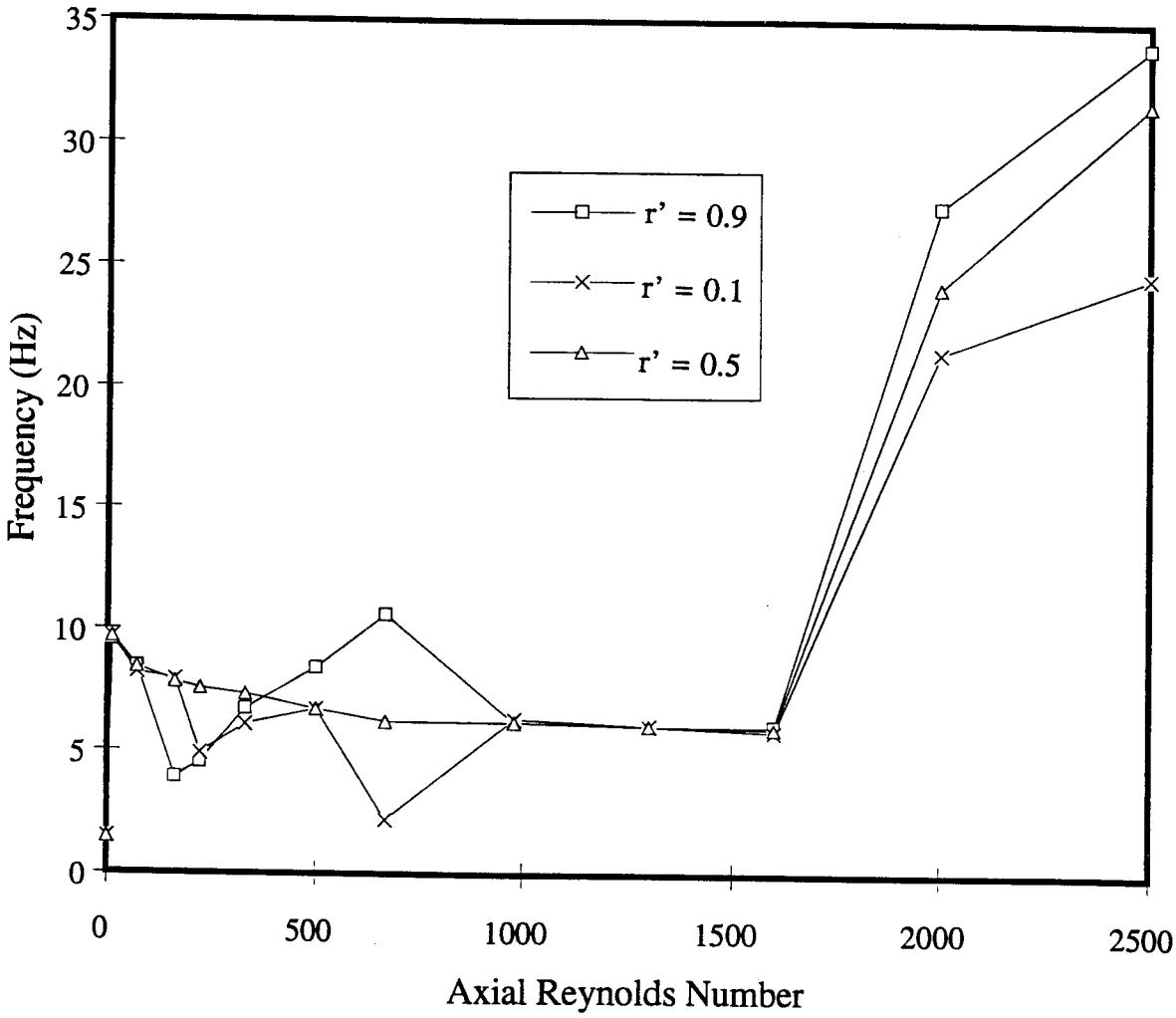

Figure 3.32 Frequency with the greatest power vs. axial Reynolds number at l/b = 20 and various gap locations, Ta = 1.6×10^7.

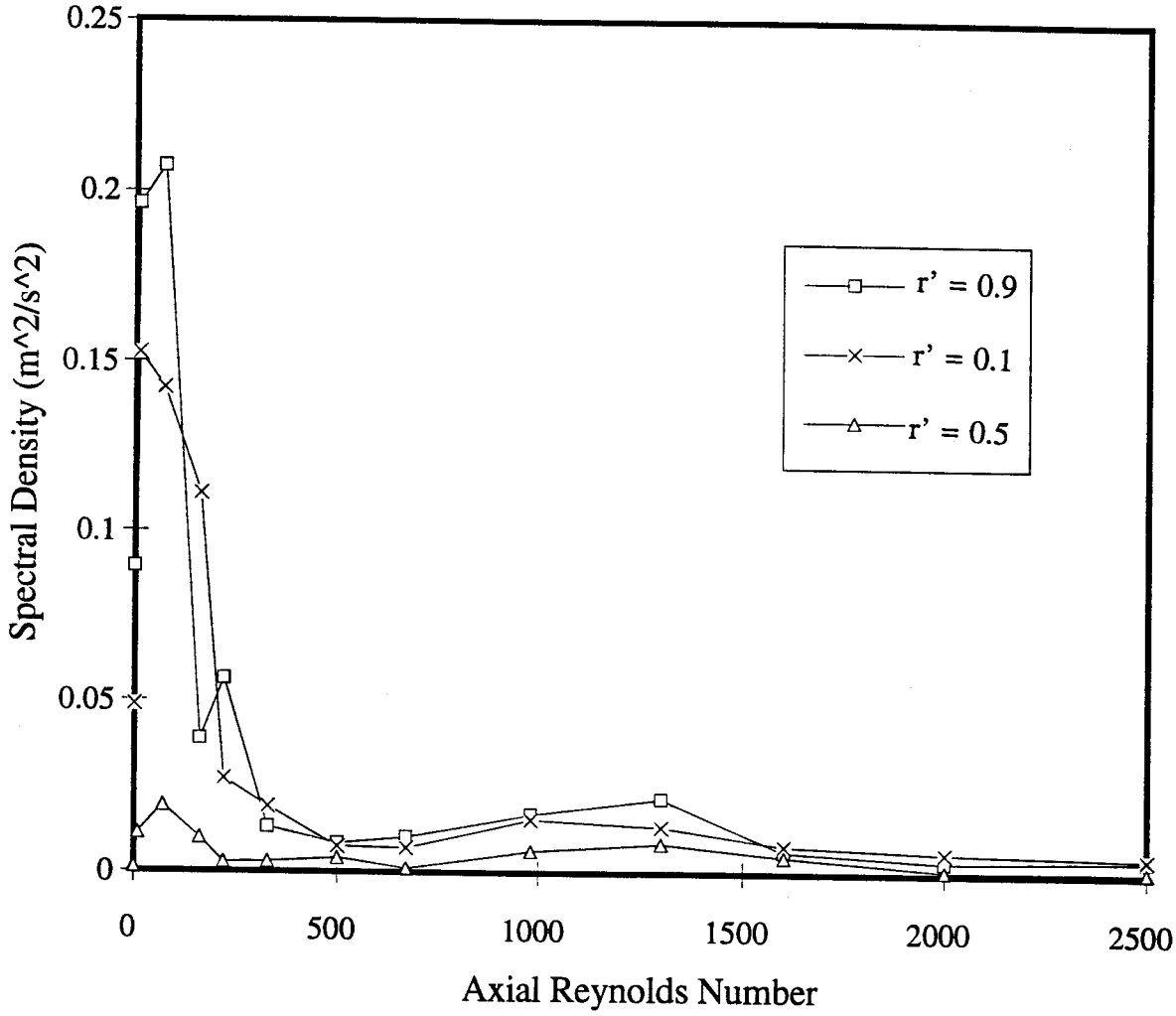

Figure 3.33 Strength of the maximum peak of the velocity spectrum vs. axial Reynolds number at l/b = 20 and various gap locations, Ta = 1.6 x 10^7.

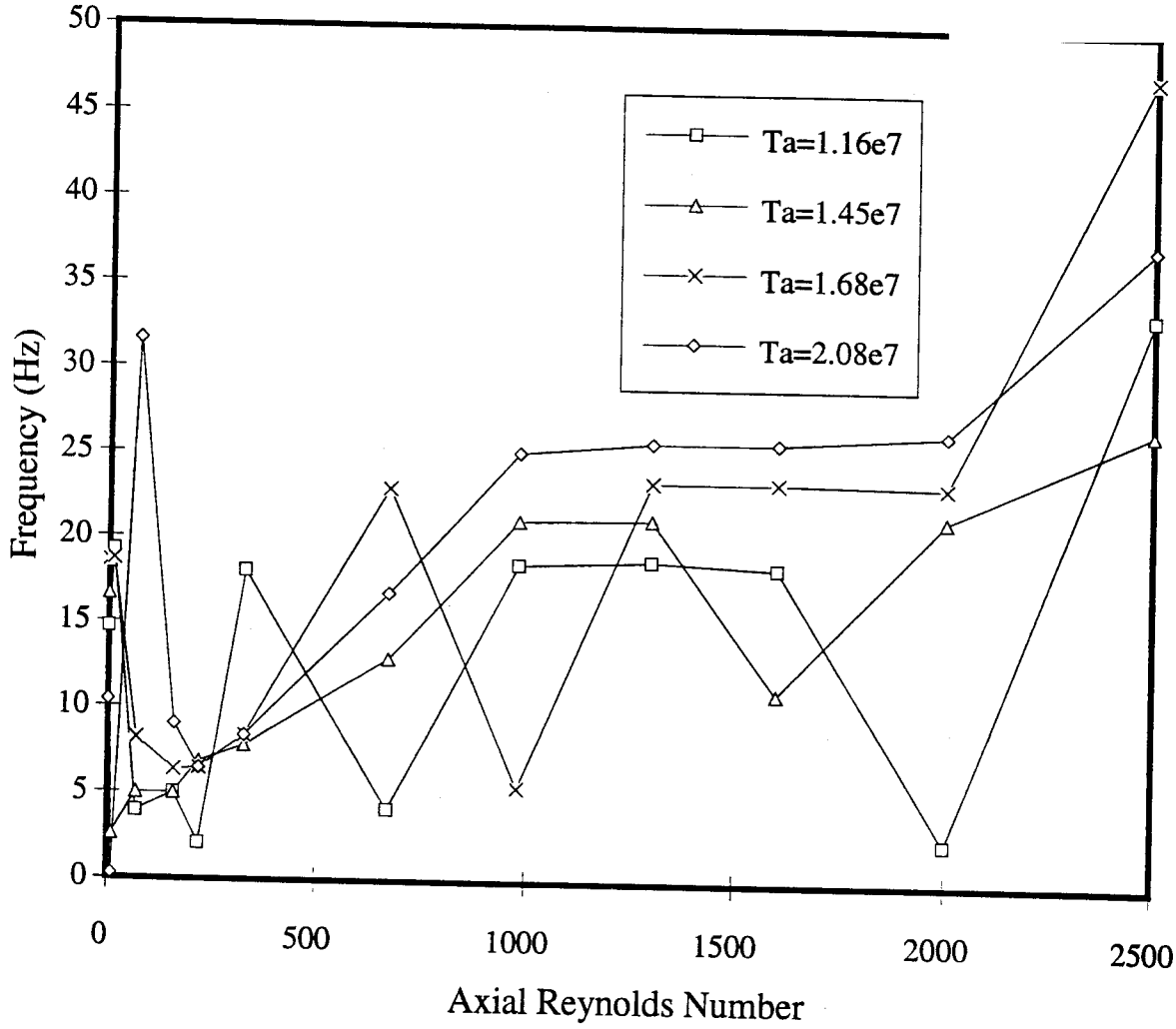

Figure 3.34 Frequency with the greatest power vs. axial Reynolds number at l/b = 37 for different Taylor numbers.

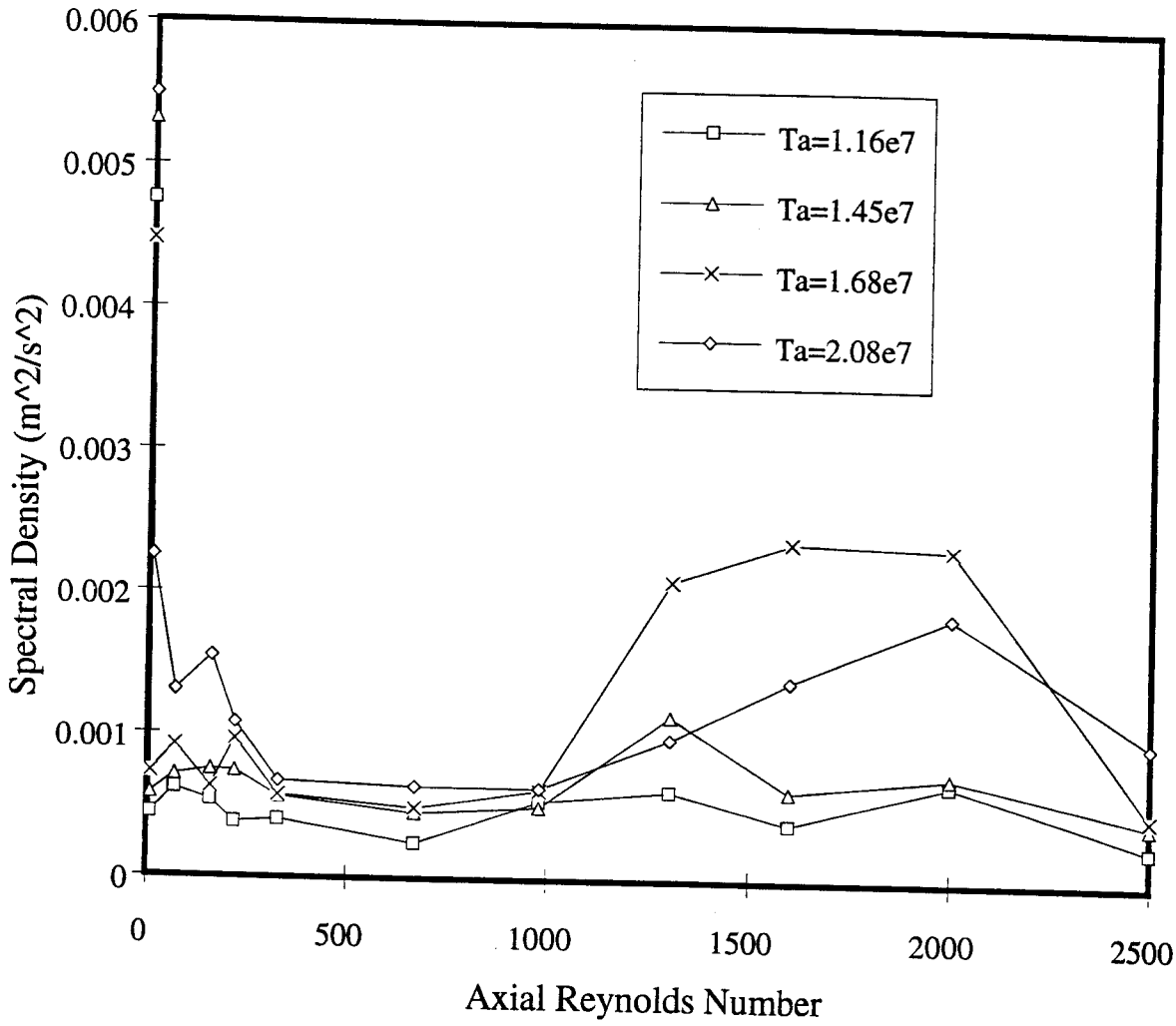

Figure 3.35 Strength of the maximum peak of the velocity spectrum vs. axial Reynolds number at l/b = 37 for different Taylor numbers.

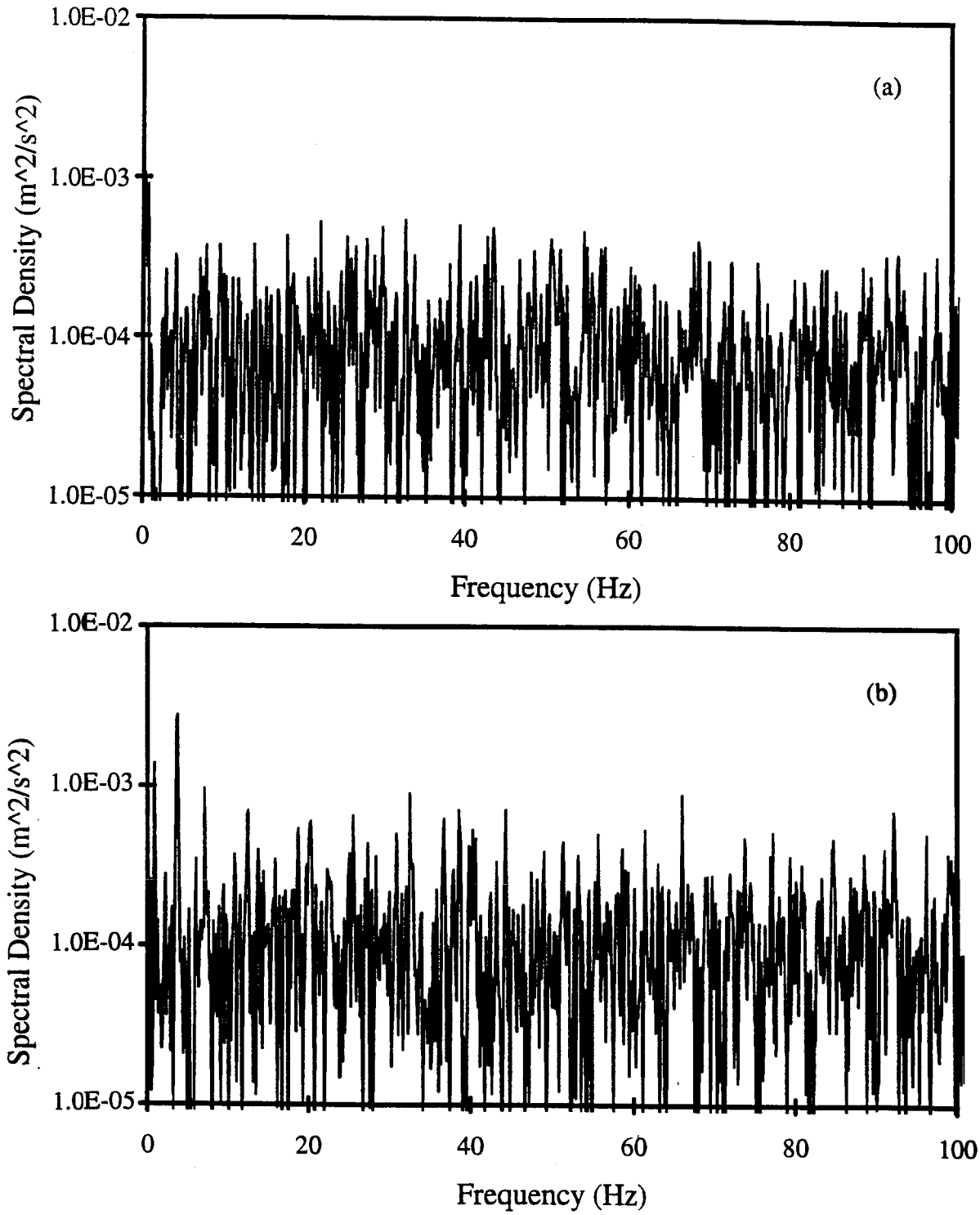

Figure 4.1 Power spectra of the tangential velocity component with Ta = 1.48 x 10^7 and Gr_a = 2600, at l/b = 20 and at various axial Reynolds numbers: (a) Re_a = 0 (b) Re_a = 10 (c) Re_a = 670 (d) Re_a = 1300.

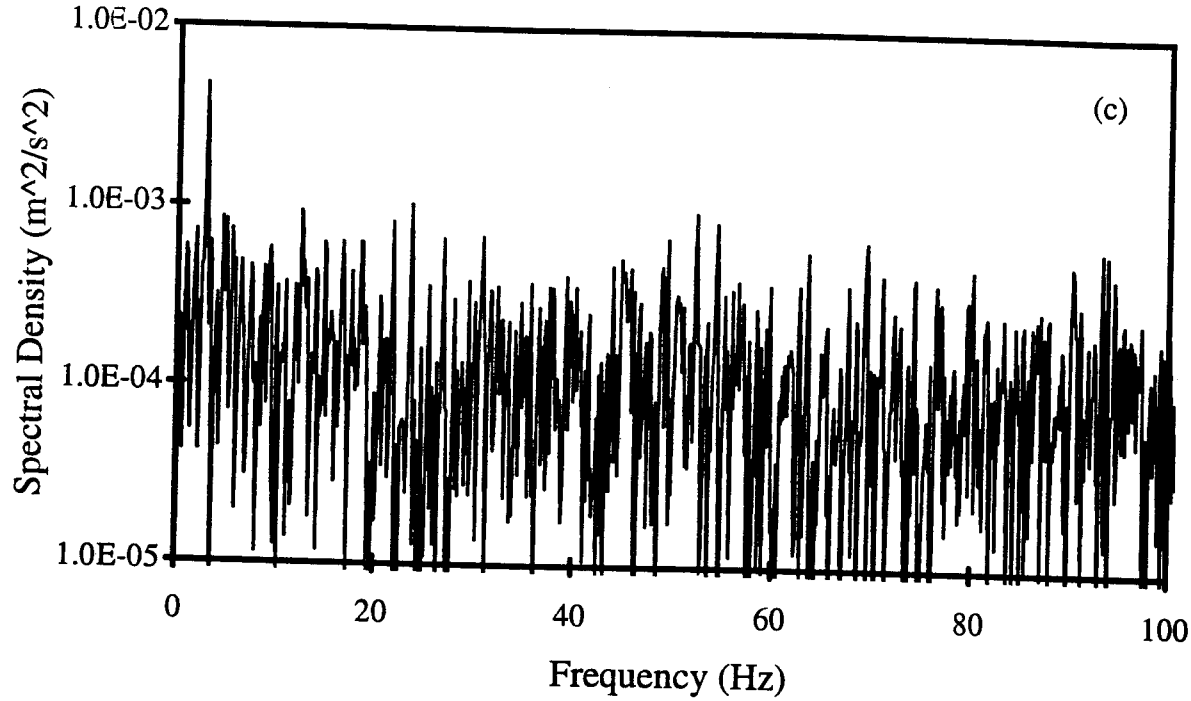
1.0E-02
1.0E-03
1.0E-04
1.0E-05
Spectral Density (m^2/s^2)
(c)
0
20
40
60
80
100
Frequency (Hz)

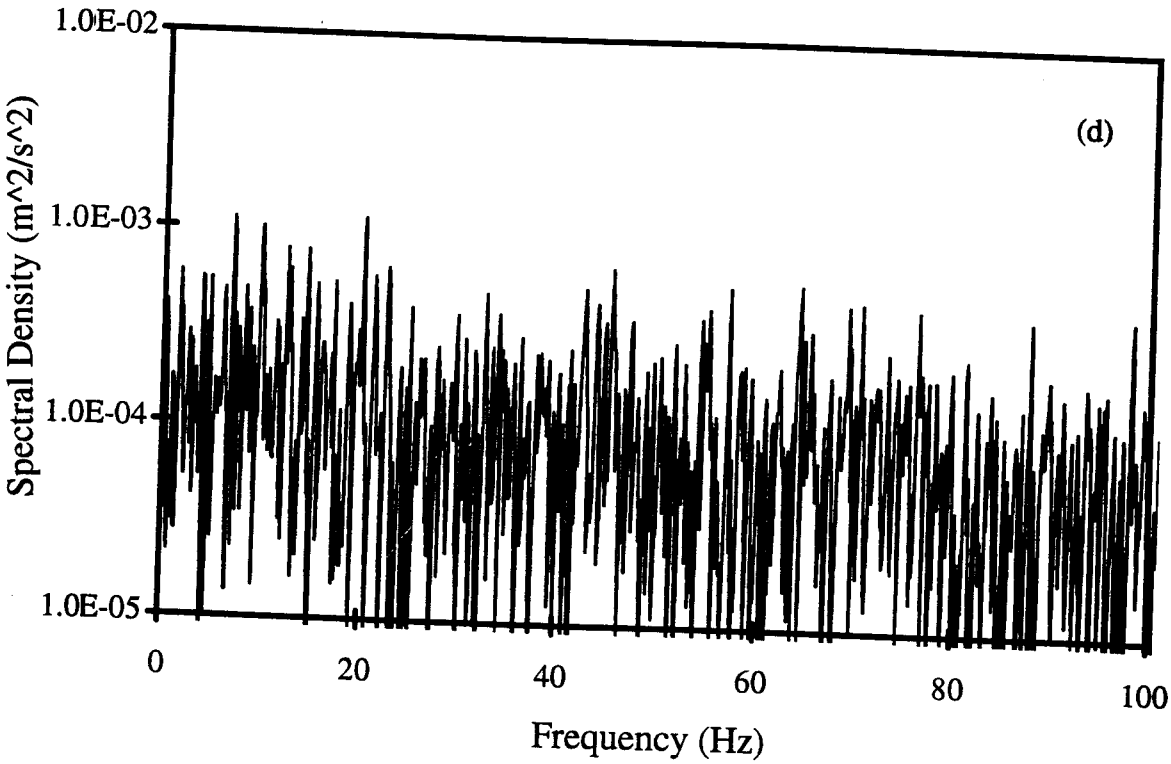
1.0E-02
1.0E-03
1.0E-04
1.0E-05
Spectral Density (m^2/s^2)
(d)
0
20
40
60
80
100
Frequency (Hz)

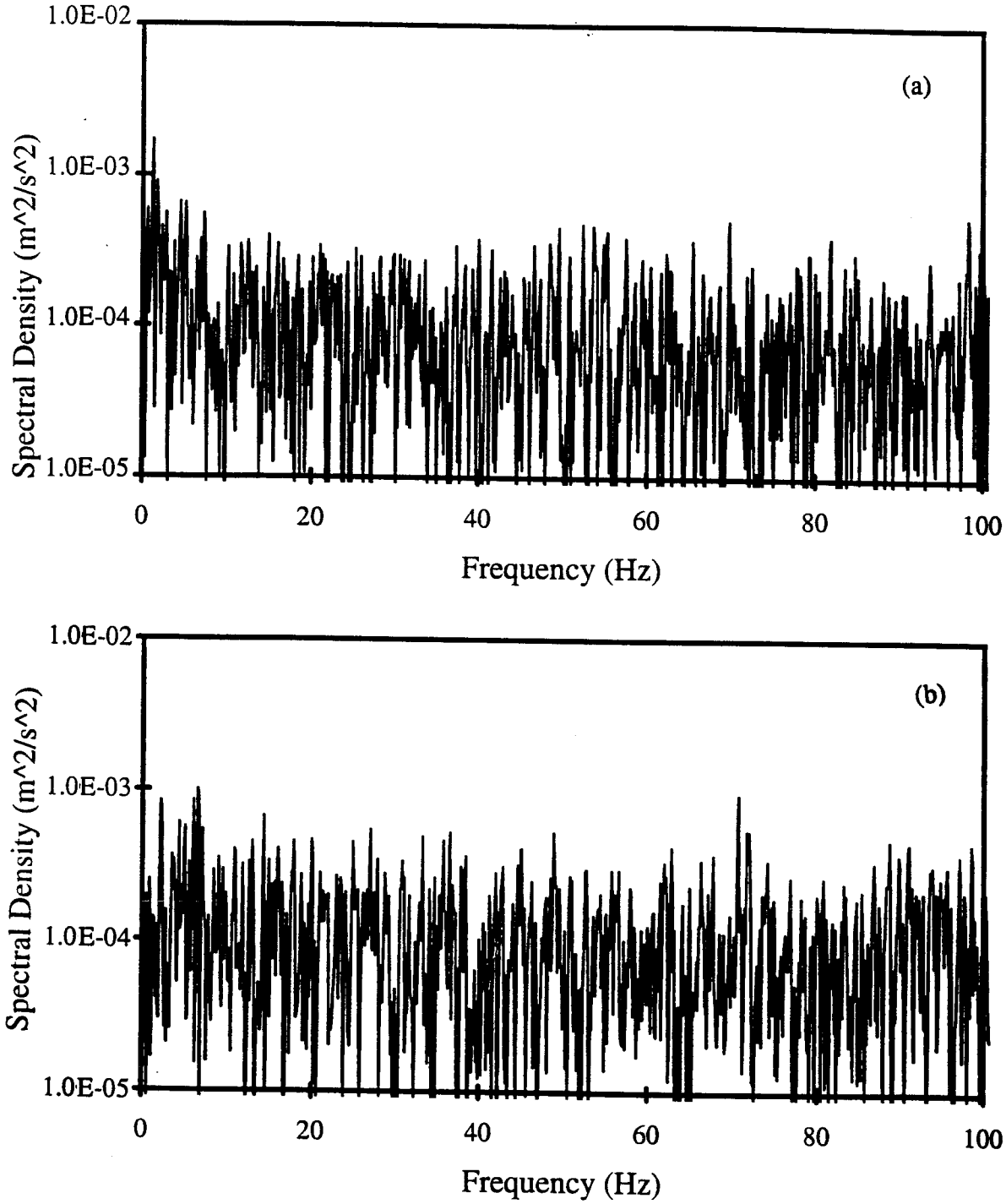

Figure 4.2 Power spectra of the tangential velocity component with Ta = 1.48 x 10^7 and Gr_a = 4800, at l/b = 20 and at various axial Reynolds numbers: (a) Re_a = 0 (b) Re_a = 10 (c) Re_a = 670 (d) Re_a = 1300.

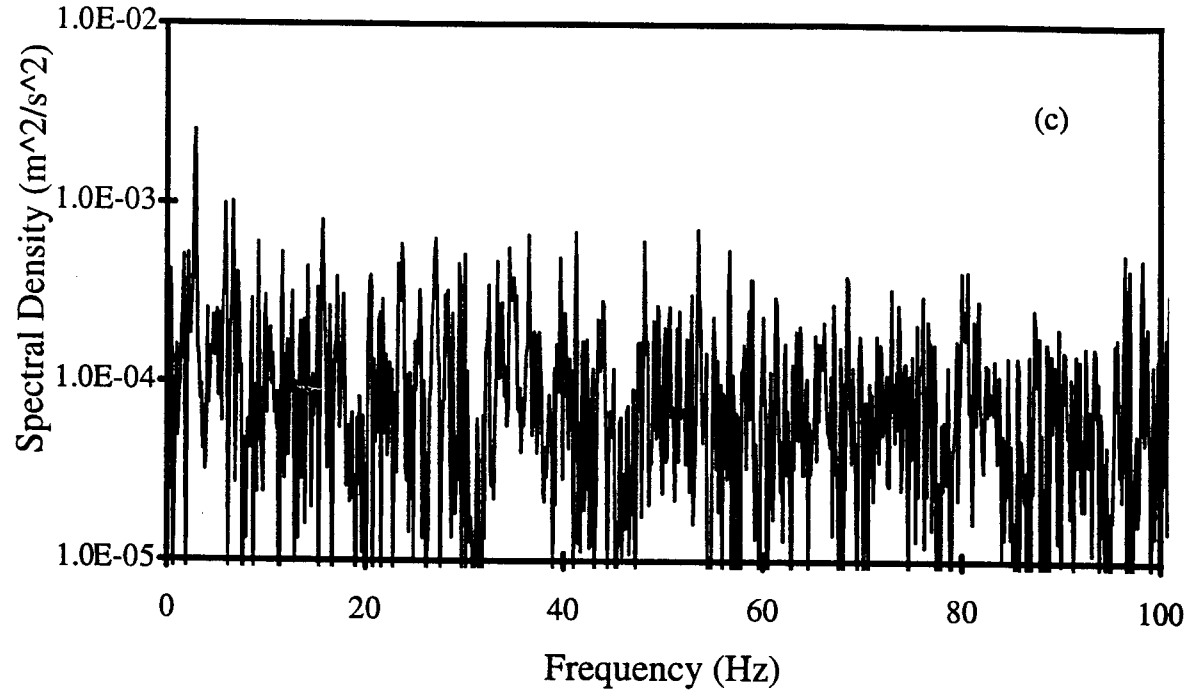
1.0E-02
1.0E-03
1.0E-04
1.0E-05
Spectral Density (m^2/s^2)
(c)
0
20
40
60
80
100
Frequency (Hz)

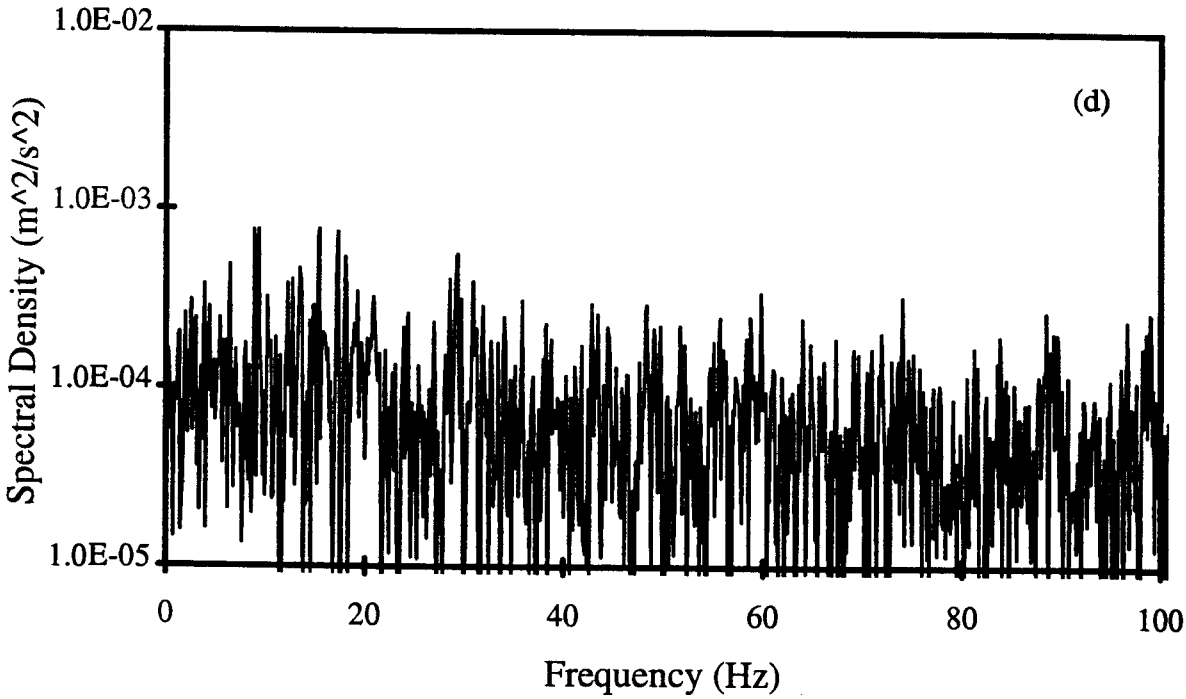
1.0E-02
1.0E-03
1.0E-04
1.0E-05
Spectral Density (m^2/s^2)
(d)
0
20
40
60
80
100
Frequency (Hz)

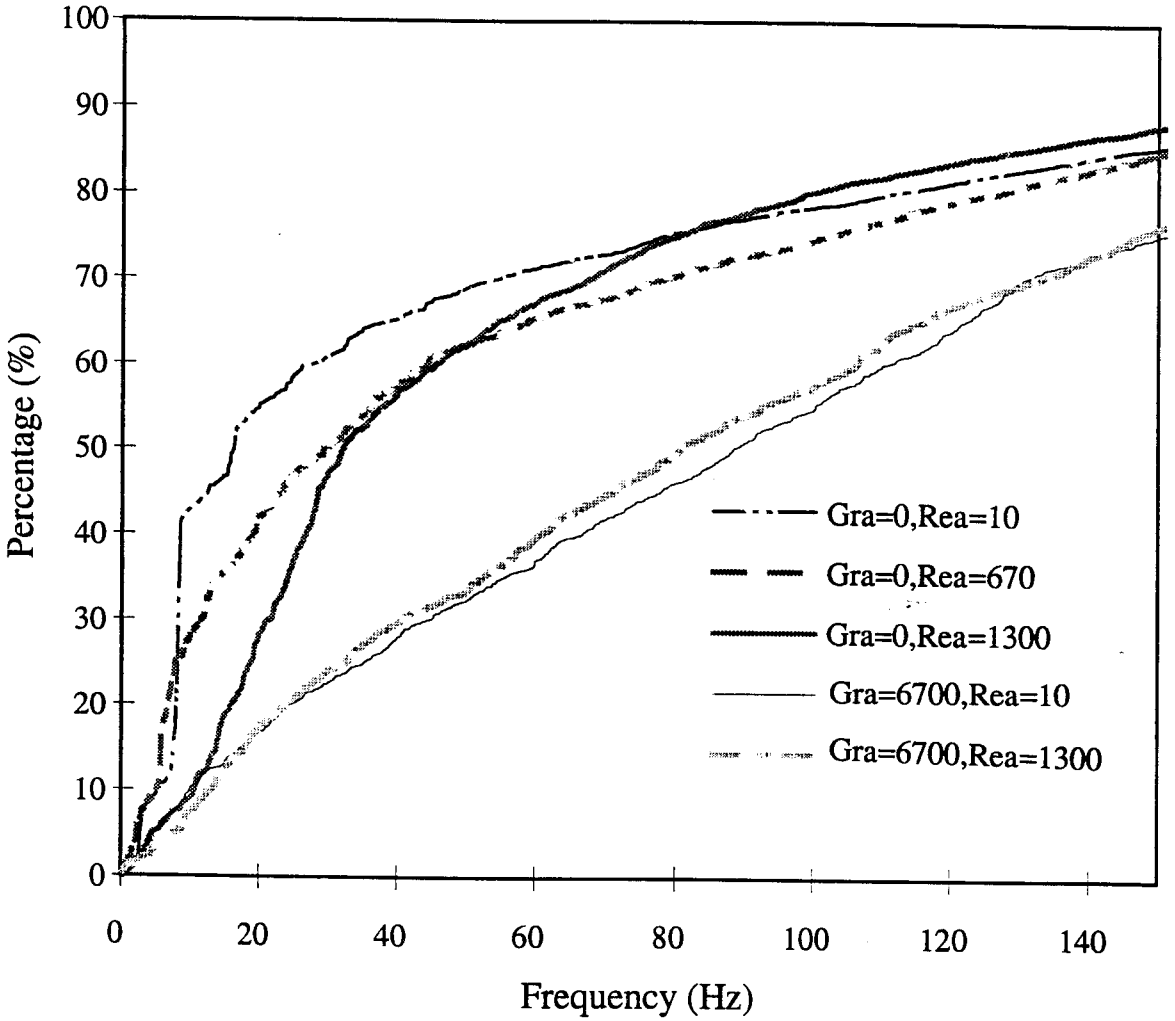

Figure 4.3 Percentage of the accumulative energy contribution as a function of frequency and different axial Reynolds numbers with different Grashof numbers, at l/b = 20.

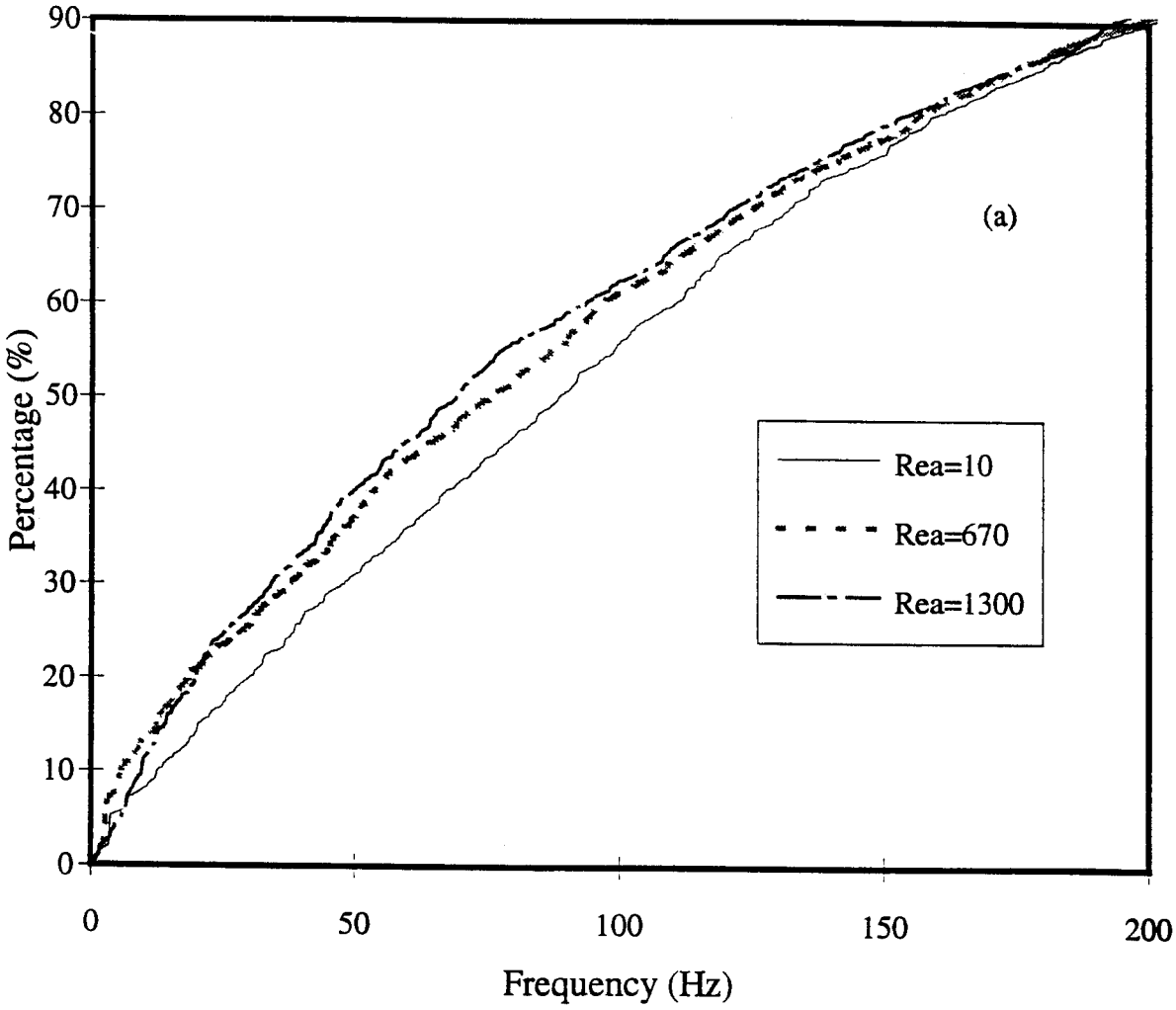

Figure 4.4 Percentage of the accumulative energy contribution as a function of frequency and axial Reynolds number, with various Grashof numbers at l/b = 20: (a) Gr_a = 2600 (b) Gr_a = 4800 (c) Gr_a = 6700.

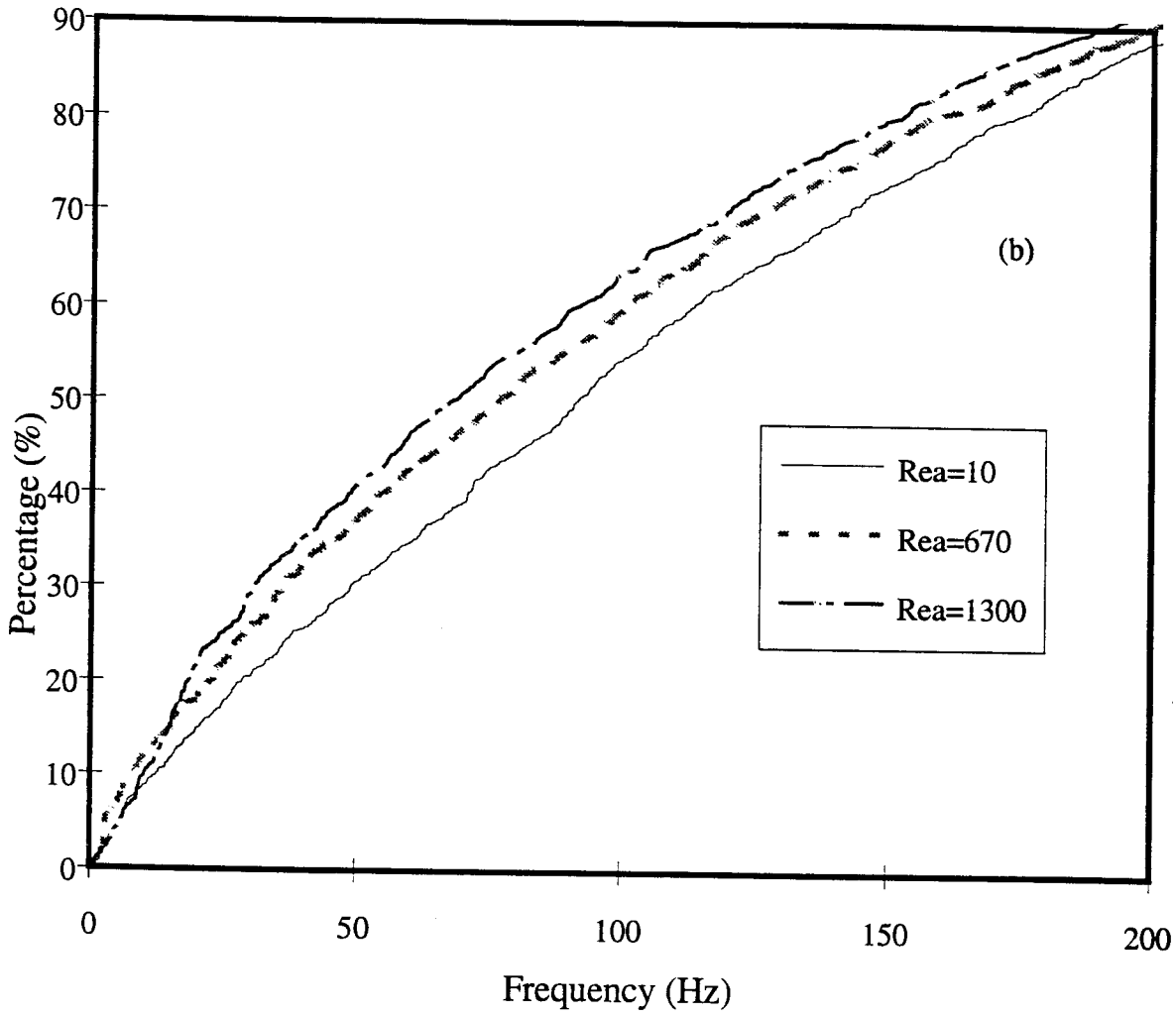
90
80
70
60
50
40
30
20
10
0
Percentage (%)
0
50
100
150
200
Frequency (Hz)
(b)
Rea=10
Rea=670
Rea=1300

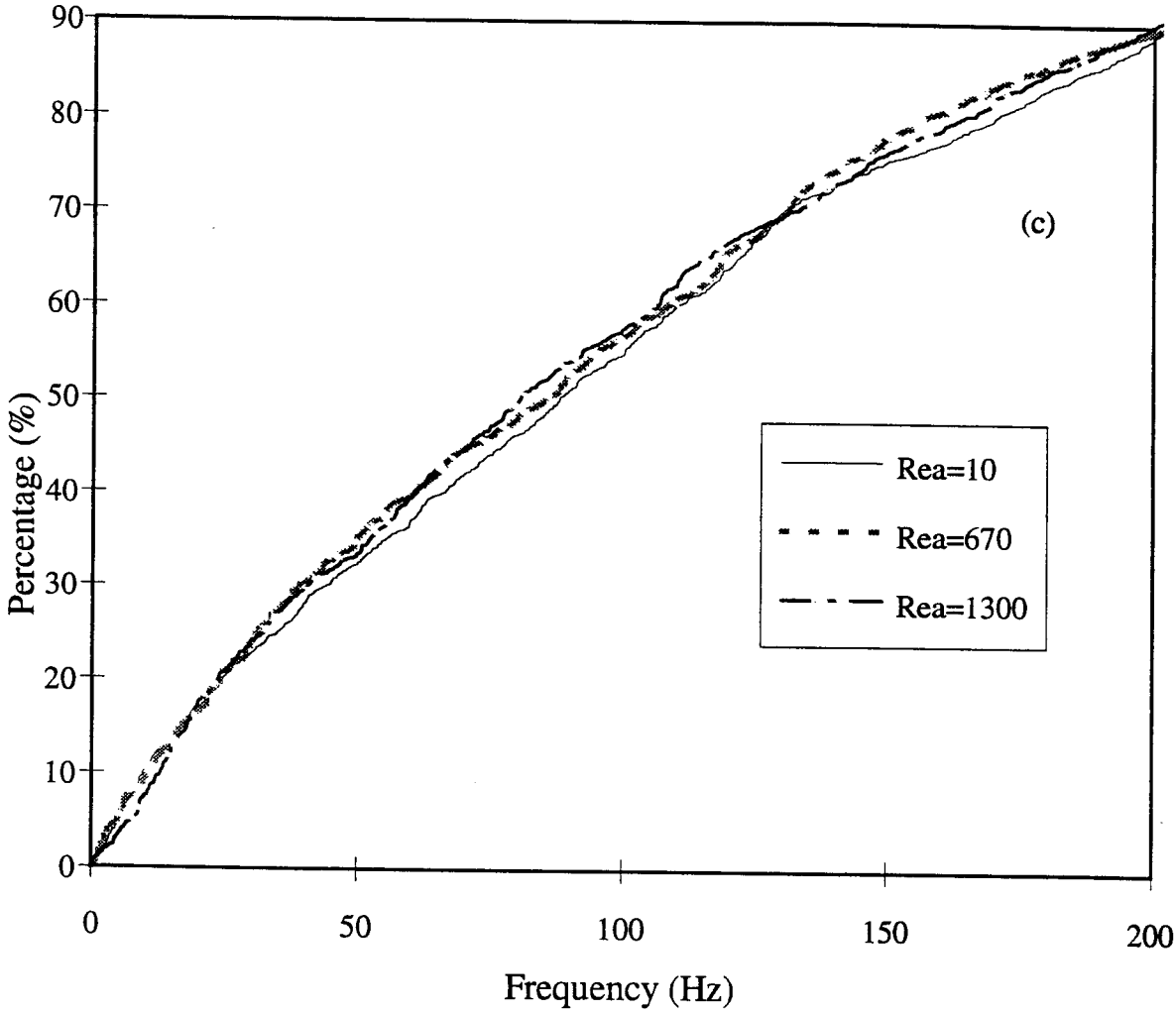
90
80
70
60
50
40
30
20
10
0
Percentage (%)
0
50
100
150
200
Frequency (Hz)
(c)
Rea=10
Rea=670
Rea=1300

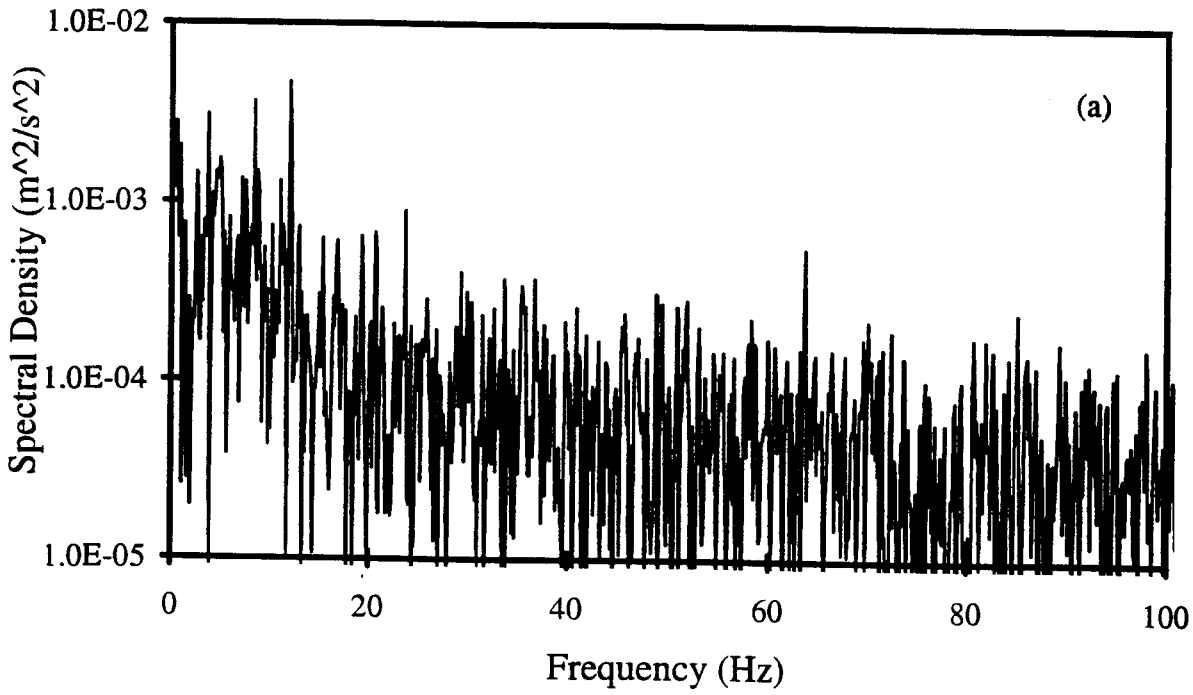

Figure 4.5 Power spectra of the tangential velocity component with Ta = 1.48 x 10^7 and Gr_a = 2600, at l/b = 37 and at various axial Reynolds numbers: (a) Re_a = 0 (b) Re_a = 10 (c) Re_a = 670 (d) Re_a = 1300 (e) Re_a = 2000.

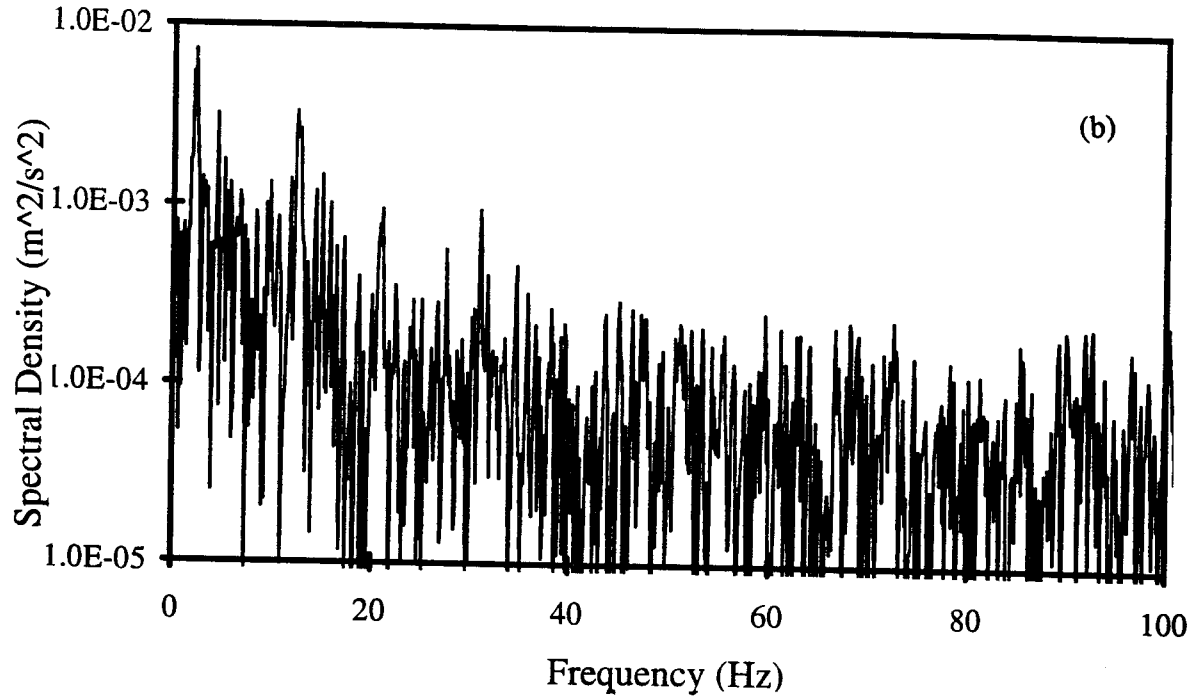
1.0E-02
1.0E-03
1.0E-04
1.0E-05
Spectral Density (m^2/s^2)
(b)
0
20
40
60
80
100
Frequency (Hz)

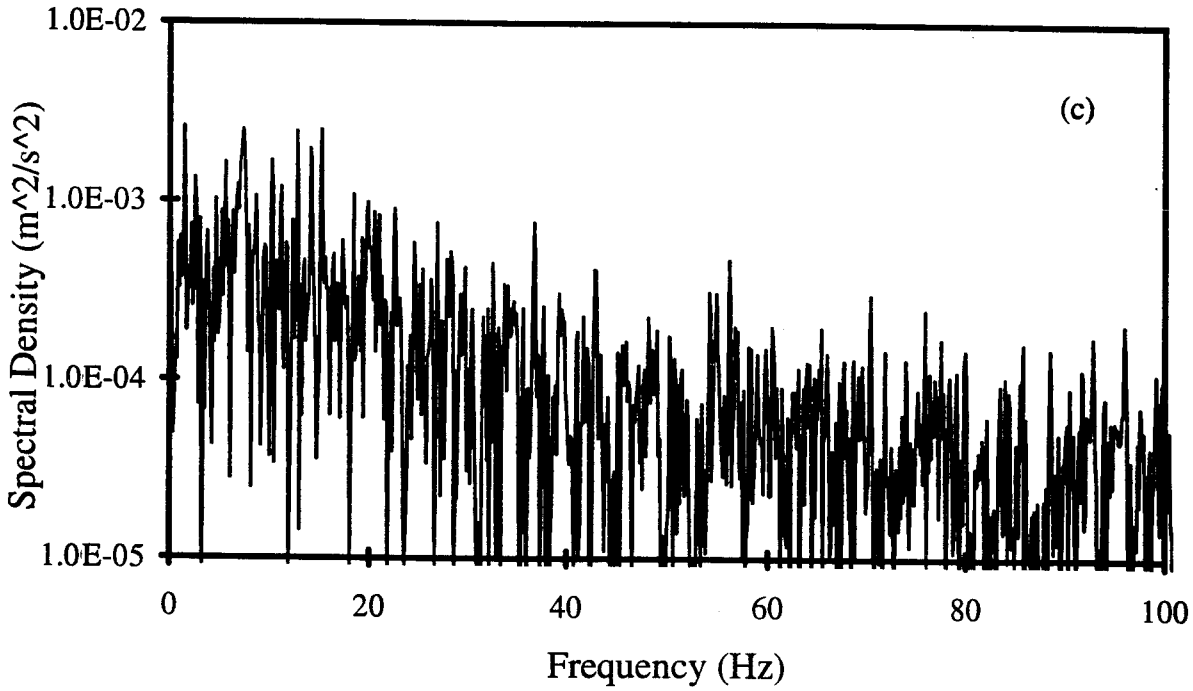
1.0E-02
1.0E-03
1.0E-04
1.0E-05
Spectral Density (m^2/s^2)
(c)
0
20
40
60
80
100
Frequency (Hz)

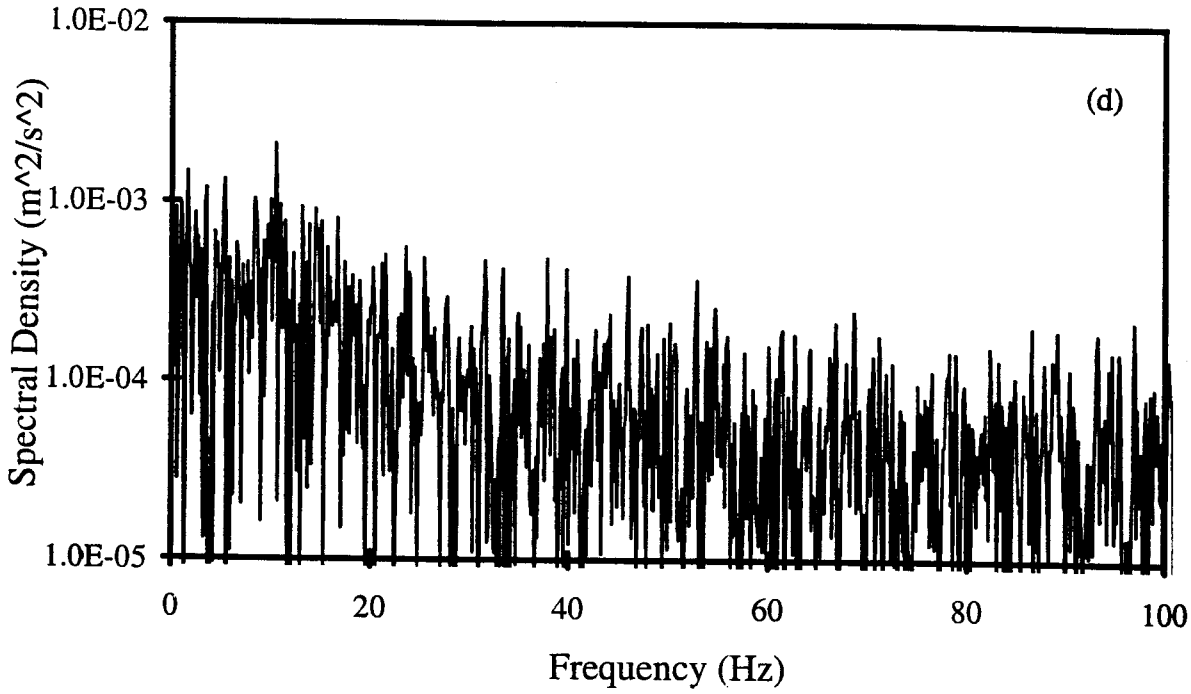
1.0E-02
1.0E-03
1.0E-04
1.0E-05
Spectral Density (m^2/s^2)
(d)
0
20
40
60
80
100
Frequency (Hz)

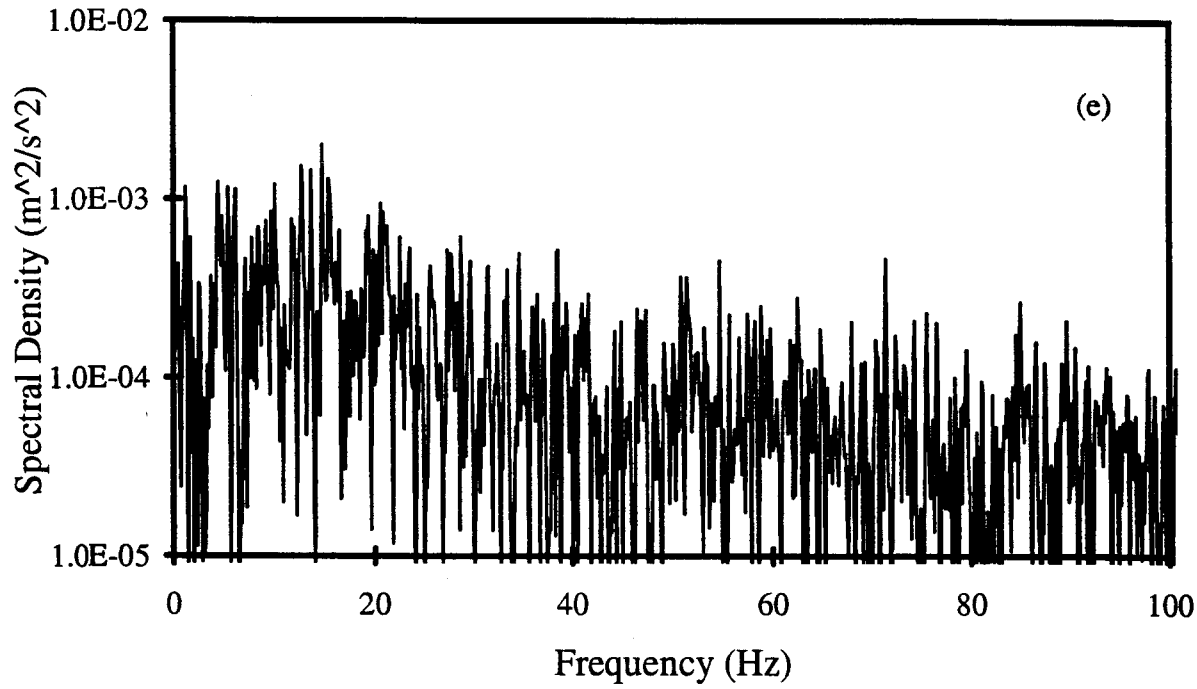
1.0E-02
1.0E-03
1.0E-04
1.0E-05
Spectral Density (m^2/s^2)
(e)
0
20
40
60
80
100
Frequency (Hz)

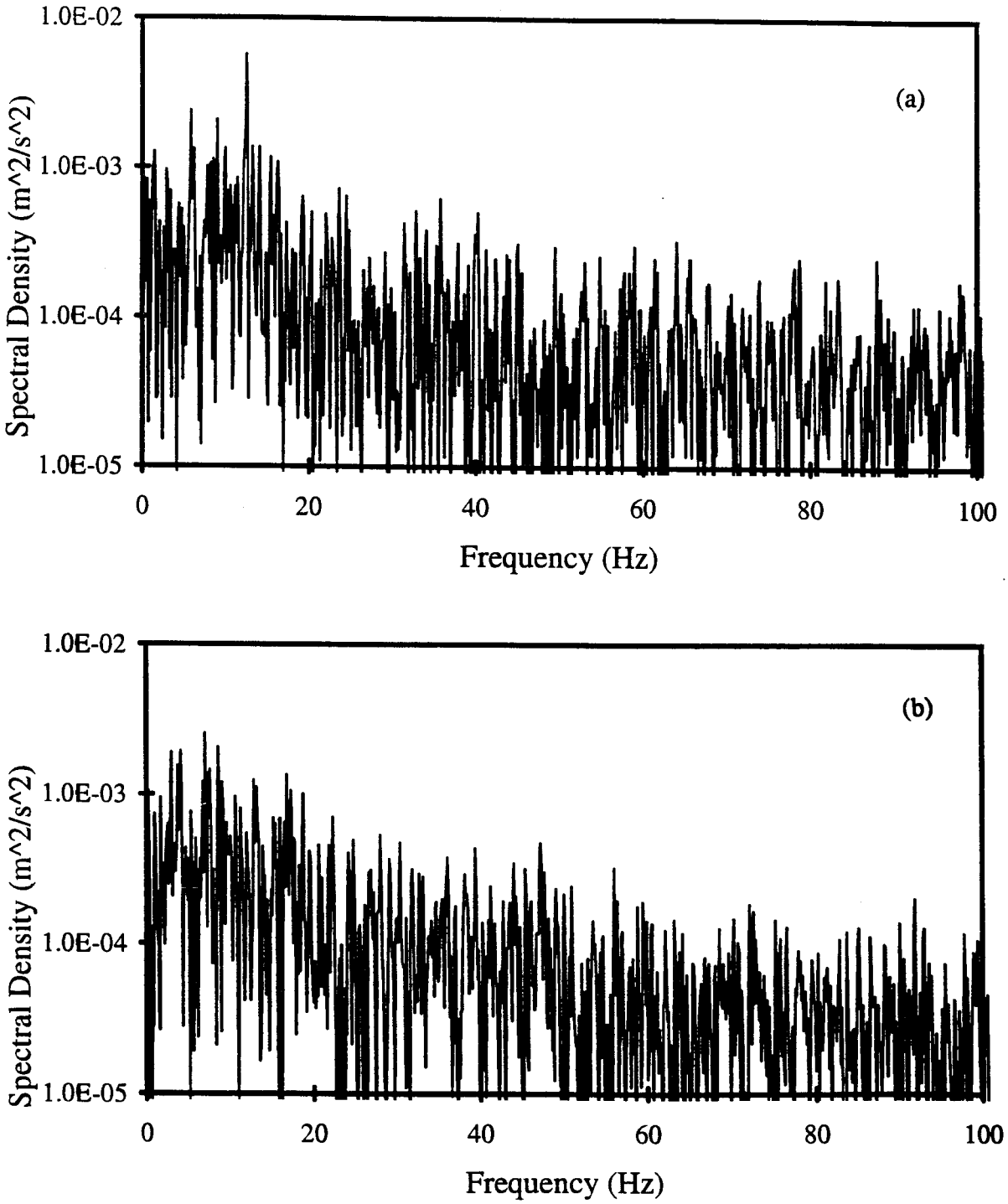

Figure 4.6 Power spectra of the tangential velocity component with Ta = 1.48 x 10^7 and Gr_a = 6700, at l/b = 37 and at various axial Reynolds numbers: (a) Re_a = 0 (b) Re_a = 10 (c) Re_a = 670 (d) Re_a = 1300.

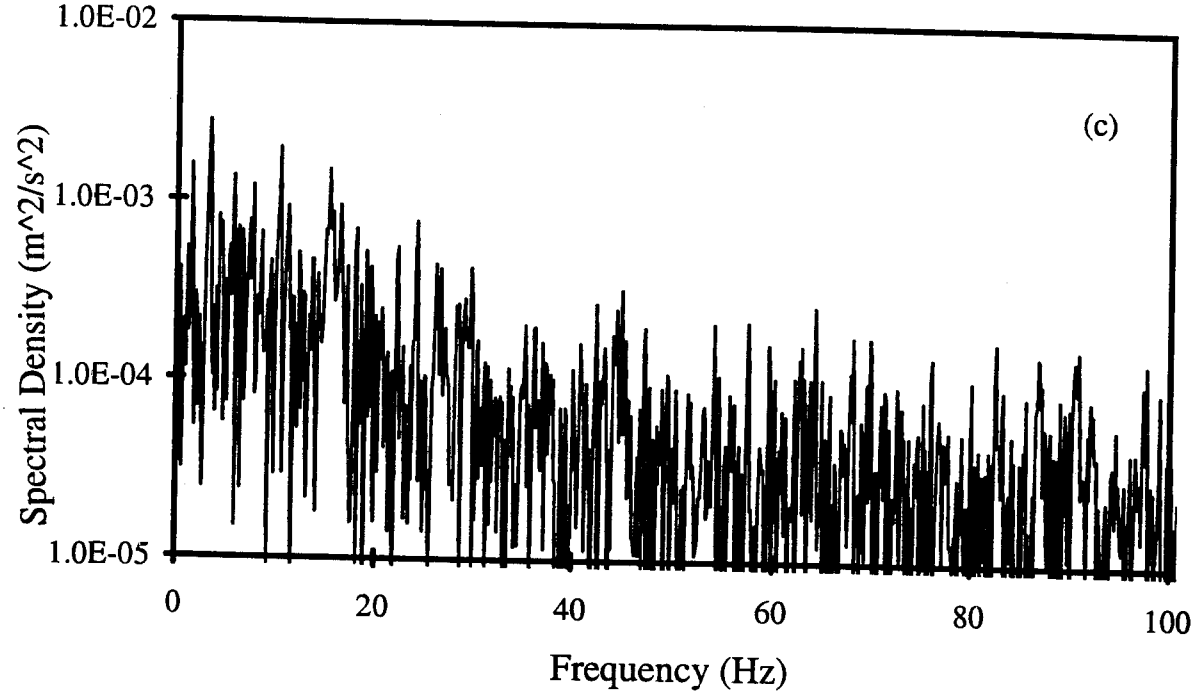
1.0E-02
1.0E-03
1.0E-04
1.0E-05
Spectral Density (m^2/s^2)
(c)
0
20
40
60
80
100
Frequency (Hz)

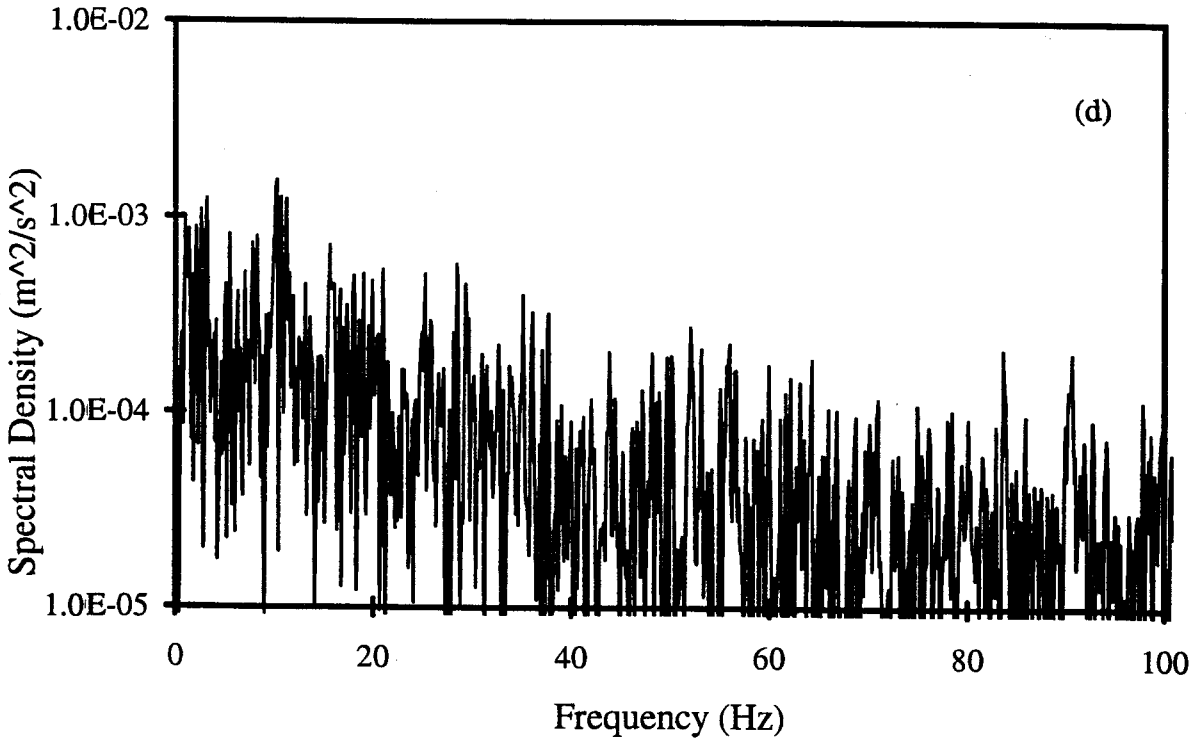
1.0E-02
1.0E-03
1.0E-04
1.0E-05
Spectral Density (m^2/s^2)
(d)
0
20
40
60
80
100
Frequency (Hz)

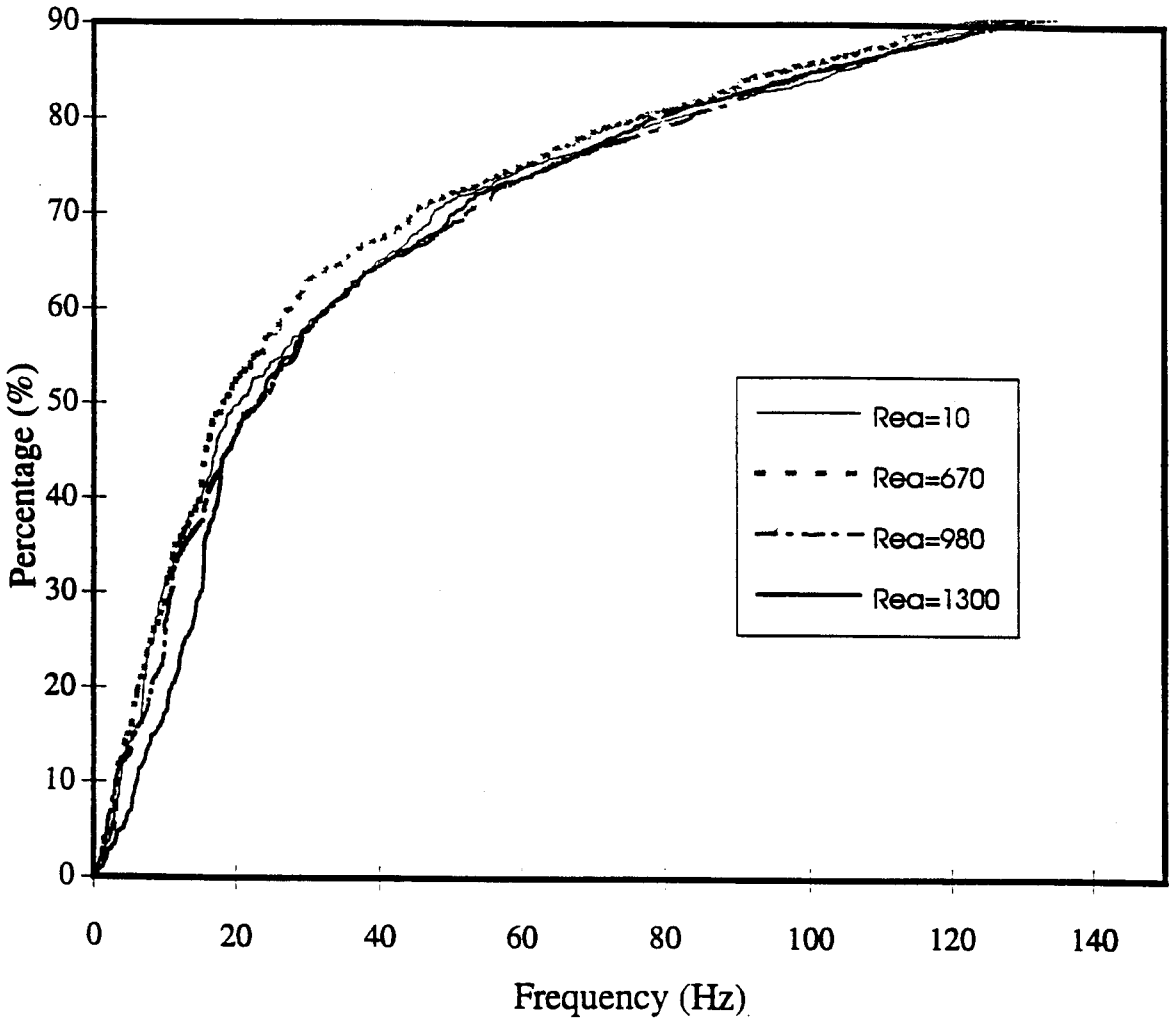

Figure 4.7 Percentage of the accumulative energy contribution as a function of frequency and axial Reynolds numbers with Gr_a = 6700, at l/b = 37.

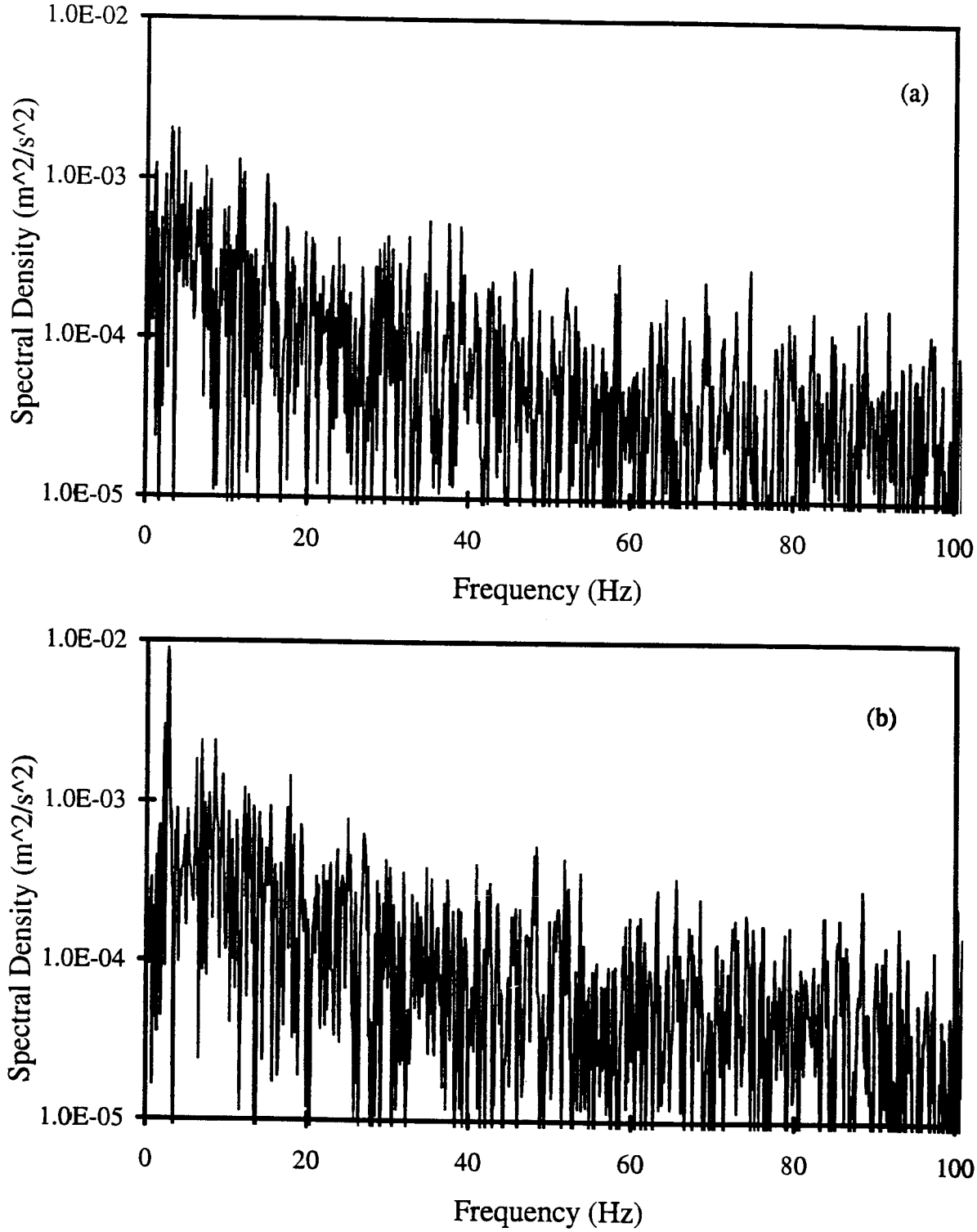

Figure 4.8 Power spectra of the tangential velocity component at l/b = 20 for Re_a = 10 and Gr_a = 3600 and different Taylor numbers: (a) Ta = 1.2 x 10^7 (b) Ta = 1.6 x 10^7 (c) Ta = 1.9 x 10^7 (d) Ta = 2.4 x 10^7.

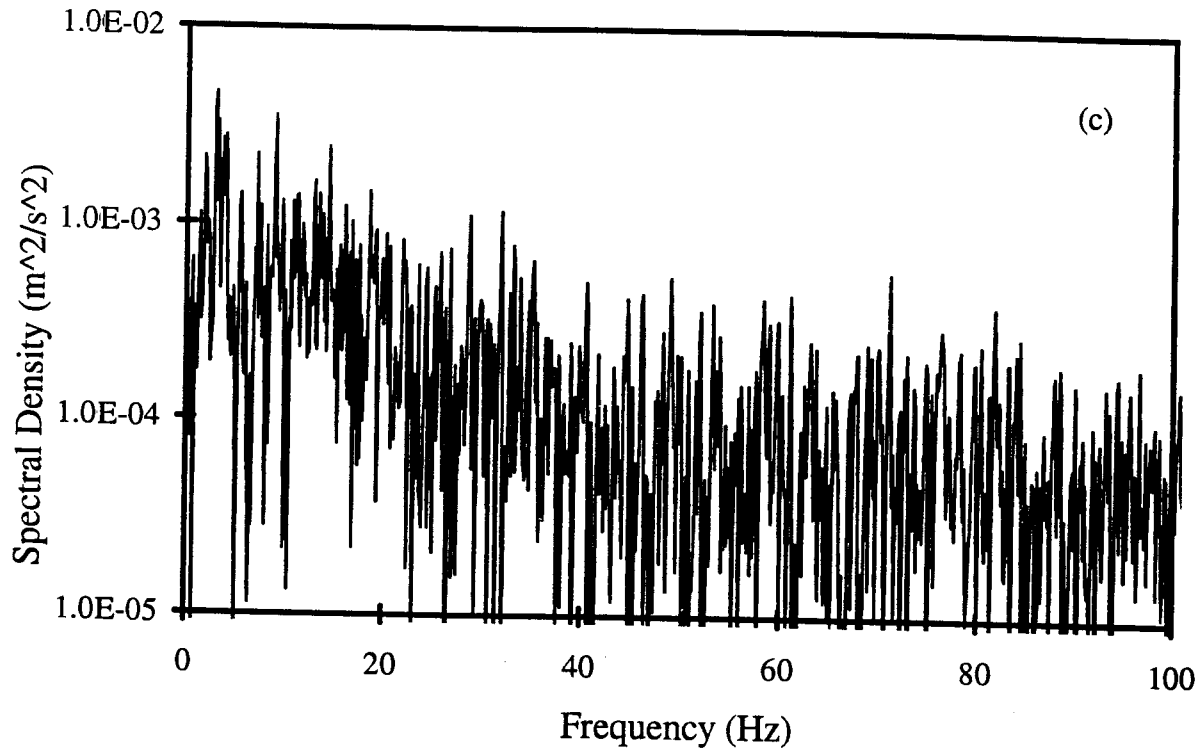
1.0E-02
1.0E-03
1.0E-04
1.0E-05
Spectral Density (m^2/s^2)
(c)
0
20
40
60
80
100
Frequency (Hz)

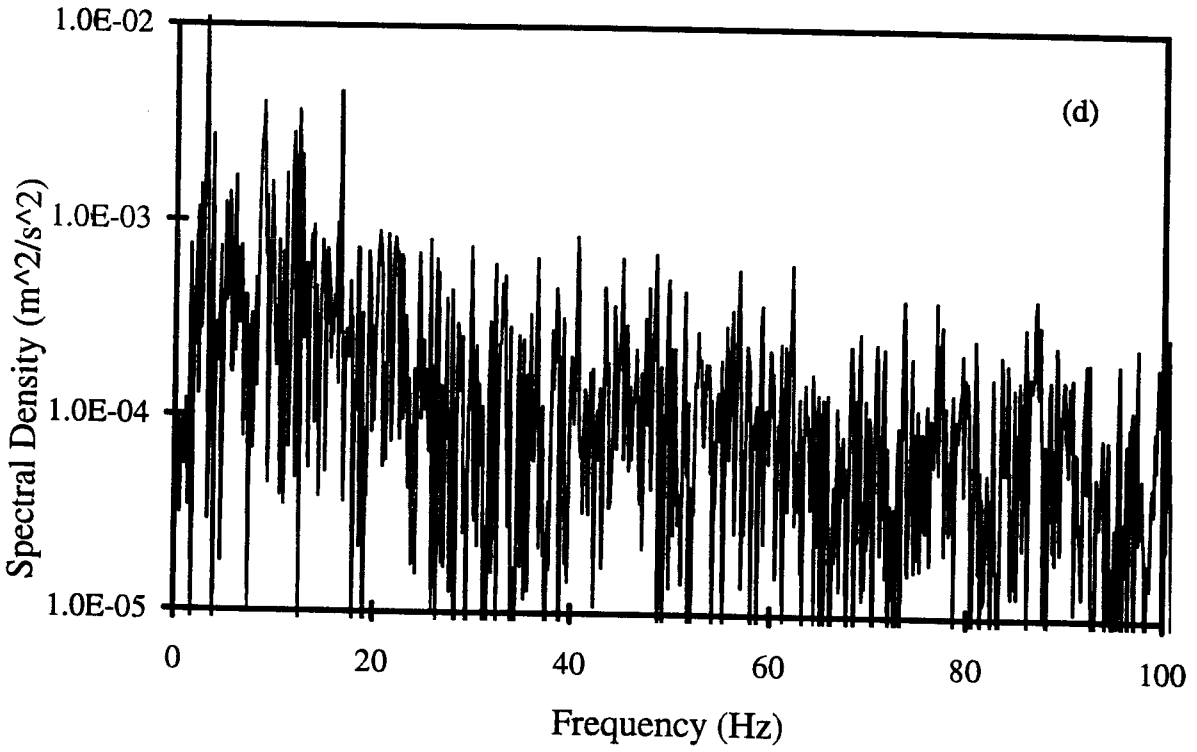
1.0E-02
1.0E-03
1.0E-04
1.0E-05
Spectral Density (m^2/s^2)
(d)
0
20
40
60
80
100
Frequency (Hz)

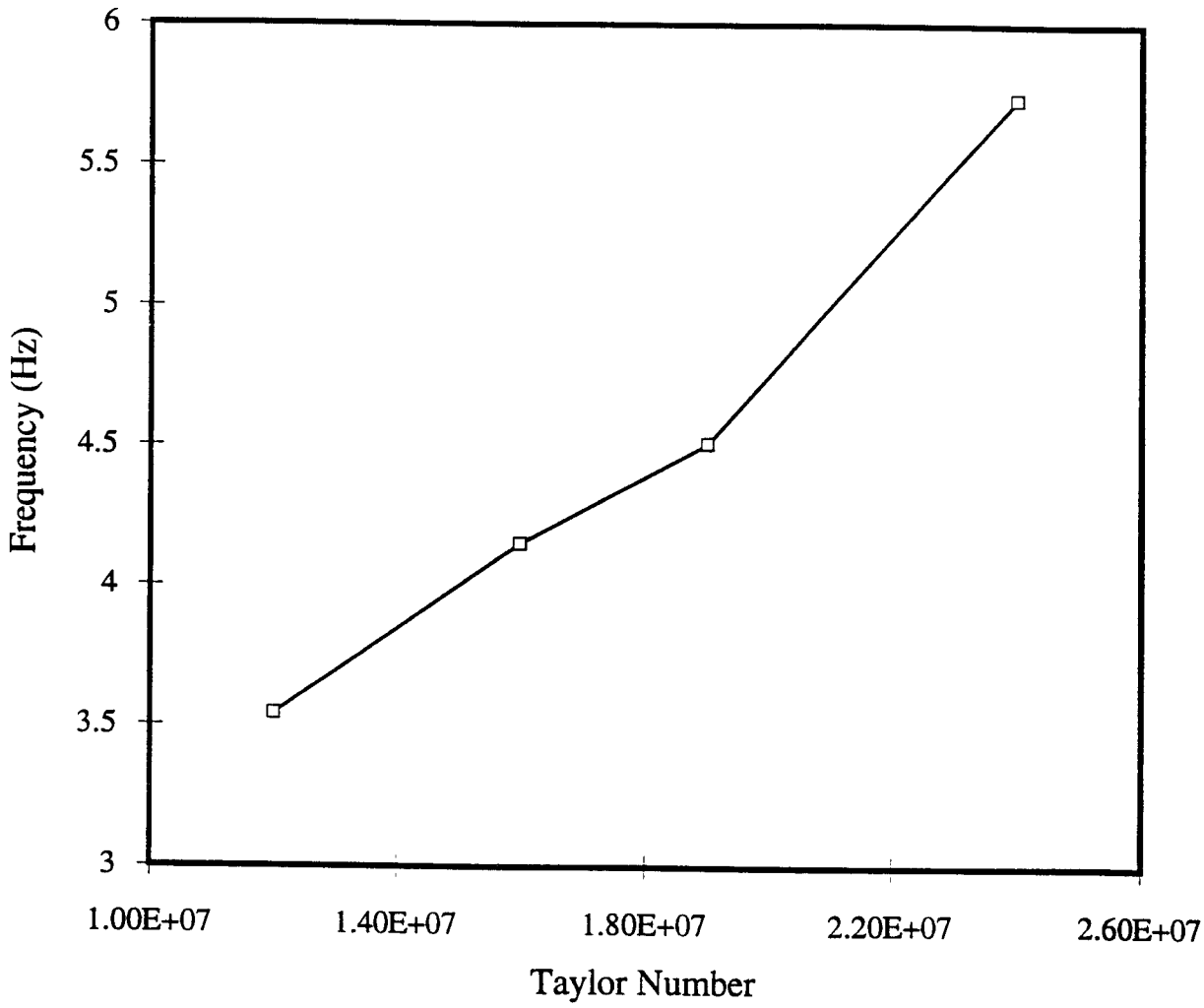

Figure 4.9 Frequency with the greatest power as a function of the Taylor number at l/b = 20 for Re_a = 10 and Gr_a = 3600.

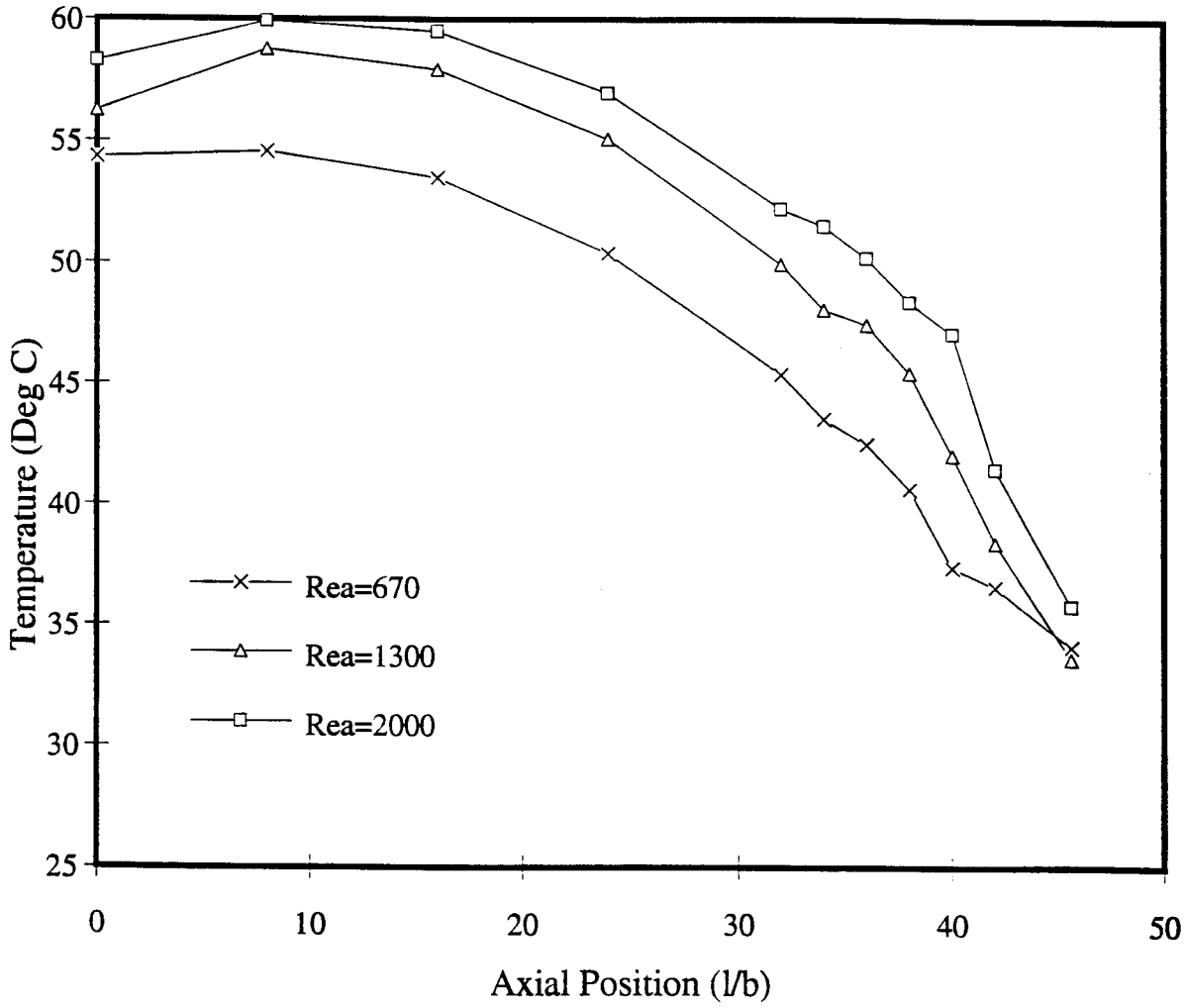

Figure 4.10 Axial temperature distribution for Gr_a = 6700 and various axial Reynolds numbers.

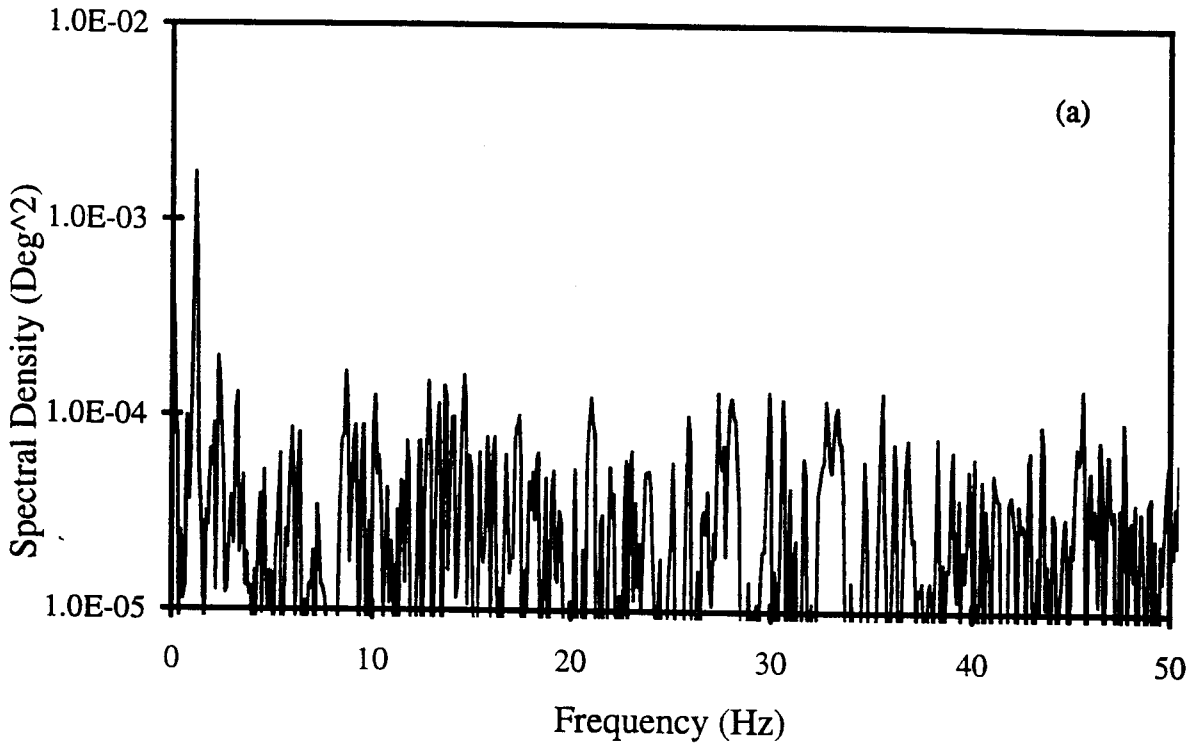

Figure 4.11 Power spectra of the temperature with Ta = 1.48 x 10^7 and Gr_a = 4800, at l/b = 20 and at various axial Reynolds numbers: (a) Re_a = 0 (b) Re_a = 10 (c) Re_a = 670 (d) Re_a = 1300 (e) Re_a = 2000.

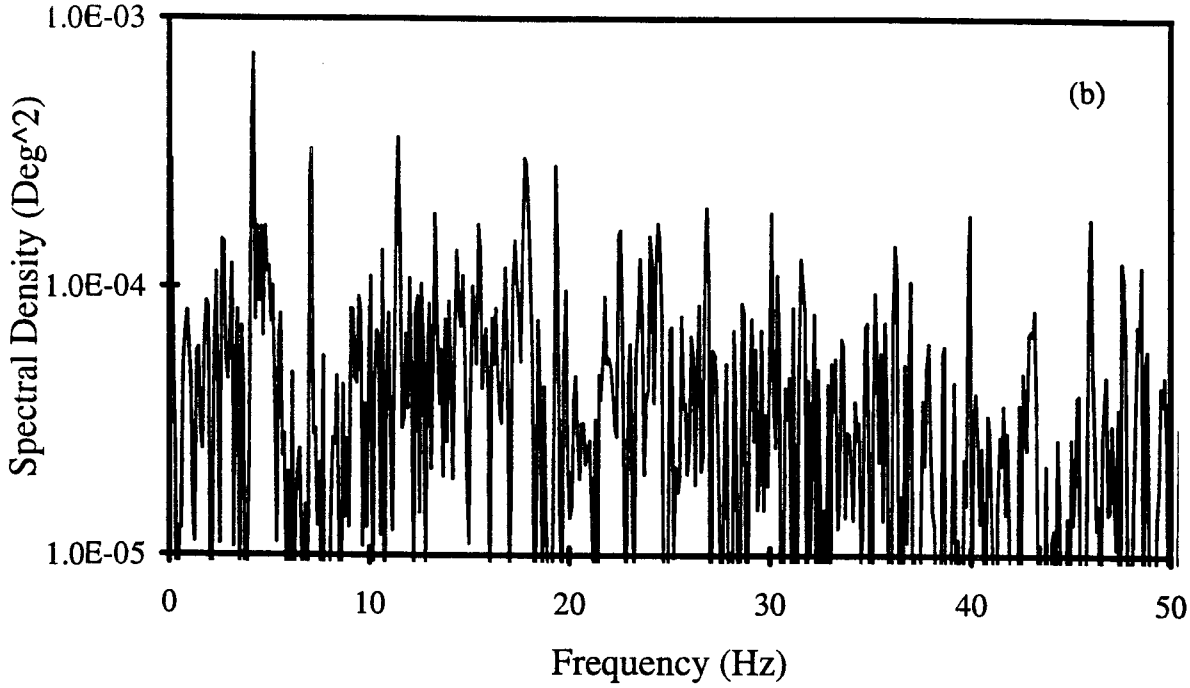
1.0E-03
1.0E-04
1.0E-05
Spectral Density (Deg^2)
(b)
0
10
20
30
40
50
Frequency (Hz)

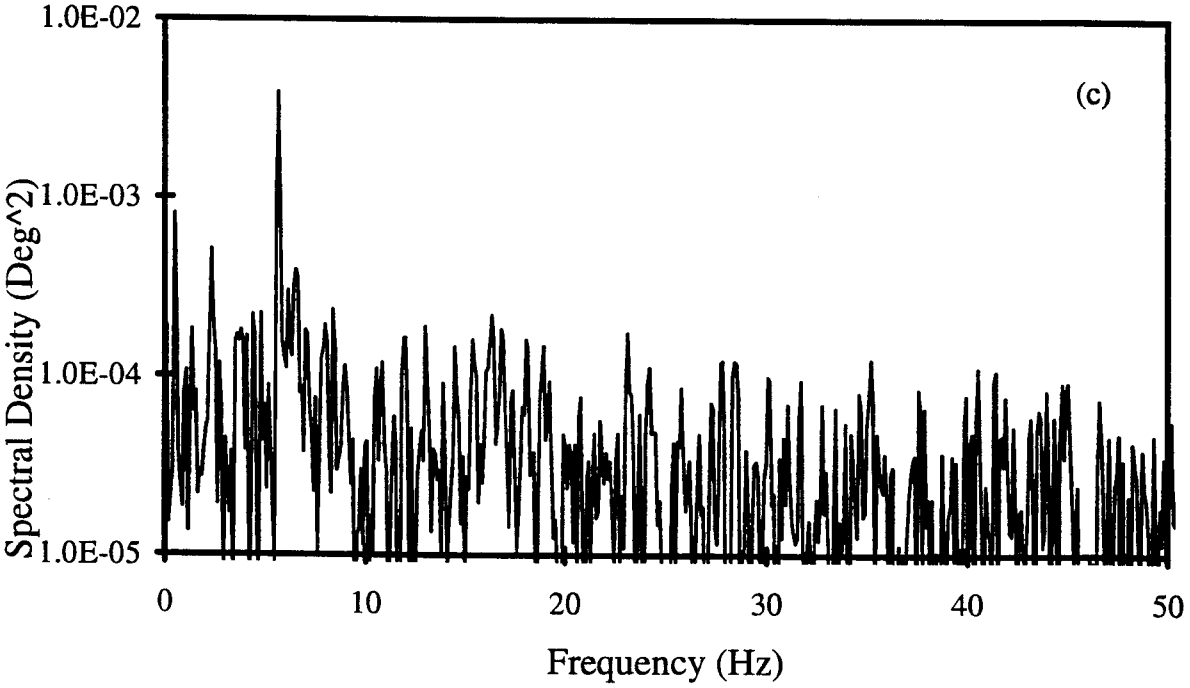
1.0E-02
1.0E-03
1.0E-04
1.0E-05
Spectral Density (Deg^2)
(c)
0
10
20
30
40
50
Frequency (Hz)

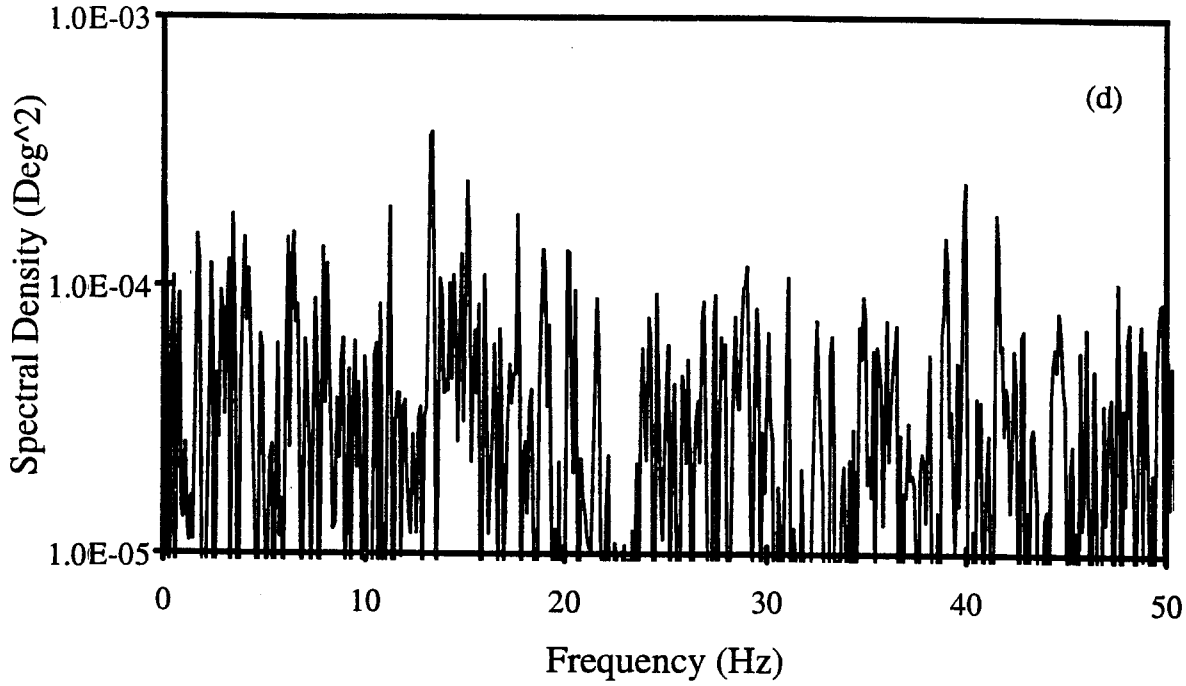
1.0E-03
1.0E-04
1.0E-05
Spectral Density (Deg^2)
(d)
0
10
20
30
40
50
Frequency (Hz)

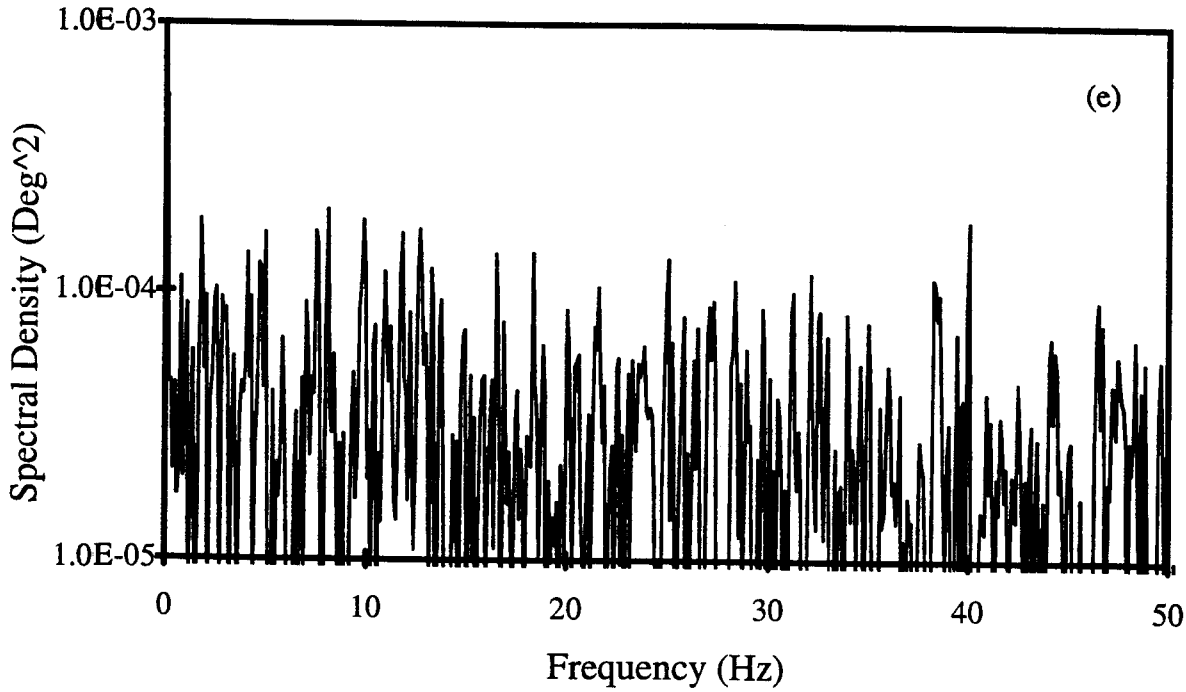
1.0E-03
1.0E-04
1.0E-05
Spectral Density (Deg^2)
(e)
0
10
20
30
40
50
Frequency (Hz)

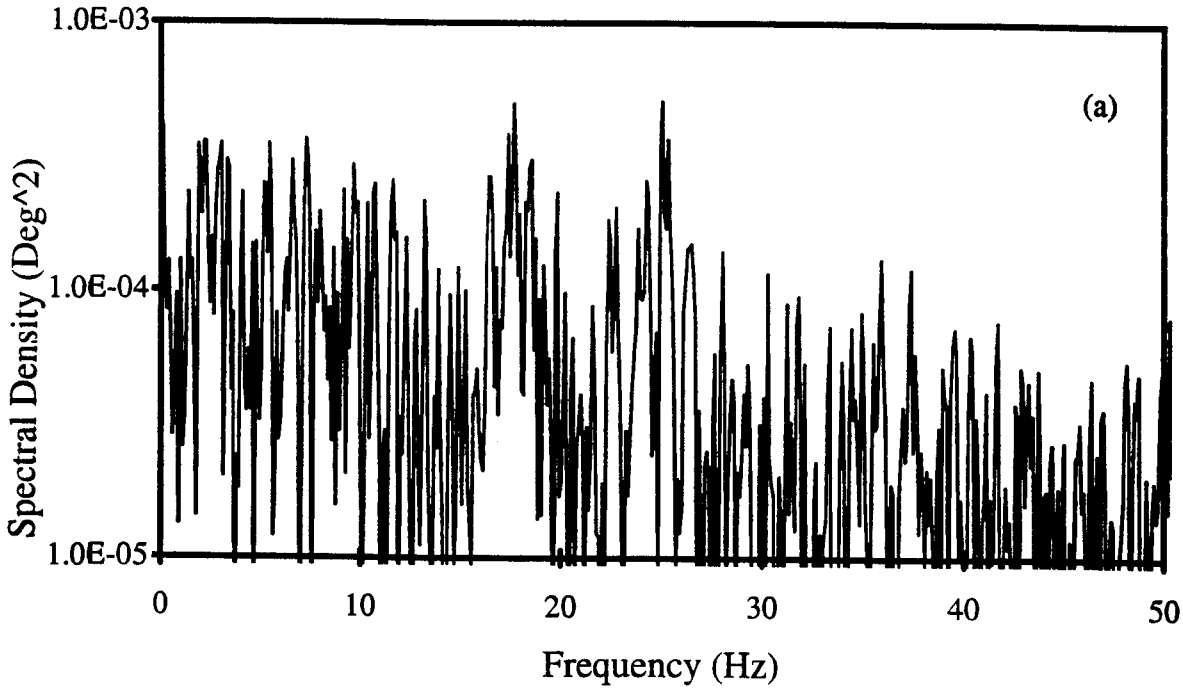

Figure 4.12 Power spectra of the temperature with Ta = 1.48 x 10^7 and Gr_a = 4800, at l/b = 37 and at various axial Reynolds numbers: (a) Re_a = 0 (b) Re_a = 10 (c) Re_a = 670 (d) Re_a = 1300 (e) Re_a = 2000.

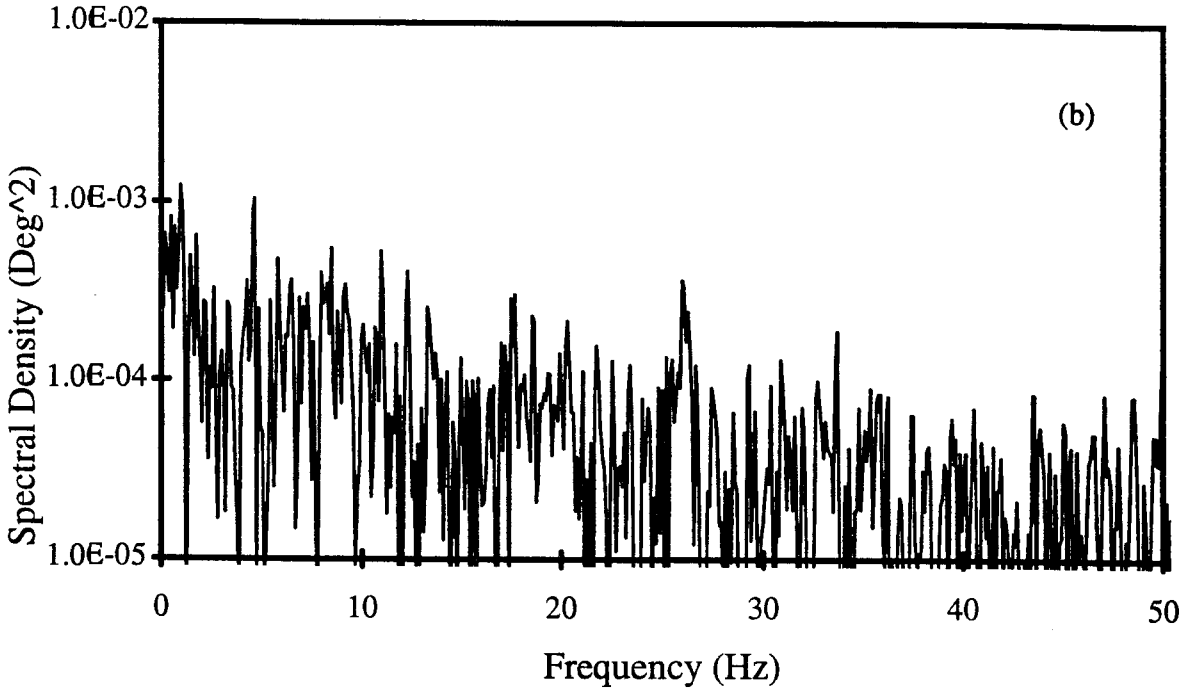
1.0E-02
1.0E-03
1.0E-04
1.0E-05
Spectral Density (Deg^2)
(b)
0
10
20
30
40
50
Frequency (Hz)

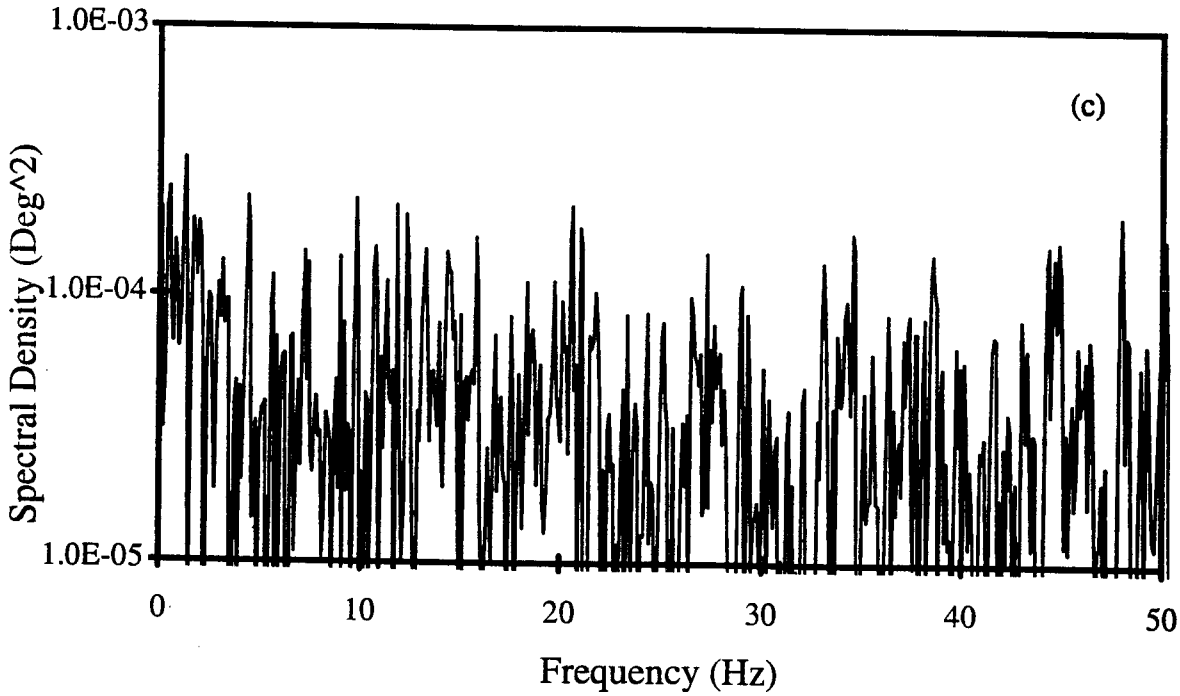
1.0E-03
1.0E-04
1.0E-05
Spectral Density (Deg^2)
(c)
0
10
20
30
40
50
Frequency (Hz)

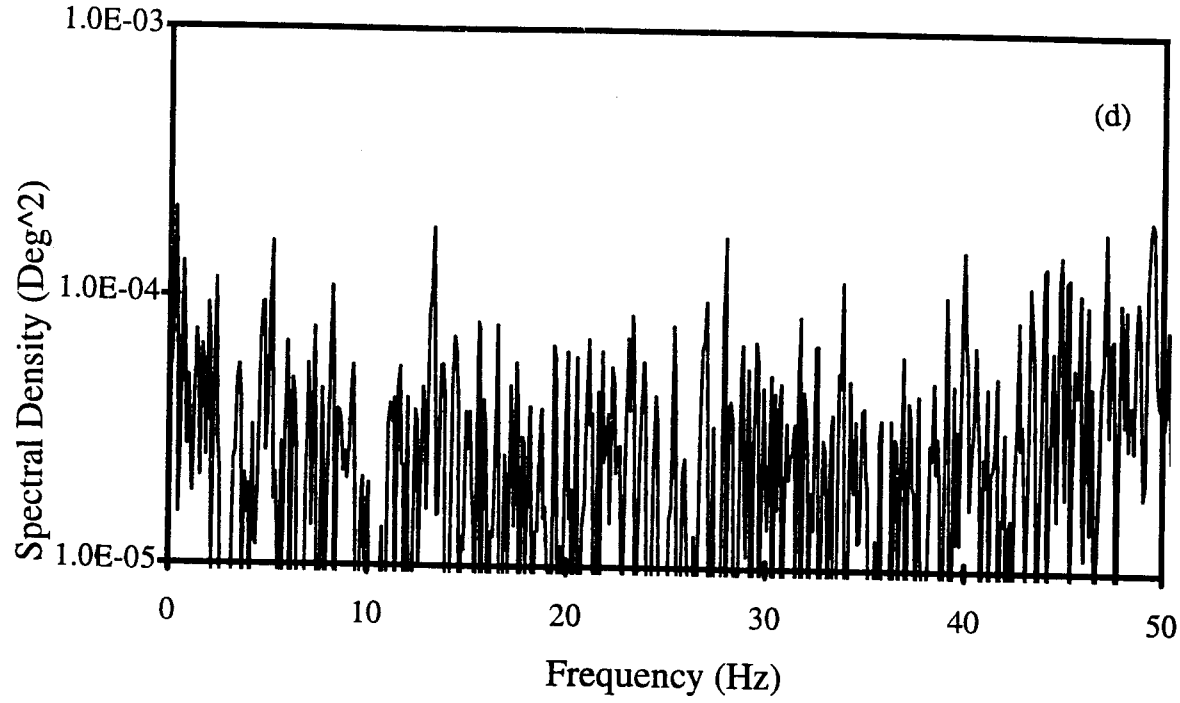
1.0E-03
1.0E-04
1.0E-05
Spectral Density (Deg^2)
(d)
0
10
20
30
40
50
Frequency (Hz)

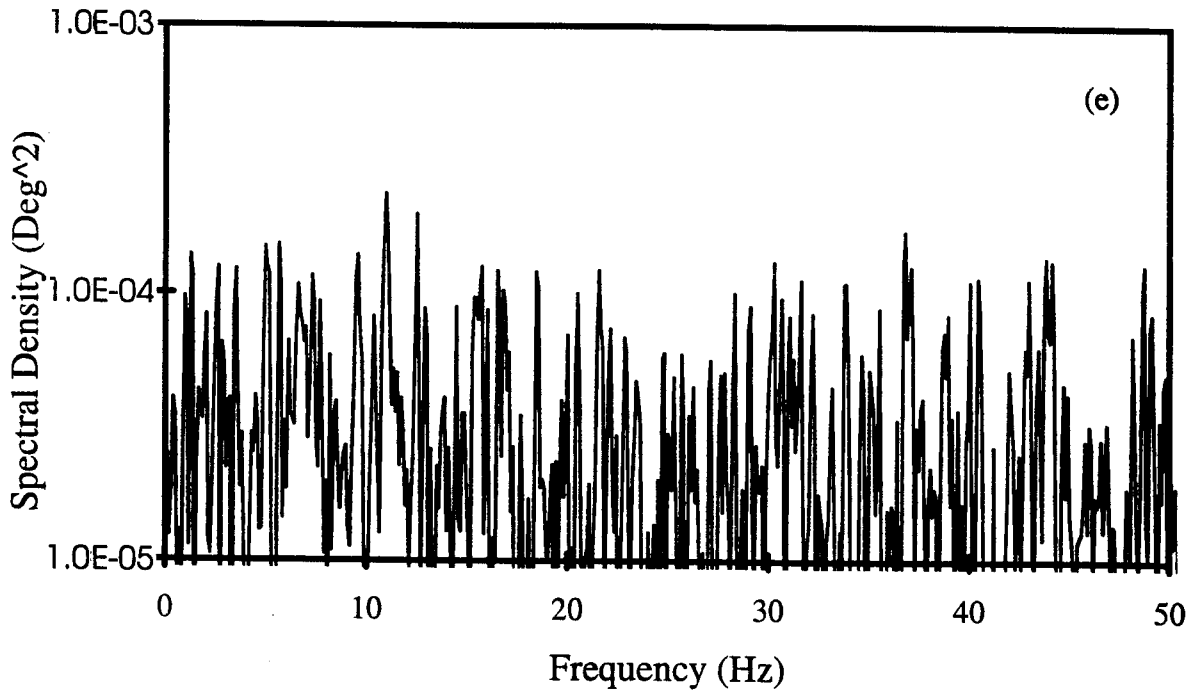
1.0E-03
1.0E-04
1.0E-05
Spectral Density (Deg^2)
(e)
0
10
20
30
40
50
Frequency (Hz)

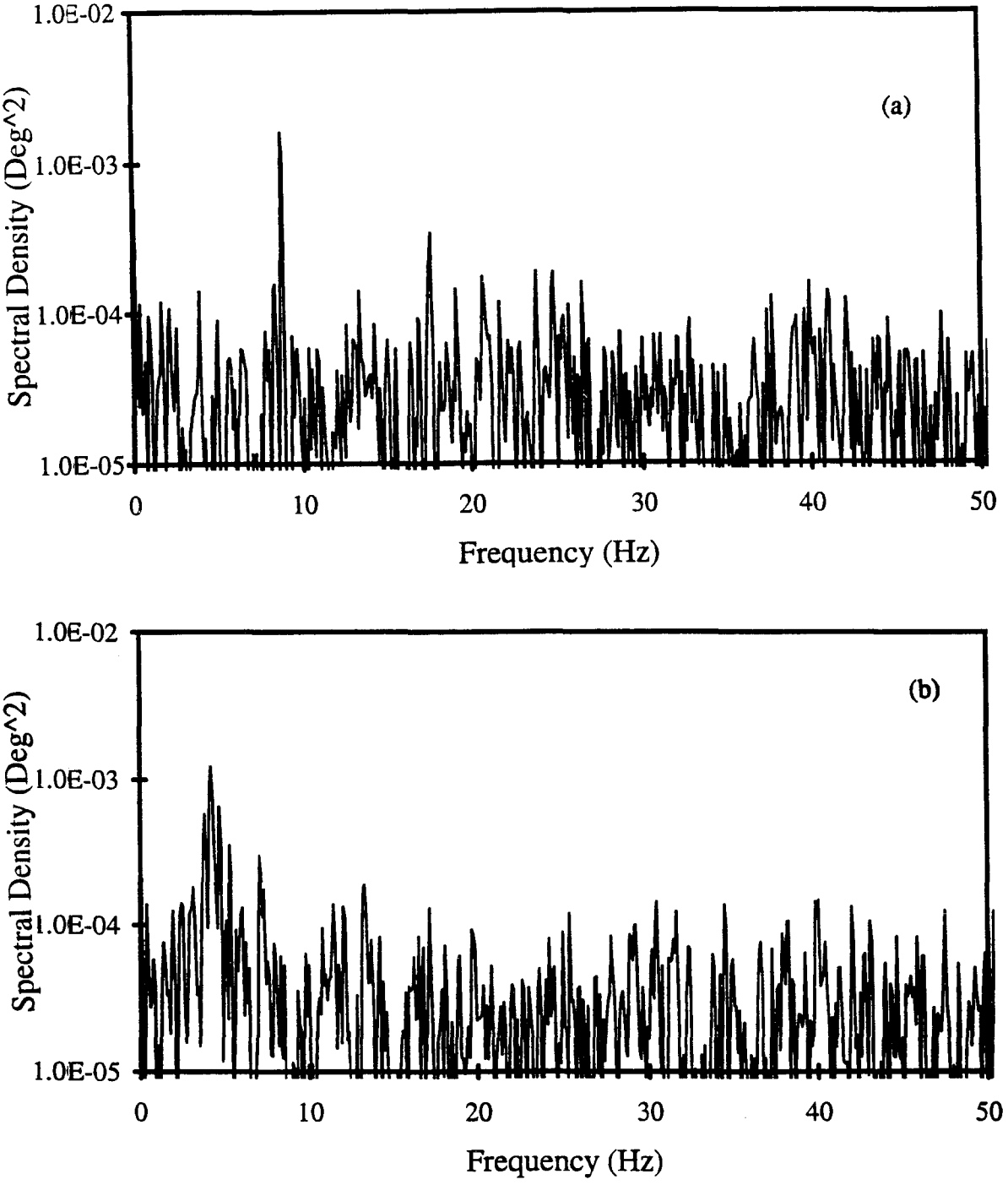

Figure 4.13 Power spectra of the temperature with Ta = 1.48 x 10^7 and Gr_a = 6700, at l/b = 20 and at various axial Reynolds numbers: (a) Re_a = 0 (b) Re_a = 10 (c) Re_a = 670 (d) Re_a = 1300.

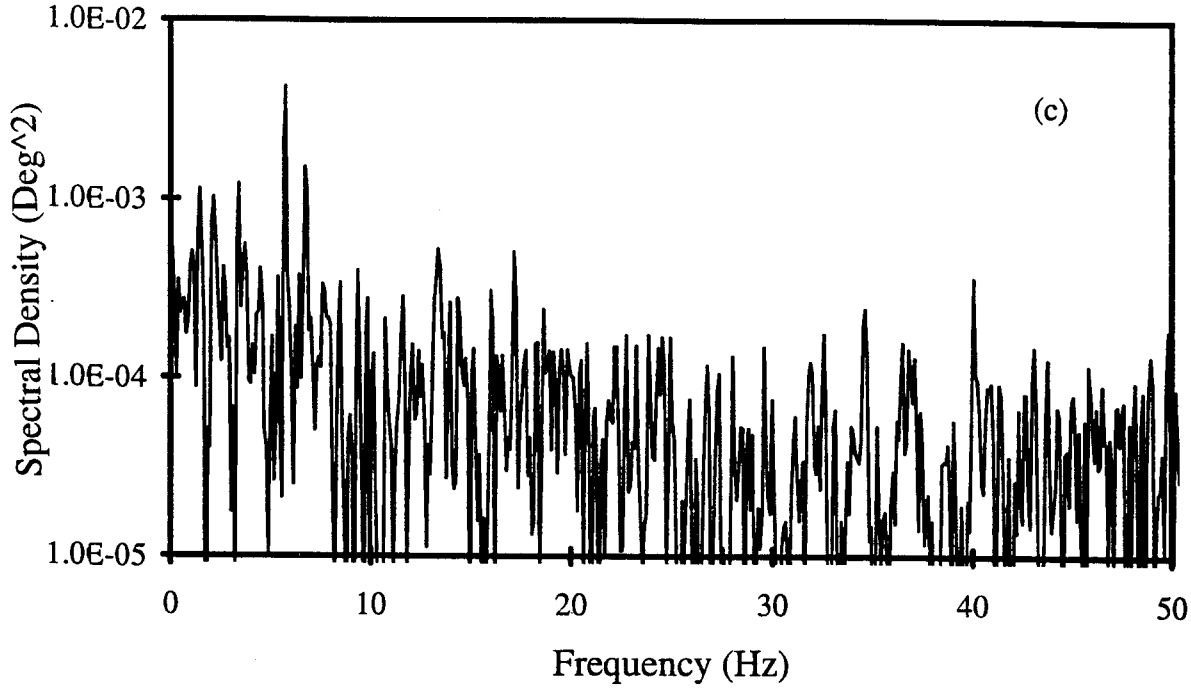
1.0E-02
1.0E-03
1.0E-04
1.0E-05
Spectral Density (Deg^2)
(c)
0
10
20
30
40
50
Frequency (Hz)

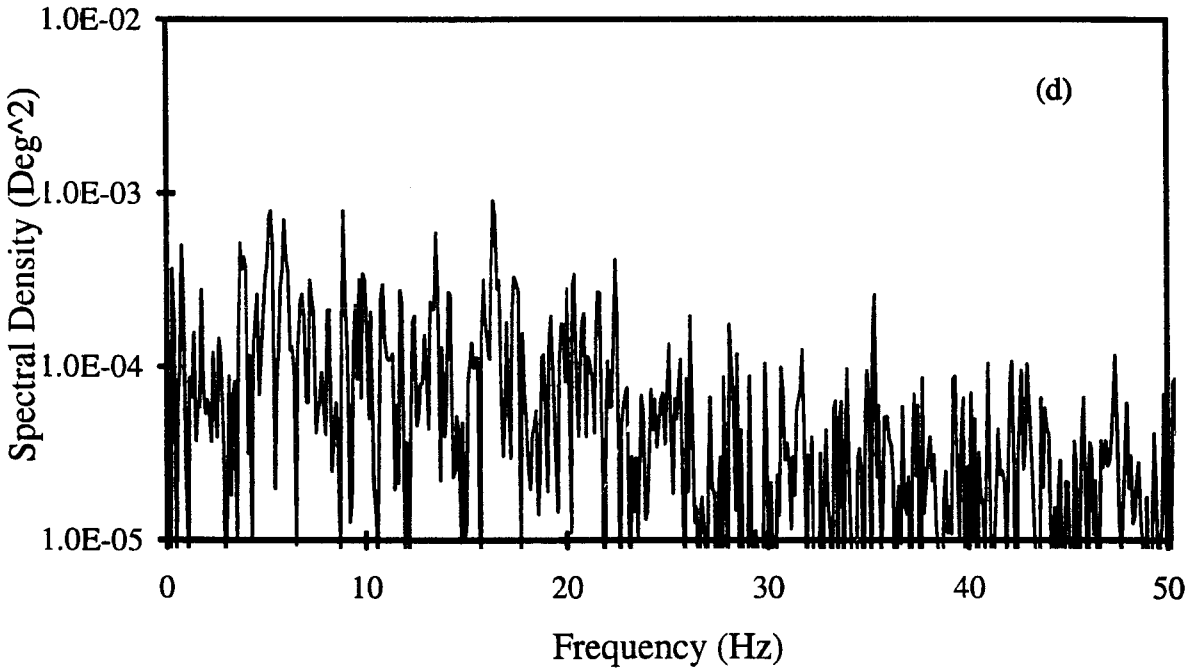
1.0E-02
1.0E-03
1.0E-04
1.0E-05
Spectral Density (Deg^2)
(d)
0
10
20
30
40
50
Frequency (Hz)

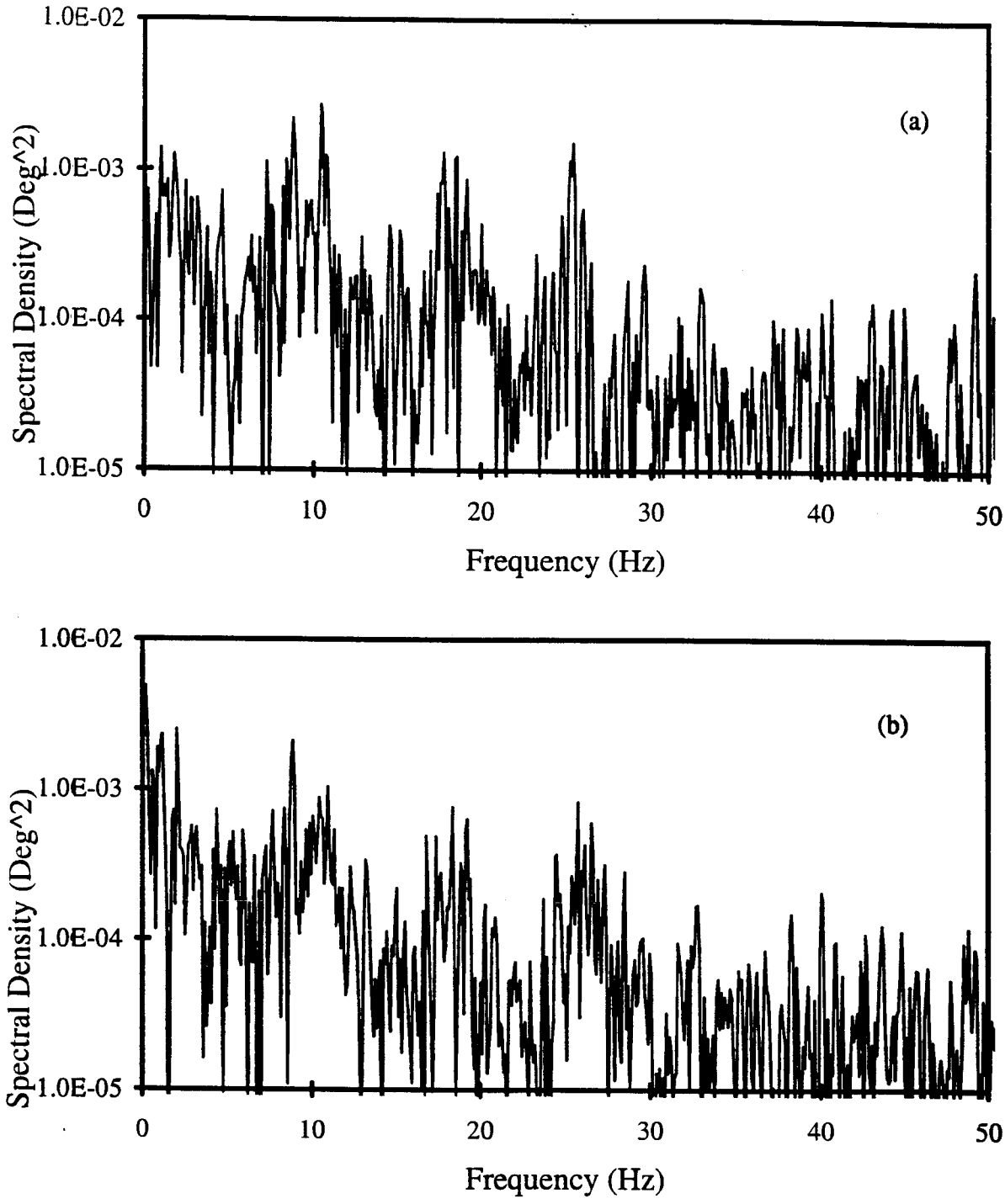

Figure 4.14 Power spectra of the temperature with Ta = 1.48 x 10^7 and Gr_a = 6700, at l/b = 37 and at various axial Reynolds numbers: (a) Re_a = 0 (b) Re_a = 10 (c) Re_a = 670 (d) Re_a = 1300.

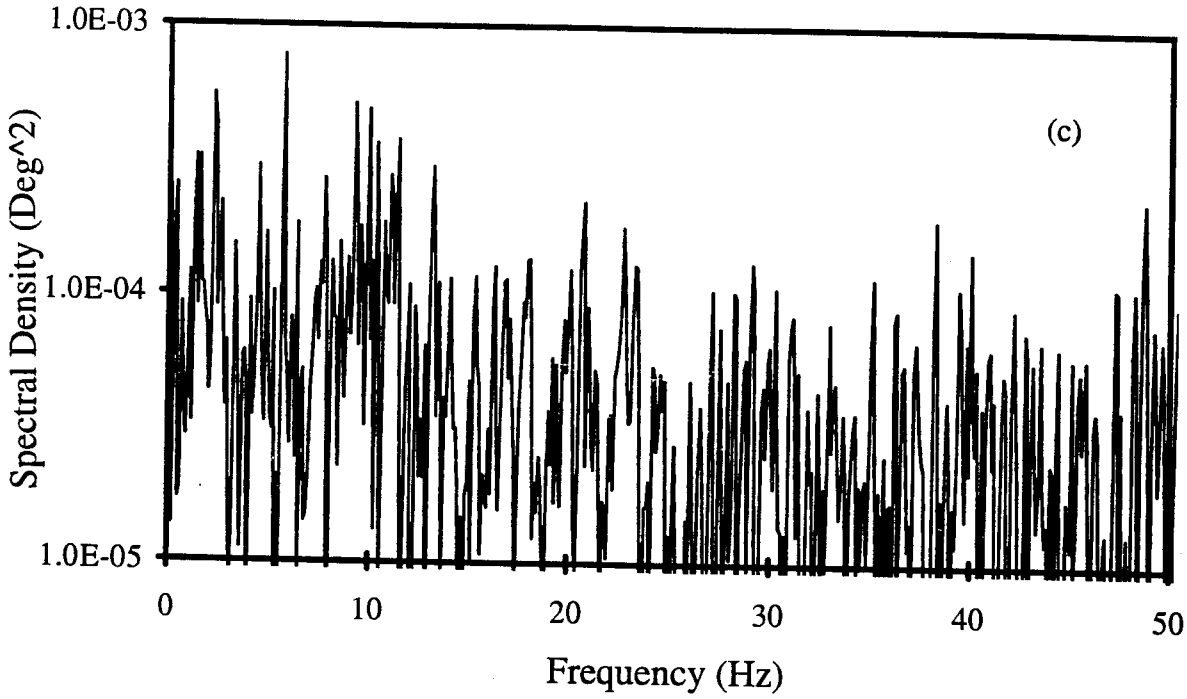
1.0E-03
1.0E-04
1.0E-05
Spectral Density (Deg^2)
(c)
0
10
20
30
40
50
Frequency (Hz)

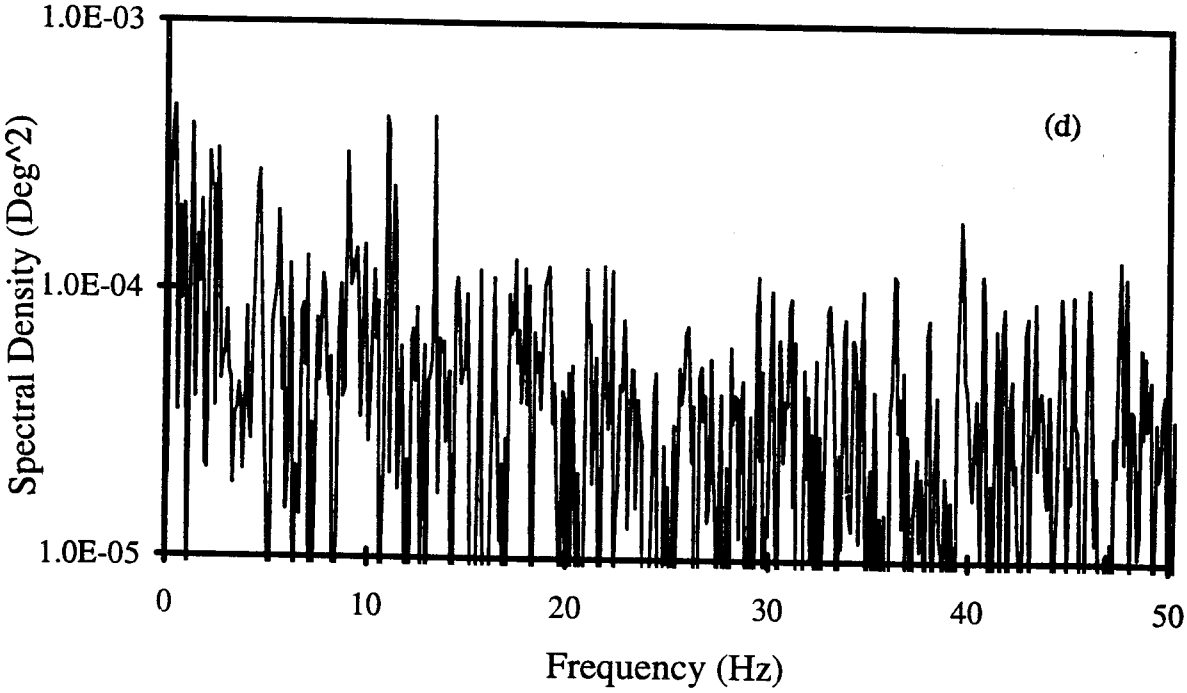
1.0E-03
1.0E-04
1.0E-05
Spectral Density (Deg^2)
(d)
0
10
20
30
40
50
Frequency (Hz)

		Re_a=0	Re_a=10	Re_a=670	Re_a=1300	Re_a=2000
Gr_a=2600	Vel.,l/b=20	0.24 Hz	3.66 Hz	2.81 Hz	6.84 Hz	10.9 Hz
	Temp.,l/b=20	0.12 Hz	3.02 Hz 8.4 Hz	5.66 Hz	N/A	5.07 Hz
	Vel.,l/b=37	0.49 Hz 3.66 Hz 8.3 Hz 12 Hz	2.19 Hz	1.46 Hz 7.32 Hz 12.8 Hz 15.3 Hz	10.5 Hz	14.9 Hz
	Temp.,l/b=37	8 Hz	5.76 Hz 7.03 Hz	N/A	N/A	N/A
Gr_a=4800	Vel.,l/b=20	1.22 Hz	2.19 Hz 6.59 Hz	2.93 Hz	9.39 Hz 15.5 Hz	N/A
	Temp.,l/b=20	1.17 Hz	4.19 Hz 7.12 Hz	N/A	13.4 Hz	N/A
	Vel.,l/b=37	12.6 Hz	2.31 Hz	N/A	10.4 Hz	10.7 Hz 13.4 Hz 15.6 Hz 16.7 Hz
	Temp.,l/b=37	17.4 Hz	0.97 Hz 4.68 Hz	1.27 Hz	0.29 Hz	10.9 Hz
Gr_a=6700	Vel.,l/b=20	4.39 Hz 8.66 Hz	N/A	1.46 Hz 2.56 Hz 6.22 Hz	9.27 Hz	17.0 Hz 22.7 Hz 29.8 Hz
	Temp.,l/b=20	8.79 Hz	4.2 Hz	5.76 Hz	N/A	0.68 Hz
	Vel.,l/b=37	12.6 Hz	8.66 Hz	3.29 Hz	10.3 Hz	15.6 Hz
	Temp.,l/b=37	8.8 Hz 10.5 Hz	0.195 Hz 1.17 Hz 2.05 Hz 8.89 Hz	5.76 Hz	0.39 Hz 10.9 Hz 11.3 Hz	1.76 Hz 2.24 Hz 3.71 Hz 8.5 Hz

Table 4.1 List of frequencies with the maximum spectral strength in both the temperature and velocity spectra at l/b = 20 and 37.

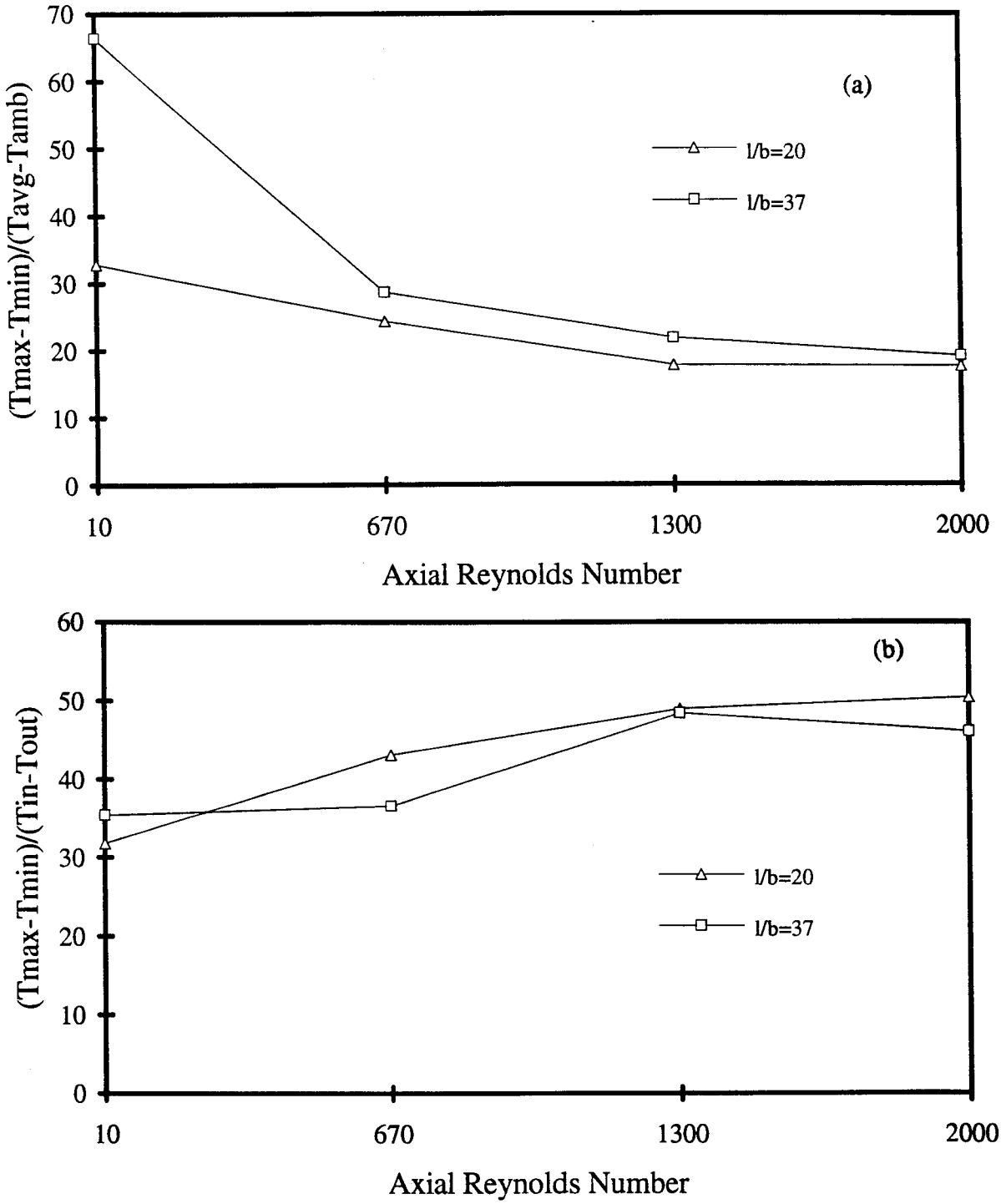

Figure 4.15 Percentage of temperature fluctuation as a function of the axial Reynolds number and different temperature ratio definitions for Gr_a = 6700 at different axial locations (a) $(T_{max} - T_{min})/(T_{avg} - T_{amb})$ (b) $(T_{max} - T_{min})/(T_{in} - T_{out})$.

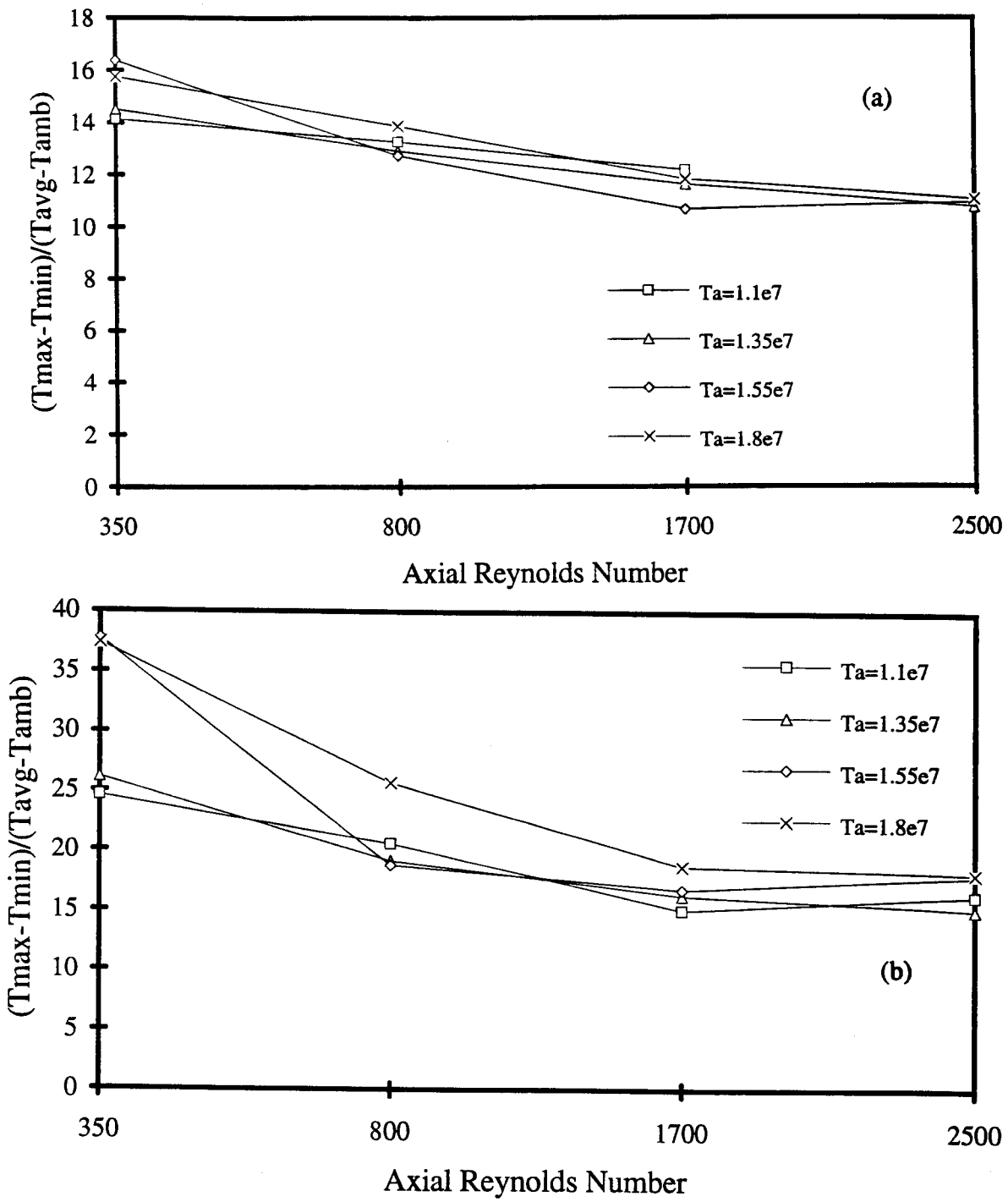

Figure 4.16 Percentage of temperature fluctuation as a function of the axial Reynolds number, Taylor number, and different temperature ratio definitions for Gr_a = 6700 at different axial locations (a) $(T_{max} - T_{min})/(T_{avg} - T_{amb})$, l/b = 20 (b) $(T_{max} - T_{min})/(T_{avg} - T_{amb})$, l/b = 37 (c) $(T_{max} - T_{min})/(T_{in} - T_{out})$, l/b = 20 (d) $(T_{max} - T_{min})/(T_{in} - T_{out})$, l/b = 37.

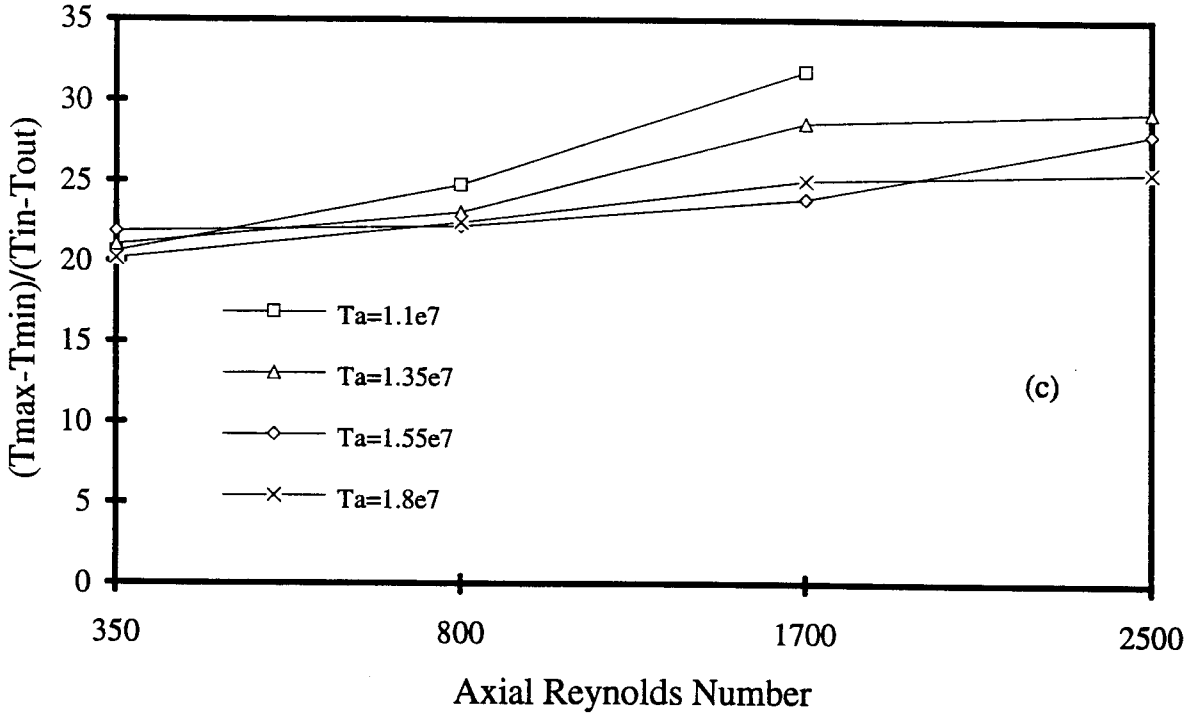
(Tmax-Tmin)/(Tin-Tout)
35
30
25
20
15
10
5
0
350
800
1700
2500
Axial Reynolds Number
Ta=1.1e7
Ta=1.35e7
Ta=1.55e7
Ta=1.8e7
(c)

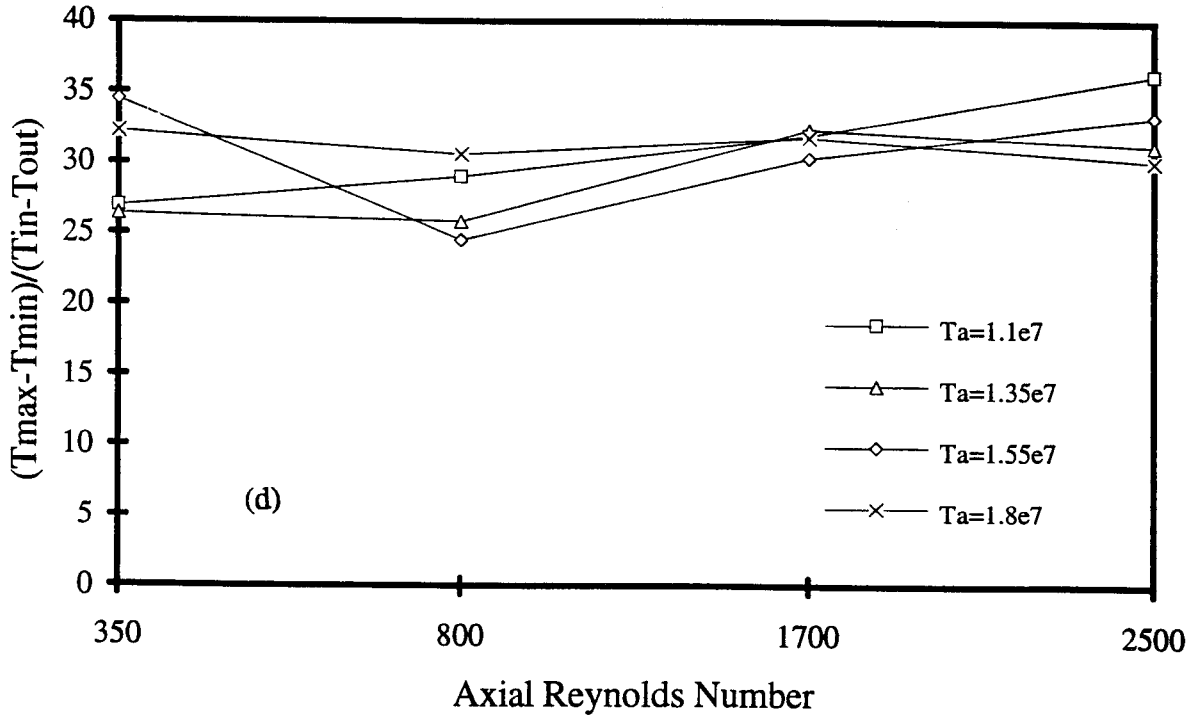
(Tmax-Tmin)/(Tin-Tout)
40
35
30
25
20
15
10
5
0
350
800
1700
2500
Axial Reynolds Number
Ta=1.1e7
Ta=1.35e7
Ta=1.55e7
Ta=1.8e7
(d)